Efficient finite element approach for structural-acoustic applicationns including 3D modelling of sound absorbing porous materials

Romain Rumpler

CONSERVATOIRE NATIONAL DES ARTS ET MÉTIERS

—

ROYAL INSTITUTE OF TECHNOLOGY

le cnam

KTH VETENSKAP OCH KONST

ROYAL INSTITUTE OF TECHNOLOGY

École Doctorale du Conservatoire National des Arts et Métiers

Laboratoire de Mécanique des Strucutres et des Systèmes Couplés (LMSSC)

THÈSE DE DOCTORAT

présentée par : **Romain RUMPLER**

soutenue le : **13 Mars 2012**

pour obtenir le grade de : **Docteur du Conservatoire National des Arts et Métiers**

Spécialité : **Mécanique**

EFFICIENT FINITE ELEMENT APPROACH FOR STRUCTURAL-ACOUSTIC APPLICATIONS INCLUDING 3D MODELLING OF SOUND ABSORBING POROUS MATERIALS

Jury composé de:

M. ATALLA N.	Université de Sherbrooke, Canada	*Rapporteur*
M. DESMET W.	Katholieke Universiteit Leuven (KU Leuven), Belgique	*Rapporteur*
M. RICE H.J.	Trinity College Dublin, Irlande	*Examinateur*
M. CHAMPANEY L.	École Normale Supérieure de Cachan, France	*Président*
M. LEGAY A.	Cnam, France	*Co-encadrant de thèse*
M. GÖRANSSON P.	Royal Institute of Technology (KTH), Suède	*Co-directeur de thèse*
M. DEÜ J.-F.	Cnam, France	*Directeur de thèse*

CONSERVATOIRE NATIONAL
DES ARTS ET MÉTIERS
–
ROYAL INSTITUTE
OF TECHNOLOGY

le cnam

KTH VETENSKAP OCH KONST
ROYAL INSTITUTE OF TECHNOLOGY

School of Engineering Sciences

The Marcus Wallenberg Laboratory for Sound and Vibration Research (MWL)

DOCTORAL THESIS

defended by : **Romain RUMPLER**

Date of defense : **March 13, 2012**

Subject : **Technical Acoustics**

EFFICIENT FINITE ELEMENT APPROACH FOR STRUCTURAL-ACOUSTIC APPLICATIONS INCLUDING 3D MODELLING OF SOUND ABSORBING POROUS MATERIALS

Examination committee composed of:

M. ATALLA N.	University of Sherbrooke, Canada	*Reviewer*
M. DESMET W.	Katholieke Universiteit Leuven (KU Leuven), Belgium	*Reviewer*
M. RICE H.J.	Trinity College Dublin, Ireland	*Opponent*
M. CHAMPANEY L.	École Normale Supérieure de Cachan, France	*President*
M. LEGAY A.	Cnam, France	*Co-supervisor*
M. GÖRANSSON P.	Royal Institute of Technology (KTH), Sweden	*Main supervisor*
M. DEÜ J.-F.	Cnam, France	*Main supervisor*

Acknowledgements

The work presented in this thesis has been carried out within the "Structural Mechanics and Coupled Systems Laboratory" (LMSSC) at Cnam for the first part, and within the "Marcus Wallenberg Laboratory for Sound and Vibration Research" (MWL) at KTH for the last two years. It has been partially supported by a Ph.D. fellowship from the French Ministry of Higher Education and Research, as well as Early Stage Researcher fellowships from the EU Marie-Curie projects *Smart-Structures* (www.smart-structures.eu) and *Mid-Frequency* (www.midfrequency.org). The financial support together with the flexibility offered to produce research works in areas of personal interest are gratefully acknowledged.

I would first like to thank the people who have made this joint PhD possible: Roger Ohayon for welcoming me at the LMSSC lab, and for the nice morning discussions during my time at Cnam, Jean-Françcois Deü for your guidance towards relevant works of the literature, for your kindness and reactive support all along this thesis, and Peter Göransson for welcoming me at KTH, making my life and work over the past two years so enjoyable. Thank you for organizing this collaboration, which gave me, among many other benefits, the opportunity to witness and experience two different approaches of the academic world.

I would also like to thank Antoine Legay for the nice discussions on the finite element method (and for FEAP!), as well as for sharing your teaching experience and passion for it. I owe Georges Venizelos the great teaching opportunities I have been offered during my time at Cnam. Thank you, also, Nils-Erik Hörlin for the interesting discussions on porous materials, and for the useful feedbacks and suggestions you gave on my work.

I gratefully acknowledge the members of the Jury who have accepted the invitation to evaluate this work: Professors Noureddine Atalla and Wim Desmet for their role as reviewers of the manuscript for this thesis, Professors Henry Rice and Laurent Champaney for accepting to be opponent and president of the Jury respectively.

To all the people I met at Cnam and KTH, staff and PhD candidates, who have contributed to create a really nice work environment on a daily basis, which has been so helpful to make these past 3.5 years rich in good memories. Among all, I have to single out Martin for the very pleasant time I had sharing the office with you.

I can't help mentioning Ann-Britt, as well as Ingela and Britt-Inger, for your help in administrative-related issues, and mostly for your patience and support in my massacre of the Swedish language!

Thank you also to the nice friends we have made here in Stockholm, for the lovely moments spent together despite my unpredictable availability during the past few months!

To my family, for the chances and support that I have been given, which have made me quite fulfilled up to this point! My thoughts also go to the regular attentions I have received from my in-laws during these years. Yes, I may soon be finished with "school"!

Finally, I want to thank my wonderful loving wife, Priscilla, primarily for the fantastic journey we have had together, and also for your support and endurance through the rough and uneven path leading to the very end of this work.

Tack alla!

Abstract

Abstract: In the context of interior noise reduction, the present work aims at proposing Finite Element (FE) solution strategies for interior structural-acoustic applications including 3D modelling of homogeneous and isotropic poroelastic materials, under time-harmonic excitations, and in the low frequency range. A model based on the Biot-Allard theory is used for the poroelastic materials, which is known to be very costly in terms of computational resources. Reduced models offer the possibility to enhance the resolution of such complex problems. However, their applicability to porous materials remained to be demonstrated.

First, this thesis presents FE resolutions of poro-elasto-acoustic coupled problems using modal-based approaches both for the acoustic and porous domains. The original modal approach proposed for porous media, together with a dedicated mode selection and truncation procedure, are validated on 1D to 3D applications.

In a second part, modal-reduced models are combined with a Padé approximants reconstruction scheme in order to further improve the efficiency.

A concluding chapter presents a comparison and a combination of the proposed methods on a 3D academic application, showing promising performances. Conclusions are then drawn to provide indications for future research and tests to be conducted in order to further enhance the methodologies proposed in this thesis.

Keywords: Noise reduction, Poroelastic materials, Reduced model, Component mode synthesis, Padé approximants, Structural-acoustics, Finite element method, Fluid-structure interaction.

Résumé

Résumé Dans le contexte de lutte contre les nuisances sonores, cette thèse porte sur le développement de méthodes de résolution efficaces par éléments finis, pour des problèmes de vibroacoustique interne avec interfaces dissipatives, dans le domaine des basses fréquences. L'étude se limite à l'utilisation de solutions passives telles que l'intégration de matériaux poreux homogènes et isotropes, modélisés par une approche fondée sur la théorie de Biot-Allard. Ces modèles étant coûteux en terme de résolution, un des objectifs de cette thèse est de proposer une approche modale pour la réduction du problème poroélastique, bien que l'adéquation d'une telle approche avec le comportement dynamique des matériaux poreux soit à démontrer.

Dans un premier temps, la résolution de problèmes couplés elasto-poro-acoustiques par sous-structuration dynamique des domaines acoustiques et poreux est établie. L'approche modale originale proposée pour les milieux poroélastiques, ainsi qu'une procédure de sélection des modes significatifs, sont validées sur des exemples 1D à 3D.

Une deuxième partie présente une méthode combinant l'utilisation des modèles réduits précédemment établis avec une procédure d'approximation de solution par approximants de Padé. Il est montré qu'une telle combinaison offre la possibilité d'accroître les performances de la résolution (allocation mémoire et ressources en temps de calcul).

Un chapitre dédié aux applications permet d'évaluer et comparer les approches sur un problème académique 3D, mettant en valeur leurs performances encourageantes. Afin d'améliorer les méthodes établies dans cette thèse, des perspectives à ces travaux de recherche sont apportées en conclusion.

Mots clés: Matériaux poroélastiques, Modèles réduits, Sous-structuration dynamique, Approximants de Padé, Vibroacoustique interne, Éléments finis, Interaction fluid-structure.

Contents

List of Tables

List of Figures

Introduction

The present work aims at proposing solution strategies for interior structural-acoustic applications including 3D modelling of homogeneous and isotropic poroelastic materials, under time-harmonic excitations, and in the low frequency range. The systems studied are limited to simple test applications, consisting of enclosed acoustic fluid cavities, coupled to a flexible structure and/or a porous sound absorbing material domain.

In this introduction, the scientific context of the present work is first given, presenting the background as well as the objectives, followed by a description of the practical organization of the thesis in the context of a cotutelle agreement between the Conservatoire National des Arts et Métiers (Cnam), Paris and the Royal Institute of Technology (KTH), Stockholm. The last two sections will introduce the structure of the manuscript, as well as the main contributions achieved during this thesis.

Scientific context. In the transport industry (automotive, aerospace, rail, ...), there is an increasing challenge to satisfy customer's comfort, e.g. considering noise and vibration levels, together with constraints in terms of safety, cost, fuel efficiency, environmental requirements, ... Among the existing solutions to control the interior noise and vibration levels, passive solutions, closely linked to the structural design, have been extensively used. Their popularity lies in their ease of use, range of possible designs and combinations, and in the fact that no external source of energy is required. To mention a few, viscoelastic sandwich configurations are used to reduce the level of structural vibrations, while poroelastic materials have been widely introduced in the design of sound packages to reduce both structure- and air-borne noise. These latter are appreciated for their high noise-reduction-efficiency-to-weight ratio. On the other hand, efforts are done to propose active control solutions, particularly in the range where they perform better than passive solutions (e.g. in the low frequency range [1]), or for some specific applications such as the vibration control of rotating blades in aeronautics.

The wide range of possible solutions together with conflicting constraints imply trade-offs in the design, which have to be taken into account in an integrated way during the

early steps of the process. Furthermore, the existing possibilities are usually combined to take full advantage of their complementary properties, thus offering increasingly complex assemblies. From a design perspective, an early integration of such combinations of materials, e.g. metallic, viscoelastic, poroelastic, composite, requires various degrees of detailed multiphysics computational approaches. Therefore, tools capable of a fine modelling of the physics in an efficient way are of the utmost importance to satisfy the design requirements under industrial constraints.

Among these tools, the Finite Element Method (FEM) has been widely used, due to its suitability and performance in a wide range of situations. However, modelling industrial structural-acoustic problems using the FEM can lead to very large models, which may be prohibitively costly in terms of computational resources (time and memory). There are several potential reasons driving the computational costs:

- the geometrical dimension of the problem, if complete systems are modelled at once,
- the multiphysics nature of the problem including different materials, involving refined meshes in regions with shorter wavelengths (e.g. poroelastic materials),
- the frequency range of interest, as extending the models towards medium-frequencies also implies refined meshes,
- the need to capture local geometrical complexities.

Furthermore, the need for cost-efficient simulation tools is very important not only in the scope of very large models, but also in areas where repeated analyses are required. For instance, optimization procedures, such as topology optimization, involve the analysis of several problems of comparable size. Therefore, any small improvement can make a substantial difference over the cumulated analyses. Similarly, deterministic approaches for the analysis of propagation of uncertainties (increasingly important when reaching the medium-frequency range) respond to the same need of efficiency due to repeated simulations. This is even emphasized if multi-frequency direct solutions are performed, such as for the examples considered in this thesis. Finally, inverse estimations of parameters for sophisticated material models, such as for poroelastic materials, is another area involving multiple analyses, benefiting from efficient solution strategies.

In the low frequency range, the use of modal synthesis together with substructuring strategies has been widely used for conservative systems. In fact, it allows an overall reduction of the size of the problem to solve, which is mostly beneficial for repeated calculations. Furthermore, it is compatible with a segmented concurrent approach between several teams of engineers, working on the design of different areas of a mechanical system. However, it is reputed as rather inappropriate for dissipative systems including

non-proportional damping, such as sound absorbing porous materials. Recent works have nonetheless questioned the possibility to use such an approach in the case of poroelastic materials, and it is one of the objectives of the present thesis to explore such a possibility in more depth.

Work environment and description. The work for this thesis has been performed in the context of a joint supervision ("cotutelle" agreement) between the 'Structural Mechanics and Coupled Systems Laboratory' at Cnam, Paris, and the 'Marcus Wallenberg Laboratory for Sound and Vibration Research' at KTH, Stockholm. It can be decomposed into two parts which approximately correspond to the periods of time spent first at Cnam, and then at KTH.

The first half of the thesis mostly consisted in the implementation of FE tools in an existing Fortran code, FEAP, a general purpose finite element analysis program developed by Prof. R.L. Taylor at the University of California, Berkeley, USA. It is very well suited for the implementation of user elements, which I performed at the beginning of the thesis. As such, the following isoparametric elements were implemented, or adapted for further use in coupled structural-acoustic problems in the frequency domain: 8-node acoustic brick element, 8-node equivalent fluid poroelastic element, 8-node displacement ($\mathbf{u}_s$,$\mathbf{u}_f$) poroelastic element, adaptation of a quad shell element accounting for hysteretic damping, as well as the 4-node quad coupling elements between structure and acoustic elements, acoustic and poroelastic elements. Of course, as for any implementation, depending on your personal starting point, many challenging surprises come along the way. One example is the retrieval of the efficient mapping of local-to-global degrees of freedom (dofs), as acoustic pressure, solid displacement and poroelastic displacements variables are simultaneously used in a coupled problem. Other features such as the implementation of global indicators (mean quadratic pressure in a cavity, mean quadratic velocity on a plate) had to be integrated. Once the elementary tools implemented for the analysis of porous damped structural-acoustic problems, two objectives arose: (i) to test the performances of a standard Component Mode Synthesis (CMS) applied only to the conservative part of such a coupled problem, and (ii) to estimate the influence of sound absorbing boundary conditions. This led to the implementation, at global FE level (working on the assembled global matrices), of a restrained-interface substructuring approach for the modal-based reduction of acoustic subdomains. Although being a more engineering-related than research-oriented part of the thesis, this was the first step towards an extension to the modal-based reduction of poroelastic materials. While rather interesting, implementation-wise, it turned out to be a very time-consuming step, from which I extracted a few personal conclusions: (i) it is rather complicated to get involved into someone else's code (especially in parts not

specifically documented for user implementation), particularly if most of the needed information are to be retrieved form the code itself, (ii) the evaluation of a model reduction has to account both for its performance, and its potential ease of implementation in existing codes.

Following this first half, started a period entirely dedicated to the testing of potential efficient solution approaches for poroelastic materials. This was mostly performed over the second half of the thesis, taking place in the host laboratory, MWL, in Stockholm. Considering the impracticalities of implementations at a global level in FEAP for mere testing, it was dropped and replaced by simple Matlab models (following works initiated at Cnam), well suited for quicker implementation and testing. Among these tests, the conclusive trials are summarized in the present work.

Structure of the document. The present document is organized into 6 chapters. In **chapter 1**, a presentation of the scientific areas, related to the present work, is presented. It includes a literature review of the existing models for sound absorbing porous materials, together with comments on the numerical methods used for structural-acoustic problems. Following this presentation, the choices made for the thesis in terms of models and numerical methods are introduced. **Chapter 2** presents a restrained-interface component mode synthesis approach for the acoustic domain of a coupled structural-poro-acoustic problem. It is implemented in a Fortran code, and the analysis draws conclusions about the performance and limitations of the approach. In **chapter 3**, the poroelastic equations for the classical displacement formulation are rearranged, in order to be suitable for a modal-based analysis. Consequently, a modal-approach is proposed, based on a standard eigenvalue problem for the coupled poroelastic equations. It is enhanced in **chapter 4** where a sorting and selection procedure of the calculated modes is proposed, leading to a further reduced problem. **Chapter 5** presents a reconstruction strategy based on Padé approximants, suited for the efficient calculation of frequency responses. It is applied to poro-acoustic applications formulated after the propositions made in chapters 3 and 4. Thus its combination to reduced models is tested, and the complementarity between the two approaches is illustrated. Furthermore, a simple scheme for the automatic selection of main frequencies is proposed, thus allowing an efficient adaptive frequency sweep. Conclusive remarks together with perspectives for future works are given in **chapter 6**.

Overview of the main contributions. The main contributions included in the present thesis are summarized as follows:

- The performance analysis of a restrained-interface CMS technique for acoustic subdomains is presented for coupled elasto-poro-acoustic problems. The implementation

is entirely done in an existing FE code, in Fortran (*chapter 2*).

- An FE approach for 3D modelling of poroelastic materials is proposed, suitable for standard modal analysis of the coupled equations (*chapter 3*).
- A modal-based reduction of a poroelastic domain included in a poro-acoustic application is proposed. Its ease of implementation and performance in simple 1D to 3D configurations are demonstrated (*chapter 3*).
- A sorting and selection procedure for poroelastic modes is presented and tested on 2D and 3D poro-acoustic simple configurations. It is shown to enhance the performances of the proposed modal approach (*chapter 4*).
- A reconstruction scheme based on Padé approximants is applied to a poro-acoustic problem. It is tested on both the non-reduced and porous-reduced forms of the problems, as proposed in the previous chapters (*chapter 5*).
- An adaptive scheme for the choice of main frequencies in the Padé-based approach is proposed. It enables an efficient automatic calculation and reconstruction of entire frequency responses (*chapter 5*).

Chapter 1

An introduction to 3D modelling of sound absorbing porous materials in structural-acoustic applications

Abstract: *This chapter introduces the scientific fields related to the thesis. A literature review of the existing models for sound absorbing porous materials is presented, together with an overview of suitable numerical techniques developed for the modelling of damped structural-acoustic problems. Conclusions are drawn in terms of objectives and choices made for the works included in this thesis.*

Contents

1.1 Introduction

In this chapter, an overview of the scientific areas related to this thesis are presented. It includes the presentation of sound absorbing porous materials and structural-acoustic models together with their dedicated numerical techniques. The aim is to position the present work in its scientific context, and to draw conclusions in terms of assumptions and objectives. The chapter is organized around four parts. The first part is entirely dedicated to the review of related works in the literature. It includes a definition of sound absorbing porous materials as assumed in this work, a historical background of the corresponding models, and a presentation of the models and numerical techniques used both for poroelastic materials and more generally structural-acoustic applications. The second part illustrates the benefits of using complex 3D models for porous materials. An overview of the most commonly used formulations for poroelastic materials is then presented in a third section. Finally, modal-based reduced models are presented, in the scope of their applicability to damped structural-acoustic applications.

1.2 Modelling of porous materials in structural-acoustic applications

What is a porous material? In the context of this work, porous materials refer to heterogeneous materials made of an elastic solid frame saturated by a fluid. It thus consists of two phases interacting with each other, namely a solid phase defining the skeleton of the material, and a fluid phase which occupies the remaining space, or the pores. There are two types of pores, as illustrated in Fig. 1.1, those corresponding to cavities enclosed in the skeleton, and those interconnected, which are referred to as open pores (open cells is also commonly found in the literature). The former type can be considered, from a mechanical viewpoint, as part of the skeleton, modifying its local material properties [2]. The second type, due to significant fluid-structure interaction triggered by dynamic disturbances, induces dissipation processes which can be put to advantage in acoustics for noise reduction purposes. In addition, porous dissipating materials may be separated into two categories: geomaterials (studied in the context of oil prospection for instance), and sound absorbing materials. The latter are considered in the scope of the present work.

Sound absorbing porous materials, whose pores are filled with a compressible fluid such as air, exhibit interesting dissipative properties which make them a popular solution for passive noise reduction. Three types of mechanisms contribute to the energy dissipation: (i) damping due to irreversible losses in the frame (structural damping), (ii) thermal losses due to thermal transfer between solid and fluid phases, and (iii) viscous losses due to small

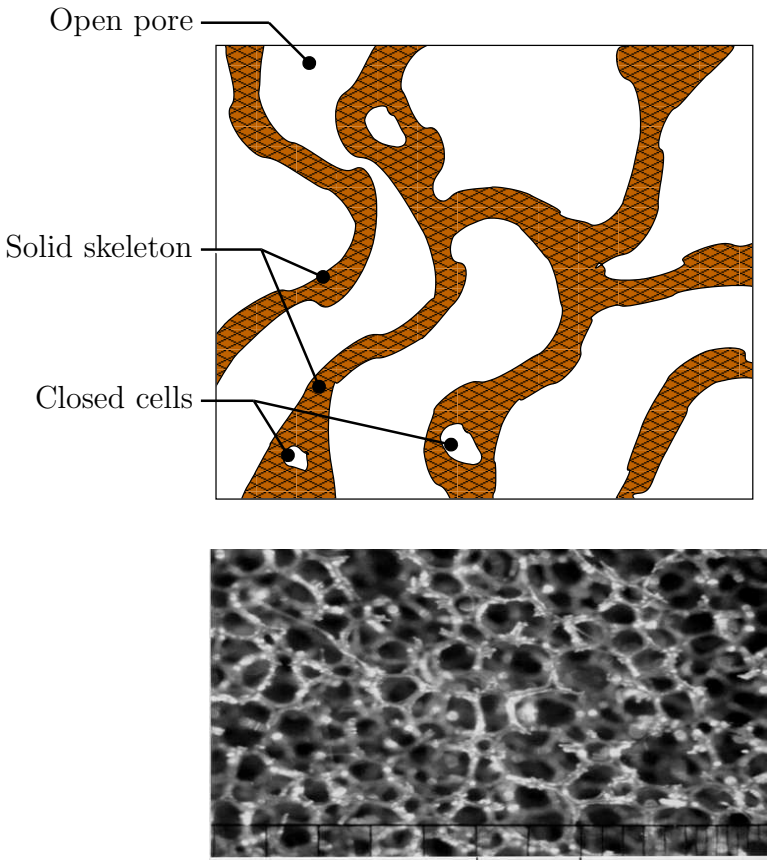

Figure 1.1: A porous material: Top, 2D illustration; Bottom, picture (Courtesy of KU Leuven Laboratory of Acoustics and Thermal Physics).

dimensions of the pores compared to wavelength, possibly implying significant boundary layer effects in which viscous interactions (viscous drag) between the solid and fluid phases lead to inertial coupling and viscous dissipation.

The multiphysics nature of sound absorbing porous media together with their complex phenomenology have been given extensive attention over the past 60 years, giving rise to the theory of sound absorbing porous materials. It provides a description of the mechanical behaviour of porous materials for accurate modelling, thus offering the possibility to refine tailored design for industrial applications. The main developments leading to the models used in the present work, which are based on the Biot-Allard theory for sound absorbing porous materials, are presented in the next section.

A review of the theory for modelling porous sound absorbing materials. The work by Zwikker and Kösten [3], in 1949, is considered as a consistent early contribution to porous materials modelling. Strong assumptions limited the generality of their approach:

solid and fluid phases were treated separately, the solid phase was partially treated as motionless, and the pores were considered cylindrical, of circular section, and having the same direction. However, it included several contributions, further developed since then, leading to the present version of the theory, introducing: (i) a decoupling frequency above which acoustic waves propagating in the fluid do not involve motion of the solid phase, (ii) viscous interactions via an equivalent fluid density, complex and frequency-dependent, and (iii) thermal interactions via an equivalent bulk modulus, complex and frequency-dependent. Thus, viscous effects associated with inertial phenomena, as well as thermal effects included into the constitutive behavior, are two contributions that have remained in the present theories for modelling sound absorbing porous materials.

Among enhancements following the work by Zwikker and Kösten, Attenborough proposed, in 1983 [4], a modified formulation accounting for more complex geometries of the pores. In parallel, Delany and Bazley provided a significant simplified approach for fibrous materials, in 1970 [5], based on two material parameters only: the flow resistivity and the density. Given its simplicity, it is still used today although with some improvements.

However, the major novelty in the history of sound propagation modelling in fluid-saturated porous media was introduced by Biot from 1956 [2, 6, 7]. He proposed a continuum mechanics approach for modelling porous materials as an equivalent homogeneous material. His idea was to consider a time and space superposition of the two continua at the macroscopic scale, typically large compared to heterogeneous characteristic length (size of the pores). Thus, at a macroscopic scale, he assumed the existence of a Representative Elementary Volume (REV), sufficiently small with respect to the wavelength of the phenomena, for which a homogenized description of the superposed solid and fluid coupled phases could be derived. This presented a significant step, leading to the modelling of a heterogeneous material with an homogeneous description. Biot further established the idea of three propagating waves within the media: two compressional waves, a slow and fast wave, respectively propagating out of phase and in phase in the solid and fluid domains, as well as a shear wave. Initially developed for geomechanics, the theory proposed by Biot is today the basis for most commonly accepted formulations in acoustics of poroelastic media, with refinements made to better account for dissipative processes.

Among the significant refinements made to the Biot theory, Johnson et al. [8] proposed an improved description of the viscous effects. They introduced a viscous characteristic length Λ, accounting for the frequency-dependence of viscous effects. Similarly to the contribution made for viscous effects, Champoux and Allard [9] introduced a thermal characteristic length Λ', accounting for the frequency-dependence of thermal effects.

To that point of the theoretical refinements, Allard published a synthesis of the latest advances in a book considered as a standard reference [10] in the field. Even though

further improvements have been proposed since then, the so-called Johnson-Champoux-Allard model of the Biot theory is the most commonly used today. It is fully documented in the reference book by Allard [10, 11], outlining the refinements made to the Biot theory, often referred to as the Biot-Allard theory.

Recent contributions to the theory include those by Lafarge et al. [12], who introduced an additional parameter, the static thermal permeability k_0', to better account for the frequency-dependent thermal effects, particularly in the low frequency range.

Furthermore, following the introduction of anisotropic modelling by Biot [7], recent developments have been added in this area [13–17]. They have been partly encouraged by the increased capabilities of computational resources. However, developments regarding the modelling of inhomogeneous porous materials or the modelling of non-linear behavior, are beyond the scope of the present work.

Numerical techniques for modelling of poroelastic materials. Refinements of the Biot theory have been paralleled with the development of numerical methods. Over the past 20 years, the improved theory has been included in increasingly advanced numerical models, leading to a wide range of proposed methods. Analytical solutions put aside (as limited to very simple configurations), numerical techniques used to solve complex configurations can be separated into two categories: the semi-analytical methods which take partly advantage of analytical solutions under suitable assumptions, and the discretization methods which apply for more general cases.

Semi-analytical methods: Under strong assumptions, impedance boundary conditions can be used to account for poroelastic materials. For instance, in the context of the finite element method, it is very tempting to use such an approach when applicable, as it implies a costless change of boundary conditions [18–24]. However, it is valid exclusively under the assumption of a locally reacting surface to a normal or set oblique incidence, backed with either a rigid wall or another type of semi-infinite layer. The normal incidence acoustic impedance can be easily determined experimentally using the Kundt's tube apparatus. If a poroelastic material has been characterized according to the Biot theory, both analytical and numerical 1D solutions can be used to establish the relation between pressure and normal velocity at the surface of the sample. This step is actually often used as an early validation test for the implementation of numerical formulations. Even though not always applicable, it has been used extensively both in academic and industrial applications. Its ease of implementation and its computational efficiency make it an attractive tool for early estimations in the design process.

In an extended approach for bidimensional configurations, the Transfer Matrix Method (TMM) was developed [25, 10, 11]. It establishes a layer-wise relation between stresses

and velocities on each side of the layer. Its convenience lies in the low computational cost, and its efficient handling of multilayer sound packages, for which an equivalent transfer matrix results from a simple multiplication of transfer matrices established for each layer. It is however limited to infinite bidimensional plane setups. Even if corrections have been proposed to account for finite size conditions [26, 27], the rather strong assumptions make it difficult to adapt to complex situations. It is nonetheless very well suited for qualitative testing of multilayer sound packages.

Increasing the geometrical complexity of the problems that can be handled, the Wave Based Method (WBM) [28], which has proved its efficiency for structural-acoustic applications [29–33], has recently been applied to poroelastic materials [34, 35]. It is a numerical technique, which, rather than being based on an element discretization, applies globally defined wave functions satisfying the governing dynamic equations. The response at a given frequency is thus expressed as a summation of wave function contributions, which result from an integral formulation of the problem boundary conditions. Its main limitations lie in the admissible geometrical complexity of the problems to deal with. In fact, it was shown [28] that a sufficient condition for its convergence is to have convex geometries. Problems not satisfying this condition imply a need for decomposition in subdomains or coupling to element discretization methods. Furthermore, the applicability of the method to 3D modelling of poroelastic materials is still under development.

Element discretization techniques: Due to their suitability for dynamic analysis of arbitrarily shaped systems, the element based methods have been given extensive attention in order to propose accurate 3D modelling of sound absorbing porous materials in structural-acoustic applications. In addition, due to their ability to accurately represent well a large range of problems, they are widely used in the industry for structural-acoustic applications when 3D modelling of porous media is not considered. Thus, it was a natural extension to include such formulations in the existing tools.

Among the element discretization methods, the Finite Element Method (FEM) and the Boundary Element Method (BEM) have been mostly used for vibro-acoustic purposes. The main difference between these two approaches is the fact that a volume discretization is required for the FEM, while using a fundamental solution in the formulation for BEM leads to an approximation made on the boundaries, thus involving a surface discretization. The direct consequence is a reduced size of problems to solve, with for practical purposes the disadvantage associated with loss of matrix symmetries and the fully populated nature of the matrices. While the BEM can be particularly advantageous for problems with high volume-to-surface ratios, which makes it well suited for problems involving large cavities or external acoustics [36, 37], most of the contributions regarding porous media have been made using the FEM [11].

The main issue raised with the use of FEM for 3D modelling of porous materials is the high computational cost involved. Two reasons explain this limitation: (i) the formulations proposed in line with the original Biot theory naturally implied 6 degrees of freedom per node, associated with the displacement fields of the solid and fluid phases, and (ii) the physics of sound propagation in porous materials involves short wavelengths when compared to other media, which consequently implies a need for refined discretization. Thus, the increased complexity of the problem cones with the expense of the computational cost. In the case of porous materials, it remains prohibitive for large problems, despite the progress made in terms of computational resources.

To improve this issue, several formulations have been proposed in order to increase the computational efficiency, or to propose simplified models, suitable under appropriate assumptions (see details of some selected formulations in Section 1.4). With this objective, equivalent fluid formulations were introduced, as early as 1978, when Craggs proposed an eight-node isoparametric finite element to represent a rigid porous absorbing material [38]. The idea is to describe the porous material with the Helmholtz equation, using a modified complex and frequency-dependent speed of sound. It is practically done using complex and frequency-dependent equivalent expressions of the density and the bulk modulus. The advantage of such formulations is the fact that they involve pressure fluctuation as a primary variable, which makes them most efficient as they involve one degree of freedom per node. Other equivalent fluid formulations, suitable under the assumption of a porous materials with a rigid frame, can be found in the literature [39, 10, 40, 41]. Alternatively, for a limp porous material, a simplified symmetric formulation was proposed by Göransson [42]. The frame material is in this case supposed to be of negligible stiffness, but accounted for its flexibility through an inertial correction.

A much heavier computational burden is involved if the full description of porous media is done using a model based on the Biot-Allard theory. The first formulation, using displacement primary variables both for the solid and fluid phases (denoted $(\mathbf{u}_\mathrm{s}, \mathbf{u}_\mathrm{f})$ in this manuscript), was introduced by Kang and Bolton in 1995, for a 2D case [43]. It was later extended to 3D applications [44, 45]. At the same time, other works proposed displacement formulations involving solid phase displacement and the displacement of the fluid relative to the solid as primary variables (denoted $(\mathbf{u}_\mathrm{s}, \mathbf{w})$ in this manuscript) [46, 47]. In an attempt to reduce the size of the problems to deal with, formulations have then been proposed using a scalar field for the fluid phase. Thus, under the assumption of an irrotational fluid, the fluid displacement potential was introduced by Göransson in order to propose a 5-dof formulation involving the solid phase displacement and the fluid phase pressure fluctuation (denoted $(\mathbf{u}_\mathrm{s}, p_\mathrm{f}, \Psi)$) [48]. It however suffered from an overestimation of the coupling between the fluid and the frame structure undergoing rotational deforma-

tion. The attempt to further downsize the formulations led to mixed formulations using the solid frame displacement and the pressure fluctuation in the fluid phase (denoted $(\mathbf{u}_s, p_f)$). A simplified 1-D approach was proposed by Göransson in 1995 [49], neglecting the strain couplings between the fluid and solid phases. Then, a 3-D formulation was introduced by Atalla et al. in 1998 [50], with the commonly-used assumption in acoustics that the bulk modulus of the saturating fluid and of the in vacuo porous material are negligible compared to the bulk modulus of the frame material. It was later enhanced [51] and made equivalent to the original displacement formulation assuming a time-harmonic excitation, and simplifying the coupling to elastic and poroelastic media. Further formulations have recently been developed (see Section 1.4.4), but due to its reduced number of unknowns, the $(\mathbf{u}_s, p_f)$ formulation by Atalla et al. is today considered as the most efficient.

In order to increase the efficiency, hierarchical implementation of these formulations has been done over the past ten years [52–55]. It presents the advantage of limiting the number of elements needed for discretization while offering the additional possibility to model thiner poroelastic layers than possible with standard linear elements. Moreover, their good convergence properties make it a well suited method for the modelling of multilayer poroelastic assemblies. There is nevertheless a trade-off to be found between the order of polynomial interpolation and the extra-cost involved by the increase of matrix density. They are, furthermore, not standard in commercial FE software implementations, and are limited by the difficulty to model efficiently complex geometries, in situations where the mesh refinement is dictated by the geometry.

Questions arising from the use of poroelastic materials in the scope of structural-acoustic applications. Including 3D modelling of porous materials in structural-acoustic applications raises the questions that have been discussed among the vibroacoustics community: i.e. the choice of discretization method, and the choice of formulation in terms of primary variables [56].

Regarding the choice of numerical method, focusing primarily on the low frequency range, BEM and FEM are the two main methods used today in an industrial context, as introduced in the previous section. While FEM is widely appreciated for its suitability for complex problems (complex geometry, multiphysics coupled problems, ...) at the expense of high computational cost (very dependent on the ability to produce size-optimized meshes), BEM can prove convenient and offer substantial computational efficiency improvements (simplified meshing procedure, simplified modelling of external acoustics, ...). Recently, the development of the WBM offers further increased computational efficiency, performing well over an extended frequency range. It is however still a maturing method, presenting some limitations, such as the geometrical complexity of the problems to solve.

The solutions involve either a problem decomposition into subdomains, thus somehow hampering the efficiency, or coupling to element methods, thus adding a difficulty at the interface.

In the present work, the FEM is chosen as tool for numerical modelling of structural-acoustic applications including sound absorbing materials, for the following reasons:

1. Most of the recent developments made for modelling sound absorbing porous materials using the Biot theory have been made using the FEM. Thus, this work being in the continuation of these developments (see also contributions presented in Section 1.5, [57–60]), the FEM comes as a natural practical tool for dealing with such fully coupled applications;

2. Methods such as modal-based reduction can be used to improve the computational efficiency, especially considering that the low frequency range is of prime interest;

3. It is the most widely used method, and it is an objective of the present work to explore solutions (among other existing solutions) improving its weakest point, i.e. its computational efficiency, particularly when involving 3D modelling of poroelastic materials;

4. The FEM is in the core of the culture of both laboratories in which the present work was performed.

Once the choice of a numerical method is established, the question of the set of primary variables is discussed. This has been given careful attention in the literature [56, 61–64]. In the context of vibroacoustics, in the absence of porous media, where the fluid is considered perfect, a natural set of variables traditionally used includes the pressure-fluctuation scalar field for the fluid, and the displacement vector field for the structure. However, such a formulation leads to non-symmetric coupled matrices after discretization [65–67]. This has two consequences. First, practically speaking, the implementation has to account for an efficient non-symmetric storage of the assembled matrices. It is mentioned here, that for a solution with time-harmonic excitations, the system can be mathematically symmetrized in the limit of dynamic solution, which is another practical issue to account for. Secondly, in the scope of modal analysis for the coupled system, a non-symmetric eigenvalue problem prevents the use of the most efficient solvers at hand, and thus tends to be computationally demanding. Furthermore, it was shown in [56], that it suffers from an undetermined solution in the static case, for which a constraint has to be added. This point has its importance when a modal solution based on the fluid and structure decoupled normal modes is considered for the coupled problem. In this case, accounting for the static acoustic mode in the fluid truncated basis is shown to help for the convergence [68, 56]. There

are several ways to include the acoustic static response: either by explicitly expressing the static pressure in the formulation [68], or by including the static pressure in the basis [69, 70], or by taking into account the impact of the static pressure on the structure via elastic modes [71].

To overcome the non-symmetric nature of the problem, several formulations have been proposed to establish symmetric global matrices. Among them, introducing the fluid velocity potential [72, 73] symmetrizes the problem by transferring the coupling terms to a pseudo-damping matrix, thus not improving the situation regarding the coupled eigenvalue problem. Using the displacement vector field has also been proposed [74, 75], with the major drawback related to the increase in the dimension of the problems to be solved, together with the need to impose the irrotationality of the fluid. Ohayon proposed a symmetrized version by adding a displacement potential unknown for the fluid [68, 56]. The drawback to this approach is the doubled size of the fluid partition due to the added unknown. This point can be partly overcome by a rigorous condensation of the added unknowns using the procedure described in [56] for undamped elastoacoustic problems and used in [20] for a case with dissipative interface. This approach results in proper symmetric coupled matrices at the expense of additional operations in the assembly process [62] and a loss of sparsity.

The recent developments of these solutions have led to a general implementation of formulations using the Eulerian approach in commercial FE softwares (ANSYS, MSC/Nastran, ABAQUS, SYSNOISE), using the pressure fluctuation as primary variable in the fluid domain. In the context of the present work, where time-harmonic excitations are considered, the solution of problems using formulations based on the acoustic pressure fluctuation can be easily made symmetric (the static case is excluded). Furthermore, the coupled problems treated are decomposed into components according to their nature (fluid, structure or poroelastic material). Thus, only decoupled eigenvalue problems are considered for each component, while the continuity is enforced via attachment functions. In this case, the constraint corresponding to the static case [56] is naturally satisfied. Consequently, the widely used formulation introducing the acoustic pressure fluctuation for the fluid is used in the present work. Extension to other existing formulations in the literature is a straightforward perspective to the present work.

1.3 On the cost and benefits of 3D modelling for sound absorbing materials

In this section, an introductory comparison is made between the use of a normal acoustic impedance boundary condition, as widely used in the industry, and the use of

a 3D model for the poroelastic material (Biot's theory). It is illustrated on a simple poro-acoustic problem, later considered for validation purposes in the present work (see Fig. 1.2). It consists of a hexahedral acoustic cavity with acoustically rigid boundary conditions, except on one wall where absorbing boundary conditions are defined. The absorbing region corresponds to a single porous layer backed by an impervious rigid wall. It is excited by a corner time-harmonic acoustic excitation, and the mean quadratic pressure is measured in the cavity. The theoretical details, not being of interest in this section, are

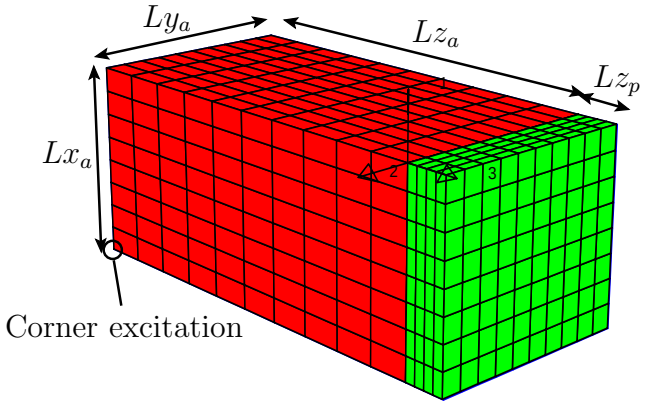

Figure 1.2: Typical poro-acoustic geometry used for comparison between acoustic impedance and 3D poroelastic modelling

given along with the validation cases in this thesis (e.g. in Chapter 2 or 3). This example is of general interest, as it corresponds to conditions for which the use of a normal acoustic impedance should perform best:

- Locally reacting surface is assumed for the poroelastic layer [76];
- The assumption of close to normal incidence is justified by a larger dimension of the cavity along the normal direction with respect to the layer, thus somehow acting as a wave guide. Furthermore, the analysis is limited to the low frequency range;
- The layer is backed by a rigid impervious wall, which corresponds exactly to the boundary conditions for which the normal acoustic impedance is determined.

A 1D finite element model is used to determine numerically the normal acoustic impedance for the poroelastic layer, which was validated against the analytical solution. Including the appropriate boundary condition for the impedance in the 3D finite element model, gives the results presented in Figs. 1.3. They are given for two slightly different geometries of the cavity. It can be observed that, as expected [77, 78], the normal acoustic impedance boundary condition gives a fairly good approximation of the full 3D problem.

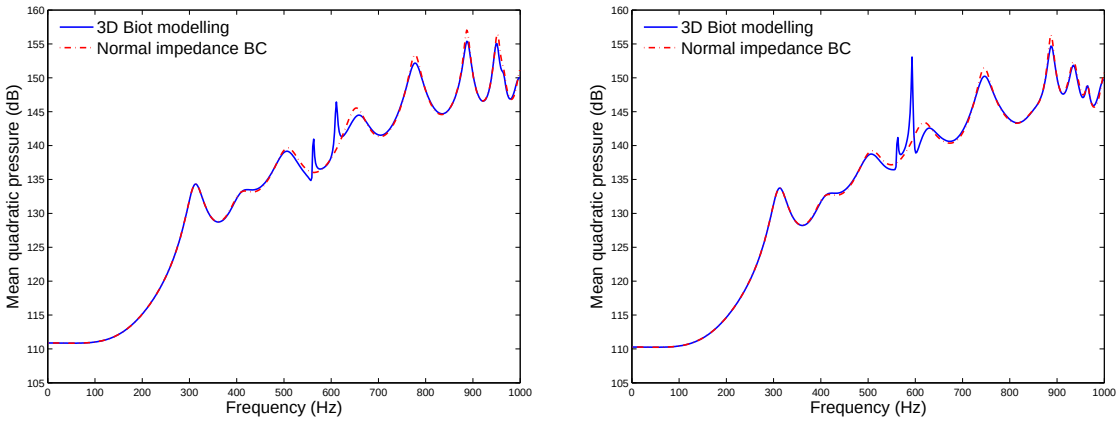

(a) (b)

Figure 1.3: Comparison of the mean quadratic pressure in the cavity using a 3D model or normal impedance boundary condition, $Lz_p = 0.05$ m: (a) $(Lx_a, Ly_a, Lz_a) = (0.28, 0.4, 0.5)$ m; (b) $(Lx_a, Ly_a, Lz_a) = (0.3, 0.4, 0.5)$ m.

However, in this very favorable situation, an overall underestimation of the damping can be observed, particularly noticeable at the damped resonances. Furthermore, in the range $[500 - 600]$ Hz, the dynamic response of the system is not properly approximated by the simplified model. In fact, two resonances of the coupled problem are not well represented using the acoustic impedance boundary condition, due to the lack of in-plane spatial coupling within the layer. The resulting error introduced in the acoustic field within the cavity, is illustrated in Figs. 1.4, where the pressure amplitude in the cavity is plotted, at 593 Hz, i.e. at the second peak of resonance in Fig. 1.3b. A major issue arising from this

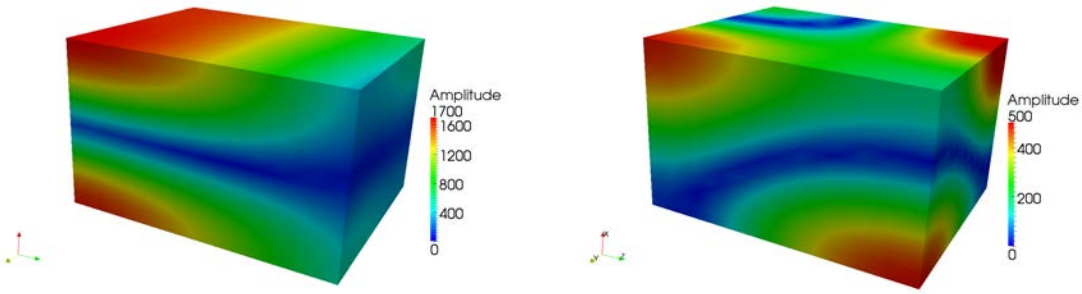

(a) (b)

Figure 1.4: Amplitude of the pressure field in the cavity $(Lx_a, Ly_a, Lz_a) = (0.3, 0.4, 0.5)$ m, $Lz_p = 0.05$ m, at 593 Hz: (a) 3D modelling of porous layer; (b) Normal acoustic impedance boundary condition.

observation, is that using such a simplified approach offers no possibility to detect a posteriori the modelling errors introduced. It remains very attractive and widely used because

there is very little added cost for the solution of the problem: no degree of freedom is added. The only extra cost involved when compared to the conservative problem solution is to solve a complex-valued system of equations. Of course, more sophisticated approaches exist going beyond the extremely restrictive locally reacting surface approach. Still, this simple example illustrates the need for refined models when more than a rough estimation is required. However, as the extra cost is a drawback under industrial constraints, a set of efficient solution strategies have to be considered.

1.4 Biot model for sound absorbing porous materials

This section recalls a few formulations for the porous materials, that have been widely used in the literature: an equivalent fluid model (p_f), the standard ($\mathbf{u}_\mathrm{s}, \mathbf{u}_\mathrm{f}$) displacement Biot-Allard model, and Atalla's mixed ($\mathbf{u}_\mathrm{s}, p_\mathrm{f}$) model. Even though detailed more thoroughly in the chapters when needed, together with the derivation of the variational formulation, an overview is given here, introducing the governing equations as well as the possible boundary conditions.

It is worth clarifying, at this point, some notations used along the thesis. In fact, the problems included in the present work involve acoustic, poroelastic and structural domains. To refer to these physical domains, the following subscripts will be used when needed: '$_\mathrm{F}$' for the acoustic fluid, '$_\mathrm{s}$' and '$_\mathrm{f}$' for the solid and fluid phases of the poroelastic medium, and '$_\mathrm{S}$', for the structural domain. The numeral indexes '$_1$' and '$_2$', classically used in the literature for the solid and fluid phases of the poroelastic material, are saved to refer to Dirichlet and Neumann boundary condition domains.

1.4.1 Equivalent fluid model (p_f)

1.4.1.1 Governing equations

The propagation of sound in a porous material, modeled by an equivalent fluid material, is governed by a modified version of the Helmholtz equation for a time-harmonic excitation. It includes complex (denoted by $\widetilde{\ }$ in the thesis) and frequency-dependent parameters, accounting for viscosity effects as well as thermal exchanges with the connecting frame.

$$\Delta p_\mathrm{f} + \frac{\omega^2}{\widetilde{c}(\omega)^2} p_\mathrm{f} = 0 \tag{1.1}$$

The equivalent speed of sound is calculated with an equivalent bulk modulus and density:

$$\widetilde{c}(\omega) = \sqrt{\frac{\widetilde{K}(\omega)}{\widetilde{\rho}(\omega)}} \tag{1.2}$$

Several models have been proposed for the expressions of $\widetilde{K}(\omega)$ and $\widetilde{\rho}(\omega)$, increasing in complexity in order to refine the captured physics [8, 9, 12]. Further details about the summary presented in this section can be found in [11], Chap. 5. The models presented in this section, as well as in the following, are based on the so-called Johnson-Champoux-Allard model, whose material parameters (solid, fluid and porous parameters) are presented in Table 1.1. Among those parameters, the 5 porous parameters, dependent on the geometry

Table 1.1: List of material parameters

Notation	Description
ρ_{s}	Density of the material constituting the frame
$(\lambda;\, \mu)$	Lamé parameters for the solid frame
η_{s}	Structural damping in the frame
ρ_{f}	Ambient fluid density
η	Ambient fluid viscosity
P_0	Ambient fluid standard pressure
γ	Heat capacity ratio for the ambient fluid
Pr	Prandtl number for the ambient fluid
ϕ	Porosity
α_∞	Tortuosity
σ	Static flow resistivity
Λ	Viscous characteristic length
Λ'	Thermal characteristic length

of the frame, are:

- the *porosity* ϕ, defined as the ratio between the air volume in the open pores and the total volume,
- the *tortuosity* α_∞, relating the actual distance the sound has to propagate to pass through a layer, to the thickness of the layer,
- the *static flow resistivity* σ ($\mathrm{Ns/m^4}$), introducing viscous losses for the sound propagation in the porous material,
- the *viscous characteristic length* Λ (m), introduced by Johnson et al. [8] as a characteristic length providing a correction for the viscous effects, particularly for a better frequency-dependent representation,
- the *thermal characteristic length* Λ' (m), introduced by Champoux and Allard [9] by analogy to the viscous characteristic length, in order to better account for the thermal effects.

The effective density can be introduced in a general form as

$$\widetilde{\rho}(\omega) = \rho_{\mathrm{f}}\,\alpha(\omega), \tag{1.3}$$

where $\alpha(\omega)$, the dynamic tortuosity, accounting for the frequency-dependence of thermal and viscous effects, was given by Johnson et al. [8],

$$\alpha(\omega) = \alpha_\infty \rho_{\mathrm{f}} \left[1 + \frac{\sigma\phi}{i\omega\rho_{\mathrm{f}}\alpha_\infty} G_J(\omega)\right], \tag{1.4}$$

with

$$G_J(\omega) = \left[1 + \frac{4i\omega\alpha_\infty^2\eta\rho_{\mathrm{f}}}{\sigma^2\Lambda^2\phi^2}\right]^{\frac{1}{2}}. \tag{1.5}$$

By analogy to the dynamic tortuosity, similar functions can be defined for the description of the thermal exchanges and the incompressibility. Such a general function, $\alpha'(\omega)$, was used by Lafarge et al. [12] as homologue to $\alpha(\omega)$ and related to the fluid bulk modulus by

$$\widetilde{K}_{\mathrm{f}}(\omega) = \frac{\gamma\, P_0}{\gamma - (\gamma-1)\left[\alpha'(\omega)\right]^{-1}}. \tag{1.6}$$

It followed the idea of Champoux and Allard [9], who showed that the effective density and the equivalent bulk modulus were controlled by different aspects of the pores geometry. Thus, they should be described by different shape factors, and they introduced the thermal characteristic length in their expression corresponding to $\alpha'(\omega)$,

$$\alpha'(\omega) = 1 + \frac{8\eta}{i\omega Pr\Lambda'^2\rho_{\mathrm{f}}}\left(1 + \frac{i\omega Pr\Lambda'^2\rho_{\mathrm{f}}}{16\eta}\right)^{\frac{1}{2}}. \tag{1.7}$$

More advanced expressions, not explicitly presented in this work, exist for $\alpha'(\omega)$ [12, 11]. It can however be mentioned that the expression of Eq. (1.7) can be found from the approach proposed in [12], assuming the thermal dynamic permeability of a porous medium with circular cylindrical pores of radius $r = \Lambda'$. The corresponding thermal dynamic permeability is $q_0' = \phi\Lambda'^2/8$. It was then shown that such an arbitrary choice can lead to a large error in the localization of the transition frequency, for which the imaginary part of the bulk modulus reaches its maximum. This does not necessarily lead to a large error in the evaluation of a surface impedance because the damping is mainly due to the viscosity via the effective density [12], (see section 5.6 in [11]).

Other equivalent fluid models exist (e.g. limp frame), but are not developed in this section as they are not further investigated in the present work.

1.4.1.2 Coupling conditions

Both normal stress continuity as well as normal displacement continuity have to be fulfilled when a porous material, modeled as an equivalent fluid, is in contact with a

structure or a fluid. The frame being considered rigid, the boundary conditions need to account for the volume displacement continuity for the porous materials, thus involving the porosity.

The different possibilities for boundary conditions of a porous material are given below, in contact with:

- an *acoustic fluid*. The normal fluid stress continuity is then expressed as

$$p = p_{\mathrm{f}}, \tag{1.8}$$

  where p_{f} and p denote the acoustic pressure fluctuation in the equivalent fluid and the acoustic fluid respectively. The normal displacement continuity is given by

$$\mathbf{u}_{\mathrm{F}} \cdot \mathbf{n}_{\mathrm{f}} = \phi \mathbf{u}_{\mathrm{f}} \cdot \mathbf{n}_{\mathrm{f}}, \tag{1.9}$$

  where $\mathbf{u}_{\mathrm{f}}$ and $\mathbf{u}_{\mathrm{F}}$ denote the fluid displacement in the equivalent fluid and the acoustic fluid respectively. The normal at the interface, $\mathbf{n}_{\mathrm{f}}$, is pointing outward from the equivalent fluid porous material.

- a *flexible structure*. The continuity between the bonded equivalent fluid and the flexible structure cannot be fulfilled due to the assumption made of a rigid frame. It is therefore assumed that there is an air gap between the structure and the porous material, and that the normal displacement continuity is satisfied at the boundary between the air gap and the structure ($\mathbf{u}_{\mathrm{F}} \cdot \mathbf{n} = \mathbf{u}_{\mathrm{S}} \cdot \mathbf{n}$, $\mathbf{u}_{\mathrm{S}}$ denoting the displacement field of the structure and $\mathbf{n}$ the normal pointing outward from the acoustic fluid domain). Thus, the normal displacement continuity writes

$$\mathbf{u}_{\mathrm{S}} \cdot \mathbf{n}_{\mathrm{f}} = \phi \mathbf{u}_{\mathrm{f}} \cdot \mathbf{n}_{\mathrm{f}}. \tag{1.10}$$

  The normal stress continuity is given by

$$\boldsymbol{\sigma}_{\mathrm{S}}\, \mathbf{n}_{\mathrm{f}} + p_{\mathrm{f}}\, \mathbf{n}_{\mathrm{f}} = 0, \tag{1.11}$$

  where $\boldsymbol{\sigma}_{\mathrm{S}}$ is the Cauchy stress tensor for the structure.

1.4.2 Classical displacement formulation ($\mathbf{u}_{\mathrm{s}}$,$\mathbf{u}_{\mathrm{f}}$) for a dissipative porous medium

This formulation is the one used in the present work due to its suitability to investigate a modal-based approach for the fluid-structure coupled porous material. The details leading to the establishment of the governing equations can be found in [10, 11], and the main results are recalled and commented in this section.

1.4.2.1 Governing equations

The dynamics of elastic porous materials is described by the Biot elastodynamic coupled equations, which are written in two different forms in this work, mainly for numerical implementation purposes. Assuming a time-harmonic dependence of the form $e^{i\omega t}$, they can be written first with the frequency-dependence explicitly detailed, separating viscous and inertial coupling,

$$\operatorname{div}\boldsymbol{\sigma}_{\mathrm{s}} - \mathrm{i}\,\omega\,\widetilde{b}(\omega)(\mathbf{u}_{\mathrm{s}} - \mathbf{u}_{\mathrm{f}}) + \omega^2\left[((1-\phi)\,\rho_{\mathrm{s}} + \rho_{\mathrm{a}})\mathbf{u}_{\mathrm{s}} - \rho_{\mathrm{a}}\mathbf{u}_{\mathrm{f}}\right] = \mathbf{0}, \tag{1.12a}$$

$$\operatorname{div}\boldsymbol{\sigma}_{\mathrm{f}} - \mathrm{i}\,\omega\,\widetilde{b}(\omega)(\mathbf{u}_{\mathrm{f}} - \mathbf{u}_{\mathrm{s}}) + \omega^2\left[-\rho_{\mathrm{a}}\mathbf{u}_{\mathrm{s}} + (\phi\rho_{\mathrm{f}} + \rho_{\mathrm{a}})\mathbf{u}_{\mathrm{f}}\right] \quad = \mathbf{0}. \tag{1.12b}$$

The complex and frequency-dependent viscous drag $\widetilde{b}(\omega)$ accounts for viscous body forces interacting between the solid and fluid phases, proportional to the relative velocity. It is a manifestation of the flow resistivity for the air particles in the pores and can be expressed, introducing $G_J(\omega)$ (Eq. (1.5)) established by Johnson et al., as

$$\widetilde{b}(\omega) = \sigma\phi^2 G_J(\omega) = \sigma\phi^2\left[1 + \frac{4i\omega\alpha_\infty^2\eta\rho_{\mathrm{f}}}{\sigma^2\Lambda^2\phi^2}\right]^{\frac{1}{2}}. \tag{1.13}$$

Furthermore, the tortuosity implies inertial interactions between the vibrating solid and fluid phases, which can be modeled as an added mass to the solid partition. Similarly, the motion of the fluid particles vibrating around the structural frame can be modeled as an increase in the fluid density. Thus the inertial coupling term, related to the tortuosity, is given by

$$\rho_a = \phi\rho_{\mathrm{f}}\,(\alpha_\infty - 1). \tag{1.14}$$

The elastodynamic coupled equations can be expressed in a condensed form if viscous and inertial effects are included into equivalent density expressions, complex and frequency-dependent,

$$\widetilde{\rho}_{\mathrm{s}}(\omega) \;= (1-\phi)\,\rho_{\mathrm{s}} - \widetilde{\rho}_{\mathrm{sf}}(\omega), \tag{1.15a}$$

$$\widetilde{\rho}_{\mathrm{f}}(\omega) \;= \phi\rho_{\mathrm{f}} - \widetilde{\rho}_{\mathrm{sf}}(\omega), \tag{1.15b}$$

$$\widetilde{\rho}_{\mathrm{sf}}(\omega) = -\rho_a + i\,\frac{\widetilde{b}(\omega)}{\omega}. \tag{1.15c}$$

Rewriting Eqs. (1.12) using the equivalent densities expressions (1.15) yields

$$\operatorname{div}\boldsymbol{\sigma}_{\mathrm{s}} + \omega^2(\widetilde{\rho}_{\mathrm{s}}\mathbf{u}_{\mathrm{s}} + \widetilde{\rho}_{\mathrm{sf}}\mathbf{u}_{\mathrm{f}}) = \mathbf{0}, \tag{1.16a}$$

$$\operatorname{div}\boldsymbol{\sigma}_{\mathrm{f}} + \omega^2(\widetilde{\rho}_{\mathrm{sf}}\mathbf{u}_{\mathrm{s}} + \widetilde{\rho}_{\mathrm{f}}\mathbf{u}_{\mathrm{f}}) \;= \mathbf{0}. \tag{1.16b}$$

$\boldsymbol{\sigma}_\mathrm{s}$ and $\boldsymbol{\sigma}_\mathrm{f}$ are the averaged stress tensors for the solid and fluid phases respectively. They satisfy the Lagrangian stress-strain relations developed by Biot:

$$\boldsymbol{\sigma}_\mathrm{s} = 2\widetilde{N}\,\boldsymbol{\varepsilon}(\mathbf{u}_\mathrm{s}) + \left(\widetilde{A}\,\mathrm{tr}\,[\boldsymbol{\varepsilon}(\mathbf{u}_\mathrm{s})] + \widetilde{Q}\,\mathrm{tr}\,[\boldsymbol{\varepsilon}(\mathbf{u}_\mathrm{f})]\right)\mathbf{I}, \tag{1.17a}$$

$$\boldsymbol{\sigma}_\mathrm{f} = -\phi\, p\,\mathbf{I} = \left(\widetilde{Q}\,\mathrm{tr}\,[\boldsymbol{\varepsilon}(\mathbf{u}_\mathrm{s})] + \widetilde{R}\,\mathrm{tr}\,[\boldsymbol{\varepsilon}(\mathbf{u}_\mathrm{f})]\right)\mathbf{I}, \tag{1.17b}$$

where $\widetilde{A}$, $\widetilde{R}$, $\widetilde{N}$, and $\widetilde{Q}$ correspond to the four elasticity coefficients introduced by Biot. They are however complex (and frequency-dependent) in order to take into account the thermal effects as well as the structural damping in the skeleton. These equations, corresponding to the constitutive laws for the solid and fluid phases, are coupled due to a dilatational coupling: the frame stress depends on the frame strain in a similar way to the behavior of an elastic solid, and is also affected by the dilatation of the fluid. Similarly, the pressure variation in the air is affected by the frame dilatation. $\widetilde{A}$ is understood as the Lamé parameter at zero fluid dilatation, and can be written as

$$\widetilde{A} = \widetilde{\lambda} + \frac{\widetilde{Q}^2}{\widetilde{R}}, \tag{1.18}$$

where it may be shown that $\widetilde{\lambda}$ is the Lamé coefficient at zero fluid dilatation. Similarly, $\widetilde{N}$ is the shear modulus of the frame, and can thus be written as $\widetilde{N} = \widetilde{\mu}$. Both $\widetilde{\lambda}$ and $\widetilde{\mu}$ may be defined complex and possibly frequency-dependent to account for structural damping in the frame [79, 80]. A simple model usually adopted in the literature to account for structural damping in the frame, is to use a hysteretic proportional damping model:

$$\widetilde{\lambda} = (1 + i\eta_s)\,\lambda, \tag{1.19a}$$

$$\widetilde{\mu} = (1 + i\eta_s)\,\mu. \tag{1.19b}$$

$\widetilde{R}$ is interpreted as the fluid phase bulk stiffness at zero frame dilatation. Finally, the dilatational coupling factor $\widetilde{Q}$ accounts for the contributions of the air dilatation to the stress in the frame, and of the frame dilatation to the pressure variation in the air in the porous material.

These four elasticity coefficients can be evaluated with the "gedanken experiments" suggested by Biot. They can thus be expressed as functions of the bulk modulus of the elastic material from which the frame is made, K_s, the *in vacuo* bulk modulus of the frame, K_b, and the equivalent bulk modulus of the fluid in the pores, K_f [10]. Due to the increased heat conduction caused by the porous frame, regulating the temperature variation during compression and extension in the acoustic wave, the latter is complex and frequency-dependent. The expression by Champoux and Allard follows from Eqs. (1.6) and (1.7),

$$\widetilde{K}_\mathrm{f}(\omega) = \frac{\gamma P_0}{\gamma - (\gamma-1)\left[1 + \frac{8\eta}{i\omega Pr\Lambda'^2\rho_\mathrm{f}}\left(1 + \frac{i\omega Pr\Lambda'^2\rho_\mathrm{f}}{16\eta}\right)^{\frac{1}{2}}\right]^{-1}}. \tag{1.20}$$

Furthermore, for porous materials with large values for the bulk modulus of the porous frame material compared to those of the frame and the fluid, which is typically the case in acoustic applications, $\widetilde{Q}$ and $\widetilde{R}$ (as well as $\widetilde{A}$) can be assumed as functions of the fluid equivalent bulk modulus $\widetilde{K}_{\mathrm{f}}(\omega)$ alone,

$$\widetilde{R} = \phi \widetilde{K}_{\mathrm{f}}(\omega), \tag{1.21a}$$

$$\widetilde{Q} = (1-\phi)\widetilde{K}_{\mathrm{f}}(\omega), \tag{1.21b}$$

$$\widetilde{A} = \widetilde{\lambda} + \frac{(1-\phi)^2}{\phi}\widetilde{K}_{\mathrm{f}}(\omega). \tag{1.21c}$$

Thus, the coupled constitutive laws of the porous material can be rewritten as functions of $\widetilde{\lambda}$, $\widetilde{\mu}$, and $\widetilde{K}_{\mathrm{f}}(\omega)$ only.

1.4.2.2 Coupling conditions

The different possibilities for boundary conditions of an elastic porous material are given below, when in contact with:

- an *acoustic fluid*. The normal stress continuity conditions are given by

$$\boldsymbol{\sigma}_{\mathrm{s}}\,\mathbf{n} + (1-\phi)\,p\,\mathbf{n} = \mathbf{0}, \tag{1.22a}$$

$$\boldsymbol{\sigma}_{\mathrm{f}}\,\mathbf{n} + \phi\,p\,\mathbf{n} = \mathbf{0}. \tag{1.22b}$$

  The normal displacement continuity at interface is expressed as

$$\mathbf{u}_{\mathrm{F}} \cdot \mathbf{n} - (1-\phi)\mathbf{u}_{\mathrm{s}} \cdot \mathbf{n} - \phi \mathbf{u}_{\mathrm{f}} \cdot \mathbf{n} = 0. \tag{1.23}$$

  These coupling conditions, for the ($\mathbf{u}_{\mathrm{s}}$,$\mathbf{u}_{\mathrm{f}}$) formulation, are taken into account in the variational formulation, leading to surface integrals similar to the classical structural-acoustic coupling terms.

- a *flexible structure*. Two types of boundary conditions can be prescribed, as the porous material can be considered either as sliding or bonded to the structure.

  A bonded porous layer on a flexible structure implies continuity of the displacement field for the solid phase and of the normal displacement component for the fluid phase,

$$\mathbf{u}_{\mathrm{s}} = \mathbf{u}_{\mathrm{S}}, \tag{1.24a}$$

$$\mathbf{u}_{\mathrm{f}} \cdot \mathbf{n}_{\mathrm{P}} = \mathbf{u}_{\mathrm{S}} \cdot \mathbf{n}_{\mathrm{P}}. \tag{1.24b}$$

  where $\mathbf{n}_{\mathrm{P}}$ is the unit normal vector pointing outward from the porous domain, and $\mathbf{u}_{\mathrm{S}}$ the solid displacement vector field.

A sliding porous layer on a flexible structure implies continuity of the normal components of the displacement fields for the solid and the fluid phases with the normal component of the structure displacement field,

$$\mathbf{u}_\mathrm{s} \cdot \mathbf{n}_\mathrm{P} = \mathbf{u}_\mathrm{S} \cdot \mathbf{n}_\mathrm{P}, \tag{1.25a}$$

$$\mathbf{u}_\mathrm{f} \cdot \mathbf{n}_\mathrm{P} = \mathbf{u}_\mathrm{S} \cdot \mathbf{n}_\mathrm{P}. \tag{1.25b}$$

For both these conditions, the continuity of the total normal stresses at interface have to be imposed,

$$(\boldsymbol{\sigma}_\mathrm{s} + \boldsymbol{\sigma}_\mathrm{f})\ \mathbf{n}_\mathrm{P} = \boldsymbol{\sigma}_\mathrm{S}\ \mathbf{n}_\mathrm{P}. \tag{1.26}$$

While the normal stress continuity is naturally taken into account, the displacement continuity conditions Eqs. (1.24) and (1.25) have to be explicitly accounted for in the variational formulation. Practically speaking, for bonded coupling conditions, the solid phase displacement continuity with the structural displacement field can be fulfilled in the assembly procedure.

- another *poroelastic domain*. Considering the case of two porous domains, supposed in a configuration where the pores of the two media are aligned at the interface, continuity of the solid-phase displacement vector fields as well as the relative mass flux across the interface have to be imposed,

$$\mathbf{u}_\mathrm{s}^{(1)} = \mathbf{u}_\mathrm{s}^{(2)}, \tag{1.27a}$$

$$\phi^{(1)} \left(\mathbf{u}_\mathrm{f}^{(1)} - \mathbf{u}_\mathrm{s}^{(1)}\right) \cdot \mathbf{n}_\mathrm{P} = \phi^{(2)} \left(\mathbf{u}_\mathrm{f}^{(2)} - \mathbf{u}_\mathrm{s}^{(2)}\right) \cdot \mathbf{n}_\mathrm{P}. \tag{1.27b}$$

Furthermore, the continuity of the total normal stresses is given by,

$$\left(\boldsymbol{\sigma}_\mathrm{s}^{(1)} + \boldsymbol{\sigma}_\mathrm{f}^{(1)}\right)\ \mathbf{n}_\mathrm{P} = \left(\boldsymbol{\sigma}_\mathrm{s}^{(2)} + \boldsymbol{\sigma}_\mathrm{f}^{(2)}\right)\ \mathbf{n}_\mathrm{P}. \tag{1.28}$$

Similarly to coupling conditions with a flexible structure, normal stress continuity is naturally satisfied while the displacement continuities have to be taken into account via surface integral terms in the variational formulation or enforced during the assembly procedure (solid phase displacement continuity).

1.4.3 Mixed formulation ($\mathbf{u}_\mathrm{s}$,p_f)

The mixed displacement-pressure formulation for poroelastic materials was developed in an effort to reduce the computational burden, using the pressure fluctuation in the pores, p_f, a scalar field, rather than the displacement of the fluid phase $\mathbf{u}_\mathrm{f}$, a vector field. The main steps leading to the governing equations are presented, together with the boundary conditions to take into account for coupling with other media.

1.4.3.1 Governing equations

The changes made with respect to the displacement formulation previously presented can be introduced in the expressions of the stress tensors, rewritten depending on the fluid pressure field rather than the fluid displacement. Thus, multiplying the fluid constitutive equation Eq. (1.17b) by $\frac{\widetilde{Q}}{\widetilde{R}}$, and substituting in Eq. (1.17a) for elimination of the terms in $\mathrm{tr}\,[\boldsymbol{\varepsilon}(\mathbf{u}_\mathrm{f})]$, yields the following expressions of the stress tensors,

$$\boldsymbol{\sigma}_\mathrm{s} = 2\widetilde{\mu}\,\boldsymbol{\varepsilon}(\mathbf{u}_\mathrm{s}) + \widetilde{\lambda}\,\mathrm{tr}\,[\boldsymbol{\varepsilon}(\mathbf{u}_\mathrm{s})]\;\mathbf{I} - \phi\,\frac{\widetilde{Q}}{\widetilde{R}}\,p\,\mathbf{I} = \hat{\boldsymbol{\sigma}}_\mathrm{s} - \phi\,\frac{\widetilde{Q}}{\widetilde{R}}\,p\,\mathbf{I}, \tag{1.29a}$$

$$\boldsymbol{\sigma}_\mathrm{f} = -\phi\,p\,\mathbf{I}, \tag{1.29b}$$

where $\hat{\boldsymbol{\sigma}}_\mathrm{s}$ is the stress tensor of the frame *in vacuo*. The updated version of the elastodynamic Eqs. (1.16) thus yields

$$\mathrm{div}\,\hat{\boldsymbol{\sigma}}_\mathrm{s} - \phi\,\frac{\widetilde{Q}}{\widetilde{R}}\,\mathbf{grad}p + \omega^2(\widetilde{\rho}_\mathrm{s}\mathbf{u}_\mathrm{s} + \widetilde{\rho}_\mathrm{sf}\mathbf{u}_\mathrm{f}) = \mathbf{0}, \tag{1.30a}$$

$$-\phi\,\mathbf{grad}p + \omega^2(\widetilde{\rho}_\mathrm{sf}\mathbf{u}_\mathrm{s} + \widetilde{\rho}_\mathrm{f}\mathbf{u}_\mathrm{f}) = \mathbf{0}. \tag{1.30b}$$

Further, the fluid phase equation Eq. (1.30b) is used to substitute for the fluid displacement vector $\mathbf{u}_\mathrm{f}$ in the solid phase equation, Eq. (1.30a), given

$$\mathbf{u}_\mathrm{f} = \frac{\phi}{\widetilde{\rho}_\mathrm{f}\,\omega^2}\,\mathbf{grad}p - \frac{\widetilde{\rho}_\mathrm{sf}}{\widetilde{\rho}_\mathrm{f}}\mathbf{u}_\mathrm{s}, \tag{1.31}$$

leading to the solid phase elastodynamic equation

$$\mathrm{div}\,\hat{\boldsymbol{\sigma}}_\mathrm{s} + \omega^2\widetilde{\rho}\mathbf{u}_\mathrm{s} + \widetilde{\gamma}\,\mathbf{grad}p = \mathbf{0}, \tag{1.32}$$

with

$$\widetilde{\rho} = \widetilde{\rho}_\mathrm{s} - \frac{\widetilde{\rho}_\mathrm{sf}{}^2}{\widetilde{\rho}_\mathrm{f}}, \tag{1.33a}$$

$$\widetilde{\gamma} = \phi\left(\frac{\widetilde{\rho}_\mathrm{sf}}{\widetilde{\rho}_\mathrm{f}} - \frac{\widetilde{Q}}{\widetilde{R}}\right). \tag{1.33b}$$

Finally, noticing that the fluid phase constitutive equation Eq. (1.17b) implies

$$-\phi\,p = \widetilde{Q}\,\mathrm{div}\,\mathbf{u}_\mathrm{s} + \widetilde{R}\,\mathrm{div}\,\mathbf{u}_\mathrm{f}, \tag{1.34}$$

to be combined with the divergence of the fluid phase equation Eq. (1.30b),

$$\Delta p - \omega^2\frac{\widetilde{\rho}_\mathrm{f}}{\phi}\,\mathrm{div}\,\mathbf{u}_\mathrm{f} - \omega^2\frac{\widetilde{\rho}_\mathrm{sf}}{\phi}\,\mathrm{div}\,\mathbf{u}_\mathrm{s} = 0, \tag{1.35}$$

for elimination of the fluid displacement vector $\mathbf{u}_\mathrm{f}$, the fluid phase elastodynamic equation reads

$$\Delta p + \omega^2 \frac{\widetilde{\rho}_\mathrm{f}}{\widetilde{R}}\, p - \omega^2 \frac{\widetilde{\rho}_\mathrm{f}}{\phi^2} \widetilde{\gamma}\, \mathrm{div}\, \mathbf{u}_\mathrm{s} = 0. \tag{1.36}$$

Therefore, the governing equations for the ($\mathbf{u}_\mathrm{s}$,p_f) formulation are the elastodynamic equations (1.32) and (1.36) for the solid and fluid phases respectively, together with the constitutive equation for the *in vacuo* solid frame included in Eq. (1.29a), and the expressions of $\widetilde{\rho}$ and $\widetilde{\gamma}$ given in Eqs. (1.33).

1.4.3.2 Enhanced coupling conditions [51]

Essentially, the coupling conditions of a porous medium described with the ($\mathbf{u}_\mathrm{s}$,p_f) formulation are very close to the previously described conditions for the ($\mathbf{u}_\mathrm{s}$,$\mathbf{u}_\mathrm{f}$) formulation. However, slight differences arise in the way they are accounted for in a finite element approach, which are mentioned in the following. Thus, considering a porous material coupled to:

- an *acoustic fluid*. A pressure continuity condition is added to Eqs. (1.22) and (1.23), between the fluid pore pressure and the acoustic pressure in the acoustic fluid domain,

  $$p = p_\mathrm{f}. \tag{1.37}$$

  Thus, standard structural-acoustic coupling conditions arise in the variational formulation for the solid phase of the porous medium, while the pressure continuity can directly be imposed in the assembly procedure.

- a *flexible structure*. It was shown that coupling a porous material described with the ($\mathbf{u}_\mathrm{s}$,p_f) formulation leads to simplified coupling with the flexible structure, as only the solid displacement continuity (Eq. (1.24a) or (1.25a)) has to be explicitly enforced. Furthermore, in the case of a bonded porous layer (Eq. (1.24a), it can be imposed during the assembly procedure.

- another *poroelastic domain*. Similarly to the coupling conditions with an acoustic domain, the pressure continuity in the pores between two connected porous media has to be enforced, adding

  $$p_\mathrm{f}^{(1)} = p_\mathrm{f}^{(2)}, \tag{1.38}$$

  to the coupling conditions expressed in Eqs. (1.27) and (1.28). Again, it was shown that the coupling conditions for the ($\mathbf{u}_\mathrm{s}$,p_f) formulation are easier to take into account. In fact, only the solid phase displacement and the fluid phase pressure continuity need to be explicitly accounted for, which can be done directly in the assembly procedure.

1.4.4 Other formulations, and choice made for the thesis

The summary of the two main formulations for modelling poroelastic materials, the ($\mathbf{u}_s$,$\mathbf{u}_f$) and ($\mathbf{u}_s$,p_f), presented in the previous section, highlighted the reasons for the recent success for the ($\mathbf{u}_s$,p_f) formulation: despite an intricate physical interpretation [81] and some conditioning issues, the numerical advantage due to the reduction to 4 dofs per node in an FE code, as well as the simplified handling of coupling conditions have made it most popular. In the objective of a simplification of the displacement-based formulation, a strain-decoupled formulation ($\mathbf{u}_s$,$\mathbf{u}_w$) [82] has been proposed, thus proposing simpler expressions of the different parameters of Biot's model. Following the idea of simplifying the displacement-based formulations, a solid phase and total displacement formulation ($\mathbf{u}_s$,$\mathbf{u}_t$) was recently derived [59] exhibiting a diagonal by block stiffness matrix together with natural coupling conditions with an acoustic fluid domain or another porous medium. In addition, an efficient modal-based solution strategy was proposed. It uses real-valued decoupled modes from two different eigenvalue problems, and was shown to be promising for future extensions to 3D and more complex applications.

The present work is oriented towards the same objectives. However, after reviewing works done in the context of modal-based reduction, it appeared that, even though being challenging for non-proportional damping, use of coupled modes would exhibit some advantages (See Section 1.5). For this reason, the original ($\mathbf{u}_s$,$\mathbf{u}_f$) formulation will be used for most of the present work, with the aim to propose more efficient solution approaches.

1.5 Modal-based reduction methods

Modal-based reduced models in structural-acoustics. The modal-based approach for reduced models consists in a change of basis from nodal coordinates to modal coordinates. Thus, a projection is done on a truncated basis composed of normal modes calculated from a conservative eigenvalue problem. The outcome for conservative problems is a reduction in the number of unknowns corresponding to a set of linearly independent equations, thus resulting in a very efficient solution. Furthermore, it is a well-known result of modal-based reduction techniques, that the convergence can be improved by completing the modal basis with a static response of the system as a correction for the truncated higher order normal modes.

For coupled problems such as structural-acoustic applications, the starting point is generally the use of decoupled modal bases, i.e. calculated from the eigenvalue problems of the structure *in vacuo* and the acoustic cavity with interfaces made rigid. It is however recalled that a choice of appropriate variables could give the option of calculating coupled

modes. Projecting the structural and acoustic domains on their modal basis results in a reduced coupled problem in terms of modal coordinates, with modal coupling at interface. However, this approach suffers from some difficulties in terms of convergence [83, 84], which can be partly explained by the use of an acoustic pressure field leading to displacement incompatibilities at the interface with the structural domain. In the literature, the convergence has been improved by enriching the acoustic basis by vectors accounting for the coupled nature of the problem. Such improvements have been proposed by Ohayon, using formulations suitable for the static response of coupled structural-acoustic problems, and enriching the acoustic fluid basis with its response under structural static deformation [56, 71]. Further improvements have been proposed enriching the bases with residual responses, thus involving an iterative scheme, controlled using an error estimator [70, 63].

Another way to account for the coupling compatibility is to consider a component approach. Several methods, have been proposed, mostly in the scope of purely structural applications, grouped under the so-called Component Mode Synthesis (CMS) technique [85–100]. It consists in decomposing the problem into several components, which can be independently reduced using normal modes not satisfying the coupling conditions, and enforcing the coupling between components by a set of attachment functions. The different methods differ from each other depending on the combination of normal modes (real-valued or possibly complex-valued) used, i.e. restrained-interface modes, free-interface modes, hybrid-interface modes, together with the type of attachment function which can be based on the primal or dual variables. Few studies have extended this approach to structural-acoustic coupled problems. The classical restrained-interface method attributed to Craig and Bampton [85] has been adapted to fluid domains [101], showing promising performance for fluid-structure interaction problems. It can be argued that the standard modal approach, using only the decoupled structural and acoustic modal bases for the change of coordinates, is a particular type of component mode synthesis. It would correspond to a so-called free-interface normal modes technique, with attachment functions consisting of the coupling conditions expressed in the modal coordinates.

Both approaches exhibit advantages depending on the specific applications. In the context of FEM, reducing the number of interface functions (projected coupling conditions in the case of modal synthesis) is of prime importance as it leads to a loss of sparsity in the global matrices. Thus, despite a reduction in the number of dofs, it is partly hampered by the loss in efficiency for a solution using sparse solvers. In the modal synthesis approach, these densely populated submatrices depend on the number of modes retained for each domain, as well as the nature of the problem. In fact, for a problem with weak coupling, some modal coupling terms may be neglected. On the contrary, for a problem with strong coupling (e.g. with heavy fluid), this assumption is not valid, and the modal

bases themselves need to account for the strong coupling to improve the convergence. With a component approach, the increased density of the matrices is triggered by the choice of the attachment functions. Thus, in the classical restrained-interface CMS, it is controlled by the number of interface degrees of freedom, which implies some constraints in the choice of subdomains. This point can however be partly overcome with further reduction of interface dofs [102–104], or by the choice of specific interface functions [86].

While still requiring some attention in the context of non-damped coupled problems, the applicability of these methods for dissipative problems demands even greater consideration, as they are often depicted as not suited for such applications.

Dealing with damped problems, and perspectives for poroelastic materials. Excluding the case of proportional damping, modal methods for damped problems are sometimes erroneously deemed as inappropriate. While this may be true to a certain extent, the convergence being by nature harder to achieve, the same basic questions remain as for the reduction models using decoupled bases for coupled problem. Either spend computational efforts directly building an appropriate basis, possibly in some non-conventional way, e.g. based on coupled modes for structural-acoustic applications, or find an approximate basis enriched by some correction vectors. For non-damped problems, this last approach has been the most investigated in the literature. For damped problems, this has also been the case, considering for instance the use of viscoelastic damping in structural applications [105–108]. Recently, such methods have been successfully extended to structural-acoustic applications with dissipative interfaces [70, 63]. These works are a source of inspiration to propose efficient modal approaches for poroelastic materials, which however combine several difficulties: strong coupling, dissipative properties, and "volume" coupling as opposed to surface interface coupling.

On this topic, Dazel has recently proposed and initiated several works. First, in [57, 58], the approach could be considered, similarly to the use of coupled modes for non-damped structural-acoustics, as the expensive a priori search of an optimal basis with limited corrections. Convergence for simple applications was demonstrated, although major drawbacks in terms of the complex and expensive generation of the modal basis, indicated difficulties for further efficient use of the method. In 2006, Davidsson [109] proposed the construction of a basis in two steps: first involving the calculation of decoupled modes in order to establish several interface-dependent Lanczos vectors for each mode, and then using these modes to calculate coupled modes. The method was shown accurate and promising in terms of dofs reduction, but the computational efficiency of the approach was not presented, being a key aspect of the procedure considering the operations involved in the reduction process. More recently, an approach based on decoupled bases was presented by

Dazel [59, 60]. It was either suitable under the assumption of neglected shear in the porous material [59], or demonstrated on 1D applications, thus not involving shear waves [60], but showing promising performances for extension to more complex problems.

However, it seems, from the present literature review, that an approach based on decoupled modes for such strongly coupled problems, might imply difficulties in the choice of decoupled modes to include in the basis. Furthermore, due to the fully coupled nature of the equations (in the sense of "volume" coupling), a reduction based on decoupled normal modes will result in a fully coupled reduced set of equations, i.e. fully populated coupling submatrices. This, added to the coupling that has to be done with other physical domains, may strongly hamper the potential efficiency of such methods.

For these reasons, the approach attempted in the present work, is to propose an approximate modal basis based on the fully coupled poroelastic problem, which, upon necessity, could be corrected with methods proposed in the literature (static-like responses, residual responses, ...).

1.6 Conclusion

In this introductory chapter, a selective overview of the scientific topics related to the thesis was presented. Following the analysis, two main choices have been exposed regarding the modelling of coupled poro-elasto-acoustic problems, as included in the present work:

- The widely used displacement-pressure set of variables ($\mathbf{u}_S$-p) is chosen to describe the acoustic fluid and the structure in coupled structural-acoustic problems. In a direct solution scheme for time-harmonic excitations, the FE problem is artificially symmetrized, excluding the static case;
- The ($\mathbf{u}_s$,$\mathbf{u}_f$) displacement formulation based on the Biot-Allard theory will be used to model poroelastic materials, in order to propose a modal approach. Although a priori less efficient than the mixed formulation, this choice exhibits further advantages discussed in the manuscript. These arise from a number of choices made in this work for the implementation.

The following chapter introduces the implementation of these classical formulations, integrated into a Component Mode Synthesis approach for the acoustic domain.

Chapter 2

Restrained-interface CMS for damped structural-acoustic applications

Abstract: *This chapter presents a CMS technique for the reduction of acoustic components in structural-acoustic problems with poroelastic interfaces. Its implementation into a general purpose Fortran FE code allows a consistent analysis in terms of performances and limitations of the method.*

Contents

2.1 Introduction

In this chapter, the efficiency of a restrained-interface modal-based reduction technique is discussed, in the scope of structural-acoustic problems with dissipative interfaces. Although this reduction technique is relatively common in the literature of CMS, particularly in structural mechanics, few studies have explored the limitations of such an approach in the context of damped structural-acoustics. An elasto-poro-acoustic problem is proposed, involving a classic displacement-pressure description of the structural-acoustic domain, while the porous medium is described using a 3D model based on the $(\mathbf{u}_\mathrm{s}, \mathbf{u}_\mathrm{f})$ formulation of the Biot-Allard theory [2, 6, 7, 10]. The solution of the forced time-harmonic problem is done using a direct approach at each excitation frequency. Considering the substantial proportion of acoustic fluid in the considered applications, its reduction to interface degrees of freedom is evaluated on a large range of academic problems. The evaluation of the efficiency, as well as the limitations of the technique is sought. For this purpose, the solution strategy presented in this chapter has been fully implemented in a general FE Fortran code [110], according to the steps detailed in the presentation of the method, thus giving consistent data regarding the computational cost estimations reported.

The chapter is composed of three main sections. In the first part, the general elasto-poro-acoustic problem is presented, along with the associated FE formulation derived in response to a time-harmonic excitation. In the scope of a direct solution, it is shown that the problem can be solved as a symmetric problem. The following section presents the restrained-interface CMS applied to the acoustic domain of the chosen applications. A general computationally oriented description of the method is detailed, making it directly applicable to other conservative media (e.g. structure). In this section, the described reduction method is applied to acoustic, structural-acoustic, and poro-acoustic academic applications from which conclusions are drawn regarding its limitations in accuracy. In addition, an iterative test is presented in order to clarify the use of truncation criteria based on the eigenfrequencies in the scope of fixed-interface CMS. The last part presents the model reduction of a larger scale elasto-poro-acoustic application. The computational efficiency of the method is quantified, and two limitations in accuracy are identified: *i)* the restrained-interface CMS shows some precision issues at frequencies close to the eigenfrequencies of the structural domain acting as a source of excitation, and *ii)* these difficulties are emphasized when the concerned acoustic component is treated with damping properties such as using a porous material.

2.2 Finite element formulation for the elasto-poro-acoustic problem

A fluid-structure interaction problem with dissipative porous media at the acoustic boundary is considered, whose description and notations are presented in Fig. 2.1. The acoustic fluid, the structure and the porous medium, occupy the domains Ω_{F}, Ω_{S}, and Ω_{P} respectively. The compressible fluid domain is described using pressure (p) as primary variable (Subsection 2.2.1.1), while displacement ($\mathbf{u}_{\mathrm{S}}$) is used for the structural part (Subsection 2.2.1.2). As for the porous medium introduced in Subsection 2.2.1.3, fluid and solid phases homogenized displacements ($\mathbf{u}_{\mathrm{s}}, \mathbf{u}_{\mathrm{f}}$) are retained as primary variables. Their boundaries are separated into contours of:

- imposed Dirichlet boundary conditions denoted $\partial_1\Omega_{\mathrm{F}}$, $\partial_1\Omega_{\mathrm{S}}$ and $\partial_1\Omega_{\mathrm{P}}$,
- prescribed Neumann boundary conditions denoted $\partial_2\Omega_{\mathrm{F}}$, $\partial_2\Omega_{\mathrm{S}}$ and $\partial_2\Omega_{\mathrm{P}}$,
- coupling interfaces between the acoustic fluid and the structure (Γ_{FS}), and between the acoustic fluid and the porous medium (Γ_{FP}).

The finite element formulation is presented for a steady state time-harmonic response at angular frequency ω.

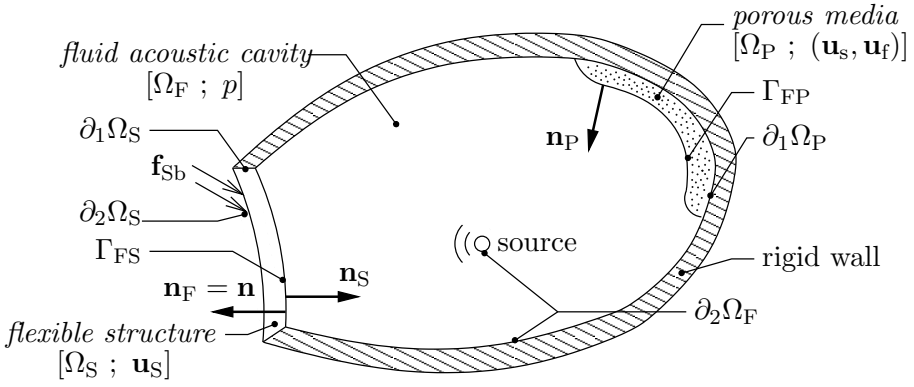

Figure 2.1: Description and notations of the elasto-poro-acoustic interaction problem

2.2.1 Dynamic equations and constitutive laws

2.2.1.1 Compressible fluid (p)

The internal fluid within the cavities is assumed to be compressible and inviscid, satisfying the classical Helmholtz equation derived from the equations of motion, continuity,

and state,

$$\Delta p + \frac{\omega^2}{c_0^2} p = 0 \quad \text{in } \Omega_{\mathrm{F}}, \tag{2.1}$$

where c_0 is the constant sound speed in the fluid, and p the pressure fluctuation scalar field. The limit case where $\omega = 0$ is not given by equation (2.1). For this matter, the solution is given by the static solution of the coupled fluid-structure problem, as described in [56]. Henceforth, in the scope of the present work, it will be assumed that $\omega \neq 0$.

2.2.1.2 Structure ($\mathbf{u}_{\mathrm{S}}$)

The structural domain is assumed satisfying the elastodynamic linearized equation at angular frequency ω,

$$\operatorname{div} \boldsymbol{\sigma}_{\mathrm{S}} + \omega^2 \rho_{\mathrm{S}} \mathbf{u}_{\mathrm{S}} = \mathbf{0} \quad \text{in } \Omega_{\mathrm{S}}, \tag{2.2}$$

where ρ_{S} is the constant density per unit volume, $\boldsymbol{\sigma}_{\mathrm{S}}$ the Cauchy stress tensor, given by

$$\boldsymbol{\sigma}_{\mathrm{S}} = \mathbf{D}_{\mathrm{S}}\, \boldsymbol{\varepsilon}(\mathbf{u}_{\mathrm{S}}) \quad \text{in } \Omega_{\mathrm{S}}. \tag{2.3}$$

$\mathbf{D}_{\mathrm{S}}$ is the classical Hooke's linear elasticity tensor, and $\boldsymbol{\varepsilon}(\mathbf{u}_{\mathrm{S}})$ the strain tensor associated with the displacement vector field $\mathbf{u}_{\mathrm{S}}$, defined as

$$\boldsymbol{\varepsilon}(\mathbf{v}) = \frac{1}{2} \left(\mathbf{grad}\, \mathbf{v} + \mathbf{grad}^T \mathbf{v} \right). \tag{2.4}$$

This definition of $\boldsymbol{\varepsilon}$ as a function of $\mathbf{v}$ is used later in the description of the Biot theory for modelling of porous materials.

2.2.1.3 Porous media Biot theory ($\mathbf{u}_{\mathrm{s}}, \mathbf{u}_{\mathrm{f}}$)

Considering the fact that sound propagation in a porous medium occurs both in the air inside the pores and in the flexible frame, the Biot-Allard theory ([2, 6, 10]) is used for the air-saturated porous medium. It describes the fluid and the structural partitions as well as their coupling, using the homogenized equations of linear continuum mechanics.

Following the presentation of the equations made in Section 1.4.2 for the $(\mathbf{u}_{\mathrm{s}}, \mathbf{u}_{\mathrm{f}})$ formulation, the main equations are briefly recalled to establish the variational formulation. The list of material parameters is given in Table 1.1. The poroelastic medium satisfies the following elastodynamic linearized equations at angular frequency ω, taking into account inertia and viscous coupling effects between the solid and the fluid phases,

$$\operatorname{div} \boldsymbol{\sigma}_{\mathrm{s}} + \omega^2 (\widetilde{\rho}_{\mathrm{s}} \mathbf{u}_{\mathrm{s}} + \widetilde{\rho}_{\mathrm{sf}} \mathbf{u}_{\mathrm{f}}) = \mathbf{0} \quad \text{in } \Omega_{\mathrm{P}}, \tag{2.5a}$$

$$\operatorname{div} \boldsymbol{\sigma}_{\mathrm{f}} + \omega^2 (\widetilde{\rho}_{\mathrm{sf}} \mathbf{u}_{\mathrm{s}} + \widetilde{\rho}_{\mathrm{f}} \mathbf{u}_{\mathrm{f}}) = \mathbf{0} \quad \text{in } \Omega_{\mathrm{P}}, \tag{2.5b}$$

where $\mathbf{u}_\mathrm{s}$ and $\mathbf{u}_\mathrm{f}$ are the solid phase and fluid phase averaged displacements in the sense of Biot theory, respectively. In addition, $\widetilde{\rho}_\mathrm{s}$, $\widetilde{\rho}_\mathrm{f}$ and $\widetilde{\rho}_\mathrm{sf}$ are equivalent complex densities per unit volume taking into account viscous effects as well as inertial coupling term (See Eqs. (1.15)).

$\boldsymbol{\sigma}_\mathrm{s}$ and $\boldsymbol{\sigma}_\mathrm{f}$ are the averaged stress tensors for the solid and fluid phases respectively. They satisfy the Lagrangian stress-strain relations developed by Biot, Eqs. (1.17), which can be written using the Voigt notation,

$$\boldsymbol{\sigma}_\mathrm{s} = \widetilde{\mathbf{D}}_\mathrm{s}\,\boldsymbol{\varepsilon}(\mathbf{u}_\mathrm{s}) + \widetilde{\mathbf{D}}_\mathrm{sf}\,\boldsymbol{\varepsilon}(\mathbf{u}_\mathrm{f}), \tag{2.6a}$$

$$\boldsymbol{\sigma}_\mathrm{f} = \widetilde{\mathbf{D}}_\mathrm{sf}^T\,\boldsymbol{\varepsilon}(\mathbf{u}_\mathrm{s}) + \widetilde{\mathbf{D}}_\mathrm{f}\,\boldsymbol{\varepsilon}(\mathbf{u}_\mathrm{f}), \tag{2.6b}$$

where $\boldsymbol{\varepsilon}(\mathbf{u}_\mathrm{s})$ and $\boldsymbol{\varepsilon}(\mathbf{u}_\mathrm{f})$ are the strain tensors associated with the averaged displacements $\mathbf{u}_\mathrm{s}$ and $\mathbf{u}_\mathrm{f}$, as defined in Eq. (2.4). $\widetilde{\mathbf{D}}_\mathrm{s}$, $\widetilde{\mathbf{D}}_\mathrm{f}$ and $\widetilde{\mathbf{D}}_\mathrm{sf}$ are complex and frequency-dependent elasticity tensors of the solid phase, the fluid phase, and the coupling between both phases respectively. Their developed expressions include the materials parameters $\widetilde{A}$, $\widetilde{Q}$, $\widetilde{R}$ given by Eqs. (1.21) and the shear modulus of the frame $\widetilde{\mu}$,

$$\begin{bmatrix}\sigma^s_{11}\\ \sigma^s_{22}\\ \sigma^s_{33}\\ \sigma^s_{12}\\ \sigma^s_{13}\\ \sigma^s_{23}\end{bmatrix} = \begin{bmatrix}\widetilde{A}^* & \widetilde{A} & \widetilde{A} & 0 & 0 & 0\\ \widetilde{A} & \widetilde{A}^* & \widetilde{A} & 0 & 0 & 0\\ \widetilde{A} & \widetilde{A} & \widetilde{A}^* & 0 & 0 & 0\\ 0 & 0 & 0 & \widetilde{\mu} & 0 & 0\\ 0 & 0 & 0 & 0 & \widetilde{\mu} & 0\\ 0 & 0 & 0 & 0 & 0 & \widetilde{\mu}\end{bmatrix}\begin{bmatrix}\epsilon^s_{11}\\ \epsilon^s_{22}\\ \epsilon^s_{33}\\ 2\epsilon^s_{12}\\ 2\epsilon^s_{13}\\ 2\epsilon^s_{23}\end{bmatrix} + \begin{bmatrix}\widetilde{Q} & \widetilde{Q} & \widetilde{Q} & 0 & 0 & 0\\ \widetilde{Q} & \widetilde{Q} & \widetilde{Q} & 0 & 0 & 0\\ \widetilde{Q} & \widetilde{Q} & \widetilde{Q} & 0 & 0 & 0\\ 0 & 0 & 0 & 0 & 0 & 0\\ 0 & 0 & 0 & 0 & 0 & 0\\ 0 & 0 & 0 & 0 & 0 & 0\end{bmatrix}\begin{bmatrix}\epsilon^f_{11}\\ \epsilon^f_{22}\\ \epsilon^f_{33}\\ 2\epsilon^f_{12}\\ 2\epsilon^f_{13}\\ 2\epsilon^f_{23}\end{bmatrix}, \tag{2.7a}$$

$$\begin{bmatrix}\sigma^f_{11}\\ \sigma^f_{22}\\ \sigma^f_{33}\\ \sigma^f_{12}\\ \sigma^f_{13}\\ \sigma^f_{23}\end{bmatrix} = \begin{bmatrix}\widetilde{Q} & \widetilde{Q} & \widetilde{Q} & 0 & 0 & 0\\ \widetilde{Q} & \widetilde{Q} & \widetilde{Q} & 0 & 0 & 0\\ \widetilde{Q} & \widetilde{Q} & \widetilde{Q} & 0 & 0 & 0\\ 0 & 0 & 0 & 0 & 0 & 0\\ 0 & 0 & 0 & 0 & 0 & 0\\ 0 & 0 & 0 & 0 & 0 & 0\end{bmatrix}\begin{bmatrix}\epsilon^s_{11}\\ \epsilon^s_{22}\\ \epsilon^s_{33}\\ 2\epsilon^s_{12}\\ 2\epsilon^s_{13}\\ 2\epsilon^s_{23}\end{bmatrix} + \begin{bmatrix}\widetilde{R} & \widetilde{R} & \widetilde{R} & 0 & 0 & 0\\ \widetilde{R} & \widetilde{R} & \widetilde{R} & 0 & 0 & 0\\ \widetilde{R} & \widetilde{R} & \widetilde{R} & 0 & 0 & 0\\ 0 & 0 & 0 & 0 & 0 & 0\\ 0 & 0 & 0 & 0 & 0 & 0\\ 0 & 0 & 0 & 0 & 0 & 0\end{bmatrix}\begin{bmatrix}\epsilon^f_{11}\\ \epsilon^f_{22}\\ \epsilon^f_{33}\\ 2\epsilon^f_{12}\\ 2\epsilon^f_{13}\\ 2\epsilon^f_{23}\end{bmatrix}, \tag{2.7b}$$

with

$$\widetilde{A}^* = \widetilde{A} + 2\widetilde{\mu}. \tag{2.8}$$

2.2.2 Fluid-structure interaction problem

In this subsection, boundary and coupling conditions are recalled for the elasto-poro-acoustic coupled problem presented in Fig. 2.1, in order to establish the complete basis for the discretized finite element problem.

2.2.2.1 Elasto-poro-acoustic coupling and boundary conditions ($\mathbf{u}_S$−p−($\mathbf{u}_s$, $\mathbf{u}_f$))

Prescribed displacements and forces are imposed on the external structural boundaries $\partial_1\Omega_S$ and $\partial_2\Omega_S$ respectively,

$$\mathbf{u}_S = \mathbf{0} \quad \text{on } \partial_1\Omega_S, \tag{2.9}$$

$$\boldsymbol{\sigma}_S\, \mathbf{n}_S = \mathbf{f}_{Sb} \quad \text{on } \partial_2\Omega_S, \tag{2.10}$$

where $\mathbf{n}_S$ is the unit normal vector pointing outward from Ω_S.

At the interface between the structural domain and the acoustic fluid, normal stress and normal displacement continuity conditions are given by

$$\boldsymbol{\sigma}_S\, \mathbf{n} + p\, \mathbf{n} = \mathbf{0} \quad \text{on } \Gamma_{FS}, \tag{2.11}$$

$$(\mathbf{u}_F - \mathbf{u}_S) \cdot \mathbf{n} = 0 \quad \text{on } \Gamma_{FS}, \tag{2.12}$$

where $\mathbf{n}$ is the unit normal vector pointing outward from the fluid domain. $\mathbf{u}_F$ is the fluid displacement vector, which can be related to the pressure field using the linearized Euler equation expressed for a harmonic solution at angular frequency ω,

$$\mathbf{grad}\, p \cdot \mathbf{n} = \omega^2 \rho_F\, \mathbf{u}_F \cdot \mathbf{n}. \tag{2.13}$$

At an external boundary of the acoustic fluid domain, rigid impervious cavity conditions correspond to a free pressure field. A time-harmonic excitation is prescribed via an acoustic source,

$$\mathbf{u}_F \cdot \mathbf{n} = u_{Fb} \quad \text{on } \partial_2\Omega_F, \tag{2.14}$$

where u_{Fb} is set to zero except for the location of the acoustic source included in $\partial_2\Omega_F$.

Coupling at an interface Γ_{FP} is given by normal stress and normal displacement continuity conditions between the acoustic fluid and both the fluid and the solid phases of the porous medium (see Section 1.4.2.2),

$$\boldsymbol{\sigma}_s\, \mathbf{n} + (1-\phi)\, p\, \mathbf{n} = \mathbf{0} \quad \text{on } \Gamma_{FP}, \tag{2.15a}$$

$$\boldsymbol{\sigma}_f\, \mathbf{n} + \phi\, p\, \mathbf{n} = \mathbf{0} \quad \text{on } \Gamma_{FP}, \tag{2.15b}$$

$$\mathbf{u}_F \cdot \mathbf{n} - (1-\phi)\mathbf{u}_s \cdot \mathbf{n} - \phi \mathbf{u}_f \cdot \mathbf{n} = 0 \quad \text{on } \Gamma_{FP}, \tag{2.16}$$

where ϕ is the porosity of the porous material, i.e. the volume fraction of fluid.

No external force is applied to the outer boundary of the porous medium beside at interface Γ_{FP}. Therefore, $\partial_2\Omega_P = \emptyset$ in the considered problem. Finally, at an external boundary $\partial_1\Omega_P$, two types of boundary conditions can be prescribed, the porous material being considered either as sliding or bonded to a rigid wall:

For a *bonded* porous layer on a rigid wall, the following conditions arise – fixed displacement of the solid phase and normal displacement of the fluid phase – and have to be satisfied,

$$\mathbf{u}_\mathrm{s} = \mathbf{0} \quad \text{on } \partial_1\Omega_\mathrm{P}, \tag{2.17a}$$

$$\mathbf{u}_\mathrm{f} \cdot \mathbf{n}_\mathrm{P} = 0 \quad \text{on } \partial_1\Omega_\mathrm{P}; \tag{2.17b}$$

For a *sliding* porous layer on a rigid wall the following conditions arise – fixed normal displacement of the solid phase and fluid phase – and have to be satisfied,

$$\mathbf{u}_\mathrm{s} \cdot \mathbf{n}_\mathrm{P} = 0 \quad \text{on } \partial_1\Omega_\mathrm{P}, \tag{2.18a}$$

$$\mathbf{u}_\mathrm{f} \cdot \mathbf{n}_\mathrm{P} = 0 \quad \text{on } \partial_1\Omega_\mathrm{P}, \tag{2.18b}$$

where $\mathbf{n}_\mathrm{P}$ is the unit normal vector pointing outward from Ω_P.

2.2.2.2 Finite element discretized problem

The test-function method is used to derive the variational formulation of the coupled problem. For this purpose, the spaces of sufficiently smooth functions $C_{\mathbf{u}_\mathrm{S}}$, C_p, $C_{\mathbf{u}_\mathrm{s}}$ and $C_{\mathbf{u}_\mathrm{f}}$ are introduced, associated with the field variables $\mathbf{u}_\mathrm{S}$, p, $\mathbf{u}_\mathrm{s}$ and $\mathbf{u}_\mathrm{f}$ respectively.

- Let $\delta\mathbf{u}_\mathrm{S}$ be the frequency-independent test function, associated with $\mathbf{u}_\mathrm{S}$, belonging to the admissible space $C^*_{\mathbf{u}_\mathrm{S}} = \{\delta\mathbf{u}_\mathrm{S} \in C_{\mathbf{u}_\mathrm{S}} | \delta\mathbf{u}_\mathrm{S} = \mathbf{0} \quad \text{on } \partial_1\Omega_\mathrm{S}\}$. Multiplying Eq. (2.2) combined with Eq. (2.3) by $\delta\mathbf{u}_\mathrm{S} \in C^*_{\mathbf{u}_\mathrm{S}}$, applying a Green's formula and taking Eqs. (2.10) and (2.11) into account leads to

$$\begin{aligned}\int_{\Omega_\mathrm{S}} \mathrm{tr}\left[\mathbf{D}_\mathrm{S}\,\boldsymbol{\varepsilon}(\mathbf{u}_\mathrm{S})\,\boldsymbol{\varepsilon}(\delta\mathbf{u}_\mathrm{S})\right]\,\mathrm{d}V - \omega^2 \int_{\Omega_\mathrm{S}} \rho_\mathrm{S}\mathbf{u}_\mathrm{S}\cdot\delta\mathbf{u}_\mathrm{S}\,\mathrm{d}V - \int_{\Gamma_\mathrm{FS}} p\,\mathbf{n}\cdot\delta\mathbf{u}_\mathrm{S}\,\mathrm{d}\Sigma \\ = \int_{\partial_2\Omega_\mathrm{S}} \mathbf{f}_\mathrm{Sb}\cdot\delta\mathbf{u}_\mathrm{S}\,\mathrm{d}\Sigma.\end{aligned} \tag{2.19}$$

- Let δp be the frequency-independent test function, associated with p, belonging to the admissible space C_p. Multiplying Eq. (2.1) by $\delta p \in C_p$, applying a Green's formula and taking Eqs. (2.12), (2.14) and (2.16) into account leads to

$$\begin{aligned}\int_{\Omega_\mathrm{F}} \mathbf{grad}p\cdot\mathbf{grad}\delta p\,\mathrm{d}V - \frac{\omega^2}{c_0^2}\int_{\Omega_\mathrm{F}} p\,\delta p\,\mathrm{d}V - \omega^2\rho_\mathrm{F}(1-\phi)\int_{\Gamma_\mathrm{FP}} \mathbf{u}_\mathrm{s}\cdot\mathbf{n}\,\delta p\,\mathrm{d}\Sigma \\ -\omega^2\rho_\mathrm{F}\phi\int_{\Gamma_\mathrm{FP}} \mathbf{u}_\mathrm{f}\cdot\mathbf{n}\,\delta p\,\mathrm{d}\Sigma - \omega^2\rho_\mathrm{F}\int_{\Gamma_\mathrm{FS}} \mathbf{u}_\mathrm{S}\cdot\mathbf{n}\,\delta p\,\mathrm{d}\Sigma = \omega^2\rho_\mathrm{F}\int_{\partial_2\Omega_\mathrm{F}} u_\mathrm{Fb}\,\delta p\,\mathrm{d}\Sigma.\end{aligned} \tag{2.20}$$

- Let $\delta\mathbf{u}_\mathrm{s}$ be the frequency-independent test function, associated with $\mathbf{u}_\mathrm{s}$, belonging to the admissible space $C^*_{\mathbf{u}_\mathrm{s}} = \{\delta\mathbf{u}_\mathrm{s} \in C_{\mathbf{u}_\mathrm{s}} | \delta\mathbf{u}_\mathrm{s} = \mathbf{0} \text{ or } \delta\mathbf{u}_\mathrm{s}\cdot\mathbf{n}_\mathrm{P} = 0 \quad \text{on } \partial_1\Omega_\mathrm{P}\}$.

Multiplying Eq. (2.5a) combined with Eq. (2.6a) by $\delta\mathbf{u}_\mathrm{s} \in C^*_{\mathbf{u}_\mathrm{s}}$, applying a Green's formula and taking Eq. (2.15a) into account leads to

$$\begin{aligned}&\int_{\Omega_\mathrm{P}} \mathrm{tr}\left[\widetilde{\mathbf{D}}_\mathrm{s}\,\boldsymbol{\varepsilon}(\mathbf{u}_\mathrm{s})\,\boldsymbol{\varepsilon}(\delta\mathbf{u}_\mathrm{s})\right]\,\mathrm{d}V + \int_{\Omega_\mathrm{P}} \mathrm{tr}\left[\widetilde{\mathbf{D}}_\mathrm{sf}\,\boldsymbol{\varepsilon}(\mathbf{u}_\mathrm{f})\,\boldsymbol{\varepsilon}(\delta\mathbf{u}_\mathrm{s})\right]\,\mathrm{d}V\\ &-\omega^2\int_{\Omega_\mathrm{P}} \widetilde{\rho}_\mathrm{s}\mathbf{u}_\mathrm{s}\cdot\delta\mathbf{u}_\mathrm{s}\,\mathrm{d}V - \omega^2\int_{\Omega_\mathrm{P}} \widetilde{\rho}_\mathrm{sf}\mathbf{u}_\mathrm{f}\cdot\delta\mathbf{u}_\mathrm{s}\,\mathrm{d}V\\ &-(1-\phi)\int_{\Gamma_\mathrm{FP}} p\,\mathbf{n}\cdot\delta\mathbf{u}_\mathrm{s}\,\mathrm{d}\Sigma = 0.\end{aligned} \tag{2.21}$$

- Let $\delta\mathbf{u}_\mathrm{f}$ be the frequency-independent test function, associated with $\mathbf{u}_\mathrm{f}$, belonging to the admissible space $C^*_{\mathbf{u}_\mathrm{f}} = \{\delta\mathbf{u}_\mathrm{f} \in C_{\mathbf{u}_\mathrm{f}} | \delta\mathbf{u}_\mathrm{f}\cdot\mathbf{n}_\mathrm{P} = 0 \quad \text{on } \partial_1\Omega_\mathrm{P}\}$. Multiplying Eq. (2.5b) combined with Eq. (2.6b) by $\delta\mathbf{u}_\mathrm{f} \in C^*_{\mathbf{u}_\mathrm{f}}$, applying a Green's formula and taking Eq. (2.15b) into account leads to

$$\begin{aligned}&\int_{\Omega_\mathrm{P}} \mathrm{tr}\left[\widetilde{\mathbf{D}}_\mathrm{f}\,\boldsymbol{\varepsilon}(\mathbf{u}_\mathrm{f})\,\boldsymbol{\varepsilon}(\delta\mathbf{u}_\mathrm{f})\right]\,\mathrm{d}V + \int_{\Omega_\mathrm{P}} \mathrm{tr}\left[\widetilde{\mathbf{D}}_\mathrm{sf}\,\boldsymbol{\varepsilon}(\mathbf{u}_\mathrm{s})\,\boldsymbol{\varepsilon}(\delta\mathbf{u}_\mathrm{f})\right]\,\mathrm{d}V\\ &-\omega^2\int_{\Omega_\mathrm{P}} \widetilde{\rho}_\mathrm{s}\mathbf{u}_\mathrm{f}\cdot\delta\mathbf{u}_\mathrm{f}\,\mathrm{d}V - \omega^2\int_{\Omega_\mathrm{P}} \widetilde{\rho}_\mathrm{sf}\mathbf{u}_\mathrm{s}\cdot\delta\mathbf{u}_\mathrm{f}\,\mathrm{d}V\\ &-\phi\int_{\Gamma_\mathrm{FP}} p\,\mathbf{n}\cdot\delta\mathbf{u}_\mathrm{f}\,\mathrm{d}\Sigma = 0.\end{aligned} \tag{2.22}$$

After discretization of the various terms in Eqs. (2.19)-(2.22) using the finite element method and dividing Eq. (2.20) by ρ_F, the following matrix equation for the coupled problem is obtained,

$$\left(\begin{bmatrix}\mathbf{K}_\mathrm{S} & -\mathbf{C}_\mathrm{FS}^T & \mathbf{0} & \mathbf{0}\\ \mathbf{0} & \mathbf{K}_\mathrm{F} & \mathbf{0} & \mathbf{0}\\ \mathbf{0} & -(1-\phi)\mathbf{C}_\mathrm{Fs}^T & \widetilde{\mathbf{K}}_\mathrm{ss} & \widetilde{\mathbf{K}}_\mathrm{sf}\\ \mathbf{0} & -\phi\mathbf{C}_\mathrm{Ff}^T & \widetilde{\mathbf{K}}_\mathrm{fs} & \widetilde{\mathbf{K}}_\mathrm{ff}\end{bmatrix} - \omega^2\begin{bmatrix}\mathbf{M}_\mathrm{S} & \mathbf{0} & \mathbf{0} & \mathbf{0}\\ \mathbf{C}_\mathrm{FS} & \mathbf{M}_\mathrm{F} & (1-\phi)\mathbf{C}_\mathrm{Fs} & \phi\mathbf{C}_\mathrm{Ff}\\ \mathbf{0} & \mathbf{0} & \widetilde{\mathbf{M}}_\mathrm{ss} & \widetilde{\mathbf{M}}_\mathrm{sf}\\ \mathbf{0} & \mathbf{0} & \widetilde{\mathbf{M}}_\mathrm{fs} & \widetilde{\mathbf{M}}_\mathrm{ff}\end{bmatrix}\right)\begin{bmatrix}\mathbf{U}_\mathrm{S}\\ \mathbf{P}\\ \mathbf{U}_\mathrm{s}\\ \mathbf{U}_\mathrm{f}\end{bmatrix} = \begin{bmatrix}\mathbf{F}_\mathrm{Sb}\\ \omega^2\mathbf{U}_\mathrm{Fb}\\ \mathbf{0}\\ \mathbf{0}\end{bmatrix}. \tag{2.23}$$

This non-symmetric formulation can be symmetrized for a solution in the frequency domain by dividing the acoustic equation (second line) by ω^2 ($\omega \neq 0$).

2.3 Restrained-interface reduction method for the conservative acoustic subdomains

In the following, a reduction method is applied to the conservative acoustic domain, which is decomposed into several subdomains. A restrained-interface component mode

synthesis method is chosen in order to condense the acoustic subdomains to their interfaces adjacent to other subdomains.

2.3.1 Presentation of the proposed substructuring strategy

The proposed substructuring and modal reduction of the elasto-poro-acoustic problem introduced in Section 2.2 is presented in Fig. 2.2.

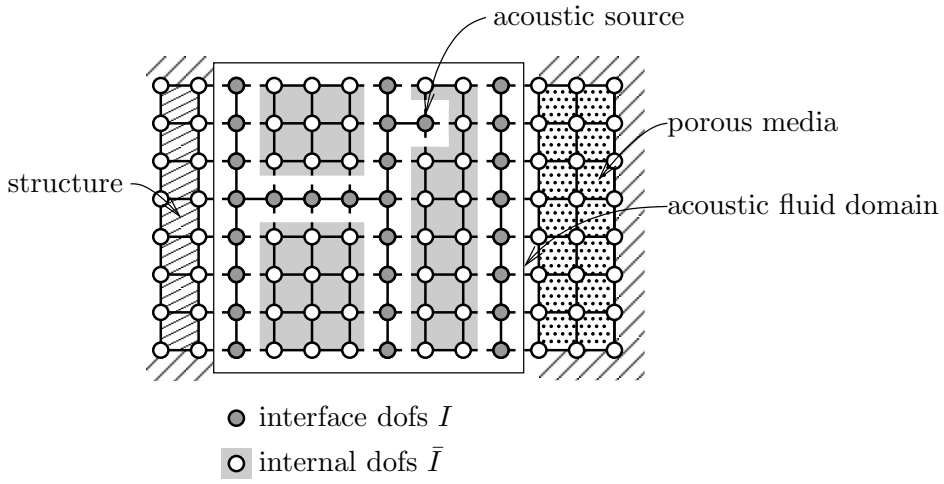

Figure 2.2: Problem description of the substructuring strategy

The subdomain decomposition can be driven either by different physical domains, or by the need to subdivide them into smaller components for computational reasons. Each component's degrees of freedom (dofs) are separated into interface and internal ones, that is into kept and condensed dofs respectively. The kept dofs, denoted by the subscript I, include:

- those connected to another acoustic component,
- those connected to another physical domain (structure or porous media in the present case),
- those for which an external load is applied (e.g. acoustic source),
- in some cases, those presenting an interest for the response evaluation, i.e., outputs in terms of physical quantities of the problem.

The remaining dofs, which are to be condensed, are denoted by the subscript $\bar{I}$. Considering this separation of dofs for the complete acoustic domain, the FE problem presented

in eq. (2.23) can be written as

$$\begin{bmatrix} \mathbf{K}_{\mathrm{S}} - \omega^2 \mathbf{M}_{\mathrm{S}} & -\mathbf{C}_{\mathrm{IS}}^T & \mathbf{0} & \mathbf{0} & \mathbf{0} \\ -\omega^2 \mathbf{C}_{\mathrm{IS}} & \mathbf{K}_{II} - \omega^2 \mathbf{M}_{II} & \mathbf{K}_{I\bar{I}} - \omega^2 \mathbf{M}_{I\bar{I}} & -\omega^2(1-\phi)\mathbf{C}_{\mathrm{Is}} & -\omega^2 \phi \mathbf{C}_{\mathrm{If}} \\ \mathbf{0} & \mathbf{K}_{\bar{I}I} - \omega^2 \mathbf{M}_{\bar{I}I} & \mathbf{K}_{\bar{I}\bar{I}} - \omega^2 \mathbf{M}_{\bar{I}\bar{I}} & \mathbf{0} & \mathbf{0} \\ \mathbf{0} & -(1-\phi)\mathbf{C}_{\mathrm{Is}}^T & \mathbf{0} & \widetilde{\mathbf{K}}_{\mathrm{ss}} - \omega^2 \widetilde{\mathbf{M}}_{\mathrm{ss}} & \widetilde{\mathbf{K}}_{\mathrm{sf}} - \omega^2 \widetilde{\mathbf{M}}_{\mathrm{sf}} \\ \mathbf{0} & -\phi \mathbf{C}_{\mathrm{If}}^T & \mathbf{0} & \widetilde{\mathbf{K}}_{\mathrm{fs}} - \omega^2 \widetilde{\mathbf{M}}_{\mathrm{fs}} & \widetilde{\mathbf{K}}_{\mathrm{ff}} - \omega^2 \widetilde{\mathbf{M}}_{\mathrm{ff}} \end{bmatrix} \times \begin{bmatrix} \mathbf{U}_{\mathrm{S}} \\ \mathbf{P}_I \\ \mathbf{P}_{\bar{I}} \\ \mathbf{U}_{\mathrm{s}} \\ \mathbf{U}_{\mathrm{f}} \end{bmatrix} = \begin{bmatrix} \mathbf{F}_{\mathrm{Sb}} \\ \omega^2 \mathbf{U}_{\mathrm{Ib}} \\ \mathbf{0} \\ \mathbf{0} \\ \mathbf{0} \end{bmatrix}, \tag{2.24}$$

and can be symmetrized by dividing the acoustic equations (lines 2 and 3) by ω^2 ($\omega \neq 0$).

2.3.2 Restrained-interface component mode synthesis for an acoustic fluid

The acoustic components are indexed by j, varying from 1 to the overall number of subdomains n. The dofs of component j are separated into interface (subscript J) and internal (subscript $\bar{J}$) ones, as illustrated in Fig. 2.3 which represents a specific component of Fig. 2.2. They can be formally linked to the previous description of dofs for the complete acoustic domain by the boolean localization matrices $\boldsymbol{\beta}_{JI}^{(j)}$ and $\boldsymbol{\beta}_{\bar{J}\bar{I}}^{(j)}$ which satisfy

$$\mathbf{P}_J = \boldsymbol{\beta}_{JI}^{(j)} \mathbf{P}_I, \tag{2.25a}$$

$$\mathbf{P}_{\bar{J}} = \boldsymbol{\beta}_{\bar{J}\bar{I}}^{(j)} \mathbf{P}_{\bar{I}}. \tag{2.25b}$$

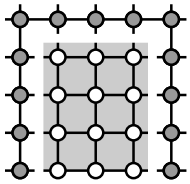

interface dofs J

internal dofs $\bar{J}$

Figure 2.3: DOFs separation within a component

The partitioned acoustic finite element problem for subdomain j is then accordingly written as

$$\left(\begin{bmatrix} \mathbf{K}_{JJ} & \mathbf{K}_{\bar{J}J}{}^T \\ \mathbf{K}_{\bar{J}J} & \mathbf{K}_{\bar{J}\bar{J}} \end{bmatrix} - \omega^2 \begin{bmatrix} \mathbf{M}_{JJ} & \mathbf{M}_{\bar{J}J}{}^T \\ \mathbf{M}_{\bar{J}J} & \mathbf{M}_{\bar{J}\bar{J}} \end{bmatrix} \right) \begin{bmatrix} \mathbf{P}_J \\ \mathbf{P}_{\bar{J}} \end{bmatrix} = \begin{bmatrix} \mathbf{f}_J \\ \mathbf{0} \end{bmatrix}. \tag{2.26}$$

Similarly to what is classically used in structural mechanics [85], an acoustic reduction basis is built using a truncated low frequency modal basis, completed by attachment modes taking into account mobility of the interface as well as contribution of higher order modes to the response. Normal modes are computed with pressure degrees of freedom "restrained" at interface, that is for imposed null pressure ($\mathbf{P}_J = \mathbf{0}$), and are solution of the following eigenvalue problem,

$$\left(\mathbf{K}_{\bar{J}\bar{J}} - \omega^2 \mathbf{M}_{\bar{J}\bar{J}}\right) \boldsymbol{\phi} = \mathbf{0}. \tag{2.27}$$

In most cases, use of restrained-interface reduction methods removes zero-frequency modes, as constraints applied to interface dofs suppress singularities from the stiffness matrix. A suitable criterion for the truncation of the modal basis is, in addition, a key aspect of modal reduction techniques, and is discussed further in Subsection 2.3.5. The m retained acoustic normal modes, for each acoustic component j, form the modal basis matrix denoted $\boldsymbol{\Phi}_{\bar{J}m}$ for subdomain j. They are normalized with respect to matrix $\mathbf{M}_{\bar{J}\bar{J}}$, so that

$$\boldsymbol{\Phi}_{\bar{J}m}{}^T \mathbf{M}_{\bar{J}\bar{J}} \boldsymbol{\Phi}_{\bar{J}m} = \mathbf{1}_m, \tag{2.28a}$$

$$\boldsymbol{\Phi}_{\bar{J}m}{}^T \mathbf{K}_{\bar{J}\bar{J}} \boldsymbol{\Phi}_{\bar{J}m} = \boldsymbol{\Omega}_m, \tag{2.28b}$$

where $\mathbf{1}_m$ is a unit matrix of dimension m, and $\boldsymbol{\Omega}_m$ a diagonal matrix of same size, with the m lowest eigenvalues of (2.27) on its diagonal.

The attachment modes, classically called static modes in structural mechanics, are computed as successive responses of the subdomain to unit prescribed Dirichlet boundary conditions at each interface DOF, while others are kept restrained (see Figure 2.4),

$$\begin{bmatrix}\mathbf{K}_{\bar{J}J} & \mathbf{K}_{\bar{J}\bar{J}}\end{bmatrix} \begin{bmatrix}\mathbf{1}_J \\ \boldsymbol{\Psi}_{\bar{J}J}\end{bmatrix} = \begin{bmatrix}\mathbf{0}\end{bmatrix} \Rightarrow \boldsymbol{\Psi}_{\bar{J}J} = -\mathbf{K}_{\bar{J}\bar{J}}^{-1}\mathbf{K}_{\bar{J}J}. \tag{2.29}$$

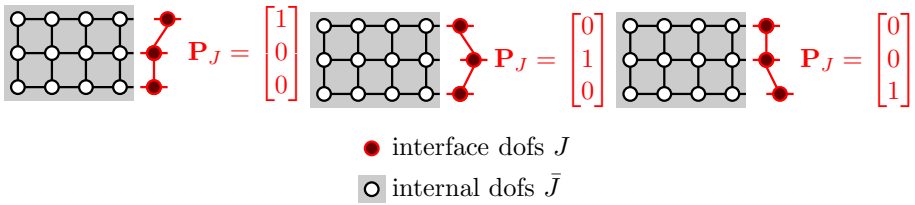

Figure 2.4: Attachment modes

It is assumed that $\mathbf{K}_{\bar{J}\bar{J}}$ is nonsingular considering the Dirichlet boundary conditions prescribed at interface DOFs. If this assumption is not satisfied, a shift on the stiffness matrix can be introduced. As a result, the restrained-interface change of basis is defined

as (the $\widehat{\ }$ symbol on solution vectors refers to an approximate solution)

$$\begin{bmatrix} \widehat{\mathbf{P}}_J \\ \widehat{\mathbf{P}}_{\bar{J}} \end{bmatrix} = \begin{bmatrix} \mathbf{1}_J & \mathbf{0} \\ \mathbf{\Psi}_{\bar{J}J} & \mathbf{\Phi}_{\bar{J}m} \end{bmatrix} \begin{bmatrix} \widehat{\mathbf{P}}_J \\ \widehat{\boldsymbol{\alpha}}_m \end{bmatrix}, \tag{2.30}$$

where $\widehat{\boldsymbol{\alpha}}_m$ is the modal coordinates vector associated with the selected normal modes of the considered restrained-interface subdomain. Due to the truncation of the modal basis, the modal coordinates vector is usually much smaller in size than the corresponding physical dofs vector. Applying change of basis (2.30) to (2.26) leads to the following reduced set of equations,

$$\left(\begin{bmatrix} \hat{\mathbf{K}}_{JJ} & \mathbf{0} \\ \mathbf{0} & \mathbf{\Omega}_m \end{bmatrix} - \omega^2 \begin{bmatrix} \left[\hat{\mathbf{M}}_{JJ} + {\mathbf{\Psi}_{\bar{J}J}}^T \hat{\mathbf{M}}_{\bar{J}J}\right] & \left[{\mathbf{\Phi}_{\bar{J}m}}^T \hat{\mathbf{M}}_{\bar{J}J}\right]^T \\ {\mathbf{\Phi}_{\bar{J}m}}^T \hat{\mathbf{M}}_{\bar{J}J} & \mathbf{1}_m \end{bmatrix} \right) \begin{bmatrix} \widehat{\mathbf{P}}_J \\ \widehat{\boldsymbol{\alpha}}_m \end{bmatrix} = \begin{bmatrix} \mathbf{f}_J \\ \mathbf{0} \end{bmatrix}, \tag{2.31}$$

with

$$\hat{\mathbf{K}}_{JJ} = \mathbf{K}_{JJ} + {\mathbf{K}_{\bar{J}J}}^T \mathbf{\Psi}_{\bar{J}J}, \tag{2.32a}$$

$$\hat{\mathbf{M}}_{JJ} = \mathbf{M}_{JJ} + {\mathbf{M}_{\bar{J}J}}^T \mathbf{\Psi}_{\bar{J}J}, \tag{2.32b}$$

$$\hat{\mathbf{M}}_{\bar{J}J} = \mathbf{M}_{\bar{J}J} + \mathbf{M}_{\bar{J}\bar{J}} \mathbf{\Psi}_{\bar{J}J}. \tag{2.32c}$$

The interest of the modal reduction lies in the mass- and stiffness-orthogonality of the computed normal modes, which allows the modal coordinates to be condensed and removed from the problem to be solved. The subset of equations described in the second line of (2.31) is then used to express the modal coordinates vector as a function of the interface unknowns,

$$\widehat{\boldsymbol{\alpha}}_m = \omega^2 \left(\mathbf{\Omega}_m - \omega^2 \mathbf{1}_m\right)^{-1} \left[{\mathbf{\Phi}_{\bar{J}m}}^T \hat{\mathbf{M}}_{\bar{J}J}\right] \widehat{\mathbf{P}}_J, \tag{2.33}$$

where the inversion of $\left(\mathbf{\Omega}_m - \omega^2 \mathbf{1}_m\right)$ is trivial at each frequency step. The substitution of the modal coordinates expression (2.33) in the set of equations (2.31) then leads to a reduced problem to be solved, downsized to the dimension of its interface degrees of freedom,

$$\Big[\hat{\mathbf{K}}_{JJ} - \omega^2 \left[\hat{\mathbf{M}}_{JJ} + {\mathbf{\Psi}_{\bar{J}J}}^T \hat{\mathbf{M}}_{\bar{J}J}\right] - \omega^4 \left[{\mathbf{\Phi}_{\bar{J}m}}^T \hat{\mathbf{M}}_{\bar{J}J}\right]^T \left(\mathbf{\Omega}_m - \omega^2 \mathbf{1}_m\right)^{-1} \left[{\mathbf{\Phi}_{\bar{J}m}}^T \hat{\mathbf{M}}_{\bar{J}J}\right]\Big] \widehat{\mathbf{P}}_J = \mathbf{f}_J. \tag{2.34}$$

The solution at the condensed degrees of freedom is obtained, if needed, in a post processing step using Eq. (2.33) into Eq. (2.30),

$$\widehat{\mathbf{P}}_{\bar{J}} = \left[\mathbf{\Psi}_{\bar{J}J} + \omega^2 \mathbf{\Phi}_{\bar{J}m} \left(\mathbf{\Omega}_m - \omega^2 \mathbf{1}_m\right)^{-1} \left[{\mathbf{\Phi}_{\bar{J}m}}^T \hat{\mathbf{M}}_{\bar{J}J}\right]\right] \widehat{\mathbf{P}}_J. \tag{2.35}$$

Finally, the dynamic condensation of the complete problem (2.23) gives the following reduced system,

$$\begin{bmatrix} \mathbf{K}_{\mathrm{S}} - \omega^2 \mathbf{M}_{\mathrm{S}} & -\mathbf{C}_{\mathrm{IS}}^T & \mathbf{0} & \mathbf{0} \\ -\omega^2 \mathbf{C}_{\mathrm{IS}} & \mathbf{K}_{II}^\star - \omega^2 \mathbf{M}_{II}^\star - \omega^4 \mathbf{M}_{II}^\circ(\omega) & -\omega^2(1-\phi)\mathbf{C}_{\mathrm{Is}} & -\omega^2 \phi \mathbf{C}_{\mathrm{If}} \\ \mathbf{0} & -(1-\phi)\mathbf{C}_{\mathrm{Is}}^T & \widetilde{\mathbf{K}}_{\mathrm{ss}} - \omega^2 \widetilde{\mathbf{M}}_{\mathrm{ss}} & \widetilde{\mathbf{K}}_{\mathrm{sf}} - \omega^2 \widetilde{\mathbf{M}}_{\mathrm{sf}} \\ \mathbf{0} & -\phi \mathbf{C}_{\mathrm{If}}^T & \widetilde{\mathbf{K}}_{\mathrm{fs}} - \omega^2 \widetilde{\mathbf{M}}_{\mathrm{fs}} & \widetilde{\mathbf{K}}_{\mathrm{ff}} - \omega^2 \widetilde{\mathbf{M}}_{\mathrm{ff}} \end{bmatrix} \times \begin{bmatrix} \widehat{\mathbf{U}}_{\mathrm{S}} \\ \widehat{\mathbf{P}}_I \\ \widehat{\mathbf{U}}_{\mathrm{s}} \\ \widehat{\mathbf{U}}_{\mathrm{f}} \end{bmatrix} = \begin{bmatrix} \mathbf{F}_{\mathrm{Sb}} \\ \omega^2 \mathbf{U}_{\mathrm{Ib}} \\ \mathbf{0} \\ \mathbf{0} \end{bmatrix}, \tag{2.36}$$

where $\mathbf{K}_{II}^\star$, $\mathbf{M}_{II}^\star$ and $\mathbf{M}_{II}^\circ(\omega)$ are obtained by an assembly procedure on the n acoustic components,

$$\mathbf{K}_{II}^\star = \sum_{j=1}^{n} {\boldsymbol{\beta}_{JI}^{(j)}}^T \hat{\mathbf{K}}_{JJ} \boldsymbol{\beta}_{JI}^{(j)}, \tag{2.37a}$$

$$\mathbf{M}_{II}^\star = \sum_{j=1}^{n} {\boldsymbol{\beta}_{JI}^{(j)}}^T \left[\hat{\mathbf{M}}_{JJ} + {\boldsymbol{\Psi}_{\bar{J}J}}^T \hat{\mathbf{M}}_{\bar{J}J} \right] \boldsymbol{\beta}_{JI}^{(j)}, \tag{2.37b}$$

$$\mathbf{M}_{II}^\circ(\omega) = \sum_{j=1}^{n} {\boldsymbol{\beta}_{JI}^{(j)}}^T \left[\left[\boldsymbol{\Phi}_{\bar{J}m}^T \hat{\mathbf{M}}_{\bar{J}J} \right]^T \left(\boldsymbol{\Omega}_m - \omega^2 \, \mathbf{1}_m \right)^{-1} \left[\boldsymbol{\Phi}_{\bar{J}m}^T \hat{\mathbf{M}}_{\bar{J}J} \right] \right] \boldsymbol{\beta}_{JI}^{(j)}. \tag{2.37c}$$

Since the two matrices $\mathbf{K}_{II}^\star$ and $\mathbf{M}_{II}^\star$ are non frequency-dependent, they are computed once in a preliminary step before the frequency loop. Although the matrix $\mathbf{M}_{II}^\circ(\omega)$ has to be recomputed at each frequency increment, it only involves matrix multiplication and a trivial inverse operation.

While not justified in the present structural-acoustic application, extension to reduction of the structural domain is a straight forward procedure. Structural dofs simply have to be seperated similarly to the acoustic dofs in Eq. (2.23), and dynamically condensed following the previous procedure. This is commonly referred to as the Craig-Bampton CMS procedure when applied to structural mechanics.

2.3.3 Application to a conservative structural-acoustic problem

The limitations in accuracy of the reduction applied to a conservative system can be identified on a small structural-acoustic problem, for which the modal basis can be enriched extensively while keeping the computational time reasonable. For this purpose, the following conservative model is built (see Fig. 2.5), consisting of two identical rigid acoustic cavities, of dimensions $0.4 \times 0.6 \times 0.75$ m^3, linked by a 4 mm-thick flexible plate of area 0.4×0.6 m^2. The cavities are meshed with $12 \times 18 \times 12$ hexahedral acoustic elements while

the plate is discretized by a 12×18 quadrilateral shell mesh. In the applications considered, an existing implementation of a quadrilateral shell element is used, including deep shell curvature corrections to the discrete Kirchhoff quadrilateral plate bending element [111]. It is a 6-dof shell element including normal drilling [112], of which only the displacement dofs are coupled to other domains (see coupling in Subsection 2.2.2.1). One of the cavities (referred to as the excited cavity) is excited via a corner harmonic excitation (unit volume velocity source), and mean quadratic pressure (L_p) in each cavity is used as sound level indicator, expressed in dB, and computed according to the following definition,

$$L_p = 10 \log \left(\frac{\int_{\Omega_F} P^2 \mathrm{d}V}{{P_{\mathrm{ref}}}^2 \int_{\Omega_F} \mathrm{d}V} \right), \tag{2.38}$$

where $P_{\mathrm{ref}} = 20\ \mu\mathrm{Pa}$ is the reference sound pressure in the air.

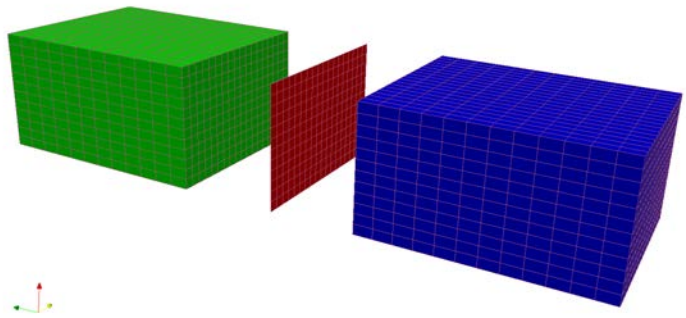

Figure 2.5: Finite element model: two acoustic rigid cavities separated by a $4\,mm$ thick plate

The convergence and the accuracy of the reduction method on a small problem, as discussed here, can then be easily checked by increasing the number of normal modes included in the basis up to its maximum, i.e. the number of internal dofs for each subdomain. The convergence on mean quadratic pressure with the associated error is shown in Fig. 2.6 (a)-(b) for the excited cavity, and in Fig. 2.7 (a)-(b) for the receiving cavity.

The only source of dissipation being a structural damping in the plate (1%), the amplitude of the error at the resonance frequencies is not significant. Instead, bandwidth of the error should be taken into consideration, as revealing a shift in the frequency response. The eigenfrequencies of the uncoupled components of the problem are presented in Table 2.1, in order to complete the interpretation of Fig. 2.6 and 2.7.

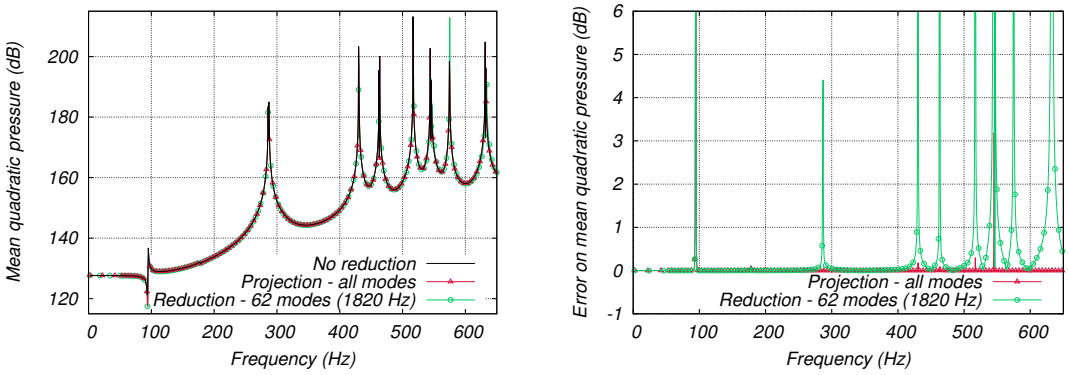

(a) (b)

Figure 2.6: Convergence of reduction in excited cavity: (a) Mean quadratic pressure in dB versus frequency (b) dB difference to unreduced problem

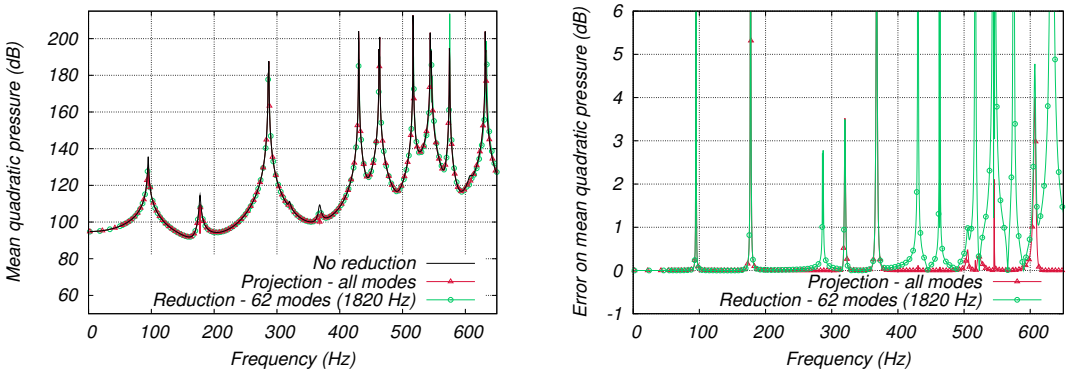

(a) (b)

Figure 2.7: Convergence or reduction in receiving cavity: (a) Mean quadratic pressure in dB versus frequency (b) dB difference to unreduced problem

Table 2.1 shows that the resonances which can be observed in the receiving cavity are either driven by acoustic modes, or plate modes. Comparing this fact with the convergence in the receiving cavity (Fig. 2.7), it appears that enriching the modal basis leads to converged results, except on resonances driven by plate modes. This failure can be well observed at the following frequencies: 93 Hz, 176 Hz, 320 Hz, 368 Hz and 608 Hz, while marginally obvious at 507 Hz and 520 Hz. This result should be taken into consideration for the accuracy study of the reduction when applied to larger problems, such as the one presented in Section 2.4.

***Cavities* (Hz)**	***Plate* (Hz)**	***Coupled problem* (Hz)**
-	93	93
-	179	176
286	286	286
-	321	320
-	369	368
430	-	430
463	-	463
-	507	507
517	-	517
-	520	518
544	-	544
575	-	575
-	608	608
632	-	632

Table 2.1: Computed eigenfrequencies of both cavities (identical), plate, and resonance frequencies of coupled problem extracted from FRF

2.3.4 Application to a dissipative poro-acoustic problem

2.3.4.1 Presentation and reference solution of the poro-acoustic problem

The implemented algorithm is further tested on a dissipative poro-acoustic example such as the cavity initially proposed in [109]. It consists of a 3D hexahedral acoustic cavity of dimensions $0.4 \times 0.6 \times 0.75$ m^3 (see Fig. 2.8), with rigid walls, and filled with air. One wall is covered with a 5 cm-thick layer of porous foam. The low frequency behavior is tested applying a harmonic volume velocity source (see Eq. (2.14)) at a corner of the cavity opposite to the porous layer.

Frame	***Fluid***	***Porous***
	$c_0 = 343$ m/s	$\phi = 0.9$
$\lambda = 1144$ kPa	$\gamma = 1.4$	$\sigma = 25$ kNs/m^4
$\mu = 286$ kPa	$Pr = 0.71$	$\alpha_\infty = 7.8$
$(1-\phi)\,\rho_\mathrm{s} = 30$ kg/m^3	$\rho_\mathrm{f} = 1.21$ kg/m^3	$\Lambda = 226\ \mu$m
	$\eta = 1.84 \cdot 10^{-5}$ Ns/m^2	$\Lambda' = 226\ \mu$m

Table 2.2: Air and porous material parameters

The cavity is discretized by an $8 \times 12 \times 15$ mesh of 8-node hexahedral elements with pressure as the single degree of freedom per node. The porous material, described by the Biot-Allard theory, is discretized by an $8 \times 12 \times 4$ mesh of 8-node hexahedral elements (see Fig. 2.8), with 6 dofs per node corresponding to the fluid and solid phase displacements (Subsection 2.2.1.3). Its material parameters are given in Table 2.2 (see Table 1.1 for the notations). The choice of parameters doesn't reflect the trend for porous materials mostly used in the literature (usually lower tortuosity and thermal characteristic length larger

than the viscous characteristic length in the literature), but can be compared to partially reticulated polyurethane foams such as those used in [43, 113].

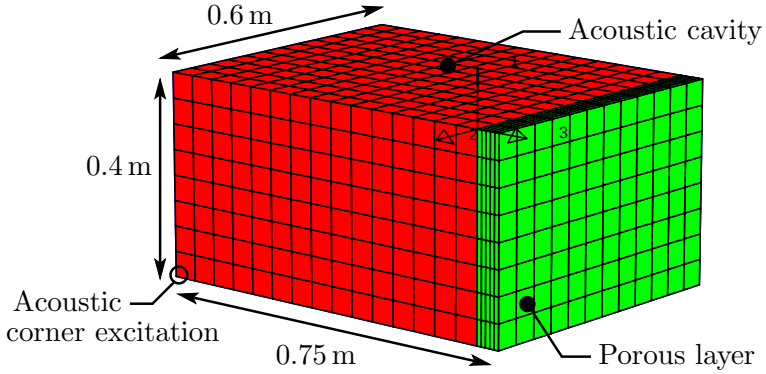

Figure 2.8: Acoustic cavity mesh and dimensions

Dirichlet boundary conditions are applied to the outer boundaries of the porous foam (see Subsection 2.2.2.1):

- sticking conditions are prescribed on the face in contact with the covered wall (see Eqs. (3.14));
- sliding conditions are prescribed on the side faces (see Eqs. (3.15)).

This leads to a finite element model with 1872 acoustic dofs, and 2648 porous dofs, i.e. 4520 dofs for the coupled problem. Fig. 2.9 presents the mean quadratic pressure frequency responses in the cavity, with and without the added porous layer, clearly illustrating the damping effect induced by the porous medium.

2.3.4.2 Reduction with no porous layer

First, the reduction is applied to the conservative problem consisting of the rigid acoustic cavity alone. It is being decomposed into two slightly different acoustic subdomains, as illustrated in Fig. 2.10, thus leading to a problem to solve of 118 kept dofs. The convergence is shown in Fig. 2.11 for two different truncation limits. Both truncations lead to a fairly good approximation of the original frequency response (Fig. 2.11 (a)). Plotting the error, as the point to point difference in dB between the unreduced and reduced frequency responses (Fig. 2.11 (b)), shows the expected improvement induced by adding normal modes into the basis. Again, due to the conservative property of the problem, errors at resonance frequencies are less significant.

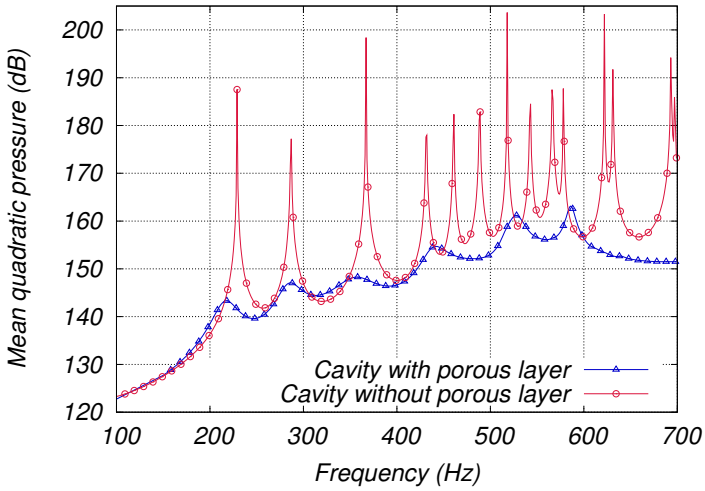

Figure 2.9: Mean quadratic pressure in cavity, with and without the porous layer

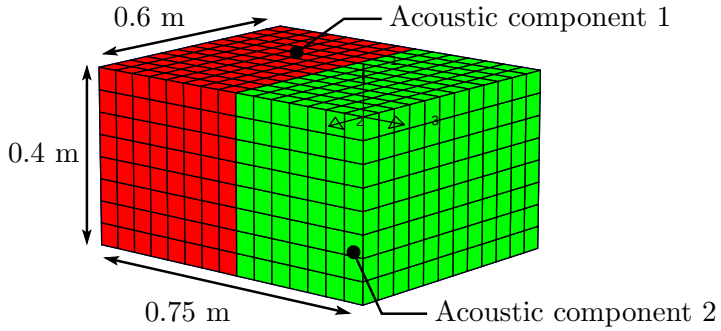

Figure 2.10: Rigid acoustic cavity decomposition into two components

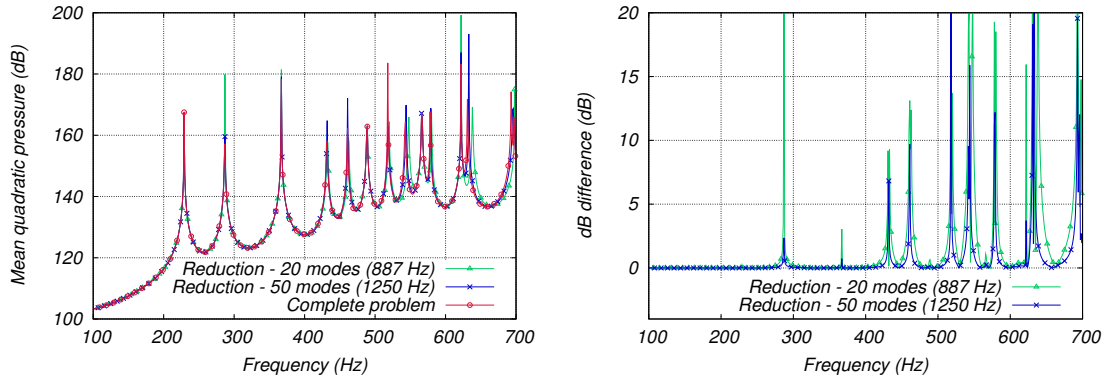

(a) (b)

Figure 2.11: Decomposition into two subdomains of the conservative problem: (a) FRF with 20 and 50 modes per component, (b) dB difference to unreduced problem

2.3.4.3 Reduced problem with porous layer

The next application includes the reduction of the acoustic part of the coupled poro-acoustic problem presented in Fig. 2.8. It is first decomposed into one acoustic component dynamically condensed to its interface with the porous medium, and then as two acoustic components defined similarly to the conservative problem shown in Fig. 2.10, involving problems to solve of respectively 2766 and 2883 kept dofs. The convergence of the single component reduction is plotted in Fig. 2.12 with truncations set at 10, 20 and 50 modes, i.e. 625 Hz, 887 Hz and 1250 Hz respectively. It shows, for this application, a good ability to approximate the original problem, with a dB difference kept lower than 0.7 dB (see Fig. 2.12 (b)) if selecting normal modes up to approximately twice the highest frequency of interest. For instance, the dB difference is lower than 0.7 dB up to 320 Hz with 10 modes included in the reduction basis, lower than 0.6 dB up to 460 Hz with 20 modes, and lower than 0.3 dB up to approximatively 600 Hz with 50 modes.

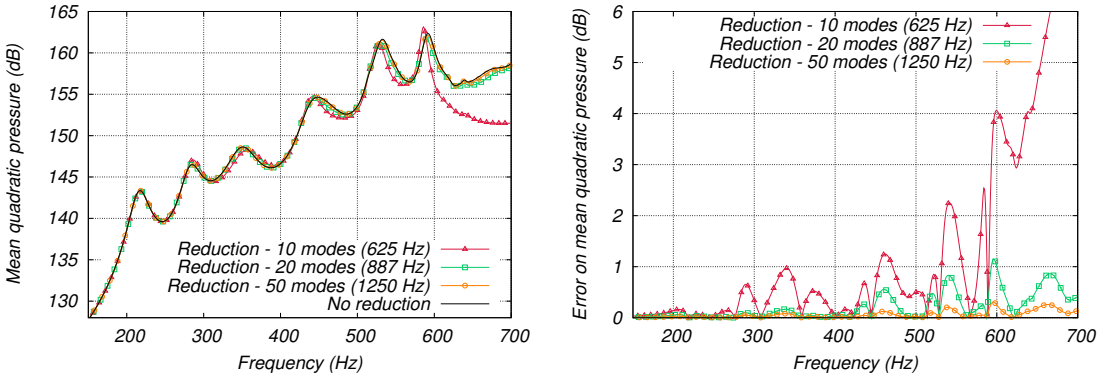

(a) (b)

Figure 2.12: Reduction of the acoustic component to its interface with porous: (a) FRF with 10, 20 and 50 modes, (b) dB difference to unreduced problem

The effect of decomposing the acoustic cavity into two components is presented in Fig. 2.13, as compared to the results of the decomposition into a single acoustic component (Fig. 2.12). The results with 50 normal modes for the single component reduction are retained, and compared with the results including 25 or 50 normal modes for each of the two acoustic components. While plotting the mean quadratic pressure frequency response shows a good approximation of the original problem (Fig. 2.13 (a)), a quantification of the error in dB compared to the unreduced problem (Fig. 2.13 (b)) gives two interesting expected conclusions: *i)* subdividing a component into several components, and including the same overall number of normal modes in the reduction process – which in this case corresponds to approximately the same truncation frequency per component – implies a

loss in precision, and *ii)*, subdividing a component into several components while keeping the number of normal modes unchanged for each component – thus implying raising the truncation frequency – leads to a more accurate approximation of the original problem. It should however be kept in mind that subdividing components, while interesting in order to increase the level of parallel computations in the reduction step, and deal with smaller eigenvalue problems, however implies an increased number of kept degrees of freedom, and thus a larger problem to solve at each frequency step. Therefore, a compromise in the substructuring strategy should be made depending on the considered problem.

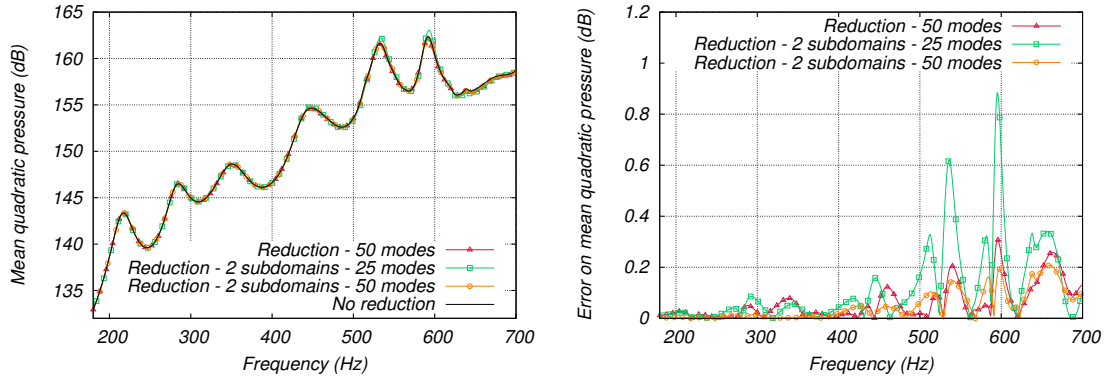

(a) (b)

Figure 2.13: Reduction with 2 acoustic components, and a porous layer: (a) FRF with 25 and 50 modes, (b) dB difference to unreduced problem

2.3.5 Truncation criterion for restrained-interface reduction

Truncation criteria for modal reduction methods are referred to, in the literature, as a frequency limit below which corresponding normal modes are selected to form part of the transformation basis. These normal modes are then completed by a set of vectors established according to the chosen reduction method, whose aim is to correct the error generated by truncation effects, and/or the chosen method (i.e. free-interface, restrained-interface, hybrid methods, see [96] for an overview). In the case of restrained-interface reduction, the question raised is to know whether the restrained-interface eigenfrequencies can be considered for truncation or not. Free-interface eigenfrequencies, as compared to a set frequency limit, might be a more suitable and reliable way to define a truncation criterion, as free-interface normal modes are closer to the physics of the original problem. Fig. 2.14 illustrates two academic problems similar to those of the previous section, used in order to compare truncation criteria based on free- or restrained-interface eigenfrequencies. They consist of a rigid acoustic cavity with one wall covered of a porous layer (5 cm-thick). Two different sizes are set for the cavities, of dimensions $0.4 \times 0.6 \times 0.75$ m^3 , and

$0.4 \times 0.6 \times 0.25$ m^3.

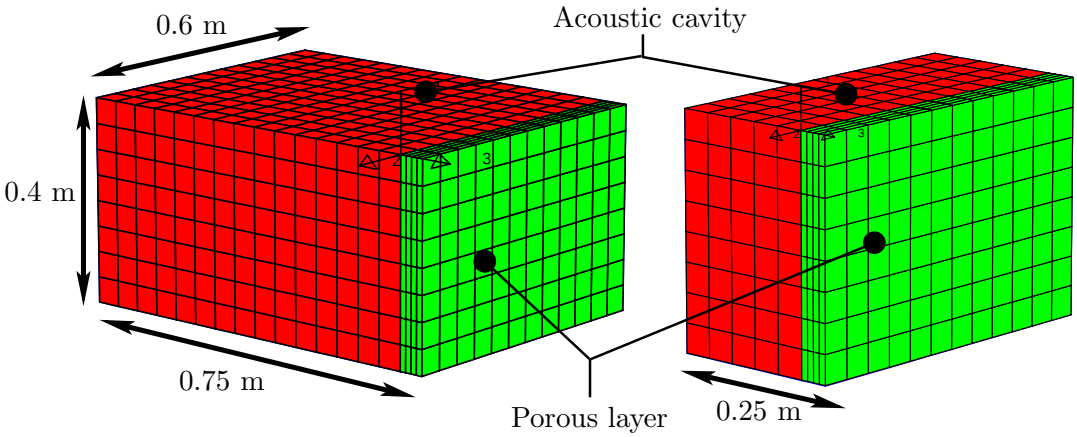

Figure 2.14: Rigid acoustic cavities used for testing the truncation limit criteria

In the next step, a restrained-interface reduction, involving a single acoustic component dynamically condensed to its interface with the porous medium, is applied to both these problems. The influence of these artificial boundary conditions for the eigenvalue problem is obviously more important for the smaller cavity. In order to test the impact of using restrained-interface eigenfrequencies for the truncation criterion, the iterative procedure presented in Fig. 2.15 is applied. While restrained-interface normal modes are used in the reduction basis of the previously described iterative procedure, free-interface normal modes are also computed. For each restrained-interface eigenfrequency saved as the last normal mode included in the transformation matrix satisfying the error criterion, the corresponding free-interface eigenfrequency is also saved.

Application of this procedure gives the frequency limit of validity of the transformation for each additional normal mode included in the transformation basis and for a given error tolerance on the mean quadratic pressure. These results are plotted in Fig. 2.16 (a)-(d) for the larger and smaller cavities, with a fixed error tolerance of 0.1 dB. Normal modes are referred to using their restrained-interface eigenfrequency (a,c) or the corresponding free-interface eigenfrequency (b,d).

First, the eigenfrequencies plotted with respect to the limit of validity of the applied transformation exhibit step functions. Discontinuities are observed at resonance frequencies of the coupled problem, which emphasizes the fact that precision (convergence) issues are concentrated around these resonance frequencies. This result is in agreement with the plots about convergence previously presented for both damped and undamped problems. In particular, errors on the mean quadratic pressure were noted to be more important around the resonance frequencies due to both an error on the level (c.f. damped problem)

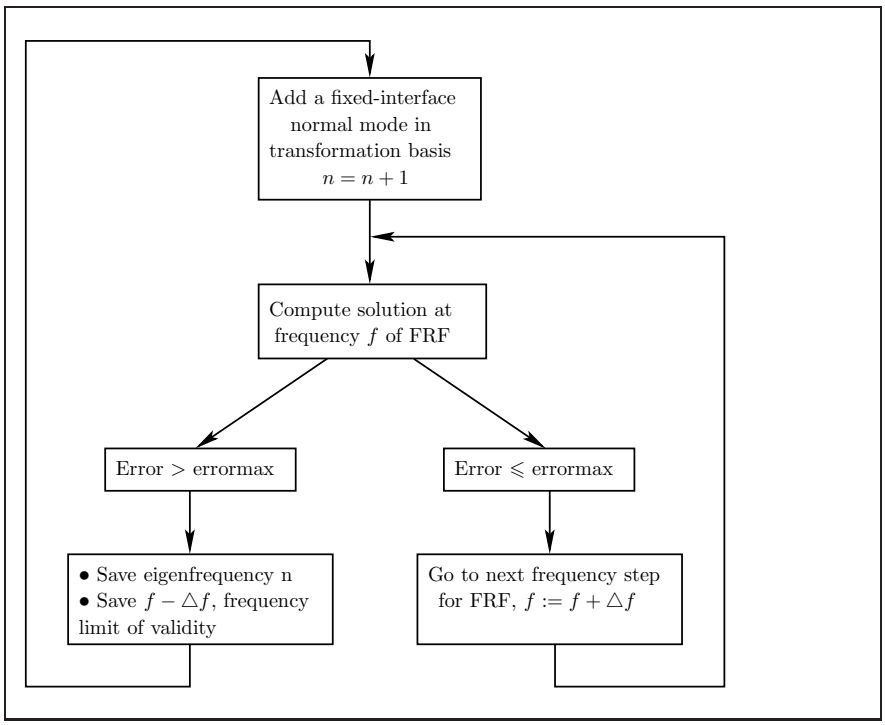

Figure 2.15: Iterative procedure to test influence of restrained or free interface truncation criterion

and a shift in frequency (c.f. undamped problem). Consequently, enriching the modal basis in fact emphasizes on reducing the error around eigenfrequencies of the problem, and is not a smooth process. However, despite the discontinuities observed in order to reach a set precision, the overall low frequency behavior of enriching the modal basis seems to be a linear function of the frequency limit of validity for both problems. This is in agreement with the classically used results in the literature where truncation criteria are specified as a multiple of the maximum frequency of interest in the problem [90]. In Figs. 2.16, these multiplying factors correspond approximatively to the slopes of the regression lines added to the numerical results. Moreover, it is interesting to notice that for both the larger and smaller cavities, the slopes of the regression lines, i.e. the truncation criteria, are the same for either free or restrained-interface eigenfrequencies. Therefore, the truncation criterion for restrained-interface reduction methods may be based on eigenfrequencies of its restrained-interface eigenvalue problem, in complete analogy to free-interface reduction methods [90, 92].

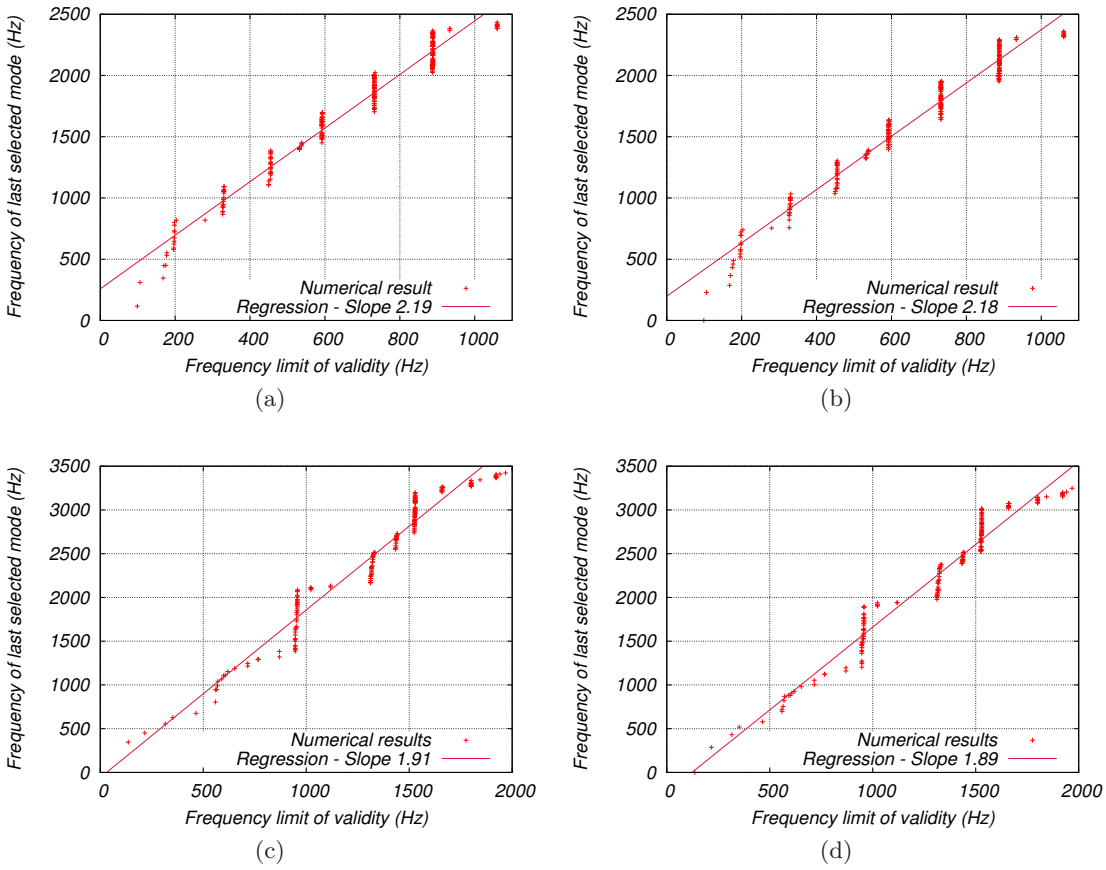

Figure 2.16: Effect of boundary conditions on truncation criterion, error tolerance of 0.1 dB: (a) Restrained-interface eigenfrequencies for largest cavity, (b) Free-interface eigenfrequencies for largest cavity, (c) Restrained-interface eigenfrequencies for smallest cavity, (d) Free-interface eigenfrequencies for smallest cavity

2.4 Application and results

In this section, the substructuring restrained-interface reduction is applied to a larger vibroacoustic problem, called the *concrete car*, which is a model based on an experimental set-up initially proposed by LMS International in Leuven. It consists of two rigid acoustic cavities separated by a firewall, which allows noise generated in the first cavity – engine cavity (EC) – to be transmitted to the second cavity, the passenger cavity (PC). The latter is optionally treated with a porous layer on one wall, in order to lower the sound level. The numerical model is first presented in Subsection 2.4.1, considering both cases with and without a porous layer, and presenting reference numerical solutions for the unreduced problem. Restrained-interface substructuring reduction strategies are then investigated in order to evaluate the efficiency of the method on problems larger than the ones previously

presented in Subsections 2.3.3 and 2.3.4.

2.4.1 Complete *concrete car* model, and effect of porous damping

As previously mentioned, the *concrete car* model is composed of two acoustic cavities, separated by a 4 mm-thick firewall. Its external dimensions are given in Fig. 2.17. The geometry is symmetric with respect to a $(\boldsymbol{x}, \boldsymbol{z})$ mirror plane.

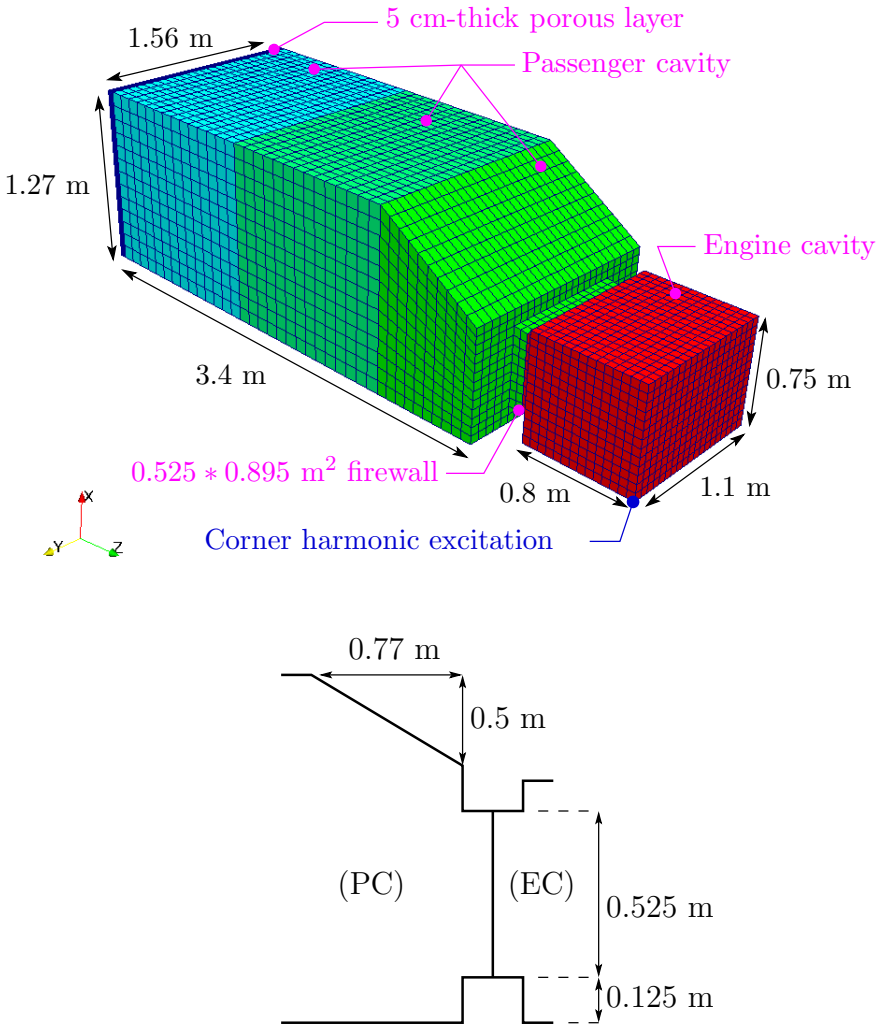

Figure 2.17: *Concrete car* FE model and external dimensions.

The mesh is composed of hexahedral elements for the acoustic cavities, involving 3728 elements for the EC, and 12620 elements for the PC. The firewall is meshed with 9×15 quadrilateral shell elements, while the porous layer is composed of $25 \times 13 \times 4$ hexahedral

elements. The firewall is considered clamped along its edges. Additional natural boundary conditions are specified for the porous material, which is fixed on one face to the rigid wall of the acoustic cavity, while sliding conditions are imposed on the four side faces of the layer.

Mean quadratic pressure frequency responses in each cavity are computed. Therefore, a frequency by frequency direct solution is adopted, with an excitation imposed at a lower corner of the EC (see Fig. 2.17). Steps of 1 Hz increments in a range of $1 - 600$ Hz are processed, both with and without the porous layer, thus providing a reference FRF for further reduction tests, as well as showing the damping effect of the porous layer in the PC.

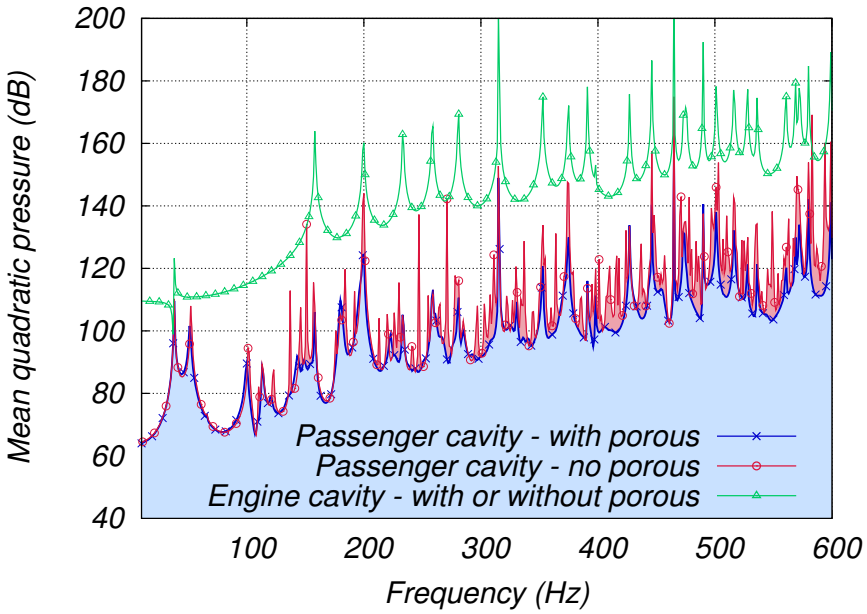

Figure 2.18: Reference FRF with and without porous layer

The mean quadratic pressure FRF in both cavities is presented in Fig. 2.18. It reveals different spectral densities in each one: while relatively low in the smaller cavity (EC), it gets increasingly higher in the PC due to the different sizes of these cavities. Plotting the solution at selected peaks of the FRFs (Fig. 2.19), as well as computing the eigenfrequencies of the uncoupled components (Table 2.3) bring further information. Thus, resonances observed in the EC are driven by its acoustic cavity modes. However, sound level peaks in the PC are either driven by its acoustic cavity modes (e.g. 52 Hz), modes of the firewall (e.g. 38 Hz), or acoustic modes of the EC (e.g. 315 Hz).

The partial treatment of the PC with a damping layer has no effect on the sound level in the EC. Regarding the PC, it is a well known result that porous media have relatively

low damping efficiency in the very low frequencies (see e.g. [80]), which can be observed in at least one third of the frequency range plotted. Damping becomes more efficient above this limit but, interestingly, all peaks are not damped with the same efficiency. Again, plots in Fig. 2.19 reveal that identified PC acoustic modes driven peaks are the most efficiently damped resonances, while EC or firewall modes driven peaks are mostly poorly damped. It is especially obvious when observing resonance frequencies in the PC that correspond to peaks of pressure in the EC.

***Engine cavity* (Hz)**	***Passenger cavity* (Hz)**	***Firewall* (Hz)**
-	-	38
-	52	-
-	-	66
-	101	-
-	110	-
-	-	114
-	-	122
-	123	-
-	137	-
-	146	-
-	-	149
-	151	-
-	157	-
158	-	-
-	176	-
-	-	180
-	184	-
-	192	-
-	-	193
199	-	-
-	200	-
-	213	-
-	220	-
-	226	-
-	230	-
233	-	-
-	241	-
-	245	-
-	247	-
-	255	-
-	-	256
258	-	-
-	260	-
⋮	⋮	⋮
-	311	-
315	-	-
-	322	-

Table 2.3: Uncoupled eigenfrequencies of the *concrete car* model

2.4.2 Performance of the substructuring method with modal reduction of the non dissipative domains

The restrained-interface reduction method presented in Section 2.3.2 is now applied to the *concrete car* model, in order to estimate the cost improvements reached as well as the

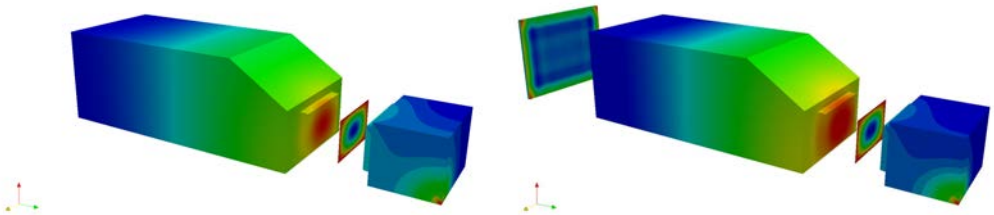

(a)

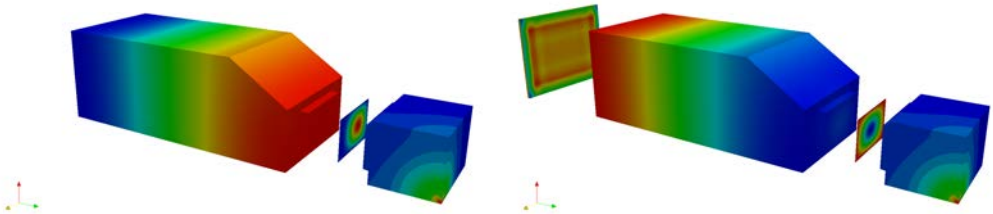

(b)

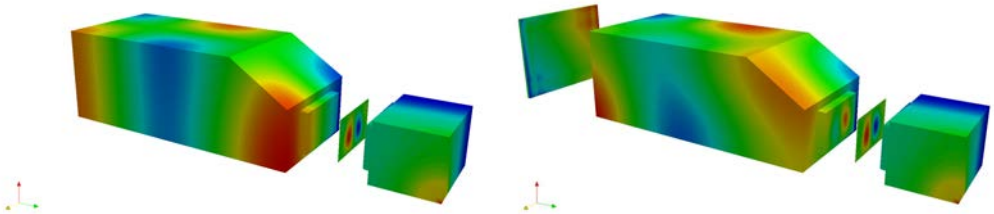

(c)

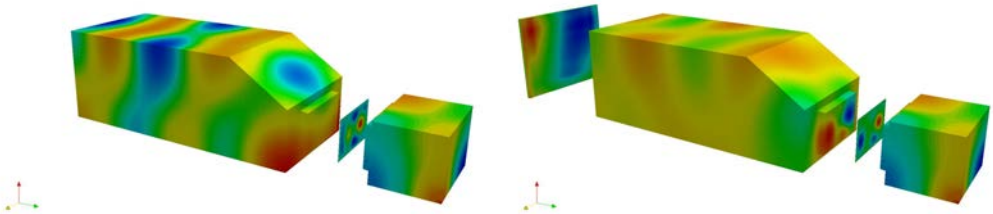

(d)

Figure 2.19: Solution without (left) and with (right) porous layer, pressure field in the acoustic cavities, normal displacement in the plate and porous domain. (a) $f = 38$ Hz, (b) $f = 52$ Hz, (c) $f = 151$ Hz, (d) $f = 247$ Hz, (e) $f = 315$ Hz

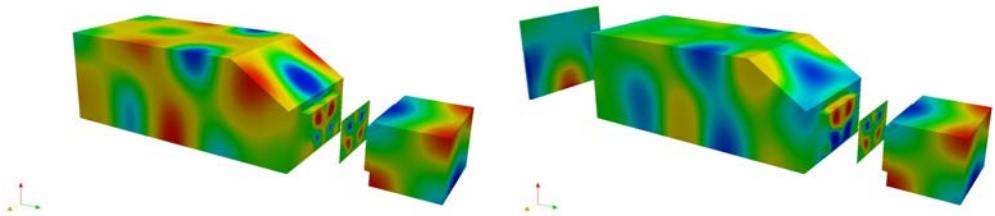

(e)

Figure 2.19: Solution without (left) and with (right) porous layer, pressure field in the acoustic cavities, normal displacement in the plate and porous domain. (a) $f = 38$ Hz, (b) $f = 52$ Hz, (c) $f = 151$ Hz, (d) $f = 247$ Hz, (e) $f = 315$ Hz

trade-off that has to be made between accuracy and computational time. First, the model is decomposed into 4 acoustic subdomains of approximately the same size (3 subdomains for the PC, and one for the EC), thus reducing the problem to be solved to the size of the acoustic interfaces, the wireframe and the porous layer with their acoustic interfaces (see Fig. 2.20). This leads to a problem downsized from 28500 to 10600 dofs, of which 8700 belong to the porous medium.

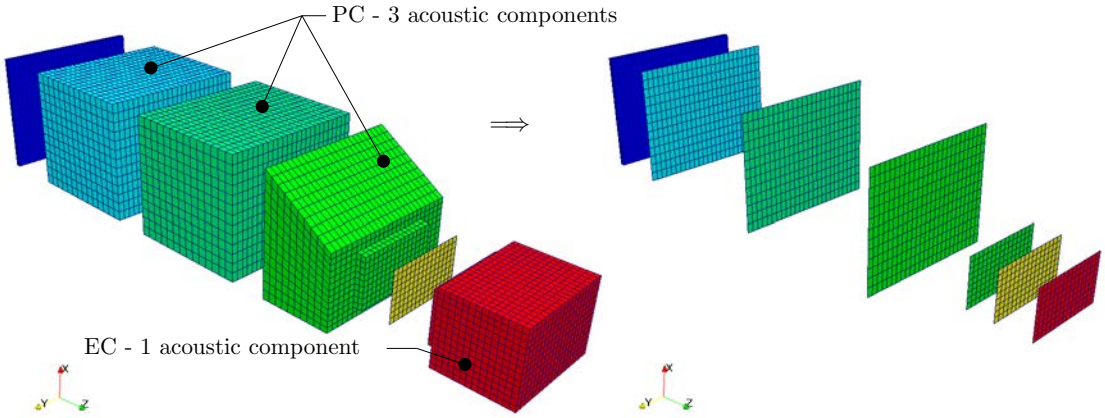

Figure 2.20: Decomposition of the *concrete car* into 4 acoustic components, and illustration of the reduced problem

Three different truncation limits for the modal basis are tested, based on eigenfrequencies of the restrained-interface modes: *i)* twice the highest frequency of interest, i.e. 1200 Hz, *ii)* 2,5 times the highest frequency of interest, i.e. 1520 Hz and *iii)* more than 3 times the highest frequency of interest, i.e. 1980 Hz. An incore eigensolver based on an iterative subspace algorithm is used to compute the modes. While rather inefficient

for large-sized problems, especially when numerous modes are to be computed, CPU time spent for this step is nevertheless included in the presented results.

Fig. 2.21 (a) shows results in terms of the mean quadratic pressure in both the EC and PC, with a truncation of the modal basis at 1200 Hz. The reference frequency response is plotted with overlapping curves, so that the error associated with the reduction can be visualized. In addition, the associated point to point dB difference is plotted as an error indicator (Fig. 2.21 (b)), and in order to clarify the results, it is also represented in a smoothed way using Bézier curves. The mean quadratic pressure FRF shows very good accuracy of the reduction for the EC whereas some subsequent errors can be noticed for the PC. This is confirmed by the dB difference plot, which shows insignificant error up to around 300 Hz for the EC, and an increasing error from then. The slight frequency shift noticeable on the mean quadratic pressure FRF (Fig. 2.21 (a)), indicates that the imposed truncation limit is mostly responsible for the accuracy issues in the EC. Regarding the PC, similar distinctions can be made, precision-wise, when comparing results under and above 300 Hz, but with substantially more significant error. Interestingly, when comparing to Fig. 2.18, the best precision seems to be achieved in the PC for peaks least affected by the porous damping effect, i.e. the EC modes driven peaks.

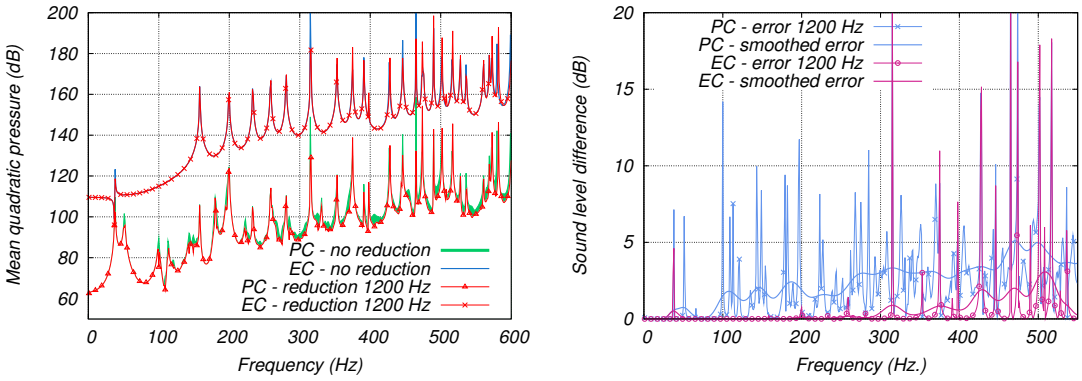

(a) (b)

Figure 2.21: Results with truncation at 1200 Hz: (a) FRF of mean quadratic pressure (b) dB difference to unreduced problem

Fig. 2.22 shows the effect of increasing the frequency limit of truncation to 1500 Hz and 1980 Hz. The mean quadratic pressure FRF in both cavities, before and after reduction, is presented in Fig. 2.22 (a), while Fig. 2.22 (b) shows the evolution of the error in a smoothed representation. It appears that the truncation of the modal basis at 1200 Hz is optimum for a range up to around 300 Hz. Enriching the basis helped reducing the error to under half a decibel for the EC, and around 3 dB for the PC. The precision achieved for the range $0 - 300$ Hz indicates that the remaining error is not associated with an enrichment

of the modal basis, and the reduction applied seems therefore unable to converge to the unreduced solution (as shown in Subsection 2.3.3).

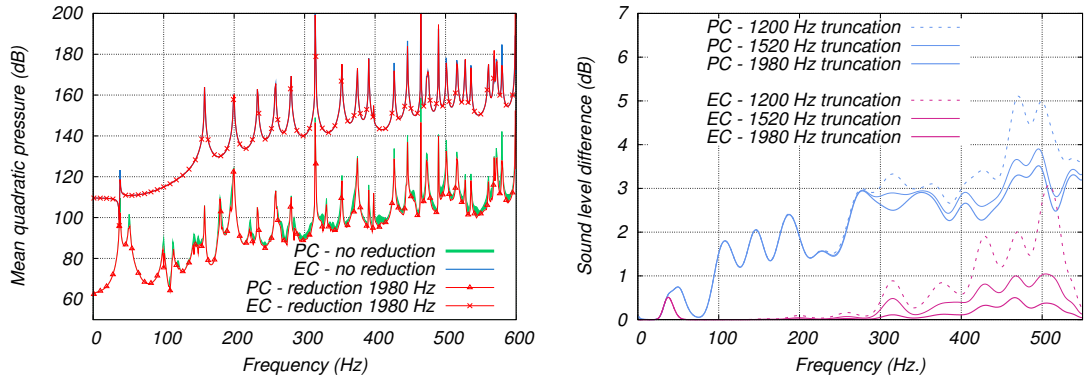

(a) (b)

Figure 2.22: Results with truncation up to 1980 Hz: (a) FRF of mean quadratic pressure (b) dB difference to unreduced problem

Fig. 2.23 presents the CPU time of the computations both with and without reduction. It clearly illustrates the benefits of the reduction over several frequency increments. The time offset due to the modal basis computation can be seen at increment 0, and, as previously mentioned, it is attributed to a rather inefficient subspace iterative algorithm. Furthermore, it is interesting to notice, as expected, that the CPU time for each increment is not much affected by the size of the modal basis. This is due, as presented in Subsection 2.3.2, to the implementation of the algorithm, in which the size of the modal basis has an influence only during the restitution phase in postprocessing. This step could actually be skipped if the solution at internal dofs was not needed, or only needed for a few dofs that would then be kept as uncondensed dofs.

2.4.3 Effect of the substructuring strategy on accuracy

In order to check possible sources of convergence difficulties other than those demonstrated in Subsection 2.3.3, the chosen decomposition strategy is here questioned. Two additional decompositions are tested. In the first one, the EC is not reduced anymore, while the three components defined previously in the PC are kept, thus leading to a problem to solve with three components instead of the 4 previously described. As no error is being made in the EC, an improvement of the accuracy could be expected in the PC, even though the error plot between $100 - 200$ Hz in Fig. 2.22 (b) indicates that few improvements if at all are to be expected. Then, the influence of subdividing the PC into three artificial components is quantified by defining it as a unique large component. The EC

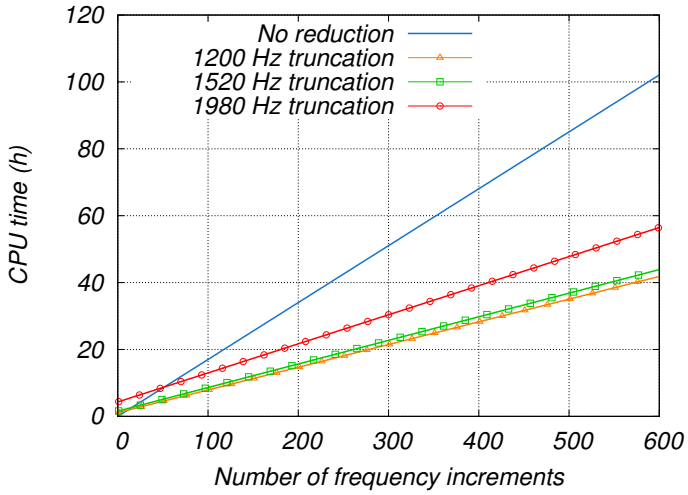

Figure 2.23: CPU time comparison

being as well reduced to its interface with the firewall, this second decomposition involves each cavity to be considered as a component. The results, presented in Fig. 2.24 for the PC, comparing mean quadratic pressure for the three proposed decompositions, show almost perfect match of the results. This suggests that sub-decomposition of the PC does not contribute significantly to the convergence difficulties observed in the PC.

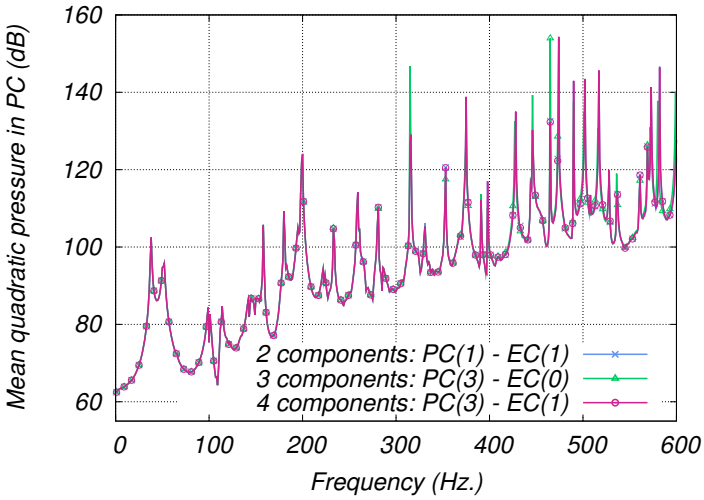

Figure 2.24: FRF in passenger cavity for different decompositions, truncation at 1200 Hz

The influence of a porous layer adjunction on the convergence issues of the method is then checked by computing the conservative solution - without porous layer - using the decomposition into 4 acoustic components, introduced in Subsection 2.4.2. The mean quadratic pressure frequency response for a 1200 Hz truncation, as well as the smoothed

dB difference for all three truncation criteria are presented in Fig. 2.25 (a) and (b). Although errors should be taken with care as the problem is not damped, and the solution at resonances is very frequency-shift sensitive, the results clearly state a good accuracy achieved, with a solution converging faster to the unreduced problem solution. This indicates that the change of boundary conditions induced by the addition of a porous layer deteriorates the convergence property of the method. This adds to the limitations highlighted in Subsection 2.3.3 regarding the accuracy of the dynamic condensation, which can be observed in the PC around 30 Hz, 110 Hz, or 180 Hz for instance.

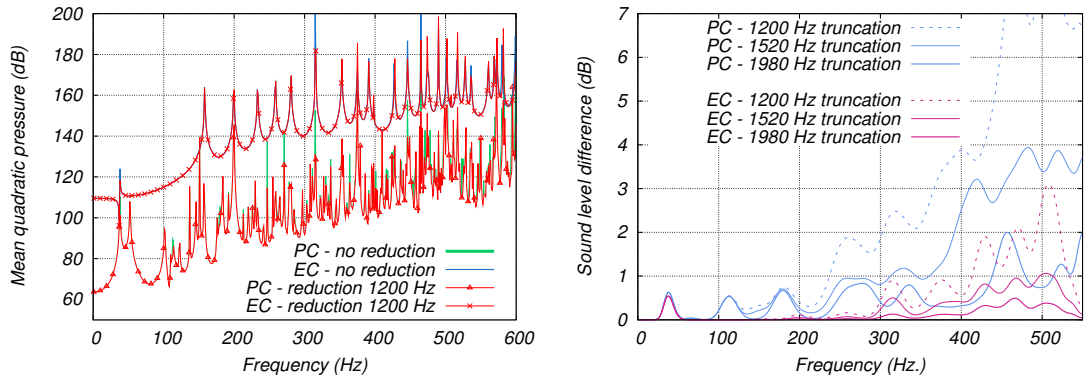

(a) (b)

Figure 2.25: Results without porous layer: (a) Mean quadratic pressure, truncation at 1200 Hz, (b) dB difference to unreduced problem, truncation up to 1980 Hz

2.5 Conclusion

In this chapter, the variational formulation of a time-harmonic elasto-poro-acoustic problem was presented, in order to test the efficiency and limitations of using a CMS strategy to reduce its final size. The substructuring reduction was detailed and applied to the conservative part of the included applications, i.e. the acoustic domain. The restrained-interface eigenfrequencies were found suitable to be used a priori for an estimation of truncation criteria. Regarding the performance of the CMS strategy used, although efficient for small scale applications, as it is mostly presented in the literature, it was shown that the computational efficiency for larger problems was gained at the expense of a loss in accuracy for specific frequency ranges.

First, the use of attachment functions built on the acoustic stiffness matrix exhibits convergence limitations at frequencies which correspond to the eigenfrequencies of the surrounding structural domain, acting as a source of excitation. On this matter, the use of similar functions as the so-called pseudo-static modes used in structural mechanics,

which take into account the inertial contribution of each component, could improve the convergence and be an extension of this work. It would however deteriorate the computation efficiency of the method, as these improved attachment functions introduce acoustic stiffness coupling between the interface and the subdomains dofs in the reduced problem.

Secondly, the addition of damping, such as including a porous layer at the boundary of the acoustic domains, further emphasizes these convergence issues. Again, refined attachment functions could substantially improve the convergence of the method.

Finally, the use of costly 3D modelling of porous media being responsible for most of the remaining computational cost, it is the objective of the following chapters to propose similar approaches for this part of the coupled problem.

In fact, solutions have been proposed in the literature to potentially respond to the first two points (see e.g. [84, 70]). It would thus be a natural extension to this part of the thesis to test these solutions for improvements of the precision. However, the level of precision achieved without further corrections is very acceptable from an engineering perspective. Consequently, the choice made for the continuation of the work is rather to investigate the so far unanswered question of applying similar methods to the very costly modelling of poroelastic materials.

Chapter 3

Modal-based reduction of porous materials in structural-acoustic applications

Abstract: *This chapter presents a modal approach based on a standard real-valued eigenvalue problem, aimed at the reduction of the poroelastic part of poro-acoustic applications. It is enabled by a rearrangement in the variational formulation of the solid and fluid phase displacements formulation ($\mathbf{u}_s$,$\mathbf{u}_f$) for the poroelastic domain. A 1D and a 3D validation cases are presented to illustrate the potential performance and the limitations of the proposed approach.*

Contents

3.1 Introduction

In this chapter, a modal approach based on a standard real-valued eigenvalue problem is proposed to reduce the poroelastic part of poro-acoustic applications. It is enabled by a rearrangement in the variational formulation of the well-established solid and fluid phase displacements formulation ($\mathbf{u}_\mathrm{s}$,$\mathbf{u}_\mathrm{f}$) for the poroelastic domain. The method is first tested on a 1D validation case. Its potential performance and limitations are then illustrated on a 3D academic application. It exhibits promising sparsity properties for the reduced system matrix. However, excluding the case of 1D applications, the convergence is shown to be relatively limited, thus suggesting the need for further investigations.

The Chapter is organized around four parts. The first section introduces the general poro-acoustic problem used, as well as the corresponding FE formulation for time-harmonic excitations. The poroelastic equations are rewritten focusing on the possibility to associate a standard eigenvalue problem. In the following section, the proposed modal reduction of porous media is presented, included in a substructuring decomposition strategy. The emphasis being to establish the modal approach feasibility rather than to investigate the chosen decomposition strategy and its performance, only the porous domain is reduced. The method being general, it can however be easily included in all forms of classically used decomposition strategies [86]. The third section of this work is then dedicated to numerical applications. A unidimensional example is first investigated to establish the potential of the proposed reduction in terms of accuracy and downsizing of dofs. Then, a 3D academic application allows to estimate the performances in terms of precision, computational time, size and sparsity of the reduced problem. While promising, it is shown that there is room for further improvements to take full advantage of the reduction strategy when applied to multidimensional applications.

3.2 Finite element formulation

Even though previously introduced in Chapters 1 or 2, the main notations and equations leading to the variational formulation are briefly repeated in the following for the sake of self-contained readability of the chapter.

A poro-acoustic problem is considered, whose description and notations are presented in Fig. 3.1. The acoustic fluid and the porous medium occupy the domains Ω_F and Ω_P respectively. The compressible fluid is described using pressure fluctuation (p) as primary variable (Section 3.2.1.1), while fluid and solid phases homogenized displacements ($\mathbf{u}_\mathrm{s}$,$\mathbf{u}_\mathrm{f}$) are retained as primary variables for the porous media (Section 3.2.1.2). The domains boundaries are separated into contours of:

- imposed Dirichlet boundary conditions denoted $\partial_1\Omega_{\mathrm{F}}$ and $\partial_1\Omega_{\mathrm{P}}$,
- prescribed Neumann boundary conditions denoted $\partial_2\Omega_{\mathrm{F}}$ and $\partial_2\Omega_{\mathrm{P}}$,
- coupling interface between the acoustic fluid and the porous medium (Γ_{FP}).

The FE formulation is presented for a time-harmonic response at angular frequency ω.

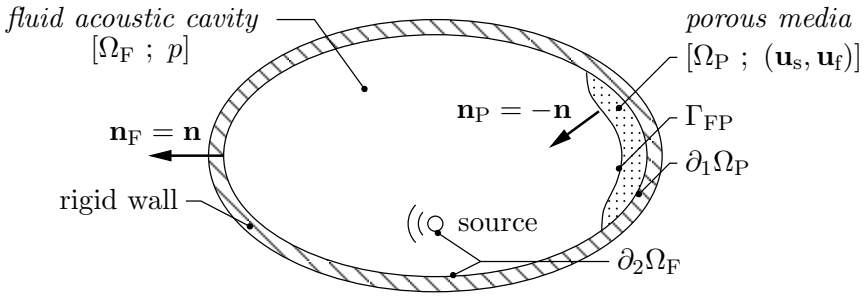

Figure 3.1: Description and notations of the poro-acoustic interaction problem

3.2.1 Dynamic equations and constitutive laws

3.2.1.1 Compressible fluid (p)

The internal fluid within cavities is assumed compressible and inviscid, satisfying the Helmholtz equation derived from the motion, continuity, and constitutive equations,

$$\Delta p + \frac{\omega^2}{c_0^2} p = 0 \quad \text{in } \Omega_{\mathrm{F}}, \tag{3.1}$$

where c_0 is the constant speed of sound in the fluid, and p the pressure fluctuation scalar field. As previously mentioned in Chapter 2, the limit case $\omega = 0$ though not considered in this work, is given by the static solution of the coupled fluid-structure problem [56, 69].

3.2.1.2 Porous media Biot theory ($\mathbf{u}_{\mathrm{s}}, \mathbf{u}_{\mathrm{f}}$)

The poroelastic equations are presented, based on the standard notations for material parameters introduced in Table 1.1 [10]. At angular frequency ω, the poroelastic medium satisfies the elastodynamic linearized equations (Eqs. (1.12)), derived in the Biot-Allard theory [10], taking into account inertial and viscous coupling effects between solid and fluid phases,

$$\operatorname{div}\boldsymbol{\sigma}_{\mathrm{s}} - \mathrm{i}\,\omega\,\widetilde{b}(\omega)(\mathbf{u}_{\mathrm{s}} - \mathbf{u}_{\mathrm{f}}) + \omega^2\left[((1-\phi)\,\rho_{\mathrm{s}} + \rho_{\mathrm{a}})\mathbf{u}_{\mathrm{s}} - \rho_{\mathrm{a}}\mathbf{u}_{\mathrm{f}}\right] = \mathbf{0}, \tag{3.2a}$$

$$\operatorname{div}\boldsymbol{\sigma}_{\mathrm{f}} - \mathrm{i}\,\omega\,\widetilde{b}(\omega)(\mathbf{u}_{\mathrm{f}} - \mathbf{u}_{\mathrm{s}}) + \omega^2\left[-\rho_{\mathrm{a}}\mathbf{u}_{\mathrm{s}} + (\phi\rho_{\mathrm{f}} + \rho_{\mathrm{a}})\mathbf{u}_{\mathrm{f}}\right] = \mathbf{0}. \tag{3.2b}$$

where $\mathbf{u}_\mathrm{s}$ and $\mathbf{u}_\mathrm{f}$ are respectively the solid phase and fluid phase averaged displacements. $\widetilde{b}(\omega)$ (henceforth denoted $\widetilde{b}$, where $\widetilde{\ }$ refers to a complex-valued quantity) and ρ_a are respectively the complex frequency-dependent viscous drag and the inertia coupling parameter, given by Eqs. (1.13) and (1.14),

$$\widetilde{b} = \sigma\phi^2 \left[1 + \frac{4i\omega\alpha_\infty^2\eta\rho_\mathrm{f}}{\sigma^2\Lambda^2\phi^2}\right]^{\frac{1}{2}}, \tag{3.3}$$

$$\rho_a = \phi\rho_\mathrm{f}\,(\alpha_\infty - 1). \tag{3.4}$$

$\boldsymbol{\sigma}_\mathrm{s}$ and $\boldsymbol{\sigma}_\mathrm{f}$ are the averaged stress tensors for the solid and fluid phases respectively. They satisfy the Lagrangian stress-strain relations developed by Biot. Under the assumption of large values for the bulk modulus of the porous frame material, which is typically the case in acoustic applications with sound absorbing materials, these stress-strain relations can be written as functions of the complex-valued and frequency-dependent equivalent bulk modulus $\widetilde{K}_\mathrm{f}(\omega)$ (see Section 1.4.2),

$$\boldsymbol{\sigma}_\mathrm{s} = 2\widetilde{\mu}\,\boldsymbol{\varepsilon}(\mathbf{u}_\mathrm{s}) + \left(\widetilde{\lambda} + \frac{(1-\phi)^2}{\phi}\widetilde{K}_\mathrm{f}(\omega)\right)\mathrm{tr}\left[\boldsymbol{\varepsilon}(\mathbf{u}_\mathrm{s})\right]\mathbf{1} + (1-\phi)\,\widetilde{K}_\mathrm{f}(\omega)\,\mathrm{tr}\left[\boldsymbol{\varepsilon}(\mathbf{u}_\mathrm{f})\right]\mathbf{1}, \tag{3.5a}$$

$$\boldsymbol{\sigma}_\mathrm{f} = (1-\phi)\,\widetilde{K}_\mathrm{f}(\omega)\,\mathrm{tr}\left[\boldsymbol{\varepsilon}(\mathbf{u}_\mathrm{s})\right]\mathbf{1} + \phi\,\widetilde{K}_\mathrm{f}(\omega)\,\mathrm{tr}\left[\boldsymbol{\varepsilon}(\mathbf{u}_\mathrm{f})\right]\mathbf{1}, \tag{3.5b}$$

where $\boldsymbol{\varepsilon}(\mathbf{u}_\mathrm{s})$ and $\boldsymbol{\varepsilon}(\mathbf{u}_\mathrm{f})$ are the strain tensors associated with the averaged displacements vector fields $\mathbf{u}_\mathrm{s}$ and $\mathbf{u}_\mathrm{f}$ respectively. $\mathbf{1}$ represents a unitary matrix. Beside the standard material parameters presented in Table 1.1, the dynamic bulk modulus $\widetilde{K}_\mathrm{f}(\omega)$ (henceforth denoted $\widetilde{K}_\mathrm{f}$) is given in Eq. (1.20) [10]. For reasons to be presented in Section 3.3.2, its expression is separated into its zero-frequency limit and complex frequency-dependent behaviour:

$$\widetilde{K}_\mathrm{f} = \frac{\gamma P_0}{\gamma - (\gamma-1)\left[1 + \frac{8\eta}{i\omega Pr\Lambda'^2\rho_\mathrm{f}}\left(1 + \frac{i\omega Pr\Lambda'^2\rho_\mathrm{f}}{16\eta}\right)^{\frac{1}{2}}\right]^{-1}} = P_0 + \left(\widetilde{K}_\mathrm{f} - P_0\right), \tag{3.6}$$

which, when introduced in Equations (3.5), leads to the following expressions of the stress-strain relations using Voigt notation,

$$\boldsymbol{\sigma}_\mathrm{s} = \mathbf{D}_\mathrm{s}^{(1)}\,\boldsymbol{\varepsilon}(\mathbf{u}_\mathrm{s}) + \mathbf{D}_\mathrm{sf}^{(1)}\,\boldsymbol{\varepsilon}(\mathbf{u}_\mathrm{f}) + \left(\widetilde{K}_\mathrm{f} - P_0\right)\left(\mathbf{D}_\mathrm{s}^{(2)}\,\boldsymbol{\varepsilon}(\mathbf{u}_\mathrm{s}) + \mathbf{D}_\mathrm{sf}^{(2)}\,\boldsymbol{\varepsilon}(\mathbf{u}_\mathrm{f})\right), \tag{3.7a}$$

$$\boldsymbol{\sigma}_\mathrm{f} = \mathbf{D}_\mathrm{sf}^{(1)}\,\boldsymbol{\varepsilon}(\mathbf{u}_\mathrm{s}) + \mathbf{D}_\mathrm{f}^{(1)}\,\boldsymbol{\varepsilon}(\mathbf{u}_\mathrm{f}) + \left(\widetilde{K}_\mathrm{f} - P_0\right)\left(\mathbf{D}_\mathrm{sf}^{(2)}\,\boldsymbol{\varepsilon}(\mathbf{u}_\mathrm{s}) + \mathbf{D}_\mathrm{f}^{(2)}\,\boldsymbol{\varepsilon}(\mathbf{u}_\mathrm{f})\right), \tag{3.7b}$$

with

$$\begin{aligned}
\mathbf{D}_{\mathrm{s}}^{(1)} &= 2\widetilde{\mu}\,\mathbf{D}' + \left(\widetilde{\lambda} + \frac{(1-\phi)^2}{\phi} P_0\right)\mathbf{D},\\
\mathbf{D}_{\mathrm{sf}}^{(1)} &= (1-\phi)\,P_0\,\mathbf{D},\\
\mathbf{D}_{\mathrm{f}}^{(1)} &= \phi\,P_0\,\mathbf{D},\\
\mathbf{D}_{\mathrm{s}}^{(2)} &= \frac{(1-\phi)^2}{\phi}\mathbf{D},\\
\mathbf{D}_{\mathrm{sf}}^{(2)} &= (1-\phi)\,\mathbf{D},\\
\mathbf{D}_{\mathrm{f}}^{(2)} &= \phi\,\mathbf{D},
\end{aligned}$$

where

$$\mathbf{D}' = \begin{bmatrix} 1 & 0 & 0 & 0 & 0 & 0\\ 0 & 1 & 0 & 0 & 0 & 0\\ 0 & 0 & 1 & 0 & 0 & 0\\ 0 & 0 & 0 & \frac{1}{2} & 0 & 0\\ 0 & 0 & 0 & 0 & \frac{1}{2} & 0\\ 0 & 0 & 0 & 0 & 0 & \frac{1}{2} \end{bmatrix} \quad \text{and} \quad \mathbf{D} = \begin{bmatrix} 1 & 1 & 1 & 0 & 0 & 0\\ 1 & 1 & 1 & 0 & 0 & 0\\ 1 & 1 & 1 & 0 & 0 & 0\\ 0 & 0 & 0 & 0 & 0 & 0\\ 0 & 0 & 0 & 0 & 0 & 0\\ 0 & 0 & 0 & 0 & 0 & 0 \end{bmatrix}.$$

For the sake of clarity and conciseness of the expressions derived in the upcoming sections, the Lamé parameters for the solid frame are considered real and frequency-independent. Thus, no structural damping is taken into account in the porous medium behaviour. However, the method presented is equally valid and straightforward to establish when hysteretic structural damping in the solid frame is included. For a hysteretic proportional structural damping parameter denoted η_{s}, the complex-valued Lamé parameters, given in Eqs. (1.19), write

$$\widetilde{\lambda} = (1 + i\eta_{\mathrm{s}})\,\lambda, \tag{3.9a}$$

$$\widetilde{\mu} = (1 + i\eta_{\mathrm{s}})\,\mu. \tag{3.9b}$$

When accounted for in the constitutive equations, Eqs. (3.7) can be rewritten as

$$\boldsymbol{\sigma}_{\mathrm{s}} = (1+i\eta_{\mathrm{s}})\left(\mathbf{D}_{\mathrm{s}}^{(1)}\,\boldsymbol{\varepsilon}(\mathbf{u}_{\mathrm{s}}) + \mathbf{D}_{\mathrm{sf}}^{(1)}\,\boldsymbol{\varepsilon}(\mathbf{u}_{\mathrm{f}})\right) + \left(\widetilde{K}_{\mathrm{f}} - (1+i\eta_{\mathrm{s}})\,P_0\right)\left(\mathbf{D}_{\mathrm{s}}^{(2)}\,\boldsymbol{\varepsilon}(\mathbf{u}_{\mathrm{s}}) + \mathbf{D}_{\mathrm{sf}}^{(2)}\,\boldsymbol{\varepsilon}(\mathbf{u}_{\mathrm{f}})\right) \tag{3.10a}$$

$$\boldsymbol{\sigma}_{\mathrm{f}} = (1+i\eta_{\mathrm{s}})\left(\mathbf{D}_{\mathrm{sf}}^{(1)}\,\boldsymbol{\varepsilon}(\mathbf{u}_{\mathrm{s}}) + \mathbf{D}_{\mathrm{f}}^{(1)}\,\boldsymbol{\varepsilon}(\mathbf{u}_{\mathrm{f}})\right) + \left(\widetilde{K}_{\mathrm{f}} - (1+i\eta_{\mathrm{s}})\,P_0\right)\left(\mathbf{D}_{\mathrm{sf}}^{(2)}\,\boldsymbol{\varepsilon}(\mathbf{u}_{\mathrm{s}}) + \mathbf{D}_{\mathrm{f}}^{(2)}\,\boldsymbol{\varepsilon}(\mathbf{u}_{\mathrm{f}})\right) \tag{3.10b}$$

The original rewriting of the constitutive equations under the forms of Eqs. (3.7) and Eqs. (3.10) is put to advantage in the variational formulation as shown in Section 3.2.2.2. It is the key enabling for the further development of a new modal approach.

3.2.2 Fluid-structure interaction problem

In this section, boundary and coupling conditions are recalled for the poro-acoustic coupled problem presented in Fig. 3.1, in order to establish the discretized FE problem.

3.2.2.1 Poro-acoustic coupling and boundary conditions

At an external boundary of the acoustic fluid domain, rigid cavity conditions are classically imposed by setting a free pressure field ($\partial_1\Omega_{\mathrm{F}} = \emptyset$). A time-harmonic excitation is prescribed via an acoustic source,

$$\mathbf{grad}\, p \cdot \mathbf{n} = \omega^2 \rho_{\mathrm{F}}\, u_{\mathrm{Fb}} \quad \text{on } \partial_2\Omega_{\mathrm{F}}, \tag{3.11}$$

where u_{Fb} is set to zero out of the acoustic source included in $\partial_2\Omega_{\mathrm{F}}$.

Coupling at an interface Γ_{FP} is given by normal stress and normal displacement continuity conditions between the acoustic fluid and both the fluid and solid phases of the porous medium,

$$\boldsymbol{\sigma}_{\mathrm{s}}\, \mathbf{n} + (1-\phi)\, p\, \mathbf{n} = \mathbf{0} \quad \text{on } \Gamma_{\mathrm{FP}}, \tag{3.12a}$$

$$\boldsymbol{\sigma}_{\mathrm{f}}\, \mathbf{n} + \phi\, p\, \mathbf{n} = \mathbf{0} \quad \text{on } \Gamma_{\mathrm{FP}}, \tag{3.12b}$$

$$\mathbf{u}_{\mathrm{F}} \cdot \mathbf{n} - (1-\phi)\mathbf{u}_{\mathrm{s}} \cdot \mathbf{n} - \phi \mathbf{u}_{\mathrm{f}} \cdot \mathbf{n} = 0 \quad \text{on } \Gamma_{\mathrm{FP}}, \tag{3.13}$$

where ϕ is the porosity of the porous material.

No external force is applied to the outer boundary of the porous medium beside at interface Γ_{FP}. Therefore, $\partial_2\Omega_{\mathrm{P}} = \emptyset$ in the considered problem. Finally, at an external boundary $\partial_1\Omega_{\mathrm{P}}$, two types of boundary conditions can be prescribed, the porous material being considered either as sliding or bonded to a rigid wall:

For a *bonded* porous layer on a rigid wall, the following conditions arise – fixed displacement of the solid phase and normal displacement of the fluid phase – and need to be satisfied,

$$\mathbf{u}_{\mathrm{s}} = \mathbf{0} \quad \text{on } \partial_1\Omega_{\mathrm{P}}, \tag{3.14a}$$

$$\mathbf{u}_{\mathrm{f}} \cdot \mathbf{n}_{\mathrm{P}} = 0 \quad \text{on } \partial_1\Omega_{\mathrm{P}}; \tag{3.14b}$$

For a *sliding* porous layer on a rigid wall, the following conditions arise – fixed normal displacement of the solid phase and fluid phase – and need to be satisfied,

$$\mathbf{u}_{\mathrm{s}} \cdot \mathbf{n}_{\mathrm{P}} = 0 \quad \text{on } \partial_1\Omega_{\mathrm{P}}, \tag{3.15a}$$

$$\mathbf{u}_{\mathrm{f}} \cdot \mathbf{n}_{\mathrm{P}} = 0 \quad \text{on } \partial_1\Omega_{\mathrm{P}}, \tag{3.15b}$$

where $\mathbf{n}_{\mathrm{P}}$ is the unit normal vector pointing outward from Ω_{P}.

3.2.2.2 Finite element discretized problem

The test-function method is used to derive the variational formulation of the coupled problem. For this purpose, the spaces of sufficiently smooth functions C_p, $C_{\mathbf{u}_\mathrm{s}}$ and $C_{\mathbf{u}_\mathrm{f}}$ are introduced, associated with the field variables p, $\mathbf{u}_\mathrm{s}$ and $\mathbf{u}_\mathrm{f}$ respectively. Let δp, $\delta\mathbf{u}_\mathrm{s}$, $\delta\mathbf{u}_\mathrm{f}$ be the frequency-independent test functions, associated with p, $\mathbf{u}_\mathrm{s}$, $\mathbf{u}_\mathrm{f}$ respectively, and belonging to their respective admissible spaces C_p, $C^*_{\mathbf{u}_\mathrm{s}} = \{\delta\mathbf{u}_\mathrm{s} \in C_{\mathbf{u}_\mathrm{s}} | \delta\mathbf{u}_\mathrm{s} = \mathbf{0}$ or $\delta\mathbf{u}_\mathrm{s}\cdot\mathbf{n}_\mathrm{P} = 0 \quad \text{on } \partial_1\Omega_\mathrm{P}\}$, and $C^*_{\mathbf{u}_\mathrm{f}} = \{\delta\mathbf{u}_\mathrm{f} \in C_{\mathbf{u}_\mathrm{f}} | \delta\mathbf{u}_\mathrm{f}\cdot\mathbf{n}_\mathrm{P} = 0 \quad \text{on } \partial_1\Omega_\mathrm{P}\}$.

Equations (3.1), (3.11), and (3.13) lead to, $\forall\,\delta p \in C_p$,

$$\begin{aligned}\int_{\Omega_\mathrm{F}} \mathbf{grad}p\cdot\mathbf{grad}\delta p\,\mathrm{d}V - \frac{\omega^2}{c_0^2}\int_{\Omega_\mathrm{F}} p\,\delta p\,\mathrm{d}V - \omega^2\rho_\mathrm{F}(1-\phi)\int_{\Gamma_\mathrm{FP}} \mathbf{u}_\mathrm{s}\cdot\mathbf{n}\,\delta p\,\mathrm{d}\Sigma \\ -\omega^2\rho_\mathrm{F}\phi\int_{\Gamma_\mathrm{FP}} \mathbf{u}_\mathrm{f}\cdot\mathbf{n}\,\delta p\,\mathrm{d}\Sigma = \omega^2\rho_\mathrm{F}\int_{\partial_2\Omega_\mathrm{F}} u_\mathrm{Fb}\,\delta p\,\mathrm{d}\Sigma.\end{aligned} \tag{3.16}$$

Equations (3.2a), (A.5a), and (3.12a) lead to, $\forall\,\delta\mathbf{u}_\mathrm{s} \in C^*_{\mathbf{u}_\mathrm{s}}$,

$$\begin{aligned}&\int_{\Omega_\mathrm{P}} \mathrm{tr}\left[\mathbf{D}^{(1)}_\mathrm{s}\,\boldsymbol{\varepsilon}(\mathbf{u}_\mathrm{s})\,\boldsymbol{\varepsilon}(\delta\mathbf{u}_\mathrm{s})\right]\,\mathrm{d}V + \int_{\Omega_\mathrm{P}} \mathrm{tr}\left[\mathbf{D}^{(1)}_\mathrm{sf}\,\boldsymbol{\varepsilon}(\mathbf{u}_\mathrm{f})\,\boldsymbol{\varepsilon}(\delta\mathbf{u}_\mathrm{s})\right]\,\mathrm{d}V \\ &+\left(\widetilde{K}_\mathrm{f} - P_0\right)\left[\int_{\Omega_\mathrm{P}} \mathrm{tr}\left[\mathbf{D}^{(2)}_\mathrm{s}\,\boldsymbol{\varepsilon}(\mathbf{u}_\mathrm{s})\,\boldsymbol{\varepsilon}(\delta\mathbf{u}_\mathrm{s})\right]\,\mathrm{d}V + \int_{\Omega_\mathrm{P}} \mathrm{tr}\left[\mathbf{D}^{(2)}_\mathrm{sf}\,\boldsymbol{\varepsilon}(\mathbf{u}_\mathrm{f})\,\boldsymbol{\varepsilon}(\delta\mathbf{u}_\mathrm{s})\right]\,\mathrm{d}V\right] \\ &+\mathrm{i}\,\omega\,\widetilde{b}\left[\int_{\Omega_\mathrm{P}} \mathbf{u}_\mathrm{s}\cdot\delta\mathbf{u}_\mathrm{s}\,\mathrm{d}V - \int_{\Omega_\mathrm{P}} \mathbf{u}_\mathrm{f}\cdot\delta\mathbf{u}_\mathrm{s}\,\mathrm{d}V\right] \\ &-\omega^2\left[\int_{\Omega_\mathrm{P}} \left((1-\phi)\,\rho_\mathrm{s} + \rho_\mathrm{a}\right)\mathbf{u}_\mathrm{s}\cdot\delta\mathbf{u}_\mathrm{s}\,\mathrm{d}V - \int_{\Omega_\mathrm{P}} \rho_\mathrm{a}\mathbf{u}_\mathrm{f}\cdot\delta\mathbf{u}_\mathrm{s}\,\mathrm{d}V\right] - (1-\phi)\int_{\Gamma_\mathrm{FP}} p\,\mathbf{n}\cdot\delta\mathbf{u}_\mathrm{s}\,\mathrm{d}\Sigma = 0.\end{aligned} \tag{3.17}$$

Equations (3.2b), (A.5b), and (3.12b) lead to, $\forall\,\delta\mathbf{u}_\mathrm{f} \in C^*_{\mathbf{u}_\mathrm{f}}$,

$$\begin{aligned}&\int_{\Omega_\mathrm{P}} \mathrm{tr}\left[\mathbf{D}^{(1)}_\mathrm{f}\,\boldsymbol{\varepsilon}(\mathbf{u}_\mathrm{f})\,\boldsymbol{\varepsilon}(\delta\mathbf{u}_\mathrm{f})\right]\,\mathrm{d}V + \int_{\Omega_\mathrm{P}} \mathrm{tr}\left[\mathbf{D}^{(1)}_\mathrm{sf}\,\boldsymbol{\varepsilon}(\mathbf{u}_\mathrm{s})\,\boldsymbol{\varepsilon}(\delta\mathbf{u}_\mathrm{f})\right]\,\mathrm{d}V \\ &+\left(\widetilde{K}_\mathrm{f} - P_0\right)\left[\int_{\Omega_\mathrm{P}} \mathrm{tr}\left[\mathbf{D}^{(2)}_\mathrm{f}\,\boldsymbol{\varepsilon}(\mathbf{u}_\mathrm{f})\,\boldsymbol{\varepsilon}(\delta\mathbf{u}_\mathrm{f})\right]\,\mathrm{d}V + \int_{\Omega_\mathrm{P}} \mathrm{tr}\left[\mathbf{D}^{(2)}_\mathrm{sf}\,\boldsymbol{\varepsilon}(\mathbf{u}_\mathrm{s})\,\boldsymbol{\varepsilon}(\delta\mathbf{u}_\mathrm{f})\right]\,\mathrm{d}V\right] \\ &+\mathrm{i}\,\omega\,\widetilde{b}\left[\int_{\Omega_\mathrm{P}} \mathbf{u}_\mathrm{f}\cdot\delta\mathbf{u}_\mathrm{f}\,\mathrm{d}V - \int_{\Omega_\mathrm{P}} \mathbf{u}_\mathrm{s}\cdot\delta\mathbf{u}_\mathrm{f}\,\mathrm{d}V\right] \\ &-\omega^2\left[\int_{\Omega_\mathrm{P}} \left(\phi\rho_\mathrm{f} + \rho_\mathrm{a}\right)\mathbf{u}_\mathrm{f}\cdot\delta\mathbf{u}_\mathrm{f}\,\mathrm{d}V - \int_{\Omega_\mathrm{P}} \rho_\mathrm{a}\mathbf{u}_\mathrm{s}\cdot\delta\mathbf{u}_\mathrm{f}\,\mathrm{d}V\right] - \phi\int_{\Gamma_\mathrm{FP}} p\,\mathbf{n}\cdot\delta\mathbf{u}_\mathrm{f}\,\mathrm{d}\Sigma = 0.\end{aligned} \tag{3.18}$$

After discretization of the various terms in Eqs. (3.16)-(3.18) using the FE method and dividing Eq. (3.16) by ρ_F, the following matrix equation for the coupled problem is

obtained,

$$\left(\begin{bmatrix} \mathbf{K}_{\mathrm{F}} & \mathbf{0} & \mathbf{0} \\ -(1-\phi)\mathbf{A}_{\mathrm{Fs}}^T & \mathbf{K}_{\mathrm{ss}}^{(1)} & \mathbf{K}_{\mathrm{sf}}^{(1)} \\ -\phi\mathbf{A}_{\mathrm{Ff}}^T & \mathbf{K}_{\mathrm{sf}}^{(1)T} & \mathbf{K}_{\mathrm{ff}}^{(1)} \end{bmatrix} + \left(\widetilde{K}_{\mathrm{f}} - P_0\right) \begin{bmatrix} \mathbf{0} & \mathbf{0} & \mathbf{0} \\ \mathbf{0} & \mathbf{K}_{\mathrm{ss}}^{(2)} & \mathbf{K}_{\mathrm{sf}}^{(2)} \\ \mathbf{0} & \mathbf{K}_{\mathrm{sf}}^{(2)T} & \mathbf{K}_{\mathrm{ff}}^{(2)} \end{bmatrix} \right. \\ \left. + \mathrm{i}\,\omega\,\widetilde{b} \begin{bmatrix} \mathbf{0} & \mathbf{0} & \mathbf{0} \\ \mathbf{0} & \mathbf{C}_{\mathrm{ss}} & \mathbf{C}_{\mathrm{sf}} \\ \mathbf{0} & \mathbf{C}_{\mathrm{sf}}^T & \mathbf{C}_{\mathrm{ff}} \end{bmatrix} - \omega^2 \begin{bmatrix} \mathbf{M}_{\mathrm{F}} & (1-\phi)\mathbf{A}_{\mathrm{Fs}} & \phi\mathbf{A}_{\mathrm{Ff}} \\ \mathbf{0} & \mathbf{M}_{\mathrm{ss}} & \mathbf{M}_{\mathrm{sf}} \\ \mathbf{0} & \mathbf{M}_{\mathrm{sf}}^T & \mathbf{M}_{\mathrm{ff}} \end{bmatrix} \right) \begin{bmatrix} \mathbf{P} \\ \mathbf{U}_{\mathrm{s}} \\ \mathbf{U}_{\mathrm{f}} \end{bmatrix} = \begin{bmatrix} \omega^2\mathbf{U}_{\mathrm{Fb}} \\ \mathbf{0} \\ \mathbf{0} \end{bmatrix}. \tag{3.19}$$

This non-symmetric formulation can be symmetrized for a solution in the frequency domain by dividing the acoustic equation by ω^2 ($\omega \neq 0$). The interest of rewriting the porous media formulation into four matrices ($\mathbf{K}_{\mathrm{P}}^{(1)}$, $\mathbf{K}_{\mathrm{P}}^{(2)}$, $\mathbf{C}_{\mathrm{P}}$, and $\mathbf{M}_{\mathrm{P}}$ as introduced for Eq. (3.20)) is already partly visible. In fact, it involves constant real-valued matrices which can be assembled once, while only the complex and frequency-dependent factors $\widetilde{K}_{\mathrm{f}}$ and $\widetilde{b}$ are recomputed at each frequency increment. If hysteretic structural damping of the solid frame is explicitly included, this statement stands, considering that damping can be introduced as a factor of the assembled matrices $\mathbf{K}_{\mathrm{P}}^{(1)}$ and $\mathbf{K}_{\mathrm{P}}^{(2)}$, as mentioned in Section 3.2.1.2, Eqs. (3.10). In addition, the amount of memory used is the same as using only two complex-valued and frequency-dependent matrices, considering that the sparsity is unchanged [44]. More importantly, the main interest, underlined in this approach, is the possibility to use such a formulation in the context of modal reduction techniques.

3.3 Modal reduction of the poroelastic media

3.3.1 Presentation of the proposed solution strategy

The proposed reduction method is applied to the dissipative porous medium of a poro-acoustic coupled problem, which is the costly part of the problem. For validation purposes, the case of a rigid acoustic cavity with a single porous layer on one wall is considered. Notations used are presented in Fig. 3.2.

Figure 3.2: Problem description for modal reduction of porous media

The acoustic dofs are separated into internal ones (subscript $\bar{I}$), and those at interface with the porous medium (subscript I). These notations allow for an easy extension of the method to problems with multiple interfaces [114]. The coupled porous

medium matrices are now considered, involving four matrices $\mathbf{K}_{\mathrm{P}}^{(1)}$, $\mathbf{K}_{\mathrm{P}}^{(2)}$, $\mathbf{C}_{\mathrm{P}}$, and $\mathbf{M}_{\mathrm{P}}$ corresponding to the set of unknowns $\mathbf{U}_{\mathrm{P}}$ such that, for each matrix indexed by P, i.e. $\mathbf{B}_{\mathrm{P}} \in \{\mathbf{K}_{\mathrm{P}}^{(1)}, \mathbf{K}_{\mathrm{P}}^{(2)}, \mathbf{C}_{\mathrm{P}}, \mathbf{M}_{\mathrm{P}}\}$,

$$\mathbf{B}_{\mathrm{P}} = \begin{bmatrix} \mathbf{B}_{\mathrm{ss}} & \mathbf{B}_{\mathrm{sf}} \\ \mathbf{B}_{\mathrm{sf}} & \mathbf{B}_{\mathrm{ff}} \end{bmatrix} \text{ and } \mathbf{U}_{\mathrm{P}} = \begin{bmatrix} \mathbf{U}_{\mathrm{s}} \\ \mathbf{U}_{\mathrm{f}} \end{bmatrix}. \tag{3.20}$$

Similarly, the coupling between the interface acoustic dofs (subscript I) and the porous dofs (subscript P) is denoted

$$\mathbf{A}_{I\mathrm{P}} = \begin{bmatrix} (1-\phi)\mathbf{A}_{I\mathrm{s}} & \phi\mathbf{A}_{I\mathrm{f}} \end{bmatrix}. \tag{3.21}$$

Consequently, for modal reduction purposes, the matrix set of equations (3.19) can be written as

$$\left[\begin{array}{c|c|c} \mathbf{K}_{\bar{I}\bar{I}} - \omega^2\mathbf{M}_{\bar{I}\bar{I}} & \mathbf{K}_{\bar{I}I} - \omega^2\mathbf{M}_{\bar{I}I} & \mathbf{0} \\ \hline \mathbf{K}_{I\bar{I}} - \omega^2\mathbf{M}_{I\bar{I}} & \mathbf{K}_{II} - \omega^2\mathbf{M}_{II} & -\omega^2\mathbf{A}_{I\mathrm{P}} \\ \hline \mathbf{0} & -\mathbf{A}_{I\mathrm{P}}^T & \begin{array}{c}\mathbf{K}_{\mathrm{P}}^{(1)} + \left(\widetilde{K}_{\mathrm{f}} - P_0\right)\mathbf{K}_{\mathrm{P}}^{(2)} + \\ \mathrm{i}\,\omega\,\widetilde{b}\,\mathbf{C}_{\mathrm{P}} - \omega^2\mathbf{M}_{\mathrm{P}}\end{array} \end{array}\right] \begin{bmatrix} \mathbf{P}_{\bar{I}} \\ \mathbf{P}_I \\ \mathbf{U}_{\mathrm{P}} \end{bmatrix} = \begin{bmatrix} \omega^2\mathbf{U}_{\bar{I}\mathrm{b}} \\ \mathbf{0} \\ \mathbf{0} \end{bmatrix}, \tag{3.22}$$

and can be symmetrized by dividing the acoustic equations (lines 1 and 2) by ω^2 ($\omega \neq 0$).

3.3.2 Modal reduction

From the proposed expression of the porous medium FE problem, real-valued normal modes can be computed associated with the conservative poroelastic eigenvalue problem,

$$\left(\mathbf{K}_{\mathrm{P}}^{(1)} - \omega^2\mathbf{M}_{\mathrm{P}}\right)\boldsymbol{\phi} = \mathbf{0}. \tag{3.23}$$

It is supposed that the Dirichlet boundary conditions imposed to the porous medium result in a nonsingular $\mathbf{K}_{\mathrm{P}}^{(1)}$ matrix, therefore removing zero-frequency modes. A modal reduction basis $\boldsymbol{\Phi}_{\mathrm{P}m}$ is built, selecting the m lowest-eigenfrequency modes. They are normalized with respect to the porous mass matrix $\mathbf{M}_{\mathrm{P}}$ so that

$$\boldsymbol{\Phi}_{\mathrm{P}m}^T\,\mathbf{M}_{\mathrm{P}}\boldsymbol{\Phi}_{\mathrm{P}m} = \mathbf{1}_m, \tag{3.24a}$$

$$\boldsymbol{\Phi}_{\mathrm{P}m}^T\,\mathbf{K}_{\mathrm{P}}^{(1)}\boldsymbol{\Phi}_{\mathrm{P}m} = \boldsymbol{\Omega}_m, \tag{3.24b}$$

where $\mathbf{1}_m$ is a unit matrix of dimension m, and $\boldsymbol{\Omega}_m$ a diagonal matrix of same size, with the m lowest eigenvalues of (3.23) on its diagonal.

There are two key points that make a reduction method computationally efficient, which are its ability to:

- converge rapidly to the expected solution when adding modes in the basis, thus allowing a substantial reduction in the number of dofs, as well as a reasonable time allocated to the computation of the modes,

- preserve or improve the sparsity of the matrices after projection, and ideally produce diagonal submatrices.

The former aspect will be examined in applications discussed in Section 3.4. Regarding the second aspect, the sparsity of matrices $\mathbf{K}_{\mathrm{P}}^{(2)}$ and $\mathbf{C}_{\mathrm{P}}$ after projection on the modal basis is fundamental in order to take advantage of the diagonal form of projected $\mathbf{K}_{\mathrm{P}}^{(1)}$ and $\mathbf{M}_{\mathrm{P}}$. The choices made for the discretization of porous media, among which the separation of the "static" and "dynamic" part of the dynamic bulk modulus of the fluid (see Eq. (3.6)), are of prime importance in order to fulfill this requirement. In fact, as will be shown in Section 3.4.2, it results in sparse reduced matrices $\mathbf{K}_{\mathrm{P}}^{(2)}$ and $\mathbf{C}_{\mathrm{P}}$, and even exhibits orthogonality of some modes with respect to these matrices. Therefore, after testing the m retained modes for their orthogonal properties with respect to $\mathbf{K}_{\mathrm{P}}^{(2)}$ and $\mathbf{C}_{\mathrm{P}}$, they are separated into o "orthogonal" ($\boldsymbol{\Phi}_{\mathrm{P}o}$) and n "non-orthogonal" ($\boldsymbol{\Phi}_{\mathrm{P}n}$) ones, such that

$$\begin{bmatrix}\boldsymbol{\Phi}_{\mathrm{P}n} & \boldsymbol{\Phi}_{\mathrm{P}o}\end{bmatrix}^T \mathbf{M}_{\mathrm{P}} \begin{bmatrix}\boldsymbol{\Phi}_{\mathrm{P}n} & \boldsymbol{\Phi}_{\mathrm{P}o}\end{bmatrix} = \begin{bmatrix}\mathbf{1}_n & \mathbf{0} \\ \mathbf{0} & \mathbf{1}_o\end{bmatrix}, \tag{3.25a}$$

$$\begin{bmatrix}\boldsymbol{\Phi}_{\mathrm{P}n} & \boldsymbol{\Phi}_{\mathrm{P}o}\end{bmatrix}^T \mathbf{K}_{\mathrm{P}}^{(1)} \begin{bmatrix}\boldsymbol{\Phi}_{\mathrm{P}n} & \boldsymbol{\Phi}_{\mathrm{P}o}\end{bmatrix} = \begin{bmatrix}\boldsymbol{\Omega}_n & \mathbf{0} \\ \mathbf{0} & \boldsymbol{\Omega}_o\end{bmatrix}, \tag{3.25b}$$

$$\begin{bmatrix}\boldsymbol{\Phi}_{\mathrm{P}n} & \boldsymbol{\Phi}_{\mathrm{P}o}\end{bmatrix}^T \mathbf{K}_{\mathrm{P}}^{(2)} \begin{bmatrix}\boldsymbol{\Phi}_{\mathrm{P}n} & \boldsymbol{\Phi}_{\mathrm{P}o}\end{bmatrix} = \begin{bmatrix}\boldsymbol{\kappa}_n & \mathbf{0} \\ \mathbf{0} & \boldsymbol{\kappa}_o\end{bmatrix}, \tag{3.25c}$$

$$\begin{bmatrix}\boldsymbol{\Phi}_{\mathrm{P}n} & \boldsymbol{\Phi}_{\mathrm{P}o}\end{bmatrix}^T \mathbf{C}_{\mathrm{P}} \begin{bmatrix}\boldsymbol{\Phi}_{\mathrm{P}n} & \boldsymbol{\Phi}_{\mathrm{P}o}\end{bmatrix} = \begin{bmatrix}\boldsymbol{\zeta}_n & \mathbf{0} \\ \mathbf{0} & \boldsymbol{\zeta}_o\end{bmatrix}, \tag{3.25d}$$

where $\mathbf{1}_n$, $\boldsymbol{\Omega}_n$ and $\mathbf{1}_o$, $\boldsymbol{\Omega}_o$, $\boldsymbol{\kappa}_o$, $\boldsymbol{\zeta}_o$ are diagonal matrices of respective dimensions n and o, while $\boldsymbol{\kappa}_n$ and $\boldsymbol{\zeta}_n$ are non-diagonal, sparse, square matrices of dimension n.

There are several options for the choice of attachment functions participating to the static correction for improved convergence. In this work, the single dof per node associated with the acoustic domain is put to advantage. Attachment functions are computed as the $\mathbf{K}_{\mathrm{P}}^{(1)}$– static responses of the poroelastic domain to unit pressure successively imposed at each interface acoustic dof,

$$\begin{bmatrix}-\mathbf{A}_{I\mathrm{P}}^T & \mathbf{K}_{\mathrm{P}}^{(1)}\end{bmatrix} \begin{bmatrix}\mathbf{1}_I \\ \boldsymbol{\Psi}_{\mathrm{P}I}\end{bmatrix} = \begin{bmatrix}\mathbf{0}\end{bmatrix} \Rightarrow \boldsymbol{\Psi}_{\mathrm{P}I} = \mathbf{K}_{\mathrm{P}}^{(1)^{-1}} \mathbf{A}_{I\mathrm{P}}^T. \tag{3.26}$$

Again, assumption is made that $\mathbf{K}_{\mathrm{P}}^{(1)}$ is not singular. If otherwise, a shift in frequency using the mass matrix $\mathbf{M}_{\mathrm{P}}$ can be set instead, to define pseudo-static attachment functions, but this is not considered in this work.

The corresponding change of basis applied to the system in Eq. (3.22), leaving acoustic

dofs uncondensed, is then (the $\widehat{\ }$ symbol refers to an approximate solution)

$$\begin{bmatrix} \widehat{\mathbf{P}}_{\bar{I}} \\ \widehat{\mathbf{P}}_{I} \\ \widehat{\mathbf{U}}_{\mathrm{P}} \end{bmatrix} = \begin{bmatrix} \mathbf{1}_{\bar{I}} & \mathbf{0} & \mathbf{0} & \mathbf{0} \\ \mathbf{0} & \mathbf{1}_{I} & \mathbf{0} & \mathbf{0} \\ \mathbf{0} & \boldsymbol{\Psi}_{\mathrm{P}I} & \boldsymbol{\Phi}_{\mathrm{P}n} & \boldsymbol{\Phi}_{\mathrm{P}o} \end{bmatrix} \begin{bmatrix} \widehat{\mathbf{P}}_{\bar{I}} \\ \widehat{\mathbf{P}}_{I} \\ \widehat{\boldsymbol{\alpha}}_{n} \\ \widehat{\boldsymbol{\alpha}}_{o} \end{bmatrix}, \tag{3.27}$$

where $\widehat{\boldsymbol{\alpha}}_n$ and $\widehat{\boldsymbol{\alpha}}_o$ are the modal coordinates vectors associated with the selected "non-orthogonal" and "orthogonal" modes respectively.

Applying a change of basis Eq. (3.27) to a symmetrized form of Eq. (3.22) and pre-multiplying by the transpose of the transformation matrix leads to the following reduced set of equations,

$$\begin{aligned} \Bigg(& \left[\begin{array}{c|c|c|c} \frac{1}{\omega^2}\mathbf{K}_{\bar{I}\bar{I}} - \mathbf{M}_{\bar{I}\bar{I}} & \frac{1}{\omega^2}\mathbf{K}_{\bar{I}I} - \mathbf{M}_{\bar{I}I} & \mathbf{0} & \mathbf{0} \\ \hline \frac{1}{\omega^2}\mathbf{K}_{I\bar{I}} - \mathbf{M}_{I\bar{I}} & \frac{1}{\omega^2}\mathbf{K}_{II} - \mathbf{M}_{II} - \mathbf{K}^{(1)}_{\mathrm{P}_{II}} & \mathbf{0} & \mathbf{0} \\ \hline \mathbf{0} & \mathbf{0} & \boldsymbol{\Omega}_n & \mathbf{0} \\ \hline \mathbf{0} & \mathbf{0} & \mathbf{0} & \boldsymbol{\Omega}_o \end{array}\right] + \left(\widetilde{K}_{\mathrm{f}} - P_0\right) \begin{bmatrix} \mathbf{0} & \mathbf{0} & \mathbf{0} & \mathbf{0} \\ \mathbf{0} & \mathbf{K}^{(2)}_{\mathrm{P}_{II}} & \mathbf{K}^{(2)}_{\mathrm{P}_{In}} & \mathbf{K}^{(2)}_{\mathrm{P}_{Io}} \\ \mathbf{0} & \mathbf{K}^{(2)}_{\mathrm{P}_{nI}} & \boldsymbol{\kappa}_n & \mathbf{0} \\ \mathbf{0} & \mathbf{K}^{(2)}_{\mathrm{P}_{oI}} & \mathbf{0} & \boldsymbol{\kappa}_o \end{bmatrix} \\ & + \mathrm{i}\,\omega\,\widetilde{b} \begin{bmatrix} \mathbf{0} & \mathbf{0} & \mathbf{0} & \mathbf{0} \\ \mathbf{0} & \mathbf{C}_{\mathrm{P}_{II}} & \mathbf{C}_{\mathrm{P}_{In}} & \mathbf{C}_{\mathrm{P}_{Io}} \\ \mathbf{0} & \mathbf{C}_{\mathrm{P}_{nI}} & \boldsymbol{\zeta}_n & \mathbf{0} \\ \mathbf{0} & \mathbf{C}_{\mathrm{P}_{oI}} & \mathbf{0} & \boldsymbol{\zeta}_o \end{bmatrix} - \omega^2 \begin{bmatrix} \mathbf{0} & \mathbf{0} & \mathbf{0} & \mathbf{0} \\ \mathbf{0} & \mathbf{M}_{\mathrm{P}_{II}} & \mathbf{M}_{\mathrm{P}_{In}} & \mathbf{M}_{\mathrm{P}_{Io}} \\ \mathbf{0} & \mathbf{M}_{\mathrm{P}_{nI}} & \mathbf{1}_n & \mathbf{0} \\ \mathbf{0} & \mathbf{M}_{\mathrm{P}_{oI}} & \mathbf{0} & \mathbf{1}_o \end{bmatrix} \Bigg) \begin{bmatrix} \widehat{\mathbf{P}}_{\bar{I}} \\ \widehat{\mathbf{P}}_{I} \\ \widehat{\boldsymbol{\alpha}}_{n} \\ \widehat{\boldsymbol{\alpha}}_{o} \end{bmatrix} = \begin{bmatrix} \mathbf{U}_{\mathrm{Fb}} \\ \mathbf{0} \\ \mathbf{0} \\ \mathbf{0} \end{bmatrix}, \end{aligned} \tag{3.28}$$

where for $\mathbf{B}_{\mathrm{P}} \in \{\mathbf{K}^{(1)}_{\mathrm{P}}, \mathbf{K}^{(2)}_{\mathrm{P}}, \mathbf{C}_{\mathrm{P}}, \mathbf{M}_{\mathrm{P}}\}$,

$$\begin{aligned} \mathbf{B}_{\mathrm{P}_{II}} &= \boldsymbol{\Psi}^T_{\mathrm{P}I} \mathbf{B}_{\mathrm{P}} \boldsymbol{\Psi}_{\mathrm{P}I}, \\ \mathbf{B}_{\mathrm{P}_{In}} &= \boldsymbol{\Psi}^T_{\mathrm{P}I} \mathbf{B}_{\mathrm{P}} \boldsymbol{\Phi}_{\mathrm{P}n} \ = \mathbf{B}^T_{\mathrm{P}_{nI}}, \\ \mathbf{B}_{\mathrm{P}_{Io}} &= \boldsymbol{\Psi}^T_{\mathrm{P}I} \mathbf{B}_{\mathrm{P}} \boldsymbol{\Phi}_{\mathrm{P}o} \ = \mathbf{B}^T_{\mathrm{P}_{oI}}. \end{aligned}$$

This reduction is established once as an initial step before the frequency sweep. It can be further improved using dynamic condensation of the "orthogonal" modal coordinates, as presented in the following section.

3.3.3 Further condensation of selected modal coordinates

To take full advantage of the partly diagonal form of the reduced matrices in Eq. (3.25), the modal coordinates corresponding to the "orthogonal" modes can be dynamically condensed on the interface dofs, at each frequency increment. First, the set of equations associated with $\boldsymbol{\alpha}_o$ in Eq. (A.11) gives

$$\widehat{\boldsymbol{\alpha}}_o = -\left[\boldsymbol{\Omega}_o + \left(\widetilde{K}_{\mathrm{f}} - P_0\right)\boldsymbol{\kappa}_o + \mathrm{i}\,\omega\,\widetilde{b}\,\boldsymbol{\zeta}_o - \omega^2\,\mathbf{1}_o\right]^{-1} \mathbf{K}^{(dyn)}_{\mathrm{P}_{oI}}\,\widehat{\mathbf{P}}_I, \tag{3.29}$$

where

$$\mathbf{K}_{\mathrm{P}_{oI}}^{(dyn)} = \left(\widetilde{K}_{\mathrm{f}} - P_0\right) \mathbf{K}_{\mathrm{P}_{oI}}^{(2)} + \mathrm{i}\,\omega\,\widetilde{b}\,\mathbf{C}_{\mathrm{P}_{oI}} - \omega^2\,\mathbf{M}_{\mathrm{P}_{oI}}. \tag{3.30}$$

Then, when introducing Eq. (3.29) into Eq. (A.11), a further reduced set of equations can be obtained at the beginning of each frequency increment. Thus, the number of dofs is reduced without altering the sparsity of the system matrix,

$$\left(\left[\begin{array}{c|c|c} \frac{1}{\omega^2}\mathbf{K}_{\bar{I}\bar{I}} - \mathbf{M}_{\bar{I}\bar{I}} & \frac{1}{\omega^2}\mathbf{K}_{\bar{I}I} - \mathbf{M}_{\bar{I}I} & \mathbf{0} \\ \hline \frac{1}{\omega^2}\mathbf{K}_{I\bar{I}} - \mathbf{M}_{I\bar{I}} & \begin{array}{c}\frac{1}{\omega^2}\mathbf{K}_{II} - \mathbf{M}_{II} \\ -\mathbf{K}_{\mathrm{P}_{II}}^{(1)} - \mathbf{K}_{\mathrm{P}_{II}}^{(dyn)}\end{array} & \mathbf{0} \\ \hline \mathbf{0} & \mathbf{0} & \boldsymbol{\Omega}_n \end{array}\right] + \left(\widetilde{K}_{\mathrm{f}} - P_0\right) \begin{bmatrix} \mathbf{0} & \mathbf{0} & \mathbf{0} \\ \mathbf{0} & \mathbf{K}_{\mathrm{P}_{II}}^{(2)} & \mathbf{K}_{\mathrm{P}_{In}}^{(2)} \\ \mathbf{0} & \mathbf{K}_{\mathrm{P}_{nI}}^{(2)} & \boldsymbol{\kappa}_n \end{bmatrix} \right. \\ \left. + \mathrm{i}\,\omega\,\widetilde{b} \begin{bmatrix} \mathbf{0} & \mathbf{0} & \mathbf{0} \\ \mathbf{0} & \mathbf{C}_{\mathrm{P}_{II}} & \mathbf{C}_{\mathrm{P}_{In}} \\ \mathbf{0} & \mathbf{C}_{\mathrm{P}_{nI}} & \boldsymbol{\zeta}_n \end{bmatrix} - \omega^2 \begin{bmatrix} \mathbf{0} & \mathbf{0} & \mathbf{0} \\ \mathbf{0} & \mathbf{M}_{\mathrm{P}_{II}} & \mathbf{M}_{\mathrm{P}_{In}} \\ \mathbf{0} & \mathbf{M}_{\mathrm{P}_{nI}} & \mathbf{1}_n \end{bmatrix} \right) \begin{bmatrix} \widehat{\mathbf{P}}_{\bar{I}} \\ \widehat{\mathbf{P}}_I \\ \widehat{\boldsymbol{\alpha}}_n \end{bmatrix} = \begin{bmatrix} \mathbf{U}_{\mathrm{Fb}} \\ \mathbf{0} \\ \mathbf{0} \end{bmatrix}, \tag{3.31}$$

where the frequency-dependent dynamic contribution to the interface dofs $\mathbf{K}_{\mathrm{P}_{II}}^{(dyn)}$ can be expressed as

$$\mathbf{K}_{\mathrm{P}_{II}}^{(dyn)} = \mathbf{K}_{\mathrm{P}_{oI}}^{(dyn)^T} \left[\boldsymbol{\Omega}_o + \left(\widetilde{K}_{\mathrm{f}} - P_0\right) \boldsymbol{\kappa}_o + \mathrm{i}\,\omega\,\widetilde{b}\,\boldsymbol{\zeta}_o - \omega^2\,\mathbf{1}_o\right]^{-1} \mathbf{K}_{\mathrm{P}_{oI}}^{(dyn)}. \tag{3.32}$$

Since this contribution involves simple operations, i.e. matrix additions, multiplications and a diagonal matrix inversion, it is reasonable to expect a substantially improved efficiency providing a sufficient number of "orthogonal" modal coordinates is involved.

3.4 Applications and results

3.4.1 Modal reduction of the porous layer in a 1D poro-acoustic application

3.4.1.1 Presentation and discussion of reference solution

The proposed modal-based reduction method for poroelastic sound absorbing materials is first validated on a unidimensional poro-acoustic academic example. As presented in Fig. 3.3, it consists of an acoustic cavity excited with a time-harmonic plane wave normally incident on an infinite poroelastic layer. The rigid cavity is 25 cm-long and covered with a 5 cm-thick poroelastic layer at its end. Appropriate Dirichlet boundary conditions are applied to the poroelastic domain to achieve unidimensional behaviour, thus allowing solid and fluid displacement in the direction normal to the layer only. In addition, it is considered backed by a rigid impervious wall (Eq. (3.14)). Material parameters of the foam are given in Table 3.1. The mesh consists of 20 linear elements for the acoustic domain, and 10 linear poroelastic elements in the thickness of the layer. Its convergence was checked for

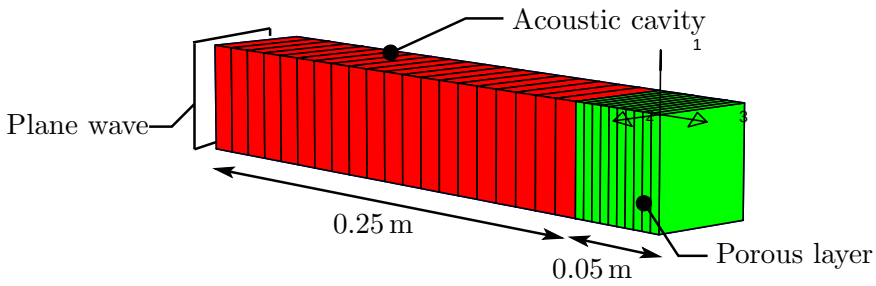

Figure 3.3: Acoustic cavity mesh and dimensions for 1D problem

the frequency range considered. The 1D FE model thus includes 21 acoustic dofs and 20 poroelastic dofs. Its simplicity is not suited for a performance estimation, but is however a relevant starting point to establish the potential interest of the proposed reduction method. For this purpose, an estimation of the absorption coefficient of the porous layer is a useful

Frame	***Fluid***	***Porous***
	$c_0 = 343$ m/s	$\phi = 0.96$
$\lambda = 905357$ Pa	$\gamma = 1.4$	$\sigma = 32$ kNs/m^4
$\mu = 264062$ Pa	$Pr = 0.71$	$\alpha_\infty = 1.7$
$(1-\phi)\rho_\mathrm{s} = 30$ kg/m^3	$\rho_\mathrm{f} = 1.21$ kg/m^3	$\Lambda = 90\ \mu$m
	$\eta = 1.84 \cdot 10^{-5}$ Ns/m^2	$\Lambda' = 165\ \mu$m

Table 3.1: Air and porous material parameters

indicator, and is calculated for a plane wave at normal incidence as

$$\widetilde{\alpha}_\mathrm{abs}(\omega) = 1 - \left| \frac{\widetilde{Z}_\mathrm{n}(\omega) - \rho_0\, c_0}{\widetilde{Z}_\mathrm{n}(\omega) + \rho_0\, c_0} \right|^2 , \tag{3.33}$$

where $\widetilde{Z}_\mathrm{n}(\omega)$ is the normal acoustic impedance given by

$$\widetilde{Z}_\mathrm{n}(\omega) = \frac{\mathrm{P}}{i\omega\left(\phi\, \mathbf{u}_\mathrm{f} \cdot \mathbf{n} + (1-\phi)\, \mathbf{u}_\mathrm{s} \cdot \mathbf{n}\right)}, \tag{3.34}$$

with P the incident acoustic pressure, $\mathbf{u}_\mathrm{s}$ and $\mathbf{u}_\mathrm{f}$ the vector displacement fields of the solid and fluid phases at the surface of the material, and $\mathbf{n}$ the vector normal to the surface, pointing outward from the fluid domain.

More generally, the mean quadratic pressure in the cavity is given as a physical quantity output, calculated as

$$L_p = 10\ \log\left(\frac{\displaystyle\int_{\Omega_\mathrm{F}} P^2 \mathrm{d}V}{{P_\mathrm{ref}}^2 \displaystyle\int_{\Omega_\mathrm{F}} \mathrm{d}V} \right), \tag{3.35}$$

and the reference solution of the problem (direct FE solution without reduction), with and without addition of the poroelastic layer, is plotted in Figs. 3.4. For the conservative problem, the two following configurations are considered for this 1D case: the poroelastic is replaced by an equivalent volume of acoustic fluid or not. The former case is more suited to a physical interpretation of the damping effect of the porous layer at the resonances. The latter is a more realistic representation of the practical consequence of adding a porous layer to an existing environment. Of course, for this academic validation, the difference between the two configurations is amplified by the rather large volume of the porous layer when compared to the dimensions of the cavity.

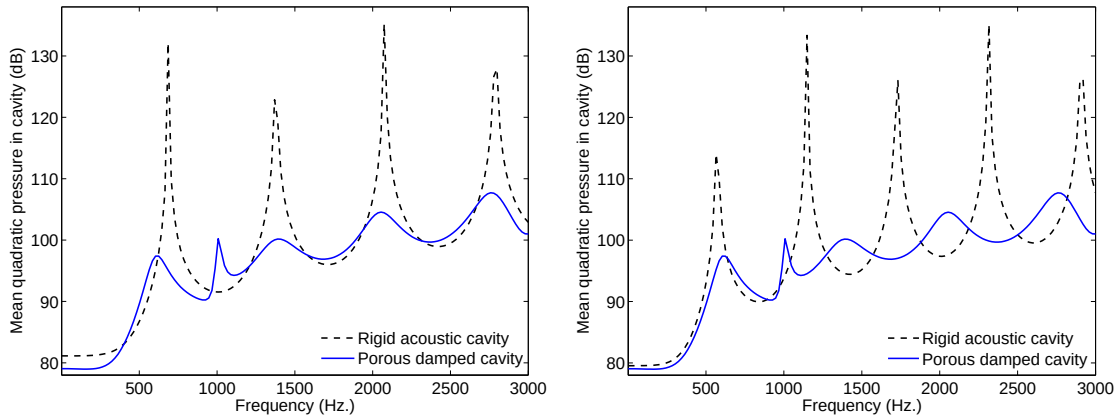

Figure 3.4: Mean quadratic pressure reference FRF, 1D problem, with for rigid cavity: (a) poroelastic volume not replaced by acoustic volume; (b) poroelastic volume replaced by acoustic volume.

Figs. 3.4 clearly show the strong damping effect of the sound absorbing foam.

Considering first Fig. 3.4a, it can be partly interpreted in terms of change of boundary condition for the acoustic cavity of constant volume. Thus, at the resonance frequencies, both a reduction of the sound pressure level and a shift towards lower frequencies are observed. This is consistent with the classical observations made for damped systems. Two additional remarks are worth mentioning: (i) the apparent constant pressure reduction at very low frequencies is mostly induced by the artificial volume increase of the cavity when the porous layer is added (for large wavelengths, the particle velocity of air near boundaries is low, and the porous layer is then inefficient (see the absorption coefficient in Fig. 3.6)); (ii) the porous layer exhibits a compressional resonance around 1000 Hz, thus reducing the frequency shift of the higher acoustic resonances compared to the first one.

Alternatively, Fig. 3.4b may be interpreted in terms of change of boundary condition

with apparent reduction of the acoustic cavity volume. In fact, this apparent reduction of the acoustic cavity volume implies a global shift of resonances towards higher frequencies. Due to the substantial change of volume involved, this overcomes the frequency shift towards low frequencies generated by the damping boundary conditions. However, this configuration better renders the very low-frequency reduction of acoustic pressure.

The nature of the compressional resonance of the porous layer around 1000 Hz is detailed in Figs. 3.5. It is due to the resonant behaviour of the porous frame (quarter

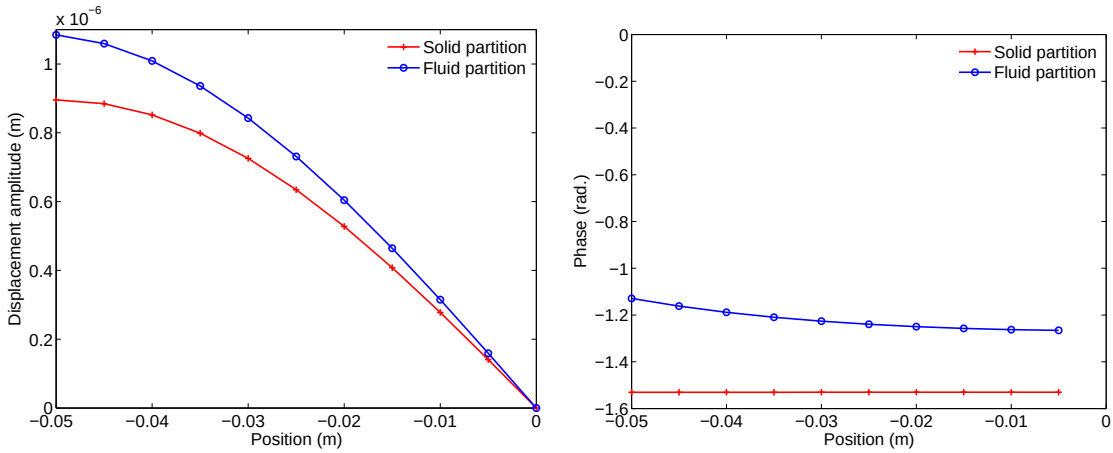

(a) (b)

Figure 3.5: Response of the solid and fluid porous partitions at 1010 Hz: (a) Displacement amplitude; (b) Phase.

wavelength resonance) excited at this specific frequency. This is confirmed by Fig. 3.5b, as all points in the solid partition are moving in phase. The tortuosity and viscous couplings between the two phases imply strong inertial and viscous interactions. Thus, at this resonance frequency, the solid and fluid partitions move with a small phase shift and with a slightly greater amplitude for the fluid phase. The resonant behaviour of the porous frame would be damped if the structural damping of the frame was taken into account, using the previously mentioned constitutive equations, Eq. (3.10). This is illustrated in Fig. 3.6, where the absorption coefficient at normal incidence is plotted for both cases (the structural damping parameter is then $\eta_s = 0.1$). However, whether the structural damping is included or not has no impact on the results presented for the modal approach proposed, and is therefore not further emphasized.

3.4.1.2 Reduced problem

The substructuring modal-based reduction method presented in Section 3.3 is applied to reduce the poroelastic part of the 1D application. The coupled solid-fluid shapes of the

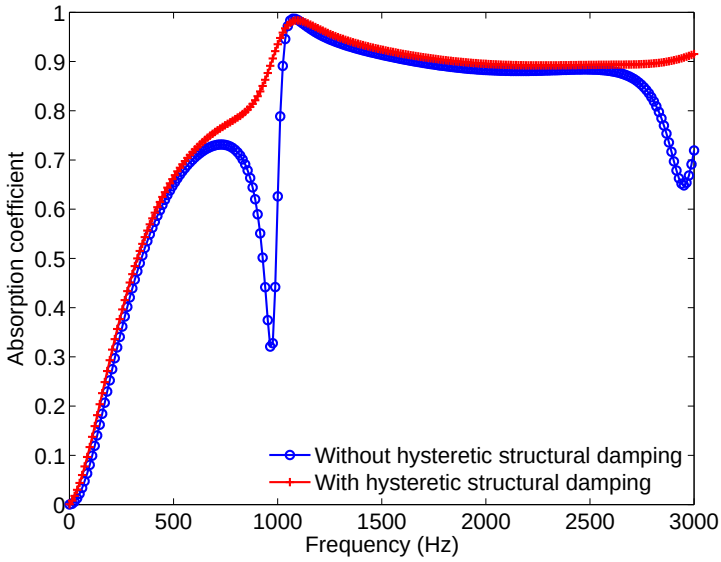

Figure 3.6: Absorption coefficient at normal incidence, impact of the structural damping ($\eta_s = 0.1$).

first 6 modes generated by the eigenvalue problem Eq. (3.23) are presented in Fig. 3.7. Their corresponding eigenfrequencies are 944 Hz, 1136 Hz, 2856 Hz, 3435 Hz, 4839 Hz and 5819 Hz. It is interesting to notice that they can be paired, and that for each couple, one

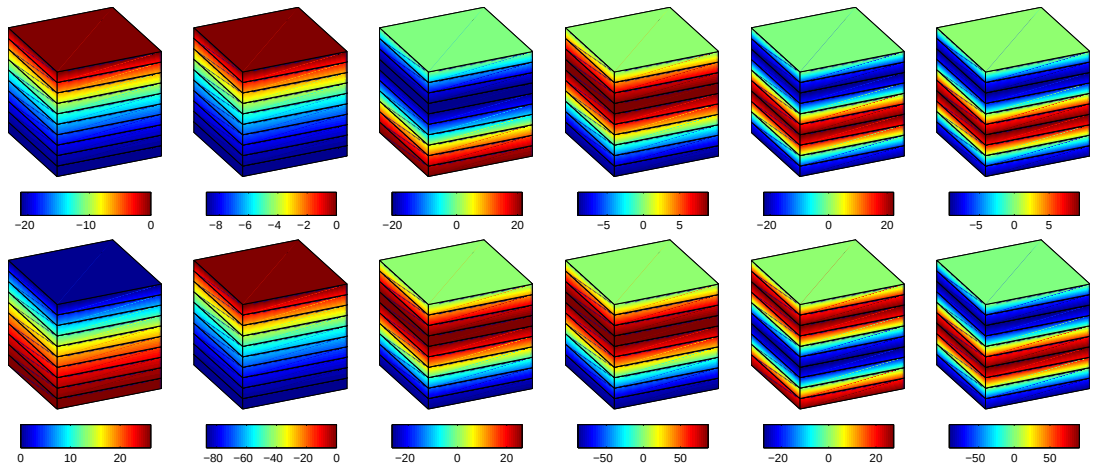

(a) 944 Hz (b) 1136 Hz (c) 2856 Hz (d) 3435 Hz (e) 4839 Hz (f) 5819 Hz

Figure 3.7: First 6 coupled mode shapes of the 1D porous layer (a) – (f), solid (top) and fluid (bottom) phases. Mesh and displacement field.

mode exhibits a standing wave in phase in the solid and fluid partitions, while for the other mode they are in antiphase. This is in good agreement with the expected behaviour of waves propagating in air-filled poroelastic materials, as the relative displacement between

the solid and fluid partitions is driven by the strong or weak coupling effects. In fact, it is consistent with the two types of compressional waves identified by Biot, the so-called fast and slow waves. While the fast wave is essentially a sound wave with the solid and fluid moving almost in phase, the slow wave represents a strongly attenuated wave, with the solid and fluid moving in antiphase.

One possible shortcoming of the generated eigenmodes could be the inability to properly render the coupling effects between the two phases. Both the constitutive coupling and the inertial coupling are taken into account in the eigenvalue problem, but the viscous drag is not, even though viscous and inertial effects are linked by the tortuosity dependency. For instance, the limit case, where the tortuosity (α_∞) is set to 1 (i.e. cylindrical-shaped pores), implies no inertial coupling while viscous coupling exists. This might involve inaccuracies in the reduced model. One possible correction is to include viscous effects in the eigenvalue problem at the cost of a lost diagonal property of the reduced mass matrix. Another possibility would be to generate additional vectors from the computed modes and the viscous terms [70], to be included in the basis. However, the tests run for a wide range of material properties and for the considered frequency range have shown no such restriction so far.

The convergence of the reduced model towards the reference FRF is presented in Figs. 3.8 for 1 to 4 modes included in the reduction basis. A satisfactory level of precision is achieved in the frequency range of interest, thus downsizing the number of poroelastic dofs from 20 to 4. Regarding the sparsity of the reduced matrices, the paired modes observed in Fig. 3.7 also imply $\mathbf{K}_{\mathrm{P}}^{(2)}$ and $\mathbf{C}_{\mathrm{P}}$ coupled contributions. Thus, although not diagonal, the system matrix corresponding to the modal coordinates still benefits from a considerably improved sparsity when compared to the unreduced problem. While CPU time performance is irrelevant for this application, both the reduction in size of the problem and the sparsity improvements suggest substantial efficiency of the proposed reduction.

The convergence rate is further tested on a more sensitive response output than the mean quadratic pressure frequency response. Thus, Fig. 3.9 presents the convergence of the calculated absorption coefficient with successive pairs of modes included in the basis. The plot on a linear scale offers better insight into the quality of the solution, which is confirmed to progressively converge towards the reference solution. It can be noted that the successive pairs contribute in increasing frequency regions of the frequency range, as observed in standard CMS methods for conservative problems. Furthermore, on this refined check of the convergence, it appears that the reduced solution does not perfectly match the reference on the upper frequency range after four pairs included in the basis. In a situation where a refined convergence is sought, this modal truncation effect is traditionally compensated by static corrections added to the modal basis. Such

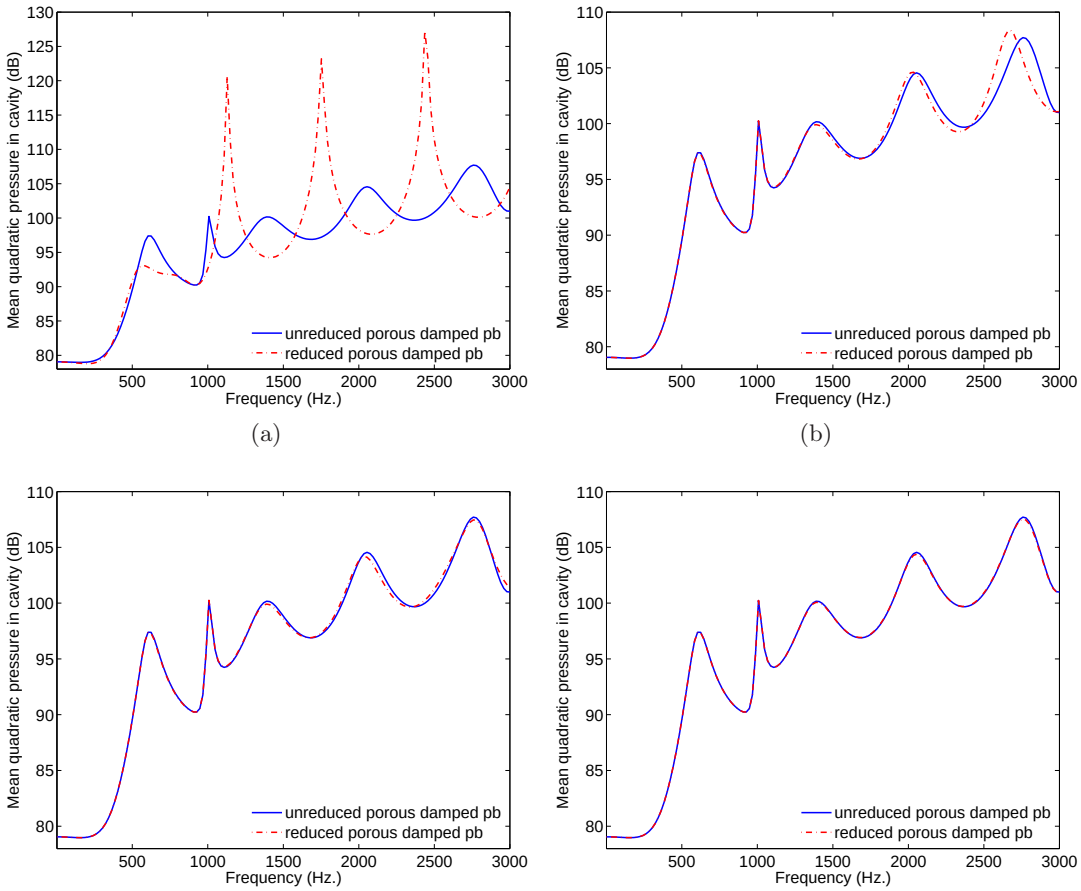

Figure 3.8: Mean quadratic pressure FRF; Convergence of the reduced model to the reference solution with added modes in the basis: (a) 1 mode, (b) 2 modes, (c) 3 modes, (d) 4 modes

an approach for this 1D case is presented in the following section.

3.4.1.3 Improved precision with the use of a static response correction

Although it may be argued that satisfactory accuracy is achieved by the proposed method when applied as is, a further enhancement of the convergence is sought using an interface dependent correction. The simplicity of the considered 1D application thus allows for the demonstration of the beneficial contribution of an orthogonalized "static" response added to the modal basis. For the 1D case, it is computed as the $\mathbf{K}_{\mathrm{P}}^{(1)}$–static response of the poroelastic domain due to a unitary plane wave with normal incidence. Application of the superposition principle implies that it can be directly obtained by summation of the poroelastic responses to successive interface dofs excitation, as detailed for the general

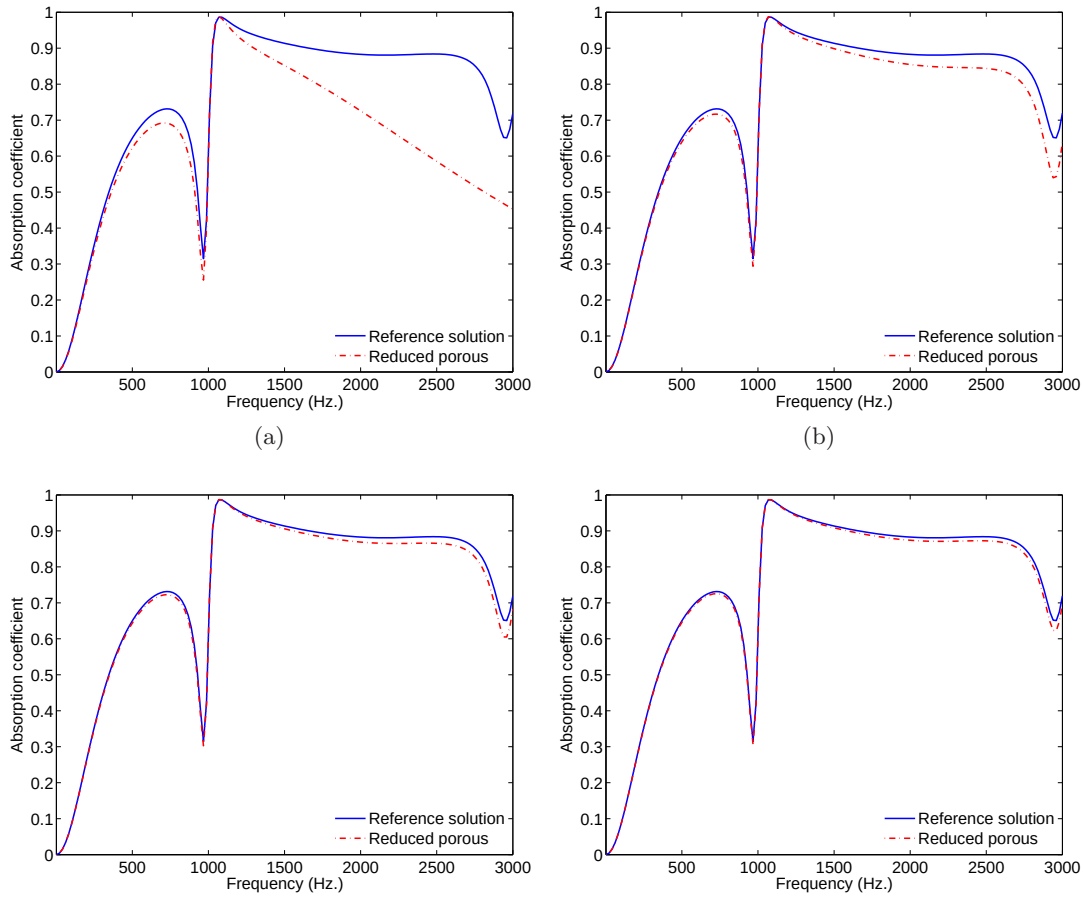

Figure 3.9: Absorption coefficient; Convergence of the reduced model to the reference solution with added modes in the basis: (a) 2 modes, (b) 4 modes, (c) 6 modes, (d) 8 modes

3D attachment functions (Eq. 3.26). Thus, the $\mathbf{K}_{\mathrm{P}}^{(1)}$–static response is related to the attachment functions,

$$\boldsymbol{\Psi}_{\mathrm{Psta}i} = \Sigma_j \boldsymbol{\Psi}_{\mathrm{P}Iij}. \tag{3.36}$$

$\boldsymbol{\Psi}_{\mathrm{Psta}}$ is by construction orthogonal to the attachment functions. A Gram-Schmidt procedure is used to orthogonalize it with respect to the selected eigenmodes and it is then $\mathbf{M}_{\mathrm{P}}$–normalized. The corresponding applied transformation is then

$$\begin{bmatrix} \widehat{\mathbf{P}}_{\bar{I}} \\ \widehat{\mathbf{P}}_{I} \\ \widehat{\mathbf{U}}_{\mathrm{P}} \end{bmatrix} = \begin{bmatrix} \mathbf{1}_{\bar{I}} & \mathbf{0} & \mathbf{0} & \mathbf{0} & \mathbf{0} \\ \mathbf{0} & \mathbf{1}_{I} & \mathbf{0} & \mathbf{0} & \mathbf{0} \\ \mathbf{0} & \boldsymbol{\Psi}_{\mathrm{P}I} & \boldsymbol{\Psi}_{\mathrm{Psta}} & \boldsymbol{\Phi}_{\mathrm{P}n} & \boldsymbol{\Phi}_{\mathrm{P}o} \end{bmatrix} \begin{bmatrix} \widehat{\mathbf{P}}_{\bar{I}} \\ \widehat{\mathbf{P}}_{I} \\ \widehat{\boldsymbol{\alpha}}_{\mathrm{sta}} \\ \widehat{\boldsymbol{\alpha}}_{n} \\ \widehat{\boldsymbol{\alpha}}_{o} \end{bmatrix}. \tag{3.37}$$

The improvements in precision are shown in Fig. 3.10. The sound pressure level differ-

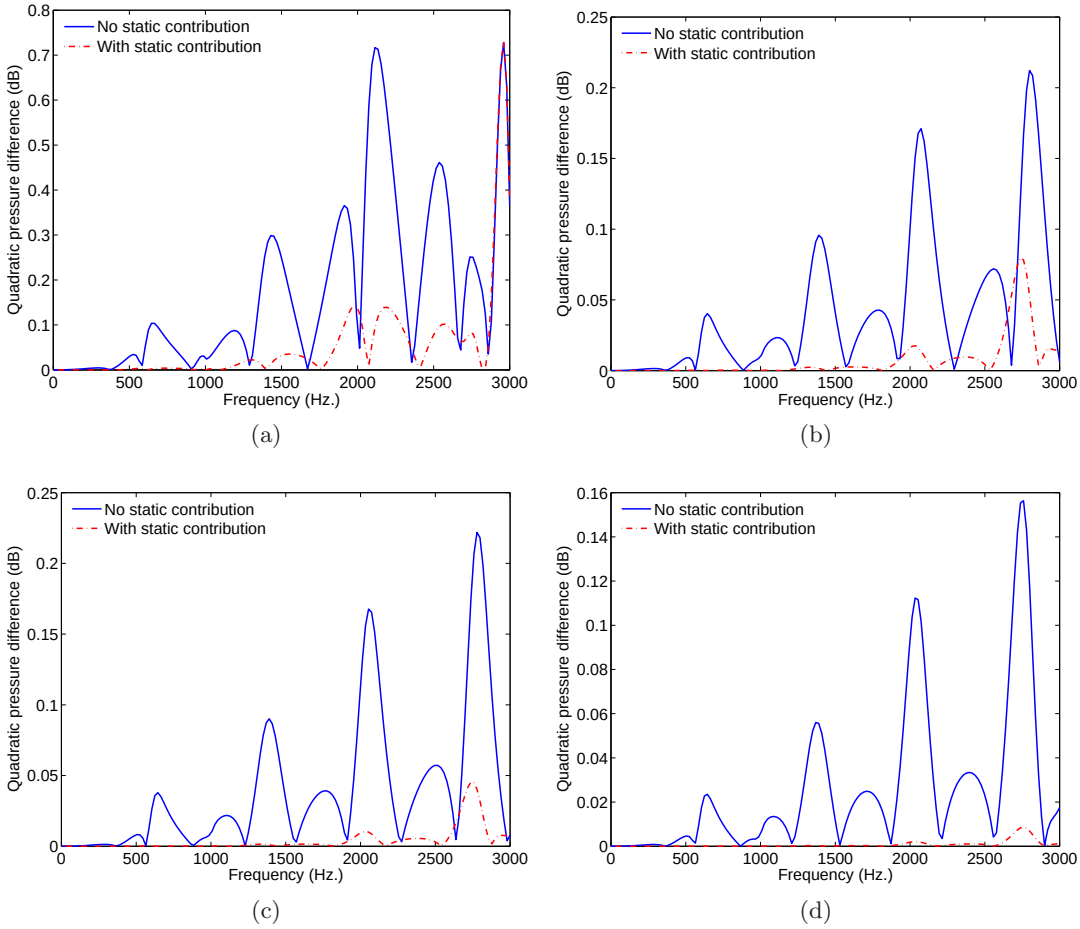

Figure 3.10: Error to reference solution (dB difference) with and without orthogonalized static response, including (a) 3 modes, (b) 4 modes, (c) 5 modes, (d) 6 modes

ence (in dB) to the reference solution is plotted for 3 to 6 normal modes included in the modal basis (note the different scales on the quadratic pressure difference axis for each plot). The convergence is clearly enhanced both in terms of dispersion (frequency shift), and error level. In addition, the orthonormalized $\mathbf{K}_{\mathrm{P}}^{(1)}$–static contribution follows the sparsity properties of the 1D eigenmodes in the sense that it is $\mathbf{K}_{\mathrm{P}}^{(2)}$– and $\mathbf{C}_{\mathrm{P}}$–orthogonal if eigenmodes are included by matching pairs, and coupled to the eigenmodes included without their matching pair. Notably, for the 1D application, it is $\mathbf{K}_{\mathrm{P}}^{(2)}$– and $\mathbf{C}_{\mathrm{P}}$–orthogonal if an even number of contiguous eigenmodes is selected for the modal basis.

Similarly to the previous section, Fig. 3.11 presents a refined estimate of the convergence using the absorption coefficient. As the convergence is much improved compared to Fig. 3.9, the plot for 4 pairs of modes included in the basis is replaced by a plot corresponding to 1 mode and the static correction (Fig. 3.11a). The solution is perfectly matching

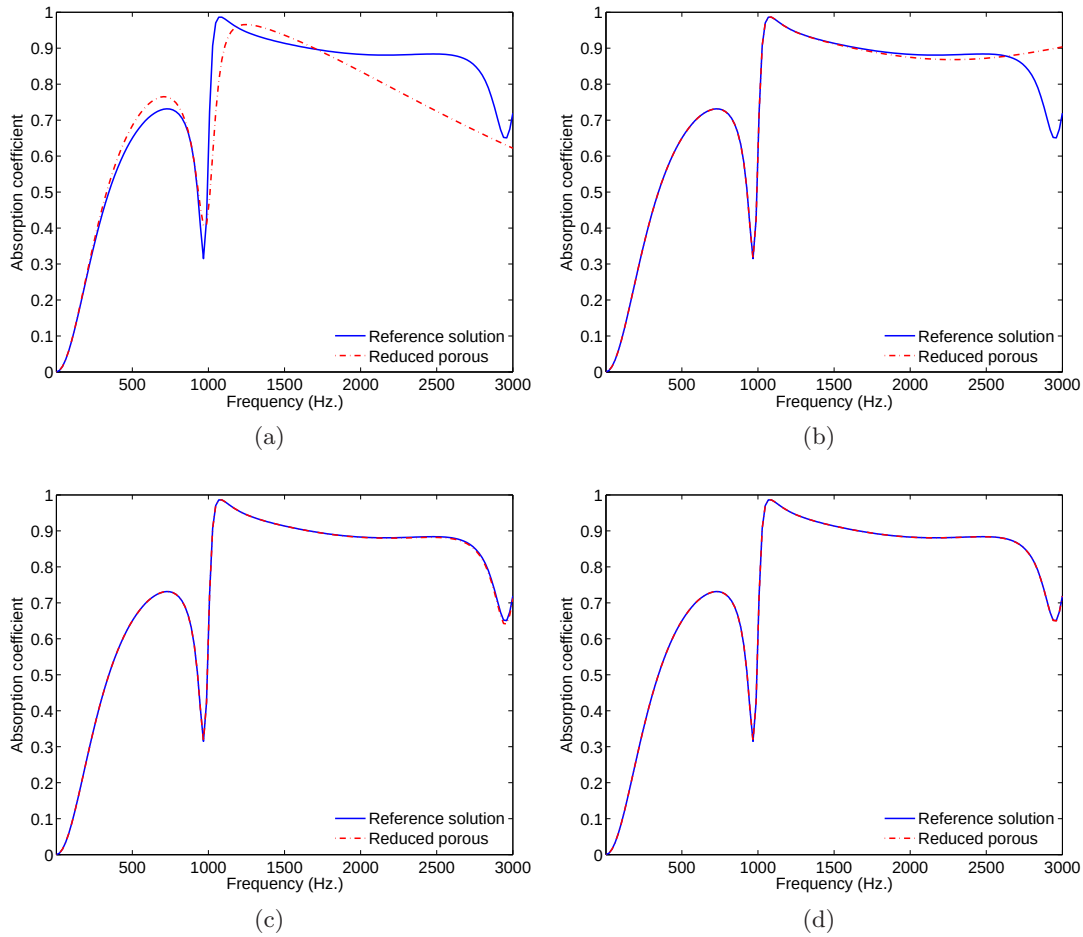

Figure 3.11: Absorption coefficient; Convergence of the reduced model to the reference solution with added modes in the basis and a low frequency correction vector: (a) 1 mode, (b) 2 modes, (c) 4 modes, (d) 6 modes

up to half the frequency range of interest with only 1 pair of modes included in the basis. The use of 2 pairs makes it suitable for the entire frequency range, and perfectly matching if 3 pairs are included. Such performance on a 1D validation case is in agreement with recent contributions in the literature made on this topic [59, 60], limited to configurations where shear waves are not involved (1D problems only, porous materials for which the shear can be neglected). Furthermore, the traditionally used truncation rule of thumb for modal synthesis (keeping modes with eigenfrequencies lower than 1.5 to 2.5 times the highest frequency of interest) applies on the 1D configurations tested.

The originality of the present approach lies in the fact that no assumption is made for the projection of the porous problem on the calculated modes. Thus, it offers the possibility to handle problems were shear effects are accounted for. The following section

initiates a direct extension of the approach to such problems. It illustrates its potential as well as its limitations in the present stage of development, on a 3D configuration, thus offering perspectives for further improvements.

3.4.2 Performance and limitations associated with the 3D case

3.4.2.1 Presentation and details of the reference solution

The extension to a 3D problem and its performance estimation are tested on a dissipative poro-acoustic example initially proposed in [109]. It consists of a 3D hexahedral acoustic cavity of dimensions $0.4 \times 0.6 \times 0.75$ m^3 (see Fig. 3.12), with rigid walls, and filled with air. One wall is covered with a 5 cm-thick porous layer. The low frequency behaviour is tested applying a time-harmonic volume velocity source (Eq. (3.11)) at a corner of the cavity opposite the layer.

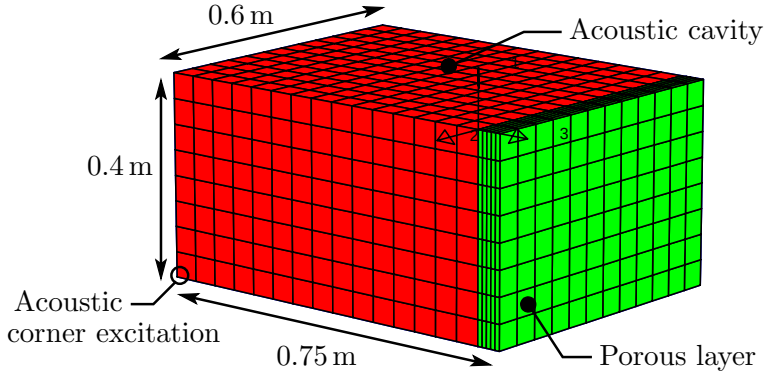

Figure 3.12: Acoustic cavity mesh and dimensions for 3D problem

The cavity is discretized by a $8 \times 12 \times 15$ mesh of 8-node hexahedral elements with pressure as single degree of freedom per node. The porous material, identical to the foam used in Section 3.4.1, is discretized by a $8 \times 12 \times 5$ mesh of 8-node hexahedral elements (Fig. 3.12), with 6 dofs per node corresponding to the fluid and solid phase displacements. Sticking Dirichlet boundary conditions are applied to the porous foam face in contact with the covered wall, and sliding conditions are prescribed on the side faces (Eqs. (3.14) and (3.15)). This leads to an FE model with 1872 acoustic dofs, and 3070 poroelastic dofs.

The mean quadratic pressure frequency response in the acoustic cavity is given as an output. The reference solution is plotted in Fig. 3.13 up to 1000 Hz, where the conservative problem consists of the acoustic geometry presented in Fig. 3.12 when the porous layer is removed (the largest dimension of the cavity is then 0.7 m). As observed for the 1D application, the damping effect of the porous layer can be clearly seen, combining a frequency-shift of the resonances towards low frequencies (particularly obvious for the

first three acoustic peaks), and a strong attenuation of the acoustic pressure level (some strongly damped resonances do not even appear at all in the dissipative solution).

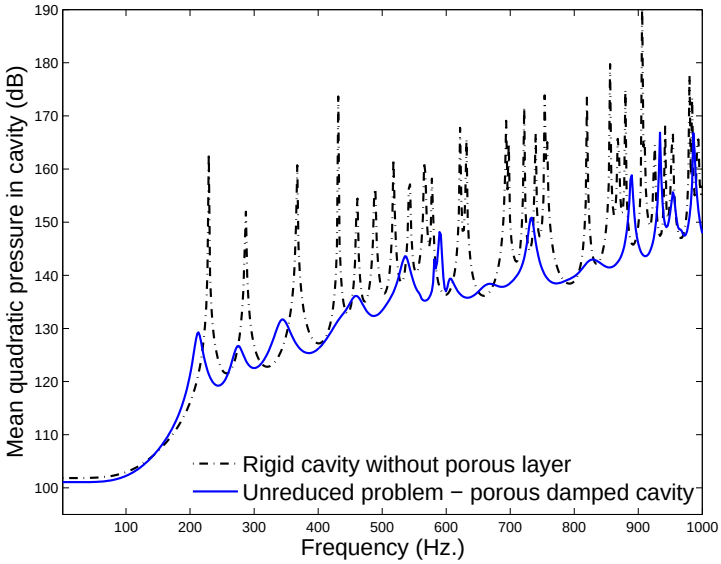

Figure 3.13: Mean quadratic pressure reference FRF, 3D problem

3.4.2.2 Reduced problem

Similarly to the 1D application, the convergence is first checked, increasing the number of modes included in the basis, for a response in the range $[0-1000]$ Hz. Although many modes are needed in order to capture the dynamic behaviour of the porous medium in the considered frequency range, the solution eventually converges towards the original solution (Fig. 3.14).

However, the interest of the proposed method specifically lies in the fact that real-valued modes are computed directly from the coupled poroelastic equations, leading to good sparsity properties. As illustrated in Figs. 3.15, the 3070 poroelastic dofs are downsized to 800 modal unknowns, of which 414 correspond to $\mathbf{K}_{\mathrm{P}}^{(2)}$– and $\mathbf{C}_{\mathrm{P}}$–orthogonal modes, as introduced in Section 3.3.2. A detailed view of the submatrix sparsity associated with the "non-orthogonal" modal coordinates is given in Fig. 3.16b.

The sparsity of the reduced system matrix is mostly affected by the use of attachment functions which fully couple interface dofs to modal unknowns. Although out of the scope of this work, reducing the number of attachment functions in the reduction procedure is therefore an important asset to enhance the performance of the method. This is particularly true when applications with high interface-to-inner-dofs ratios are considered [96, 115]. Associating attachment functions to the acoustic dofs rather than to the

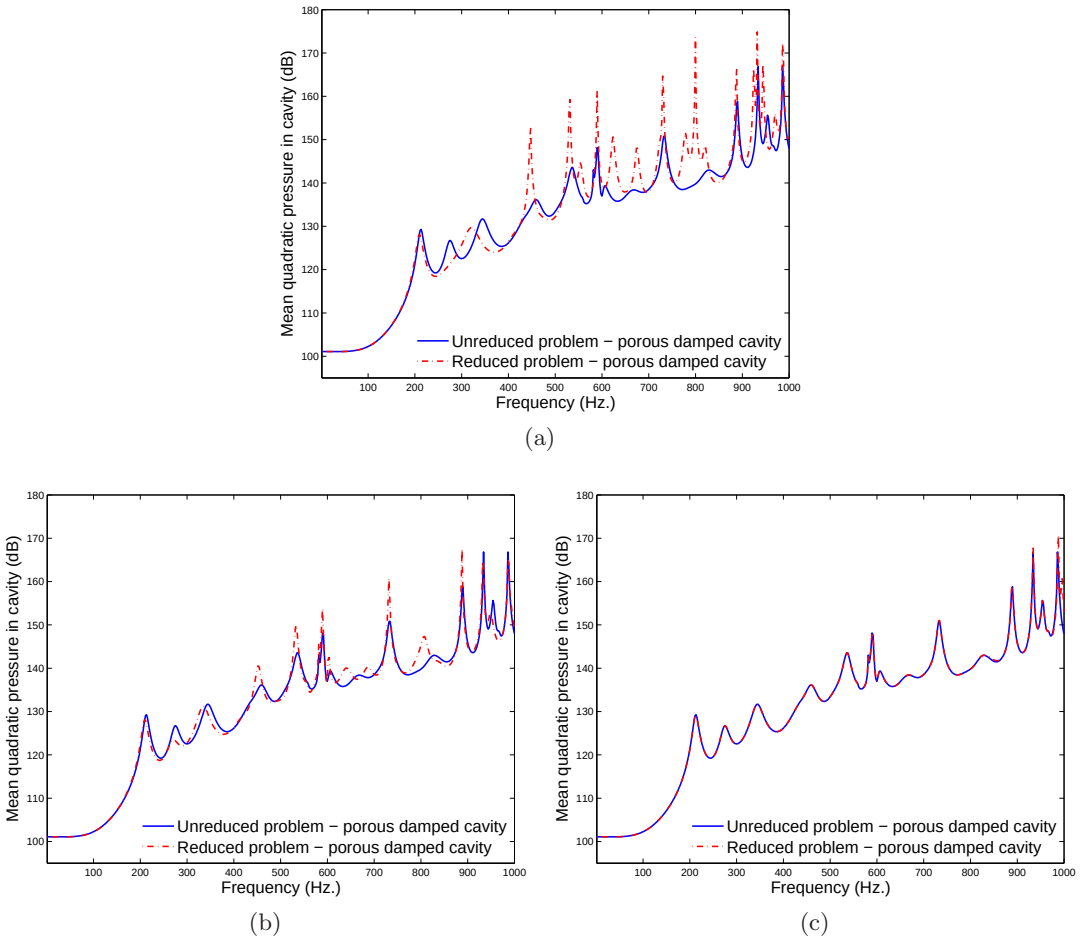

Figure 3.14: Mean quadratic pressure FRF. Convergence of the reduced model to the reference solution with added modes in the basis: (a) 100 modes, (b) 500 modes, (c) 800 modes.

poroelastic interface dofs, as established in this contribution, constitutes one step towards a reduced interface dimension. From a storage perspective, the use of $\mathbf{K}_{\mathrm{P}}^{(1)}$–static responses as attachment functions leads to uncoupled interface and modal unknowns in the reduction of $\mathbf{K}_{\mathrm{P}}^{(1)}$ (See Eq. (A.11)).

Further condensation of the modal coordinates corresponding to the $\mathbf{K}_{\mathrm{P}}^{(2)}$- and $\mathbf{C}_{\mathrm{P}}$-orthogonal modes (Section 3.3.3) leads to a contribution of 386 poroelastic dofs in the final coupled problem to be solved. Considering the relatively high proportion of orthogonal modes, substantial improvements can be expected applying this frequency-dependent additional step. The sparsity of the further condensed global system matrix, as well as a detailed view of the sparsity associated with the poroelastic part are presented in Figs. 3.16. Presented as an important condition for the scalability of the modal approach in Section 3.3.2, the submatrix sparsity associated with the "non-orthogonal" modal co-

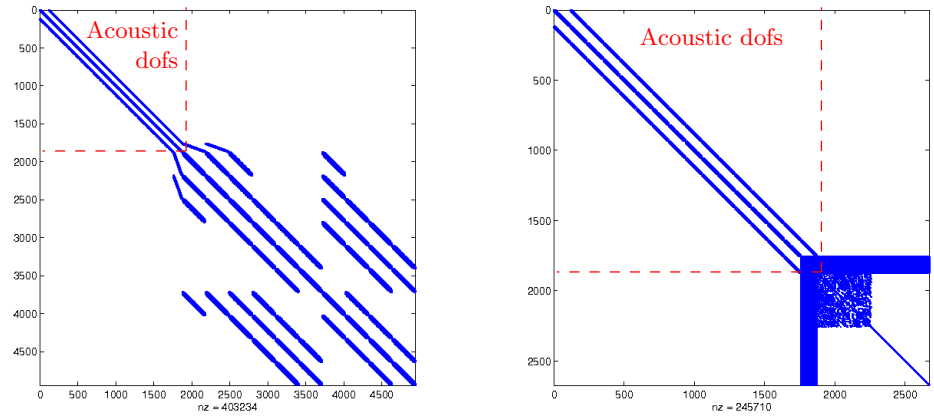

(a) (b)

Figure 3.15: Sparsity of system matrix for (a) unreduced and (b) reduced poroelastic domain

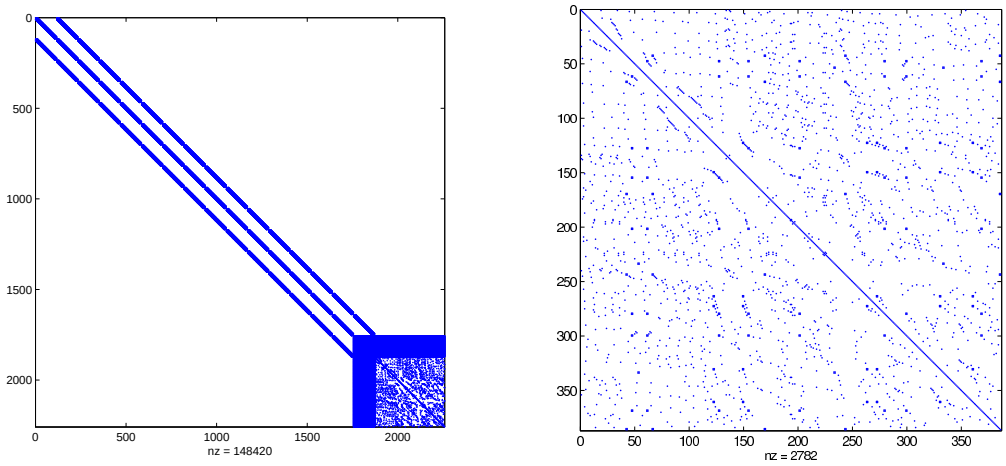

(a) (b)

Figure 3.16: (a) Sparsity of system matrix for reduced poroelastic domain with condensed "orthogonal" modal unknowns and (b) focus on the sparsity for the "non-orthogonal" modal unknowns

ordinates (Fig. 3.16b) can be quantified by its matrix density of 0.0187. As a comparison, the original coupled poro-acoustic problem exhibits a matrix density of 0.0165 (Fig. 3.15a), while its submatrix associated with the non-reduced porous equations has a matrix density of 0.0379. Thus, the reduction, only accounting for the non-orthogonal modes, even offers a matrix density improvement by a factor 2 for the studied configuration. This is of course hindered by the attachment functions coupling: the system matrix for the coupled problem with the reduced porous domain and condensation of the orthogonal coordinates (Fig. 3.16a) has a matrix density of 0.029.

Now considering an estimation of the computational time, a reduction including 800 modes in the basis leads to an enhancement factor of 2.6 to 3.5 for the CPU time (Fig. 3.17), with 500 increments computed, depending whether the offset due to modes computation is taken into account or not. Frequency-dependent condensation of part of the modal coordinates to the interface dofs further improves the efficiency, with a factor 3.1 to 4.4 for the CPU time with respect to the reference solution. However, the provided performance estimations in terms of computational time have to be taken as qualitative rather than quantitative considering the following aspects:

- The unreduced reference solution of the problem is computed as given in Eqs. (3.19) or (3.22), which involves that 4 frequency-independent matrices are assembled once initially, and combined at each frequency increment. It is likely that an industrial implementation of the unreduced problem would involve only 2 frequency-dependent matrices (equivalent mass and stiffness), thus involving assembly procedure at each frequency increment,

- The efficiency measured is dependent on the programming language as well as the quality of the implementation, especially when frequency-dependent operations such as the dynamic condensation have to be performed at each frequency increment,

- The acoustic dofs being kept unreduced, even though reduction is straightforward to establish [114], the given performance in terms of CPU time does not fully render the efficiency associated with the poroelastic reduction.

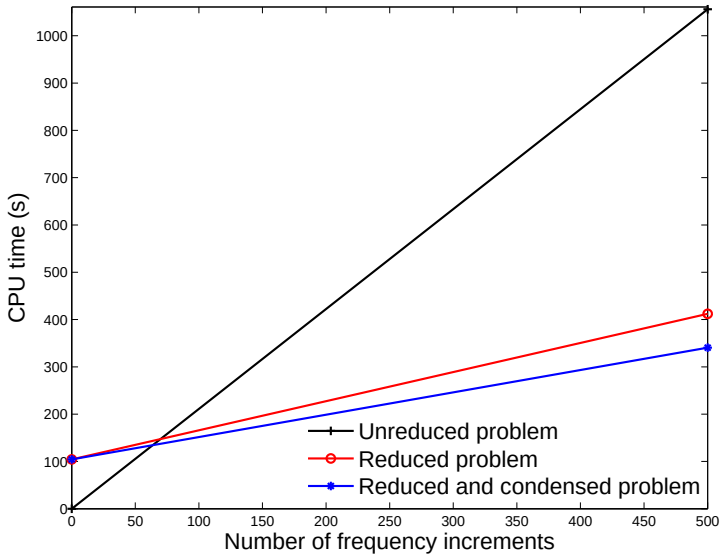

Figure 3.17: CPU time comparison for FRF computation

Nevertheless, besides the above-mentioned points, the proposed modal-based reduction of the poroelastic finite element discretization offers promising possibilities for the efficient computation of frequency response functions. Still, some major aspects have to be settled in order to make the presented method fully applicable in an industrial context: a priori truncation criteria, selection of most relevant modes, integration in complex setups (with other poroelastic domains, structural domain). The following general comments can be made with respect to these points:

- A priori criteria are needed in order to estimate the truncation of the modal basis according to the frequency range of interest. On this matter, the rule of thumb consisting in keeping the modes whose eigenfrequencies are smaller than 1.5 to 2.5 times the highest frequency of interest [90, 114] seems to work in the considered cases, but need to be confirmed on a larger range of applications and porous materials.

- In the extension to the 3D application, the convergence to the reference solution is rather slow, and some modes included in the basis seem not to bring a significant contribution. Therefore, finding a cost-efficient way to sort the modes included in the truncated basis constitutes a further enhancement of the proposed reduction method, which is treated in the following chapter.

- Once the purely modal reduction issues are settled, as initiated in the scope of this chapter, the integration of the approach into more complex situations (geometry, multiple domains) is an essential point to investigate. The difficulties are then relocated from volume considerations (e.g. costly 3D modelling of porous layers) to interface problems. As previously mentioned in this section, the high number of interface dofs for poroelastic materials presents the risk of jeopardizing the efficiency gained using a modal approach. Several contributions have been made recently on this topic, in the scope of structural-acoustics and dynamics (reduction of interface functions [102, 104], modal coupling using decoupled bases and correction Ritz vectors [105, 70], use of Lagrange multipliers [88, 93], ...). A follow-up to the present approach is therefore to test such methodologies in order to further extend the range of efficient application of the method.

3.5 Conclusion

In this chapter, an original way of solving the poroelastic equations was presented, as well as the corresponding variational formulation for poro-acoustic applications. This approach was used to define a standard eigenvalue problem for the coupled poroelastic equations, based on the solid phase and fluid phase displacements formulation. The gen-

erated modes were shown to form a well suited basis for a priori reduction of the finite element problem. The tests on a 1D poro-acoustic application, in a component mode synthesis scheme where only the poroelastic domain was reduced, confirmed the suitability of the proposed modal basis. The extension to a 3D application demonstrated the potential performance in terms of problem size reduction, associated CPU time enhancement, as well as sparsity of the reduced matrices, which is an important asset for use in larger applications. Out of the 4942 dofs involved, the 3070 belonging to the poroelastic domain were reduced to 800 modal coordinates. Among those, 414 corresponding to linearly independent equations, were dynamically condensed leading to a poroelastic domain downsized from 3070 to 386 dofs. An estimation of the CPU time enhancement leads to a factor 3.1 to 4.4, depending whether the time elapsed to build the reduction basis is taken into account or not. A priori criteria for modal basis truncation, as well as filtering of relevant modal components to be included in the basis, are two complements to this work that would make it fully applicable for larger and more industrial-like applications. The following chapter is dedicated to such improvements of the method. Furthermore, focusing on enhanced attachment functions, especially in the case where multilayer poroelastic materials are considered, would present an extension to this contribution, in order not to lose the benefits of subdomain reductions because of large interfaces.

Chapter 4

Enhancements of the poroelastic modal reduction

Abstract: *Following the convergence issues observed in the previous chapter, for the proposed modal reduction of poroelastic domains, some enhancements are presented in this chapter. First a sorting procedure of the modes in the basis is established, according to their contribution to the response. Then, a further truncation of the basis is introduced, in order to keep only the significant modes. The improvements are tested on simple 2D and 3D configurations.*

Contents

4.1 Introduction

In the previous chapter, the rewriting of the variational formulation associated with the poroelastic domain offered the possibility to define a standard eigenvalue problem, which has been used in a modal superposition reduction scheme. While promising in terms of efficiency and accuracy, the slow convergence observed, leading to a large modal basis, suggests that some possible improvements in the reduction would be needed. The approach considered in this chapter is to estimate the contribution of each mode to the response, in order to sort the modes, and select only the most significant ones to be retained in the reduction basis. An a-posteriori error estimation is also introduced in order to evaluate the accuracy achieved by the reduced model over the frequency range, without having to compute the reference solution.

This chapter is organized around four parts. First, the a-posteriori error estimator is introduced. An illustration of the convergence issues is then made on a simple 2D poro-acoustic problem, from which the possible improvements are extracted. The third part introduces the proposed sorting and truncation procedure for the modal basis. The last section validates the approach on simple 2D and 3D configurations of the chosen poro-acoustic problems.

4.2 A posteriori error estimation

For a given approximation of the solution using a reduced model, the error committed with respect to the unreduced solution can be estimated from the residue associated with the time-harmonic response. Thus, at a given angular frequency ω, the approximated solution following the resolution of a set of equations such as Eq. (A.11) is given by Eq. (3.27),

$$\begin{bmatrix} \widehat{\mathbf{P}}_{\bar{I}} \\ \widehat{\mathbf{P}}_{I} \\ \widehat{\mathbf{U}}_{\mathrm{P}} \end{bmatrix} = \begin{bmatrix} \mathbf{I}_{\bar{I}} & \mathbf{0} & \mathbf{0} & \mathbf{0} \\ \mathbf{0} & \mathbf{I}_{I} & \mathbf{0} & \mathbf{0} \\ \mathbf{0} & \mathbf{\Psi}_{\mathrm{P}I} & \mathbf{\Phi}_{\mathrm{P}n} & \mathbf{\Phi}_{\mathrm{P}o} \end{bmatrix} \begin{bmatrix} \widehat{\mathbf{P}}_{\bar{I}} \\ \widehat{\mathbf{P}}_{I} \\ \widehat{\boldsymbol{\alpha}}_{n} \\ \widehat{\boldsymbol{\alpha}}_{o} \end{bmatrix}. \tag{4.1}$$

From this approximate solution, and using the last set of equations in Eq. (3.22), a residual force vector for the porous domain is computed,

$$\mathbf{R}_{\mathrm{F_P}}(\omega) = \mathbf{A}_{I\mathrm{P}}^{T}\widehat{\mathbf{P}}_{I} - \left(\mathbf{K}_{\mathrm{P}}^{(1)} + \left(\widetilde{K}_{\mathrm{f}}(\omega) - P_0\right)\mathbf{K}_{\mathrm{P}}^{(2)} + \mathrm{i}\,\omega\,\widetilde{b}(\omega)\,\mathbf{C}_{\mathrm{P}} - \omega^2\mathbf{M}_{\mathrm{P}}\right)\widehat{\mathbf{U}}_{\mathrm{P}}. \tag{4.2}$$

Following, a $\mathbf{K}_{\mathrm{P}}^{(1)}$–residual displacement vector can be established,

$$\mathbf{R}_{\mathrm{U_P}}(\omega) = {\mathbf{K}_{\mathrm{P}}^{(1)}}^{-1}\mathbf{R}_{\mathrm{F_P}}(\omega). \tag{4.3}$$

The error estimator used is then chosen by analogy to the strain energy error estimator used in structural dynamics [103]. It is based on the residue, and can be computed at selected frequencies as

$$\varepsilon(\omega) = \frac{\mathbf{R}_{\mathrm{U_P}}^T(\omega)\mathbf{K}_{\mathrm{P}}^{(1)}\mathbf{R}_{\mathrm{U_P}}(\omega)}{\widehat{\mathbf{U}}_{\mathrm{P}}^T\mathbf{K}_{\mathrm{P}}^{(1)}\widehat{\mathbf{U}}_{\mathrm{P}}} = \frac{\mathbf{R}_{\mathrm{U_P}}^T(\omega)\mathbf{R}_{\mathrm{F_P}}(\omega)}{\widehat{\mathbf{U}}_{\mathrm{P}}^T\mathbf{K}_{\mathrm{P}}^{(1)}\widehat{\mathbf{U}}_{\mathrm{P}}}. \tag{4.4}$$

In the examples considered in this work, where the mean quadratic pressure in the acoustic domains is used as a response output, an error estimation lower than 0.1 has proved to be a conservative limit achieving satisfying precision for the frequency responses.

4.3 Illustration of modal reduction limitations

The convergence issues observed on a 3D application in the previous chapter are further illustrated on a small scale 2D application, which exhibits the same kind of difficulties as the 3D example while being small enough to manually point out the possible improvements.

4.3.1 Presentation of the 2D test application

The adaptation of the 3D example presented in Fig. 3.12 to a 2D problem is detailed in Fig. 4.1. It consists of an acoustic domain bounded by rigid walls, and treated with a porous layer on one wall. The same boundary conditions as in the 3D case are set for the poroelastic layer, i.e. sliding for the side walls and sticking for the back wall. The mesh, consisting of 7×5 linear elements both in the acoustic and porous domains, is suitable for an analysis up to 1500 Hz. The reference solution, with and without addition of the

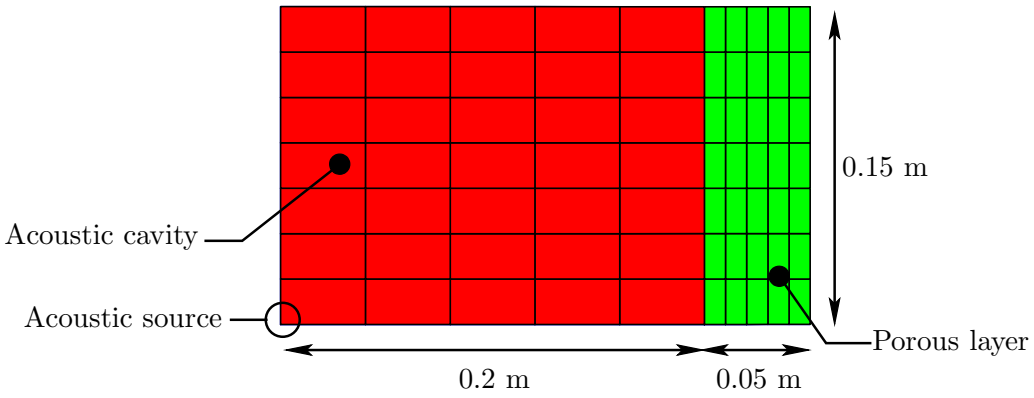

Figure 4.1: Mesh and dimensions of small 2D application

porous layer, is given in Fig. 4.2, using the mean quadratic pressure in the acoustic domain

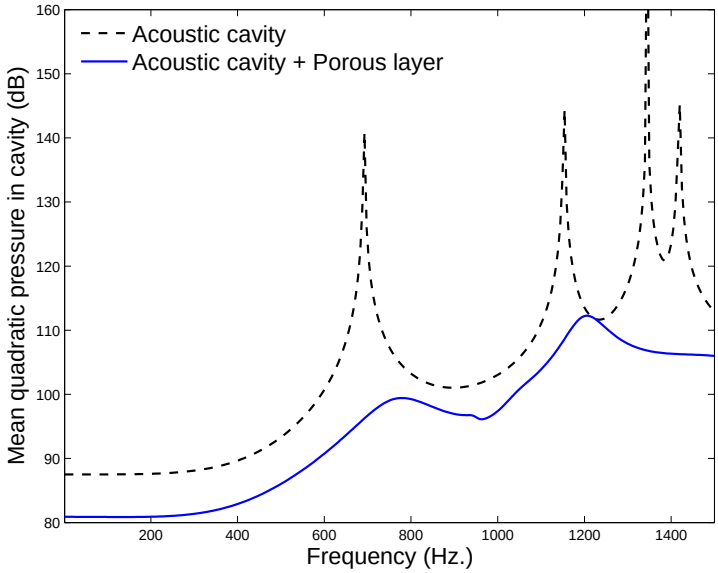

Figure 4.2: Mean quadratic pressure in the acoustic domain

as a response quantity. For the solution without the porous layer, the porous domain is replaced by an acoustic domain in order to keep the dimensions of the cavity unchanged.

For such a small problem, both in terms of dimensions and frequency content, it is possible to get an insight into the convergence issues of the modal reduction for a more complex case than a 1D problem, as the number of necessary modes is kept reasonable. It enables the observation of the convergence in terms of the frequency response when the modal shapes are manually included or excluded from the reduction basis, and thus to draw conclusions for further performance improvements.

4.3.2 Convergence of the modal reduction

In a first step the convergence of the reduced model solution towards the reference solution is checked, exhibiting the same difficulties as those encountered in the 3D problem. A satisfactory level of accuracy is obtained after 26 modes are included in the modal basis, as shown in Fig. 4.3.

As for the 3D problem of the previous chapter, the modes included exhibit uneven contributions to the response accuracy. This point can be partly understood when observing the corresponding coupled mode shapes as plotted in Fig. 4.4. In fact, some coupled mode shapes, in the low frequency range, show localized behaviour that is more likely to be observed at higher frequencies or for specific excitations, e.g. modes 6, 8, 10, 11, 14, 19, 20, 22, 23 when compared to modes such as 1, 2, 12, 15, 21. This can be confirmed if the modes that seem to bring the most significant contributions to the frequency response

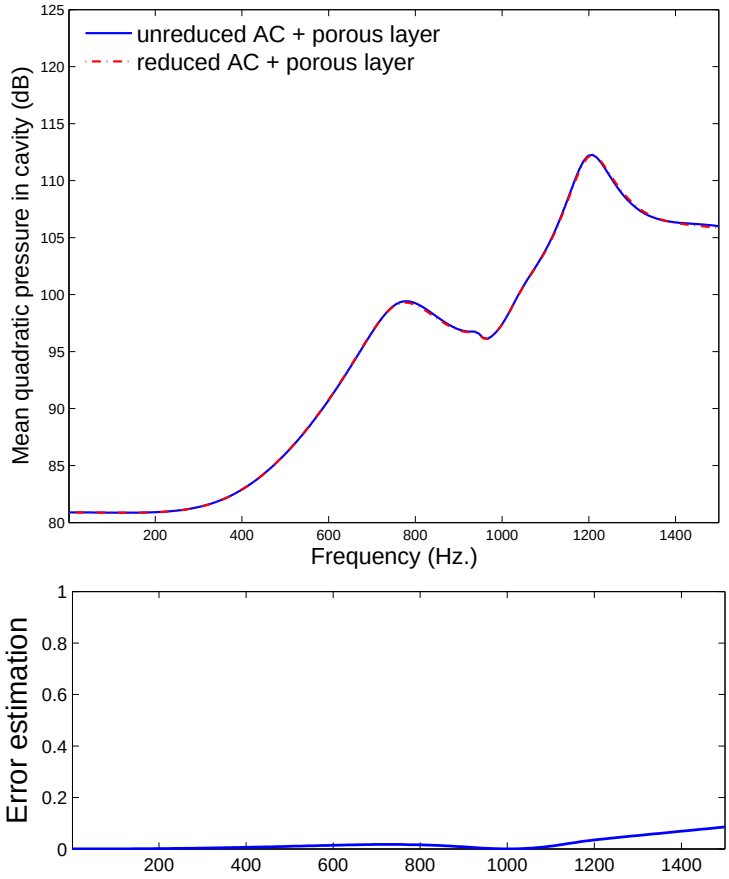

Figure 4.3: Mean quadratic pressure convergence with 26 modes and error estimation

accuracy are manually extracted from the modal basis to form a reduced basis. In the present example, these correspond to modes 1, 2, 4, 12, 15, 16, 21, 26. The corresponding convergence, when these modes are successively included in the basis, is presented in Fig. 4.5. For reasons of conciseness, the contribution of modes 4 and 16 is skipped, as being less obvious than the ones presented.

In addition, the modes bringing an apparent significant contribution to the solution improvement do not seem properly ordered in the basis, meaning, e.g., that the low frequency modes do not necessarily have an influence in the low frequency range of the response, as can be seen in Fig. 4.5. As an example, it seems that mode 21, which appears as a low order 1D mode when considering its shape, has a strong contribution in the low frequency range, and would need to be included among the first modes selected in the basis. Similarly, modes 2, 4 and 12 mostly contribute at frequencies above 1200 Hz, and could therefore be repositioned accordingly. It is the aim of the following section to provide an appropriate selection and reordering criterion to further reduce and sort the modal basis obtained from the eigenvalue problem.

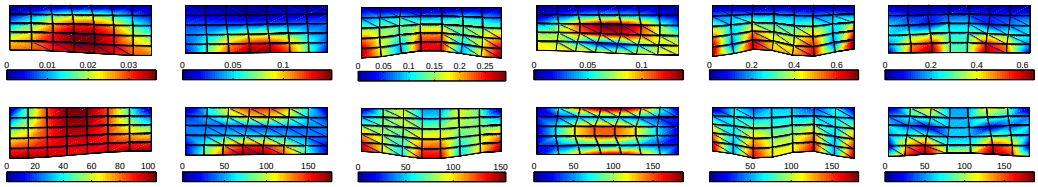

(1) 83 Hz (2) 161 Hz (3) 249 Hz (4) 299 Hz (5) 433 Hz (6) 449 Hz

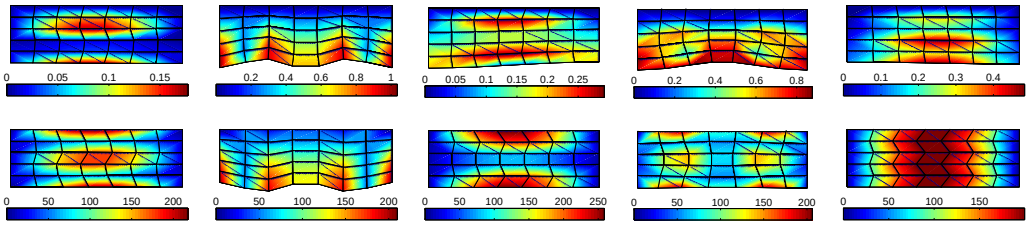

(7) 468 Hz (8) 632 Hz (9) 650 Hz (10) 676 Hz (11) 745 Hz

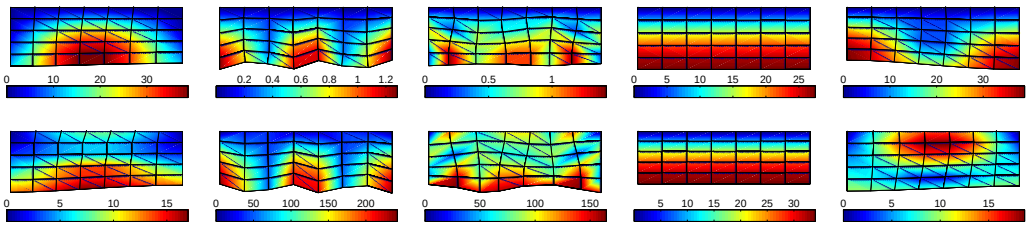

(12) 787 Hz (13) 844 Hz (14) 917 Hz (15) 947 Hz (16) 951 Hz

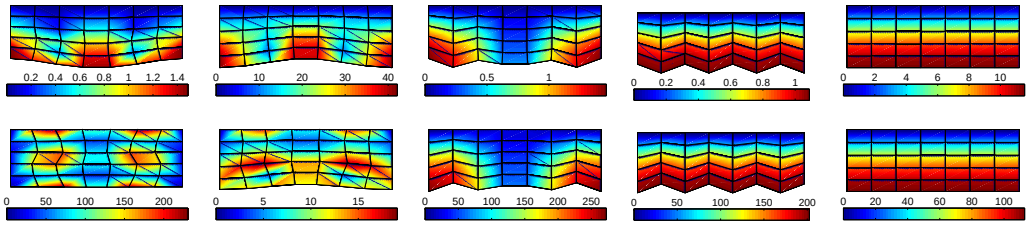

(17) 991 Hz (18) 1010 Hz (19) 1031 Hz (20) 1111 Hz (21) 1139 Hz

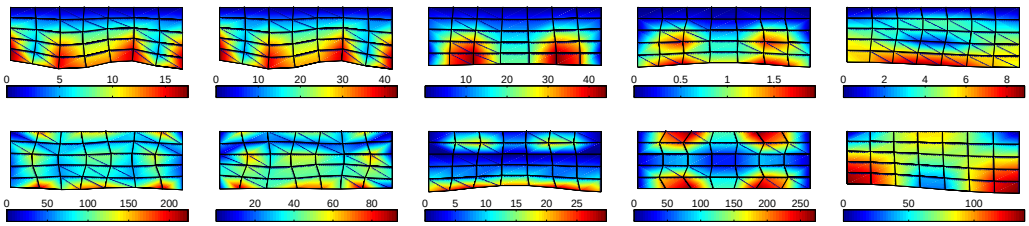

(22) 1209 Hz (23) 1255 Hz (24) 1327 Hz (25) 1342 Hz (26) 1343 Hz

Figure 4.4: Porous 2D mode shapes of modes 1-26: solid (top) and fluid (bottom) phases. Deformed mesh and norm of displacement.

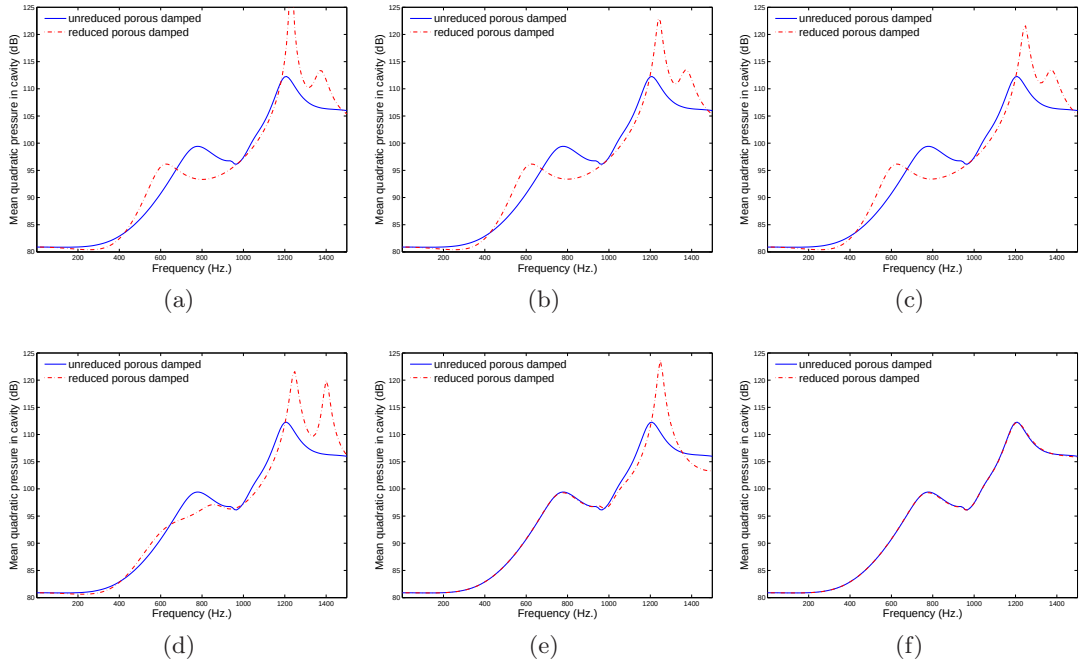

Figure 4.5: Convergence with modal superposition of manually selected modes: (a) Mode 1, (b) Modes $1, 2$; (c) Modes $1, 2, 4, 12$; (d) Modes $1, 2, 4, 12, 15$; (e) Modes 1, 2, 4, 12, 15, 16, 21; (f) Modes $1, 2, 4, 12, 15, 16, 21, 26$

4.4 Efficiency improvements using modal basis filtering

Considering the localized and complex phenomenology within the poroelastic layer, which makes it highly dependent on the excitation, the modes computed using a standard eigenvalue solver clearly do not all have a relevant contribution to the response. A selection based on the use of residual forces is therefore proposed in order to generate a more specific modal basis.

4.4.1 Modal contribution criterion using a residual force

The residual forces give a very useful insight into the quality of the reduced model, as they are directly linked to the approximation committed [103]. Therefore, in the context of modal reduction, they have been used for different matters. Among the possibilities, residual responses can be added, once orthogonalized, in reduction bases that are built iteratively [116]; they can also be used to take into account additional terms not included in the eigenvalue problem [117, 107, 63, 70], or modified parameters in an optimization procedure [118, 117]. In fact, the residue provides a natural way to correct the reduction basis as it includes missing components [116].

In the present approach, where the aim is to provide a suitable basis for a set frequency range, the residual force is used to estimate the modal contribution of the modes. By doing so, only the main components properly describing the specific problem are kept in a further reduced basis. The residual force is computed, at a given angular frequency ω_0, using the solution vector of a reduced model including only the very low frequency modes, e.g. the first mode (following Eq. (A.11) without consideration of "orthogonal" and "non-orthogonal" distinctions). Follows a poor approximate solution at ω_0 after inverse transformation,

$$\begin{bmatrix} \widehat{\mathbf{P}}_{\bar{I}} \\ \widehat{\mathbf{P}}_{I} \\ \widehat{\mathbf{U}}_{\mathrm{P}} \end{bmatrix}_{\omega_0} = \begin{bmatrix} \mathbf{I}_{\bar{I}} & \mathbf{0} & \mathbf{0} \\ \mathbf{0} & \mathbf{I}_{I} & \mathbf{0} \\ \mathbf{0} & \mathbf{\Psi}_{\mathrm{P}I} & \mathbf{\Phi}_{\mathrm{P_{LF}}} \end{bmatrix} \begin{bmatrix} \widehat{\mathbf{P}}_{\bar{I}} \\ \widehat{\mathbf{P}}_{I} \\ \widehat{\boldsymbol{\alpha}}_{\mathrm{LF}} \end{bmatrix}_{\omega_0}, \tag{4.5}$$

where $\mathbf{\Phi}_{\mathrm{P_{LF}}}$ consists of the lowest frequency mode computed by eigenvalue problem (3.23) and $\boldsymbol{\alpha}_{\mathrm{LF}}$ the corresponding modal coordinate. Noticing that no external load is applied to the poroelastic domain (see Eq. (3.22)) beside the coupling terms with the acoustic domain, a residual force vector for the porous domain can be computed directly from the last line of Eq. (3.22) at angular frequency ω_0,

$$\mathbf{R}_{\mathrm{F_P}}(\omega_0) = \mathbf{A}_{I\mathrm{P}}^{T}\widehat{\mathbf{P}}_{I_{\omega_0}} - \left(\mathbf{K}_{\mathrm{P}}^{(1)} + \left(\widetilde{K}_{\mathrm{f}}(\omega_0) - P_0\right)\mathbf{K}_{\mathrm{P}}^{(2)} + \mathrm{i}\,\omega_0\,\widetilde{b}(\omega_0)\,\mathbf{C}_{\mathrm{P}} - \omega_0^2\mathbf{M}_{\mathrm{P}}\right)\widehat{\mathbf{U}}_{\mathrm{P}_{\omega_0}} \tag{4.6}$$

A $\mathbf{K}_{\mathrm{P}}^{(1)}$-residual displacement vector follows,

$$\mathbf{R}_{\mathrm{U_P}}(\omega_0) = {\mathbf{K}_{\mathrm{P}}^{(1)}}^{-1}\mathbf{R}_{\mathrm{F_P}}(\omega_0) \tag{4.7}$$

The following step is to compare each mode shape to the content of this residue. An indicator such as the Modal Assurance Criterion (MAC) is an option that could be used for comparison between a residual displacement vector and the mode shapes, but does not carry significant physical meaning, and is likely to bring poorly conclusive results. A concept such as the modal participation factors can bring better suited results to the present request. Thus, the participation factor of the ith mode shape $\mathbf{\Phi}_{\mathrm{P}i}$ to the real part of the $\mathbf{K}_{\mathrm{P}}^{(1)}$-residual displacement vector corresponding to the residual force $\mathbf{R}_{\mathrm{F}_j}$ (e.g. $\mathbf{R}_{\mathrm{F_P}}(\omega_0)$ associated with $\mathbf{\Phi}_{\mathrm{P_{LF}}}$ in Eq. (4.6)), is defined as

$$\mu_{ij} = \frac{|{\mathbf{\Phi}_{\mathrm{P}i}}^{T}\,\mathbf{M}_{\mathrm{P}}\,{\mathbf{K}_{\mathrm{P}}^{(1)}}^{-1}\Re(\mathbf{R}_{\mathrm{F}_j})|}{\|\Re(\mathbf{R}_{\mathrm{F}_j})\|}. \tag{4.8}$$

For practical implementation purposes, it can be rewritten without the need to calculate the residual displacement vector. Using the eigenvalue problem Eq. (3.23), Eq. (4.8) becomes

$$\mu_{ij} = \frac{|\mathbf{\Phi}_{\mathrm{P}i}\cdot\Re(\mathbf{R}_{\mathrm{F}_j})|}{{\omega_i}^2\|\Re(\mathbf{R}_{\mathrm{F}_j})\|}, \tag{4.9}$$

where ${\omega_i}^2$ is the eigenvalue corresponding to the eigenvector $\mathbf{\Phi}_{\mathrm{P}i}$. A similar definition can be given with respect to the imaginary part of $\mathbf{R}_{\mathrm{F}_j}$. The procedure thereafter described can also be applied to such an imaginary part participation factor, but has shown no additional interest in the considered validation cases. It is recalled here that the eigenvector expression $\mathbf{\Phi}_{\mathrm{P}i}$ refers to a mass-normalized mode. This first approach enables a proper sorting of the mode shapes according to their modal participation to the residual vector. Furthermore, being independent of the residual force norm, the participation factors defined as such can be used to compare the relative contributions of a mode shape to a set of several residual force vectors computed at different frequencies. In the following, it is supposed that for a given residual force $\mathbf{R}_{\mathrm{F}_j}$, a set of N modes are ordered by decreasing modal participation so that

$$\mu_{1j} > \cdots > \mu_{ij} > \cdots > \mu_{\mathrm{N}j}. \tag{4.10}$$

In order to establish a truncation criterion based on these participation factors, they are normalized with respect to the smallest contribution, for a given residual force,

$$\forall\, i \in [1..\mathrm{N}] \quad \bar{\mu}_{ij} = \frac{\mu_{ij}}{\mu_{\mathrm{N}j}} \geqslant 1. \tag{4.11}$$

In practice, these factors can differ from one another by several orders of magnitude, which makes a logarithmic scale more appropriate for their representation than a linear scale, as shown in Fig. 4.6. The logarithmic representation allows to easily distinguish significant

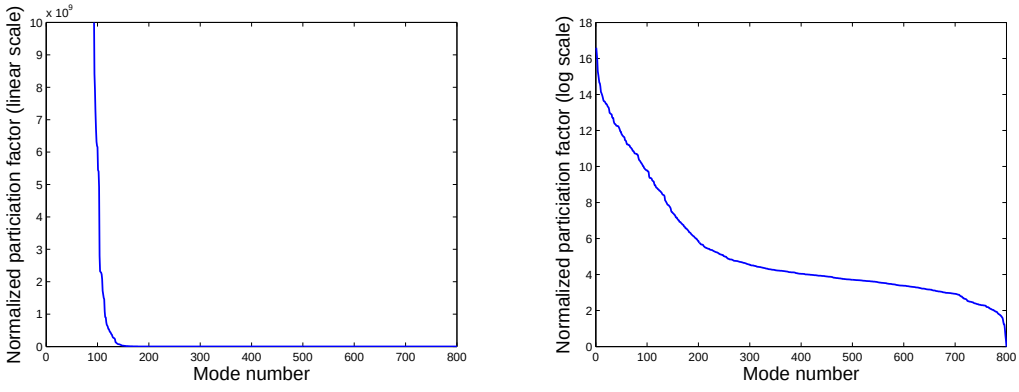

(a) (b)

Figure 4.6: Example of normalized modal participation factors: (a) linear scale and (b) logarithmic scale

contributions, either by their contribution level, or by the change of tangent slope, as can be observed in Fig. 4.6b. Therefore, several selection criteria can be proposed, e.g. based on a threshold value, a change in the tangent slope, a ratio of contribution. After

testing, the latter approach is presented in this work. Thus, for a selection of the "n" most significant modes in the truncated modal basis, the following criterion is proposed, based on a ratio of the cumulated logarithmic contributions,

$$\chi_{nj} = \frac{\sum_{i=1}^{n} \log(\bar{\mu}_{ij})}{\sum_{i=1}^{N} \log(\bar{\mu}_{ij})} \leqslant \chi_{\max}, \tag{4.12}$$

where $\chi_{\max}$ is an empirical limit, in the interval $]0, 1]$, typically found to be conservatively suitable when set to 0.4 in the presented applications.

4.4.2 Practical implementation

The mode sorting indicator presented in Eq. (4.9) together with the selection criterion (A.18) are used for filtering mode shapes computed with the standard eigenvalue problem. The quasi-orthogonality property of the modes computed allows to test them individually for their participation to the response content. For a small problem involving the combination of a narrow frequency band and a low spectral density, one residual vector might be sufficient to select the proper modes. However, for applications with broader frequency content, a selection based on several residual vectors distributed in the frequency range of interest is needed. Two approaches can be considered for a mode selection procedure based on a set of residual vectors:

- the modes are ordered after a weighted average of their participation to the residual vectors,
- the modes are successively selected according to their participation to the residual vectors ordered in increasing frequency.

The first possibility imposes a weighting to be assigned to each residual vector, particularly in the aim of ordering the modes in the modal basis according to their influence in the frequency range. The second approach offers a natural weighting of the residual vectors, provided each of them is best suited for a frequency band centered on its frequency of computation. The latter method is chosen, selecting a set of modes with respect to the first residual vector, then completed by modes successively selected among the remaining ones, using the additional residual vectors. The corresponding procedure is detailed in Algorithm 1.

Algorithm 1 Procedure for selection of significant modes

1. Compute truncated modal basis (eigenvalue problem)
2. Decomposition of $\mathbf{K}_{\mathrm{P}}^{(1)}$
3. $\mathrm{N_{LF}}$ low frequency modes retained for residual vectors computation
4. Choice of ω_j set for N_j residual vectors
5. Compute corresponding $\mathbf{R}_{\mathrm{F}_j}$
6. Include the initial $\mathrm{N_{LF}}$ low frequency modes in the basis
7. **for** $j = 0$ **to** N_j **do**
8. Compute contribution μ_{ij} for modes not yet selected
9. Sort modes in descending μ_{ij} contribution
10. Compute cumulated contributions $\chi_{\mathrm{n}j}$
11. Select modes for which $\chi_{\mathrm{n}j} \leqslant \chi_{\max}$
12. Add sorted selected modes to modal basis
13. **end for**

4.5 Applications

4.5.1 Small 2D application in low frequency

Following the test example presented in Section 4.3.1, for which the convergence issues are discussed in Section 4.3.2, the modal basis refinement procedure proposed is applied in order to evaluate its performance. Starting with a modal basis including modes up to one time the highest frequency of interest (i.e. 1500 Hz), which proved sufficient to achieve a satisfying precision, 26 modes are to be processed for an optimal selection. In this small application, one residual vector is retained for the mode selection procedure. This residual vector is computed with the lowest frequency mode included in the modal basis, and for an arbitrarily chosen low frequency of 375 Hz. The upper bound for cumulated contributions, $\chi_{\max}$, is set to 0.4. Thus, are selected as significant modal contributions, the n modes satisfying

$$\chi_{\mathrm{n}j} \leqslant 0.4. \tag{4.13}$$

The mode selection following the sorting procedure is presented in table 4.1. The modal contribution associated with mode 1, which is included in the modal basis for computation of the residual vector, is given as an indication. It reflects the expected orthogonality between the mode shape and the residual vector computed with this mode included in the modal basis. In addition, it further confirms the established link, on which the selection procedure is based, between the residual vectors and the content of the modal basis. The first 8 selected and sorted mode shapes extracted from the complete modal basis (see Fig. 4.4) are presented in Fig. 4.7.

The convergence of the solution using the further reduced modal basis is presented in

Mode	Eigenfrequency (Hz)	μ_{ij}	$\chi_{\mathrm{n}j}$
1	83	(0)	(1)
2	161	12.9	0.06
21	1139	12.0	0.12
15	947	11.9	0.17
4	299	11.1	0.23
12	787	10.4	0.28
26	1343	10.3	0.32
16	951	9.8	0.37
7	468	9.2	0.4

Table 4.1: Significant modal contributions selection

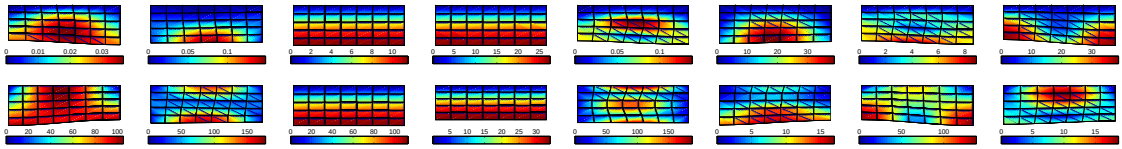

(a) 83 Hz (b) 161 Hz (c) 1139 Hz (d) 947 Hz (e) 299 Hz (f) 787 Hz (g) 1343 Hz (h) 951 Hz

Figure 4.7: Porous 2D selected and sorted mode shapes 1, 2, 21, 15, 4, 12, 26, 16: solid (top) and fluid (bottom) phases. Deformed mesh and norm of displacement.

Fig. 4.8. The precision achieved is already satisfactory when only the first 8 selected modes are included in the modal basis, which means that an upper bound of 0.38 for $\chi_{\max}$ was sufficient in this case. However, even though not represented in Fig. 4.8, including the 9th selected mode in the basis induces an error estimation lower than 0.1. Finally, it is worth noticing that the modes manually selected in Subsection 4.3.1 are well captured by the proposed procedure. Furthermore, when compared to the convergence of the solution with unsorted modes in Fig. 4.5, the proposed reordering strategy exhibits a much smoother convergence with respect to the frequency.

The computational time improvement and sparsity performance are not addressed in the 2D case. However, it can be underlined that the unreduced porous domain consists of 144 dofs, which are reduced to at best 26 dofs using a rule of thumb truncation of the complete modal basis. Use of the proposed selection procedure produces a further reduced poroelastic domain of at best 8 dofs, that is 5.5% of the original problem size, or 18 times smaller.

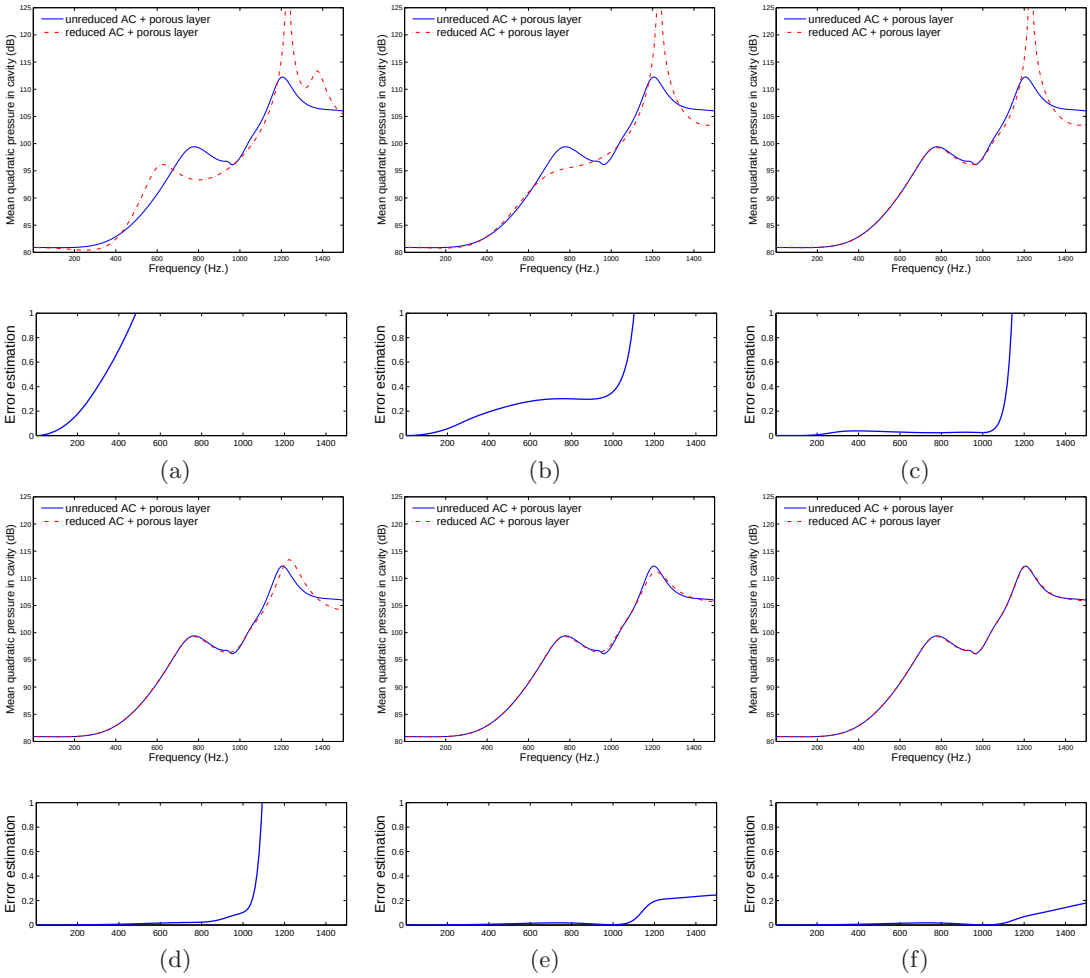

Figure 4.8: Convergence with modal superposition of selected modes for $\chi_{\max} = 0.4$: (a) Mode 1, (b) Modes $1, 2, 21$; (c) Modes $1, 2, 21, 15$; (d) Modes $1, 2, 21, 15, 4$; (e) Modes $1, 2, 21, 15, 4, 12, 26$; (f) Modes $1, 2, 21, 15, 4, 12, 26, 16$

4.5.2 Larger 2D application and increased frequency range

The application presented in the previous section is deliberately chosen small, both in terms of size and frequency content, in order to be able to manually control the mode filtering and sorting process, and thus to estimate the potential performance of the proposed criterion. However, due to its size, the problem tested is still rather close to a 1D problem, which is underlined by the selection of 1D mode shapes among the first modes selected. In this section, the established selection criterion is further tested on a larger 2D application, involving both a larger frequency content and a proper 2D geometry. Its geometry, dimensions and mesh are presented in Fig. 4.9. The mesh, consisting of 40×13 linear elements in the acoustic domain and 40×12 linear elements in the porous domain, is well suited

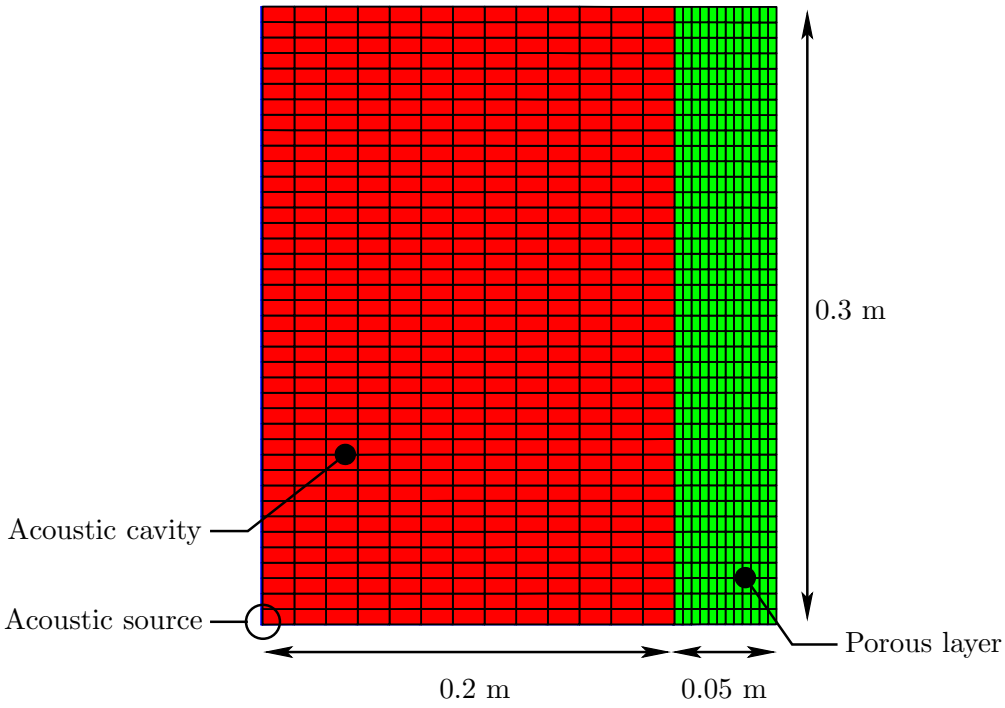

Figure 4.9: Mesh and dimensions of larger 2D application

for an analysis up to 2000 Hz. The same boundary conditions as the ones defined in the previous section are applied to the porous layer, involving a problem of 574 acoustic dofs and 1959 poroelastic dofs. The acoustic domain is excited via a time-harmonic excitation at a corner of the acoustic cavity, opposite the porous layer. The reference solution, with and without addition of the porous layer, is given in Fig. 4.10, using the mean quadratic pressure in the acoustic domain as an output (the porous domain is again replaced by acoustic elements in the conservative case).

The reduction is first applied using the complete set of modes computed from the eigenvalue problem defined in Section 3.3.2, with a rule of thumb truncation of twice the highest frequency of interest, i.e. for eigenfrequencies up to 4000 Hz. This involves 355 modes included in the basis. The convergence of the reduced solution is presented in Fig. 4.11 for enriched modal basis at significant steps including 90, 130, 180, and 355 modes. The same expected convergence difficulties are exhibited, i.e. slow convergence and uneven contributions of the modes included in the basis. Particularly, it can be noted that the convergence of the response around 1700 Hz is very slow, due to low modal contributions between modes 180 and 360.

The mode sorting and selection method is applied following the procedure in Algorithm 1. Considering the increased frequency content of the problem compared to the

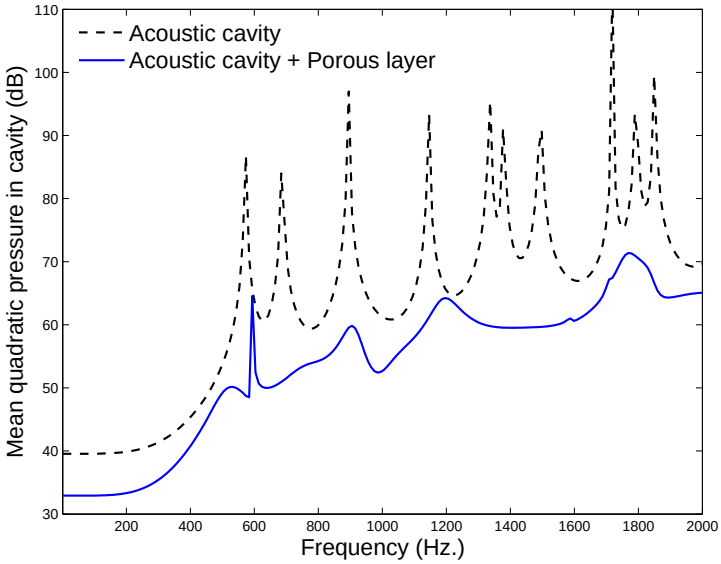

Figure 4.10: Mean quadratic pressure in the acoustic domain

previous section, two residual force vectors are used. They are computed with the lowest eigenfrequency mode included in the modal basis, and at frequencies of 450 Hz and 1450 Hz. The upper bound for cumulated contributions, $\chi_{\max}$, is set to 0.4, as done for the smaller 2D application. This produces a modal basis downsized from 360 modes to 88 modes, i.e. 24% of the original size of the modal basis, for which the convergence of the solution at significant steps is presented in Fig. 4.12. Again, a much smoother convergence is observed with respect to the frequency when the proposed enhanced modal basis is used.

The first 12 mode shapes of the original and processed modal basis are presented in Fig. 4.13 and Fig. 4.14 respectively. It can be observed once more, from this sample, that mode shapes such as those corresponding to 55 Hz, 84 Hz or 112 Hz are expected to be physically significant at higher frequencies than their eigenfrequencies. Regarding the performance of the proposed procedure, although this matter is more specifically addressed in the following section, the original problem consisting of 1959 porous dofs is downsized to 360 and 88 poroelastic dofs, using a truncated modal basis and a further processed modal basis respectively. Therefore, at best, a reduction to 4.5% of the original size of the porous domain is achieved using the proposed method.

4.5.3 Performance evaluation for a 3D example

The 3D application presented in Fig. 3.12 is used to estimate the performance of the mode selection procedure in terms of computational time, and sparsity of the system matrix. The mesh being considered best suited for frequencies up to 600 Hz, the modal basis

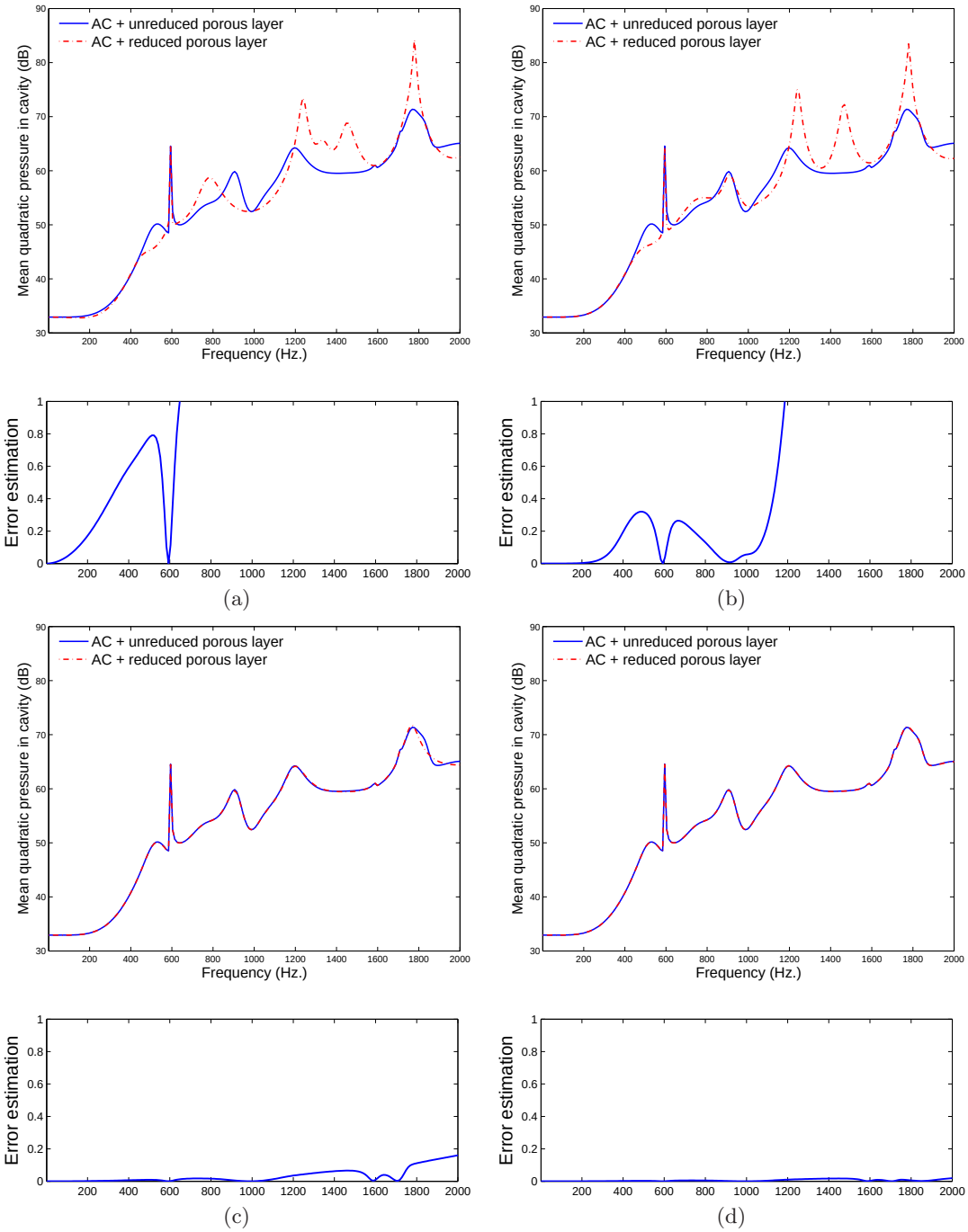

Figure 4.11: Solution convergence for the reduced model: (a) 90 modes, (b) 130 modes; (c) 180 modes; (d) 355 modes

including modes up to twice the highest frequency of interest is composed of 800 eigenvectors. Among those, it is recalled that 386 are non-orthogonal modes while the remaining 414 lead to linearly independent equations. The corresponding convergence of the reduced

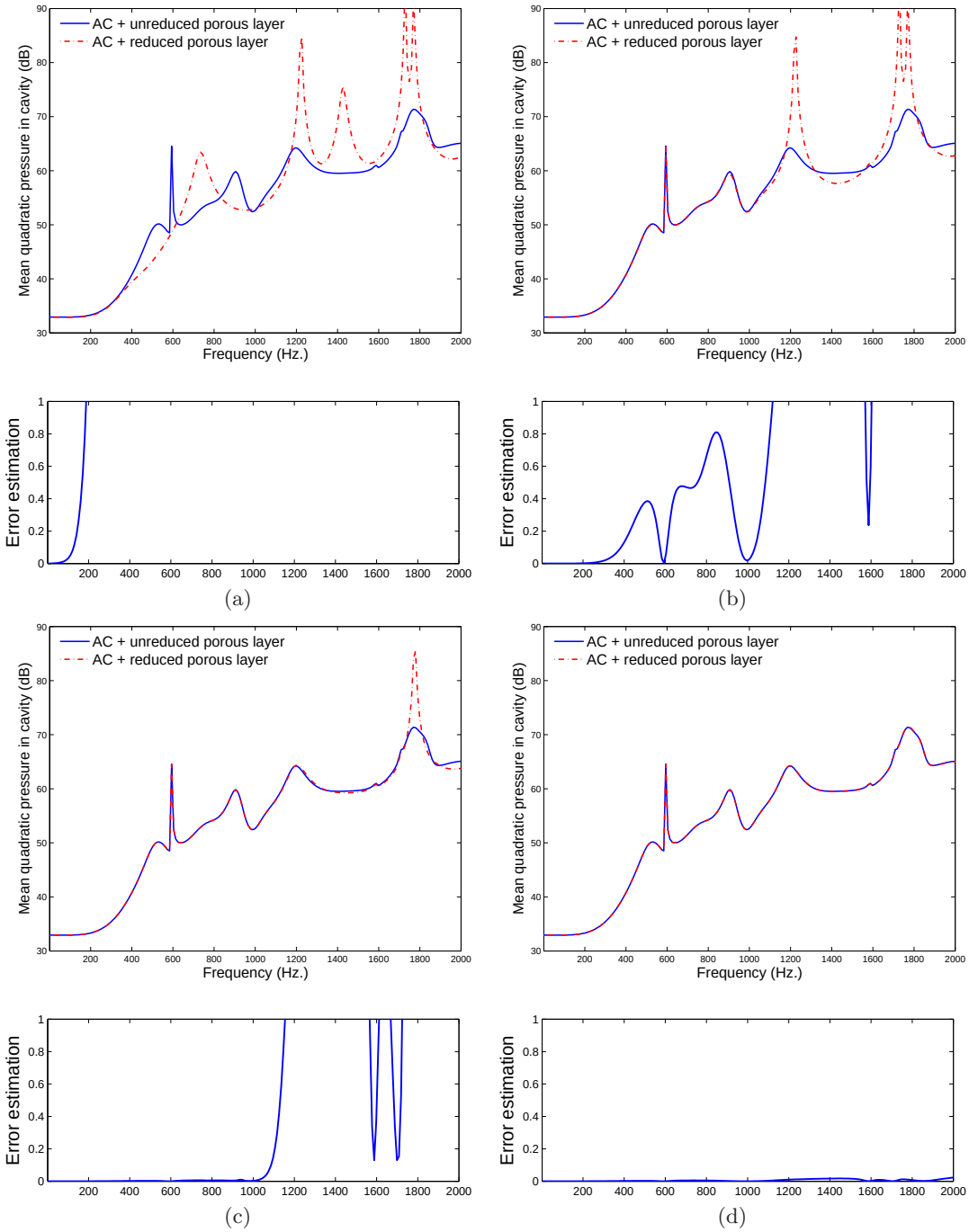

Figure 4.12: Solution convergence for the processed reduced model: (a) 4 modes, (b) 14 modes; (c) 59 modes; (d) 88 modes

problem solution was presented in Fig. 3.14, in a range of $[0 - 1000]$ Hz.

In a first approach, the mode selection procedure is applied using the previously-found

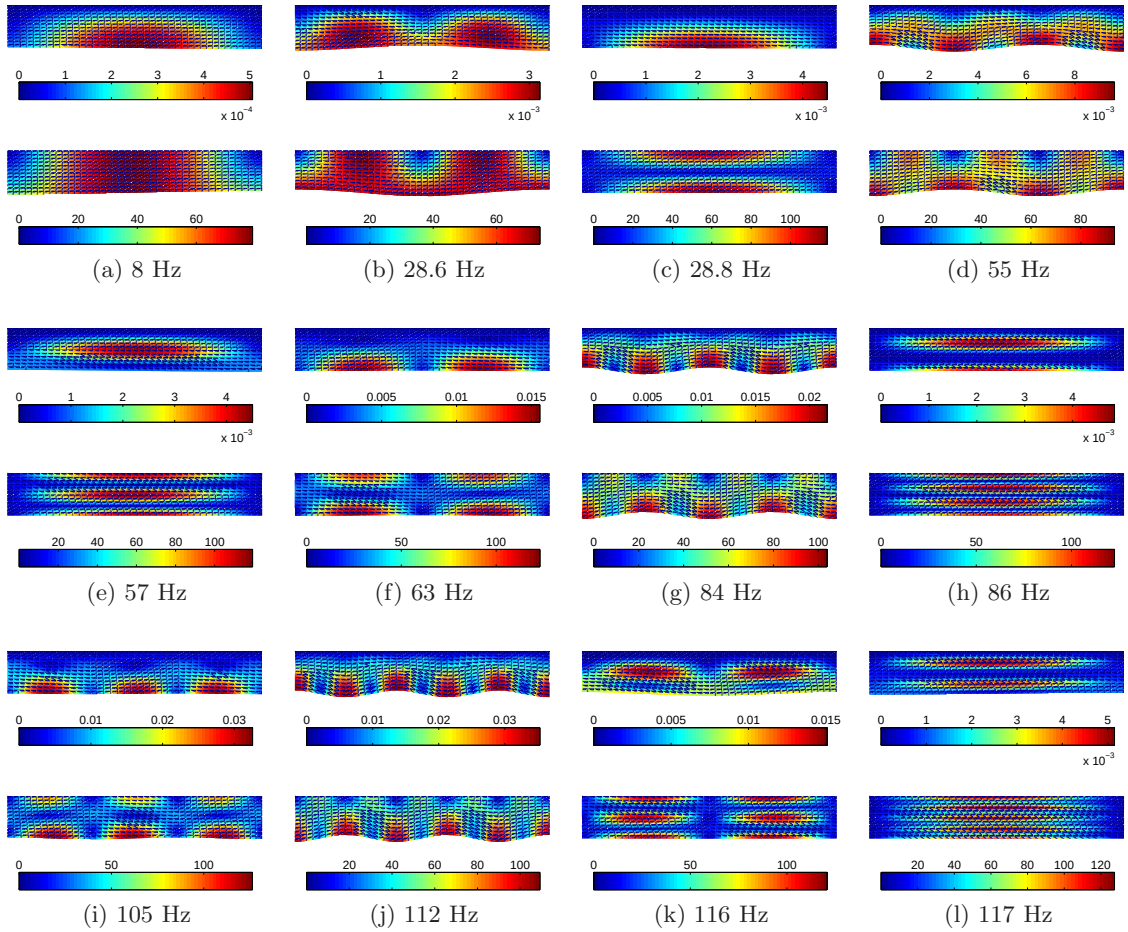

(a) 8 Hz (b) 28.6 Hz (c) 28.8 Hz (d) 55 Hz

(e) 57 Hz (f) 63 Hz (g) 84 Hz (h) 86 Hz

(i) 105 Hz (j) 112 Hz (k) 116 Hz (l) 117 Hz

Figure 4.13: Porous 2D mode shapes: solid (top) and fluid (bottom) phases. Deformed mesh and norm of displacement.

conservative value of 0.4 (in the case of 2D applications) for the cumulated contributions indicator, $\chi_{\max}$. One mode is included in the modal basis for the computation of the residual vectors. Furthermore, two residual vectors are computed at 150 Hz and 500 Hz respectively. Applying the proposed sorting and filtering method results in a modal basis of 158 eigenvectors of which 67 are orthogonal. These imply 67 modal coordinates that can be further condensed according to Section 3.3.3. A comparison of the computational times for this problem is given in Fig. 4.15. The outputs of both the porous-treated cavity and the rigid acoustic cavity (real-valued problem) are given. The former one gives the reference computation time to be improved for the considered problem, while the latter gives an unreachable lower bound for a reduced solution. In between, the computational times of the reduced problem using the complete set of 800 modes and the reduced set of 158 selected eigenvectors are presented. Each of these two results are completed with the

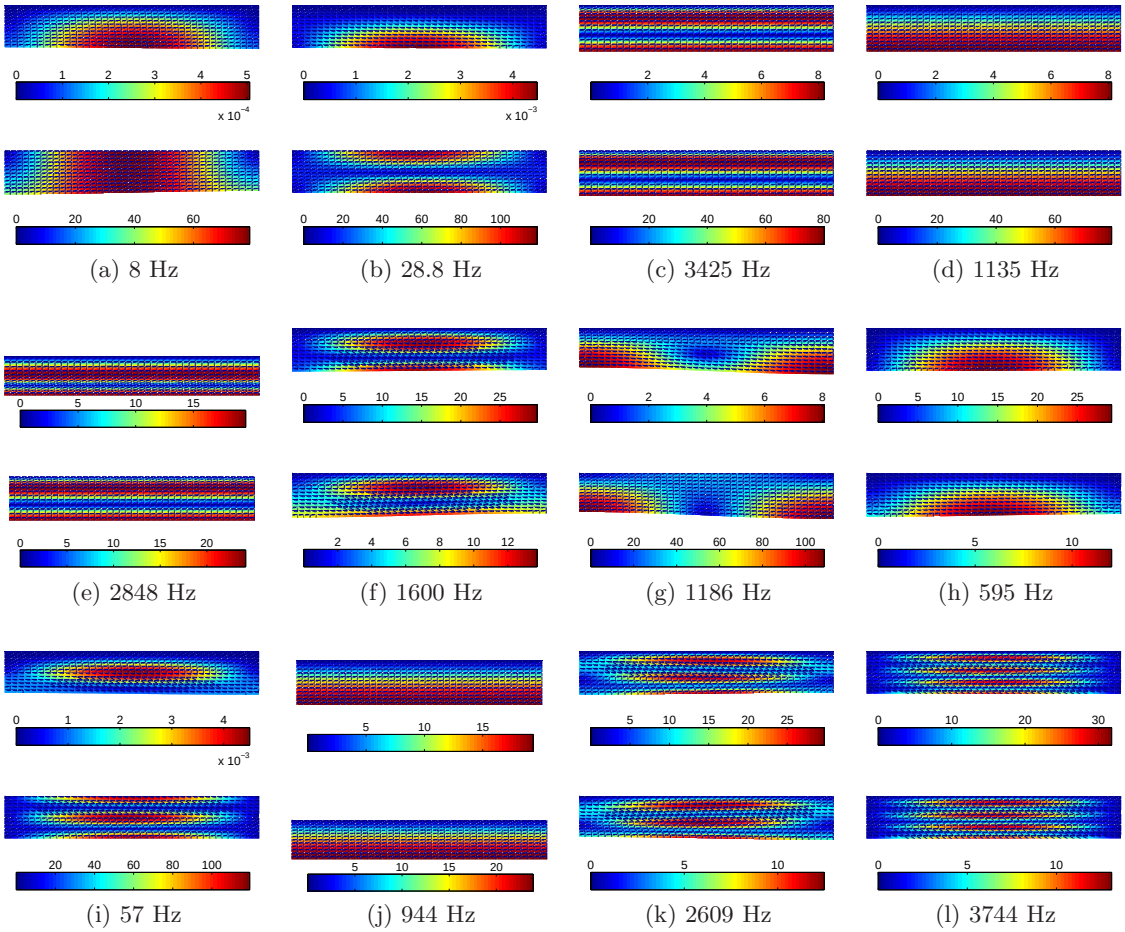

(a) 8 Hz (b) 28.8 Hz (c) 3425 Hz (d) 1135 Hz

(e) 2848 Hz (f) 1600 Hz (g) 1186 Hz (h) 595 Hz

(i) 57 Hz (j) 944 Hz (k) 2609 Hz (l) 3744 Hz

Figure 4.14: Porous 2D selected and sorted mode shapes: solid (top) and fluid (bottom) phases. Deformed mesh and norm of displacement.

corresponding version where orthogonal modes are further condensed at each frequency increment.

Several points can be underlined out of the plotted computational time improvements. First, considering the offset at the initial frequency increment for the reduced models, it appears clearly that the selection procedure proposed is comparatively costless. This is emphasized when compared to the time needed to compute the original modal basis. Secondly, although not showing reduction as spectacular as a 800-mode to 158-mode basis, the time enhancement is shown to be very significant, from 348 seconds for the original basis, to 250 seconds with the filtered basis, representing a 28% improvement. Off course, the fact that the 1872 acoustic dofs are kept unreduced has to be considered as a partial explanation. In addition, the reduction in the number of modes has, at some point, relatively less impact than keeping the number of attachment functions unchanged,

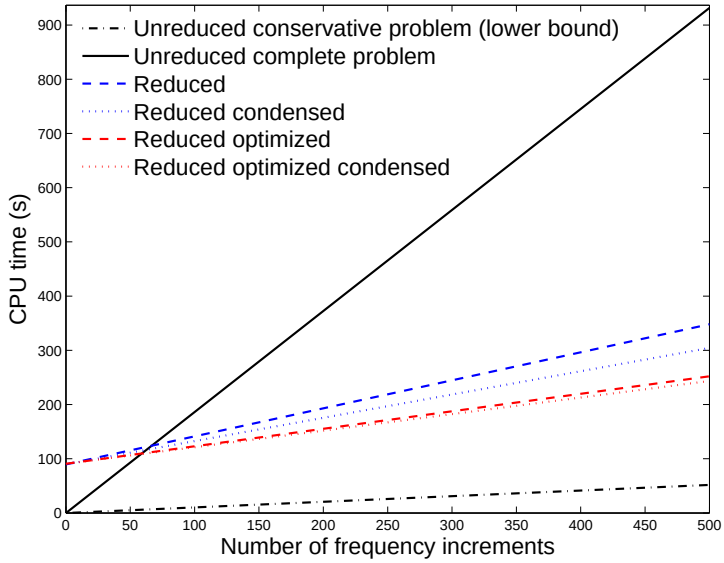

Figure 4.15: Computation time comparison for 3D problem - $\chi_{\max} = 0.4$

considering they fully couple the interface dofs and the porous modal coordinates. This point is well illustrated when observing the sparsity of the unreduced and reduced problems (Fig. 3.15 and 4.16). Finally, the condensation of modal coordinates corresponding to linearly independent porous equations appears less interesting as fewer modes are included in the basis. In fact, for smaller systems to be solved at each frequency increment, the efficiency of the condensation becomes very dependent on the implementation of the matrix manipulations involved at each frequency increment.

The sparsity and the convergence issues are addressed on a further reduced problem for which the previously-found conservative value of 0.4 for $\chi_{\max}$ is not respected. Thus, for $\chi_{\max}$ set to 0.27, the precision achieved is found identical up to 900 Hz while slightly inferior above (it is reminded here that the original mesh is best suited for a solution up to 600 Hz). This criterion involves 83 modes included in the basis, of which 31 imply linearly independent porous equations.

The corresponding analysis of the system matrix sparsity is presented in Fig. 4.16, comparing the sparsity before and after applying the mode selection procedure. It clearly shows, in this application, that the coupling involved by the 117 attachment functions at the interface acoustic dofs has a larger contribution to the solution cost than the remaining 83 porous modal dofs. This means that use of a reduced set of attachment functions, especially in the case of large interfaces, is an important asset in complement of the modal reduction itself. Several contributions can be found in the literature on this topic [102, 104], and applying interface condensation techniques is considered as an extension to this work.

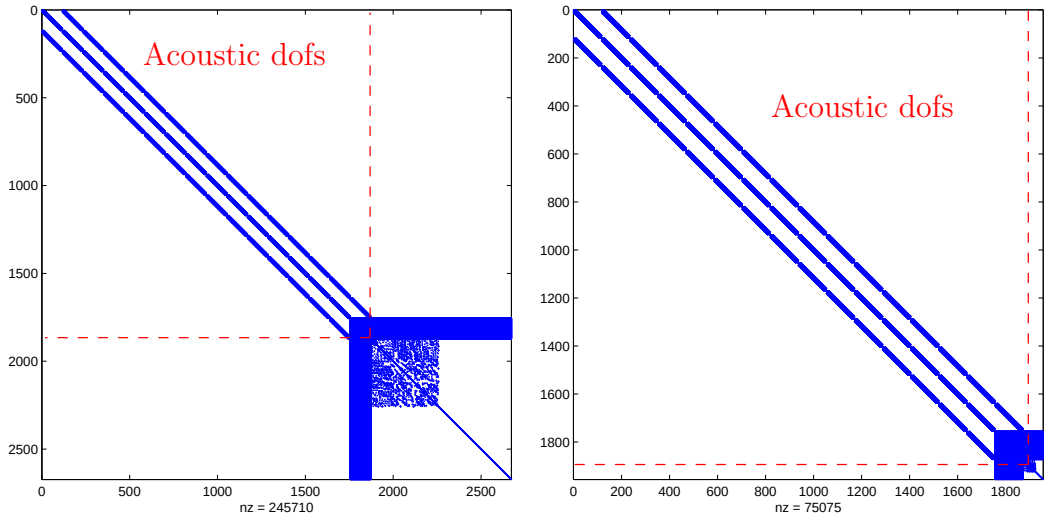

(a) (b)

Figure 4.16: Sparsity of the system matrix before and after mode selection procedure: (a) 800 modes, (b) 83 modes

The sparsities corresponding to the porous modal coordinates submatrices are further detailed in Fig. 4.17. These detailed views of the sparsity after modal transformation of

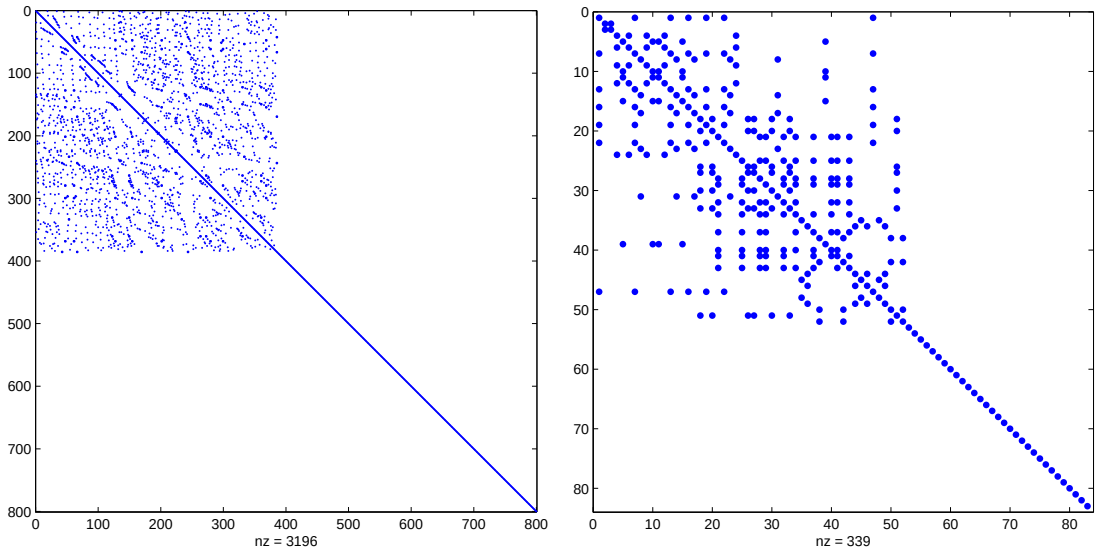

(a) (b)

Figure 4.17: Detailed sparsity corresponding to the modal dofs, before and after mode selection procedure: (a) 800 modes, (b) 83 modes

the porous equations underline its potential in the prospect of scaling the method to larger

problems. The further selection of significant modal contributions allows both reduction of the computational time, but also saves a tremendous amount of memory allocated to the system matrix. For instance, in the considered application, the storage allocated to the porous subdomain after modes selection represents a little more than 10% of the original reduction. It also illustrates the proportion of linearly independent equations kept in the process, which is a key point for the efficiency at larger scales.

The combined analysis of the computational time and the sparsity of the reduced matrices illustrate the very promising performances of the two-step reduction method proposed. Furthermore, two aspects are emphasized in the aim to further improve the reduction procedure: first, the number of attachment functions has to be kept small as previously mentioned; then, the initial computation of the modal basis is a drawback for further improvements, especially in the scope of larger applications. Regarding this second aspect, using efficient strategies such as the Automated Multi-Level Substructuring (AMLS) method [119], to generate approximate eigenvectors, could bring substantial improvements. Another possibility is to consider a more specific way of computing the needed eigenvectors, thus reducing the initial number of modes in the basis. Load-dependent Ritz vectors generated iteratively is one way to possibly enhance this initial step [120].

Finally, the convergence issue, which is however less critical than the precision and efficiency assets, is addressed for this 3D example. Fig. 4.18 illustrates the reduced solution obtained with $\chi_{\max}$ set to 0.27, compared to the reference solution, at significant numbers of modes included in the basis. When compared to Fig. 3.14, the results confirm what is observed for the 2D applications: the mode selection procedure improves the sorting, and therefore the smooth convergence observed with respect to the frequency. The direct consequence of this property is that if the selection upper bound $\chi_{\max}$ was to be chosen too small, the consequences would affect only the higher frequency range of the considered problem. This places the proposed modal reduction for sound absorbing porous domains in the same context of use as traditional modal-based methods for conservative media.

4.6 Conclusion

This chapter addressed part of the limitations raised in the previous chapter, i.e., regarding convergence issues for the proposed modal approach to reduce poroelastic domains.

For this purpose, a sorting procedure was proposed for the modes previously selected in a truncated modal basis using a standard approximate CMS truncation criterion. This procedure is based on the modes participation to the content of a poroelastic residual force calculated from a poor approximate solution. Typically, this poor approximate solution is

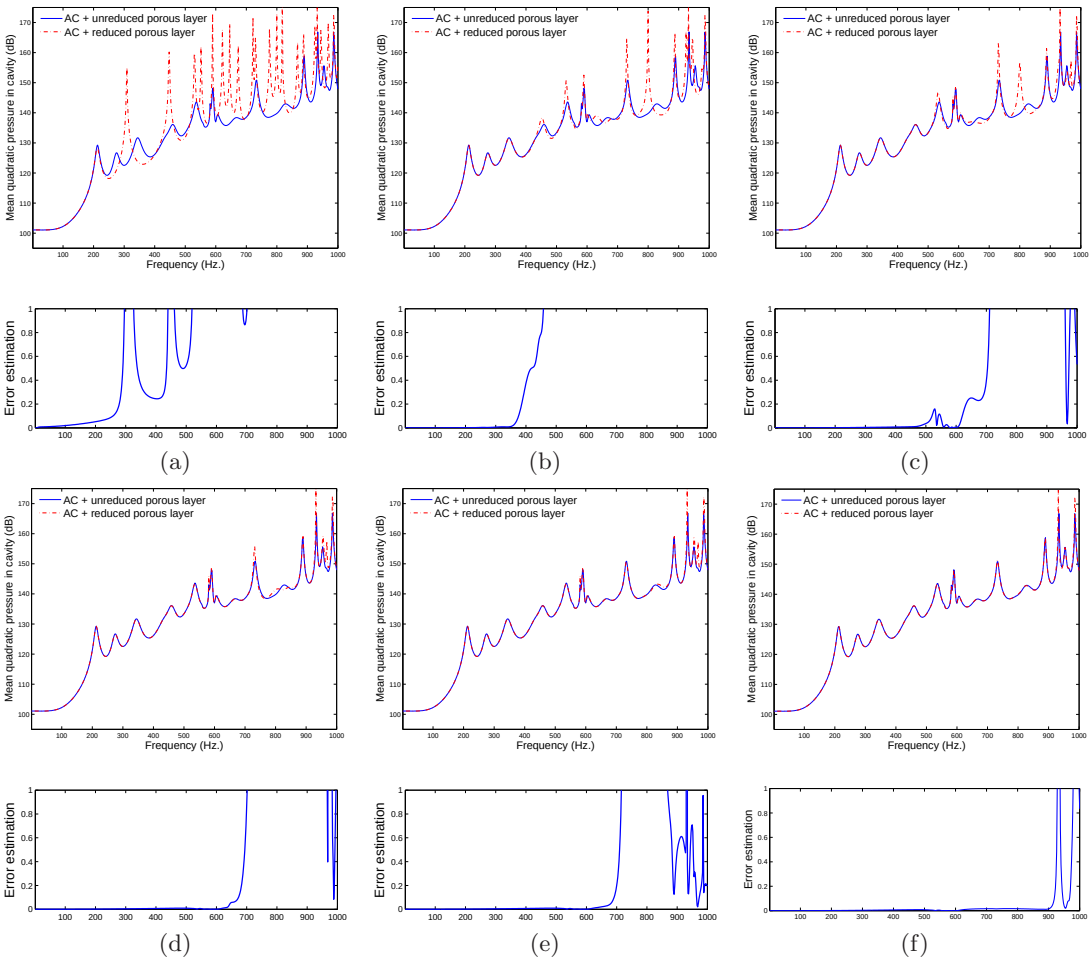

Figure 4.18: Convergence with modal superposition of selected modes for $\chi_{\max} = 0.27$: (a) 2 modes, (b) 35 modes; (c) 58 modes; (d) 71 modes; (e) 79 modes; (f) 83 modes

the outcome of a reduced model including the first, or the first few modes in the basis. An extension to more complex problems including a broader dynamic behaviour and frequency range was suggested. It involves a procedure based on multiple residual forces calculated at different frequencies in the spectrum. The procedure was shown to properly sort the modes according to their contribution in the frequency range of the response.

Furthermore, an empirical truncation criterion was introduced, thus defining a two-step truncation procedure to establish a suitable modal basis. The first truncation ensures that the dynamic content is included in the basis, while the second, after applying the sorting procedure, reduces the basis to its most significant components.

A validation case, including a performance analysis on a 3D academic problem, demonstrated the potential of the proposed approach: the procedure is costless when compared to the calculation of the modes, and exhibits promising performances in terms of stor-

age and computational efficiency. Furthermore, the modal basis thus established being equivalent to the modal bases used in CMS techniques for conservative problems, it can benefit from all the proposed modulations in the literature, among which: choice of different combinations of normal modes and interface functions, use of corrections to improve the convergence, use in a flexibility approach.

There are however a few points that were addressed only by perspectives to the present work, using methods proposed in the literature. First and most importantly, the initial step, which mostly consists in solving the eigenvalue problem, remains a drawback for extension to larger and more complex applications. For this purpose, an iterative approach could offer the perspective to improve the construction of the optimal basis. Secondly, porous materials are usually included into sound packages involving multilayer setups. Therefore, the reduction of the number of interface functions is of prime importance in order not to lose the benefits in high surface-to-volume ratio configurations. The last mentioned point concerns the extension to more complex cases. In fact, following the validations made on small 2D and 3D poro-acoustic applications, the proposed approach needs to be tested on more industrial-like problems.

Chapter 5

Use of Padé approximants for the fast reconstruction of frequency responses

Abstract: *In this chapter, an efficient solution strategy combining a modal-reduced problem with a Padé-based reconstruction approach is proposed. It thus takes advantage of the reduced-size of the model while further improving the computational efficiency by limiting the number of frequency resolutions of the original problem. An adaptive procedure is proposed, and the validation is presented on the poro-acoustic examples introduced in the previous chapters.*

Contents

5.1 Introduction

The modal-based approach proposed in the previous chapters offers a substantial reduction in the size of the problems to solve, even though hampering the sparsity of the system matrix. In fact, the use of interface functions, inducing coupled sets of equations for each subdomain, limits the computational efficiency improvements. The idea presented in this chapter is to take advantage of the reduction achieved in the number of dofs, while limiting the impact of the loss in sparsity. This is done by limiting the number of direct computations, using a reconstruction strategy.

For this purpose, a reconstruction based on Padé approximants offers a possible good complement, involving the computations of the complete solution and its derivatives at a very restricted number of frequencies, and rebuilding it around these points. The reconstruction then involves as many small-sized problems as the number of dofs, which has proved efficient in the literature when applied to single field problems [121–123].

Consequently, the combination of the two complementary methods can potentially take advantage of the best out of each of them, to offer an efficient solution scheme.

The chapter is organized around four main sections. First, a general presentation of the Padé approximant reconstruction method is given, followed, in a second part, by the derivations needed for its application to coupled poro-acoustic problems. In a third section, an adaptive procedure is proposed in order to automatically handle the choice of frequencies at which the complete solution is calculated. The last section is dedicated to the applications of the approach to the 1D, 2D and 3D poro-acoustic problems presented in the previous chapters.

5.2 Series expansion and Padé approximants

5.2.1 Padé approximants

All the problems studied in the present thesis, excited via time-harmonic excitations, exhibit the following general form,

$$\mathbf{Z}(\omega)\mathbf{u}(\omega) = \mathbf{f}(\omega), \tag{5.1}$$

where $\mathbf{f}(\omega)$ has been made frequency-independent in the considered examples, but this comes as a minor simplification in the upcoming developments. More importantly, the frequency-dependence of the system matrix $\mathbf{Z}(\omega)$ is carried by scalar functions in factor of frequency-independent global finite element matrices. This point, which proves its importance in this section, strengthens the choices made to use a displacement-displacement formulation for the porous media in comparison to a displacement-pressure formulation.

In a direct solution scheme, computing the full solution of Eq.(5.1) at a few frequency points only, while reconstructing an approximated solution in between those, has proved to be an efficient approach [122]. Thus, given a solution at angular frequency ω_0, and a sufficiently smooth function of ω, $\mathbf{u}(\omega)$, the Taylor series expansion around ω_0 gives such an approximated solution,

$$\mathbf{u}(\omega_0 + \Delta\omega) \approx \mathbf{A}_T(\Delta\omega) = \sum_{k=0}^{T} \mathbf{a}_k (\Delta\omega)^k, \tag{5.2}$$

with T being the truncation order of the series expansion. The coefficient vector $\mathbf{a}_k$ is given by

$$\mathbf{a}_k = \frac{\mathbf{u}^{(k)}(\omega_0)}{k!}, \tag{5.3}$$

where $\mathbf{u}^{(k)}(\omega_0)$ is the k^{th} derivative of $\mathbf{u}$ with respect to ω, taken at $\omega = \omega_0$, and considering that $\mathbf{u}^{(0)}(\omega_0) = \mathbf{u}(\omega_0)$. The determination of these T first derivatives of $\mathbf{u}$ is then required to estimate the approximated solution around ω_0.

However, in the scope of series expansion, it has been shown that, for a function containing poles, an expansion as a ratio of two power series generally allows a better representation (larger interval of convergence and better convergence rate) than Taylor series, for a given truncation order [124–126]. In the following, the one-point Padé approximation of $\mathbf{u}(\omega)$ is presented, deriving the methodology to determine the corresponding Padé approximants from the knowledge of system of equations (5.1). For this purpose, the vector quantities in equations (5.1) to (5.3), of dimension N (number of degrees of freedom), are now referred to as their j^{th} scalar component (corresponding to dof j). Furthermore, as there is no ambiguity on the fact that upcoming developments in this section are degree-of-freedom dependent, this indication is dropped in the rest of this section, so that

$$\mathbf{u} \quad \rightarrow u_j \rightarrow u, \tag{5.4a}$$

$$\mathbf{A}_T \rightarrow A_T^j \rightarrow A_T, \tag{5.4b}$$

$$\mathbf{a}_k \quad \rightarrow a_k^j \rightarrow a_k. \tag{5.4c}$$

Thus, each dof solution function, rather than being approximated by a Taylor series expansion, can be written as

$$u(\omega_0 + \Delta\omega) \approx \frac{P_L(\Delta\omega)}{Q_M(\Delta\omega)}, \tag{5.5}$$

with $P_L(\Delta\omega)$ and $Q_M(\Delta\omega)$ being two truncated power series in the variable $\Delta\omega$, to the

order L and M respectively, and defined as

$$P_L(\Delta\omega) = \sum_{k=0}^{L} p_k(\Delta\omega)^k, \tag{5.6a}$$

$$Q_M(\Delta\omega) = \sum_{k=0}^{M} q_k(\Delta\omega)^k. \tag{5.6b}$$

Similarly to the Taylor series expansion (5.2), the approximation to $u(\omega_0 + \Delta\omega)$ is given by the unique determination of the coefficients p_k and q_k. These coefficients can be determined in several ways [125], but a straightforward approach is to consider the Padé approximation as a re-arrangement into a rational function of the Taylor series expansion (5.2) to the order $L + M$. Follows that the p_k and q_k coefficients are solution of a system of linear equations established from the constraint

$$A_{L+M}(\Delta\omega) = \frac{P_L(\Delta\omega)}{Q_M(\Delta\omega)}. \tag{5.7}$$

The system of equations arises from the following rewriting of the constraint,

$$P_L(\Delta\omega) - A_{L+M}(\Delta\omega)Q_M(\Delta\omega) = 0, \tag{5.8}$$

where the coefficients of equal order in $\Delta\omega$ are extracted to form a set of $(L + M + 1)$ equations. In the form of Eq. (5.8), the linear system of equations allows zeros for $Q_M(\Delta\omega)$, which makes it more suited to account for resonances in the original frequency response. However, this underdetermined system of equations (5.8) gives only a solution of the $(L + M + 2)$ coefficients to within a multiplicative constant. Therefore, these are usually normalized so that the zero-order coefficient of the denominator, q_0, is set to 1 [125]. Subsequently, the following set of equations arises,

$$\left.\begin{aligned}
p_0 &= a_0 \\
p_1 - a_0 q_1 &= a_1 \\
&\vdots \\
p_L - a_{L-1}q_1 - \cdots - a_0 q_L &= a_L \\
-a_L q_1 - a_{L-1}q_2 - \cdots - a_{L-M+1}q_M &= a_{L+1} \\
&\vdots \\
-a_{L+M-1}q_1 - a_{L+M-2}q_2 - \cdots - a_L q_M &= a_{L+M}
\end{aligned}\right\}, \tag{5.9}$$

where

$$\begin{cases} a_k &= 0 \text{ if } k < 0 \\ q_k &= 0 \text{ if } k > M \end{cases}.$$

Following Eqs. (5.3) and (5.4), giving the expression of the coefficients $a_k = \dfrac{u^{(k)}(\omega_0)}{k!}$, the system of equations (5.9) can be written explicitly involving the $(L+M)$ first derivatives of $u(\omega)$ at ω_0,

$$k!\, p_k - \left(\sum_{l=1}^{k} \binom{k}{l}\, l!\, u^{(k-l)}(\omega_0) q_l \right) = u^{(k)}(\omega_0), \text{ for } k = 0, \ldots, L+M, \tag{5.10}$$

with

$$\begin{cases} p_k & = 0 \text{ if } k > L \\ q_l & = 0 \text{ if } l > M \end{cases},$$

and where the binomial coefficients are given by

$$\binom{k}{l} = \frac{k!}{l!(k-l)!}. \tag{5.11}$$

This set of equations can be solved numerically in a matrix form, for each degree of freedom j, thus involving the solution of N small problems of dimension $(L+M+1)$,

$$[\mathbf{A}]^{(j)} \begin{bmatrix} p_0 \\ \vdots \\ p_L \\ q_1 \\ \vdots \\ q_M \end{bmatrix}^{(j)} = \begin{bmatrix} u(\omega_0) \\ \vdots \\ u^{(L)}(\omega_0) \\ u^{(L+1)}(\omega_0) \\ \vdots \\ u^{(L+M)}(\omega_0) \end{bmatrix}^{(j)}, \text{ for } j = 1, \ldots, N. \tag{5.12}$$

Based on the solution at one point, $\mathbf{u}(\omega_0)$, this method is referred to as the single-point Padé approximation in the literature. It can be easily extended to several points, as presented for instance in [122]. The aim being to estimate the combination of such an approach with the reduced models established in this thesis, use of multi-point Padé approximations is considered as a natural extension to the present work.

Similarly to an approximation of the solution using Taylor series expansion, the resolution of systems of equations (5.12) requires the determination of the $(L+M)$ derivatives of the solution vector $\mathbf{u}(\omega)$ at ω_0. This aspect is developed in the following section.

5.2.2 Successive derivatives of the solution vector

The successive $(L+M)$ derivatives of $\mathbf{u}$ at angular frequency ω_0 can be derived from differentiating Eq. (5.1) with respect to ω. At the order k of differentiation, the following expression arises,

$$\sum_{j=0}^{k} \binom{k}{j} \mathbf{Z}^{(k-j)}(\omega_0)\, \mathbf{u}^{(j)}(\omega_0) = \mathbf{f}^{(k)}(\omega_0), \text{ for } k = 1, \ldots, (L+M), \tag{5.13}$$

where the zero-order derivatives correspond to the non differentiated functions. Extracting the highest-order term from the summation in Eq. (5.13) leads to the following recursive expression of the k-order derivative of $\mathbf{u}$ at ω_0,

$$\mathbf{Z}(\omega_0)\,\mathbf{u}^{(k)}(\omega_0) = \mathbf{f}^{(k)}(\omega_0) - \sum_{j=0}^{(k-1)} \binom{k}{j} \mathbf{Z}^{(k-j)}(\omega_0)\,\mathbf{u}^{(j)}(\omega_0), \text{ for } k = 1, \ldots, (L+M). \quad (5.14)$$

This implies that the successive derivatives of $\mathbf{u}$ required for the determination of the Padé approximations can be efficiently computed as the solution of a system of equations of dimension N, with multiple right-hand sides. In fact, the resolution can be performed by direct methods using a decomposition of the system matrix. The factorization, as the most time-consuming step of the solution, needs to be done once initially, providing very efficient multiple solutions of the system. Regarding the multiple right-hand side vectors, they are built from derivatives of the system matrix and lower-order-derivatives of the solution vector. The choices made in this thesis, particularly regarding the poroelastic formulation where frequency-dependence is borne by scalar functions, imply inexpensive operations to establish the right-hand side vectors.

5.2.3 Procedure for frequency response reconstruction using Padé approximants

This section summarizes the steps involved in the computation of the approximate multi-frequency solution using Padé approximation. They can be separated into two sets, corresponding to the two previous sections taken in a reversed order:

- First, at a given angular frequency ω_0, the solution as well as its successive derivatives to the order $(L+M)$ are computed according to Eq. (5.14). This implies, for each frequency around which the solution is to be approximated, the resolution of $(L+M+1)$ problems of dimension N in a multiple right-hand side scheme.
- Then, the solution around ω_0 is reconstructed, involving the resolution of N problems of dimension $(L+M+1)$ (Eq. (5.12)) to determine the Padé approximants corresponding to each degree of freedom. Follows N trivial rational fraction evaluation (Eq. (5.5)) for each $\Delta\omega$ at which the approximated solution is to be evaluated.

Given a discretization of the frequency space into intervals associated with their central angular frequency, the corresponding detailed procedure for one frequency interval is presented in Algorithm 2.

Three points can be further discussed regarding the given description of the procedure. The first one consists in choosing the coarse frequencies at which the solution will be

Algorithm 2 Steps for multi-frequency Padé approximation around angular frequency ω_0

1. Compute system matrix decomposition of Eq. (5.1) at ω_0
2. Solve Eq. (5.1) for solution $\mathbf{u}(\omega_0)$
3. **for** $j = 1$ **to** $L + M$ **do**
4. Solve Eq. (5.14) for solution derivative $\mathbf{u}^{(j)}(\omega_0)$
5. **end for**
6. **for** $j = 1$ **to** N **do**
7. Solve Eq. (5.12) for dof-dependent Padé approximants
8. Evaluate approximate multi-frequency solution around ω_0, Eq. (5.5)
9. **end for**

evaluated, i.e. setting an appropriate discretization of the frequency space. Secondly, for each coarse frequency, the order of polynomial expansions and the frequency range of evaluation around ω_0 have to be chosen accordingly, which raises the question of the values of L and M. Thirdly, one has to estimate the conditions of efficiency of such an approximation scheme.

Although the second and third points are thoroughly discussed by Avery et al. in [122], for single field structural or acoustic applications, the choice of coarse frequencies has, to the knowledge of the author, not been been given much attention in the literature. A suggestion is made in this sense in Section 5.4 of the present work. Regarding the order of polynomial expansions to consider for both the numerator (L) and the denominator (M) in Eq. (5.5), the following constraint, suggested in [122], reduces the set of possibilities, giving satisfying approximations:

$$M = L + 1. \tag{5.15}$$

Furthermore, there is an upper limit to the maximum order that can be set, due to the ill-conditioned matrix that arises from system of Eqs. (5.12). In the applications considered in this work, the upper limit was set to $L_{max} + M_{max} + 1 = 12$, thus imposing $L_{max} = 5$, $M_{max} = 6$. Consequently, depending on the frequency discretization chosen for a direct frequency sweep, the Padé-based approximation is expected to be most efficient if it is able to converge over several frequency increments around ω_0. The time allocated to solve several different linear systems of N equations is transferred to solving $(L+M+1)$ changing right-hand-side linear systems of N equations (1 decomposition, and $(L+M+1)$ solutions) as well as N systems of $(L + M + 1)$ equations, with $(L + M + 1) \ll N$. This has proved extremely efficient when applied to large single field structural or acoustic applications, with an a priori set frequency discretization of the frequency space [121, 122].

In the following, two extensions to this approach are considered: application of the method to *i)* a coupled problem such as the poro-acoustic example considered in the previous chapter, on which an adaptive frequency discretization scheme is tested, and *ii)*,

a modal-based reduced version of this system of equations, thus estimating the trade-off between the information lost via the reduction and the precision needed to establish successive derivatives of the solution. The latter situation potentially presents an interest in the situation where, e.g., a reduced-model would be mostly advantageous for memory allocation purposes, while the Padé-based reconstruction would allow substantial computational time enhancements.

5.3 Application to the poro-acoustic problem

In this section, the 3D poro-acoustic application presented in Section 3.4.2 is considered. Simplified notations are introduced in order to establish the applicability of the Padé-based reconstruction scheme both to the non-reduced and reduced set of equations.

5.3.1 Notations

The previously established sets of equations, both for the non-reduced (symmetrized version of system (3.19)) and the reduced (Eq. (A.11)) problems, can be expressed as the following frequency-dependent form, for $\omega \neq 0$,

$$\left(\frac{1}{\omega^2}\mathbf{K}_{\mathrm{F}} + \mathbf{K}_{\mathrm{P}}^{(1)} + \left(\widetilde{K}_{\mathrm{f}}(\omega) - P_0\right)\mathbf{K}_{\mathrm{P}}^{(2)} + \mathrm{i}\,\omega\,\widetilde{b}(\omega)\,\mathbf{C}_{\mathrm{P}} - \omega^2\mathbf{M}_{\mathrm{P}}\right)\mathbf{X} = \mathbf{F}, \tag{5.16}$$

where $\mathbf{K}_{\mathrm{F}}$, $\mathbf{K}_{\mathrm{P}}^{(1)}$, $\mathbf{K}_{\mathrm{P}}^{(2)}$, $\mathbf{C}_{\mathrm{P}}$ and $\mathbf{M}_{\mathrm{P}}$ are symmetric, frequency-independent and real-valued matrices. They include the acoustic "stiffness" for $\mathbf{K}_{\mathrm{F}}$, the acoustic "mass", the poro-acoustic coupling terms together with the zero-frequency porous stiffness limit for $\mathbf{K}_{\mathrm{P}}^{(1)}$, while $\mathbf{K}_{\mathrm{P}}^{(2)}$, $\mathbf{C}_{\mathrm{P}}$ and $\mathbf{M}_{\mathrm{P}}$ correspond to the porous matrices introduced in Chapter 3. In the following, these global assembled matrices refer to either their non-reduced or reduced form. According to the previous section notations, we have

$$\mathbf{Z}(\omega) = \frac{1}{\omega^2}\mathbf{K}_{\mathrm{F}} + \mathbf{K}_{\mathrm{P}}^{(1)} + \left(\widetilde{K}_{\mathrm{f}}(\omega) - P_0\right)\mathbf{K}_{\mathrm{P}}^{(2)} + \mathrm{i}\,\omega\,\widetilde{b}(\omega)\,\mathbf{C}_{\mathrm{P}} - \omega^2\mathbf{M}_{\mathrm{P}}, \tag{5.17}$$

which underlines another benefit of the choice made for the poroelastic formulation. In fact, having the system matrix frequency-dependence borne by scalar functions simplifies and enhances the application of the Padé approximation compared to a formulation for which matrix derivatives would have to be considered. For instance, use of a displacement-pressure poroelastic formulation, known to be computationally efficient, would imply solid and fluid phase-dependent derivatives, thus involving a more complex implementation of the reconstruction scheme.

5.3.2 Expression of useful function derivatives

In order to apply the procedure described in Section 5.2.3, the successive derivatives of $\mathbf{Z}$ (as presented in Eq. (5.17)) with respect to ω are needed to calculate the right-hand-side vectors in Eq. (5.14). They involve derivatives of four frequency-dependent scalar functions. Among them, $\widetilde{K}_{\mathrm{f}}(\omega)$ and $\omega\,\widetilde{b}(\omega)$, the only non-trivial derivatives, are discussed in this section. The former, introduced in Eq. (1.20), exhibits no compact analytic form of its k^{th} derivative. It is thus numerically calculated, tabulated, and referred to as $\widetilde{K}_{\mathrm{f}}^{(k)}$ in the following. Regarding $\omega\,\widetilde{b}(\omega)$, the viscous drag expression being given in Eq. (1.13), it can be written in the following form,

$$\omega\,\widetilde{b}(\omega) = A\omega\,(1+iB\omega)^{\frac{1}{2}}\,, \tag{5.18}$$

with

$$A = \sigma\phi^2, \tag{5.19a}$$

$$B = \frac{4\alpha_\infty^2\eta\rho_{\mathrm{f}}}{\sigma^2\Lambda^2\phi^2}. \tag{5.19b}$$

Follow the derivatives of $\omega\,\widetilde{b}(\omega)$,

$$\left(\omega\,\widetilde{b}(\omega)\right)^{(1)} = A\,(1+iB\omega)^{\frac{1}{2}} + i\,\frac{AB\omega}{2}\,(1+iB\omega)^{-\frac{1}{2}}\,, \tag{5.20a}$$

$$\begin{aligned}\left(\omega\,\widetilde{b}(\omega)\right)^{(k)} = {} & (-i)^{k-3}\,\frac{k}{4^{k-2}}\,\frac{|2\,(k-3)+1|!}{|(k-3)|!}AB^{k-1}\,(1+iB\omega)^{-\frac{2(k-2)+1}{2}} + \\ & (-i)^{k-2}\,\omega\,\frac{1}{4^{k-1}}\,\frac{(2\,(k-2)+1)!}{(k-2)!}AB^{k}\,(1+iB\omega)^{-\frac{2(k-1)+1}{2}} \quad \text{for } k\geq 2\end{aligned} \tag{5.20b}$$

Given $\left(\omega\,\widetilde{b}(\omega)\right)^{(k)}$ from Eq. (5.20), and the tabulated expressions of $\widetilde{K}_{\mathrm{f}}^{(k)}$, the k^{th} derivative of $\mathbf{Z}(\omega)$ for the poro-acoustic problem is given by,

$$\mathbf{Z}(\omega)^{(k)} = \begin{cases} (-1)^k\,(k+1)!\dfrac{1}{\omega^{k+2}}\mathbf{K}_{\mathrm{F}} + \widetilde{K}_{\mathrm{f}}^{(k)}\mathbf{K}_{\mathrm{P}}^{(2)} + \mathrm{i}\,\left(\omega\,\widetilde{b}(\omega)\right)^{(k)}\mathbf{C}_{\mathrm{P}} - 2\omega\mathbf{M}_{\mathrm{P}} & \text{for } k=1 \\ (-1)^k\,(k+1)!\dfrac{1}{\omega^{k+2}}\mathbf{K}_{\mathrm{F}} + \widetilde{K}_{\mathrm{f}}^{(k)}\mathbf{K}_{\mathrm{P}}^{(2)} + \mathrm{i}\,\left(\omega\,\widetilde{b}(\omega)\right)^{(k)}\mathbf{C}_{\mathrm{P}} - 2\mathbf{M}_{\mathrm{P}} & \text{for } k=2 \\ (-1)^k\,(k+1)!\dfrac{1}{\omega^{k+2}}\mathbf{K}_{\mathrm{F}} + \widetilde{K}_{\mathrm{f}}^{(k)}\mathbf{K}_{\mathrm{P}}^{(2)} + \mathrm{i}\,\left(\omega\,\widetilde{b}(\omega)\right)^{(k)}\mathbf{C}_{\mathrm{P}} & \text{for } k>2 \end{cases} \tag{5.21}$$

5.4 Adaptive approach for decomposition into frequency intervals

In order to avoid setting an a priori choice of main frequencies at which the solution is estimated by a direct computation, a simple adaptive approach is proposed. It enables a discretization of the frequency space according to the estimated capability of the

reconstruction scheme adopted. This limits the lack of precision or the loss in computational efficiency that would be induced by a too coarse or too refined choice for the main frequencies. The present approach is based on two aspects: (i) controlling the error of the reconstructed solution using an error estimation, and (ii) using the frequency interval of convergence for each main frequency to anticipate the upcoming frequency interval of convergence.

First, the error estimation used to set a convergence criterion is similar to the one presented in Section 4.2. Considering the same poro-acoustic test cases in this chapter as in the previous one, the error due to the reconstruction approach is also estimated in the poroelastic domain. Thus, it can be expressed similarly to Eq. (4.4), considering $\widehat{\mathbf{U}}_{\mathrm{P}}$ as the approximated reconstructed solution for the poroelastic field at a given angular frequency $(\omega_0 + \Delta\omega)$. The residual force and displacement vectors also arise from the porous field solution at $(\omega_0 + \Delta\omega)$, according to Eqs. (4.2) and (4.3). It is to be noted, however, that in the case of a Padé reconstruction based on a reduced system of equations for the porous part of Eq. (5.16), the matrices $\mathbf{K}_{\mathrm{P}}^{(1)}$, $\mathbf{K}_{\mathrm{P}}^{(2)}$, $\mathbf{C}_{\mathrm{P}}$ and $\mathbf{M}_{\mathrm{P}}$ in Eqs. (4.2)-(4.4) have to be taken as their modal-reduced version. Again, the estimated error is compared to a given limit ε_{max} under which the approximated solution is considered sufficiently converged. In agreement with Section 4.2, this limit is set to 0.1 for the poroelastic domain.

Secondly, as previously mentioned, it is assumed that the frequency interval of convergence for a given central frequency gives a good a priori estimation of the interval of convergence for the neighbor central frequency. This is of course a strong assumption, which might be very case-dependent. However, it is reinforced by the fact that, unlike the behavior of a Taylor series expansion out of their convergence interval, an approximation by rational function of power series exhibits a rather smooth divergence. Consequently, an underestimated interval of convergence hinders the computational efficiency by potentially increasing the number of central frequencies needed, whereas an overestimated interval of convergence implies non-contiguous converged intervals which might still render a sensible approximated solution in the gaps. Furthermore, it is also assumed that, given an increasing modal density for increasing frequencies, the interval of convergence is expected to decrease with increasing central frequencies. For these reasons, the adaptive reconstruction scheme is started from the higher frequency range, and propagated to the lower frequencies with a slight over-estimation of the intervals of convergence.

The successive steps, described in the following, are illustrated in Fig. 5.1.

(a) From the first central frequency corresponding to ω_0, in the higher end of the frequency range, the reconstruction procedure, described in Algorithm 2, is applied and combined with an error estimation of the approximated solution both towards the lower and the higher frequencies. When the convergence check, based on the error estimation, is not

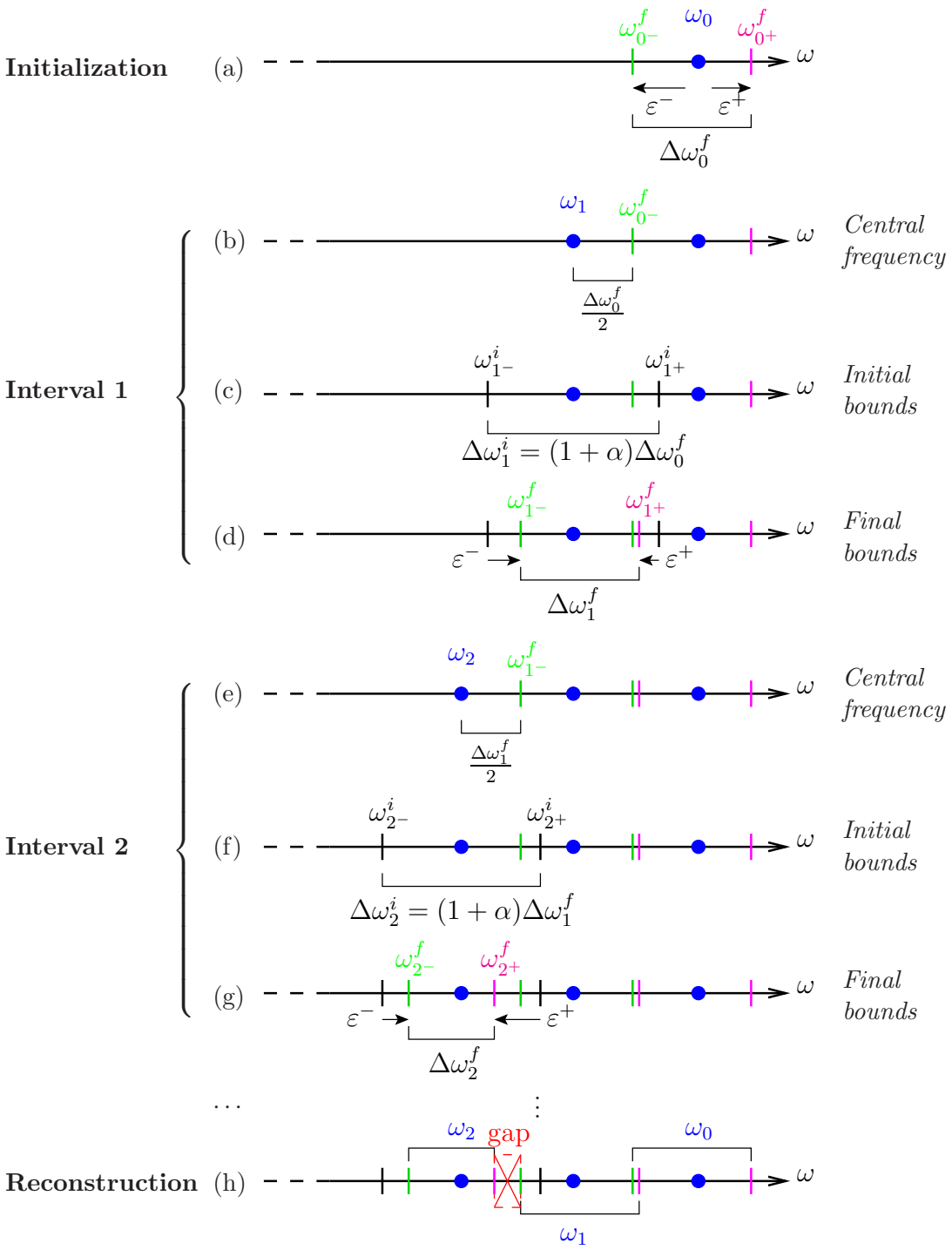

Figure 5.1: Adaptive frequency interval decomposition: blue: central frequency; magenta: upper limit; green: lower limit

satisfied anymore, the corresponding upper and lower limits $\omega_{0^+}^f$ and $\omega_{0^-}^f$ define the interval of convergence $\Delta\omega_0^f$ corresponding to the angular frequency ω_0 (the exponent f indicates the final version of these parameters, in contrast to the initial estimations, denoted by exponent i, introduced a priori for upcoming intervals). In the present approach, it is considered that the upper limit $\omega_{0^+}^f$ either exceeds the frequency domain of interest, or defines its upper bound.

(b) (resp. (e)) From the previously determined interval of convergence $\Delta\omega_0^f$ (resp. $\Delta\omega_1^f$), the central angular frequency ω_1 (resp. ω_2) associated with the lower-frequency contiguous interval is estimated. It is positioned half-a-convergence-interval $\frac{\Delta\omega_0^f}{2}$ (resp. $\frac{\Delta\omega_1^f}{2}$) lower than the lower limit $\omega_{0^-}^f$ (resp. $\omega_{1^-}^f$). Doing so, the anticipation of generally increasing intervals of convergence might lead to an overlap of two contiguous converged intervals. However, this choice is made in order to lower the risk of non-converged gaps between intervals (see Figure 5.1 (g) and (h)), appearing due to a locally reduced or asymmetric convergence interval.

(c) (resp. (f)) Once the main frequency is established, the upper and lower bounds for the interval, $\omega_{1^+}^i$ (resp. $\omega_{2^+}^i$) and $\omega_{1^-}^i$ (resp. $\omega_{2^-}^i$) respectively, are estimated a priori. They are determined assuming an interval centered on ω_1 (resp. ω_2), and of width $(1+\alpha)\Delta\omega_0^f$ (resp. $(1+\alpha)\Delta\omega_1^f$). The parameter α, which accounts for the anticipation of globally increasing intervals of convergence, is arbitrarily chosen in this work, typically smaller than 0.2. However, one could argue that α may be estimated considering the frequency-dependence of the modal density, as it relates to the expected number of discontinuities per convergence interval.

(d) (resp. (g)) When the upper and lower bounds are estimated, the reconstruction procedure described in Algorithm 2 is applied. Simultaneously, the error estimation check is done starting from the lower and higher bounds rather than the central frequency. In fact, it is expected to have less estimations to make when starting from the bounds than from the central frequency, provided the overestimation of the interval is sensible. The actual upper and lower limits of convergence, i.e. $\omega_{1^+}^f$ (resp. $\omega_{2^+}^f$) and $\omega_{1^-}^f$ (resp. $\omega_{2^-}^f$) respectively, are determined when the convergence check, based on the error estimation, is satisfied. While the mostly observed situation is that of overlapping contiguous convergence intervals (Figure 5.1(d)), a gap of non-converged reconstructed solution can arise (Figure 5.1(g) and (h)) as mentioned in (b).

In case of such gaps in the reconstructed solution, as illustrated in Fig. 5.1(h), two situations can arise. First, from the error estimations made for frequencies in the gap, and from the observed continuity of the solution at the upper bound of the gap, the approximated solution may be considered acceptable. This situation is likely possible due to the smooth

divergence of the Padé approximation out of its convergence interval, as illustrated in the results section. Otherwise, if a non acceptable discontinuity in the solution is manifest at the connection between the gap and the upper-frequency converged interval, an additional interval needs to be considered. The gap may still be appropriately bridged using an interpolation based on a third-order Hermite polynomial between the two bounds. In a more general case, the main frequency is then taken in the middle of the gap, and the reconstruction procedure is then applied, at a lower expansion order, to estimate the solution over the entire gap. The latter situation, even though probable in case of important overestimations of convergence intervals, is not considered in the present work where small values of α (typically $\alpha = 0.1$) have been taken into account. Furthermore, following the appearance of a gap, the converged interval width is presumably reduced compared to the previous established interval. This implies a reset of the overestimation to be made for upcoming intervals, and thus introduces another form of self-adaptation in the procedure. Successive gaps in the procedure consequently indicate that α is overestimated.

5.5 Results

The methods presented in the previous sections of this chapter are tested on simple poro-acoustic applications, introduced in Chapter 3. First, the impact of increasing the order of truncation is illustrated in the 1D and 2D poro-acoustic applications, together with a comparison, for the 1D case, of the precision achieved using a Taylor expansion of equivalent order. Furthermore, the influence of using Padé approximations on the modal-reduced set of equations is checked on these two examples. Then, the proposed adaptive approach is tested successively on the 2D and 3D versions of the poro-acoustic validation case.

5.5.1 Effect of order increase and approximation of a reduced model - 1D and 2D applications

First, the 1D poro-acoustic application introduced in Section 3.4.1 is used to illustrate the one-point Padé approximation presented in this chapter. In order to estimate the impact of increasing the order of truncation for the power series expansions, the entire frequency range is considered as one interval, whose main frequency is chosen as the middle frequency. The constraint $M = L + 1$ is applied, and L varies between 1 and 5. Furthermore, the procedure described in Algorithm 2 is applied both to the complete FE model, and to a model for which the poroelastic has been reduced following Sections 3.3.2 and 3.4.1. The porous modal basis includes 4 modes which proved satisfying for the mean quadratic pressure frequency response (Fig. 3.8). The results are presented in Fig. 5.2.

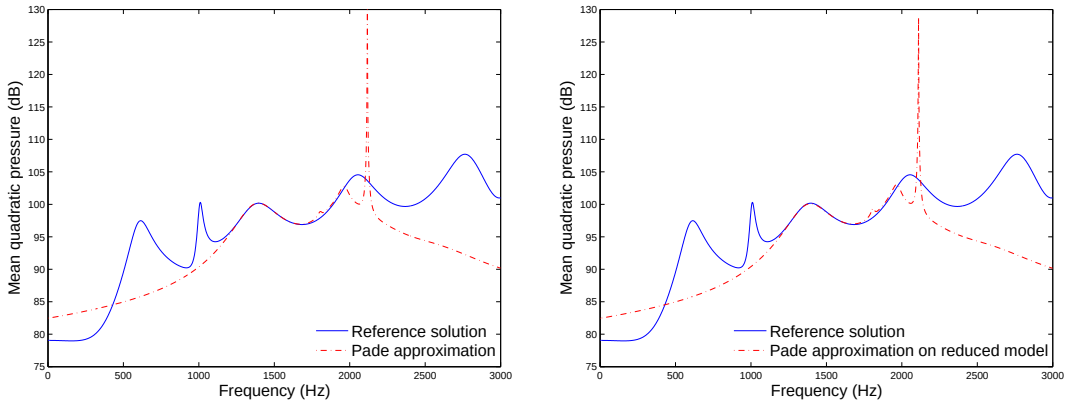

(a) $L = 1$; $M = 2$

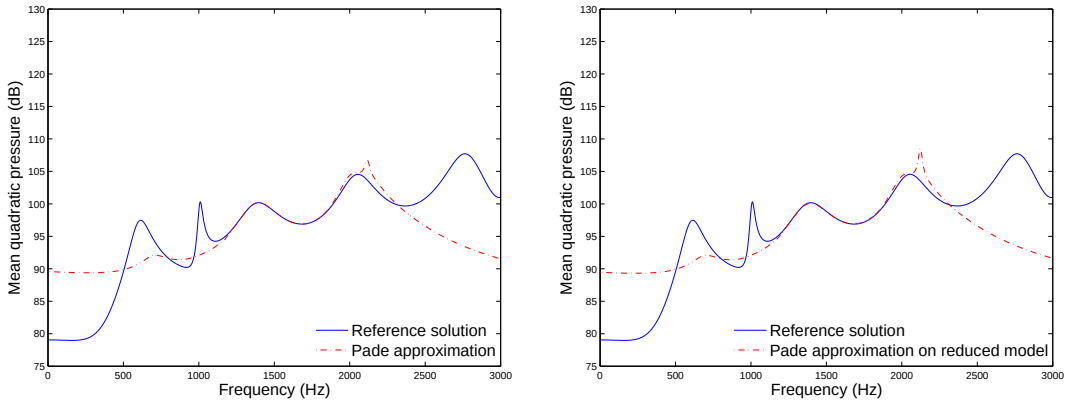

(b) $L = 2$; $M = 3$

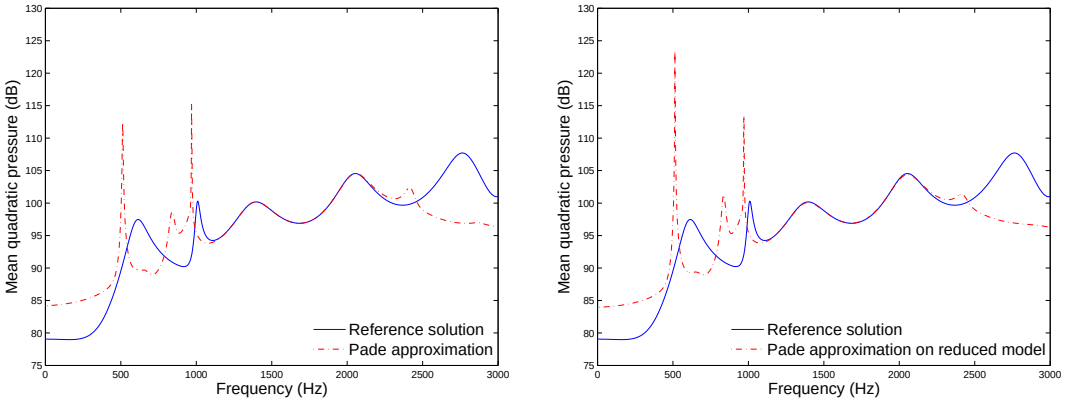

(c) $L = 3$; $M = 4$

Figure 5.2: Impact of increasing truncation order for power series - 1D poro-acoustic problem. Left: Padé on complete problem; Right: Padé on reduced problem.

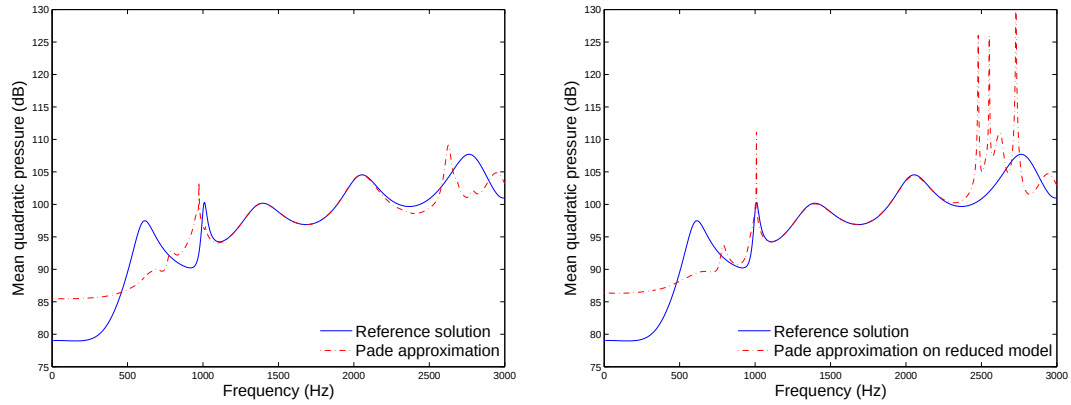

(d) $L = 4$; $M = 5$

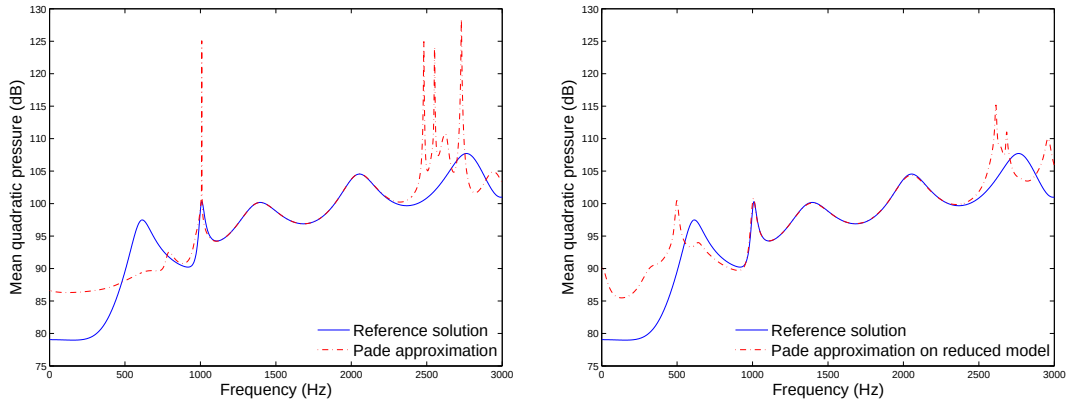

(e) $L = 5$; $M = 6$

Figure 5.2: Impact of increasing truncation order for power series - 1D poro-acoustic problem. Left: Padé on complete problem; Right: Padé on reduced problem.

Observing the convergence by increasing the order of truncation on the non-reduced set of equations (Fig. 5.2(a)-(e), left figures), illustrates quite well the potential of using the Padé approximants for reconstruction of the solution. In fact, at the 11^{th} order of truncation ($L = 5$, $M = 6$), an interval of almost 1250 Hz of width can be reconstructed from the solution and its derivatives at 1500 Hz. However, beside the fact that the Padé coefficient system to solve (Eq. (5.12)) becomes rapidly ill-conditioned for orders of truncation above 8 to 10, the convergence improvements prove very significant up to expansions ($L = 3; M = 4$), and slower for higher orders. This can be mostly observed at the upper-bound of the convergence interval for which the frequency response to approximate is a rather smooth function of the frequency (range from 2000 Hz to 2250 Hz). At that point, it is shown in [122] that a multi-point Padé approximation approach can become more efficient than an increase in the order of truncation. It is an important aspect of the method to notice that, as already mentioned, the divergence of the approximation immediately out of the convergence interval is fairly slow.

Considering the reconstruction procedure applied to the reduced set of equations (Fig. 5.2(a)-(e), right figures), it is interesting to notice that the approximation made in the modal-reduction step does not strongly affect the Padé-based reconstruction. In fact, from expansions $(L = 4; M = 5)$, the convergence interval seems to be slightly larger than its non-reduced problem equivalent, e.g. around the resonance observed at 1000 Hz. This trend has however not been reproduced for more complex problems such as the 2D problem considered in this section, or the 3D example treated in Section 5.5.3. The preserved convergence observed on this simple application is very promising for efficiency considerations of the method. Thus, for a reduced set of equations, less demanding in terms of memory allocation, the reduction in the number of sytems (5.12) to solve may partly compensate for the extra computational cost involved to establish the reduced system.

Furthermore, the precision achieved using a Padé approach rather than Taylor series is illustrated in Fig. 5.3 for this 1D application (without modal reduction). Orders of truncation corresponding to those applied with the Padé approach in Fig. 5.2 are used. The comparison clearly demonstrates the limitations in terms of interval of convergence using Taylor series, as well as the rapid divergence of the approximation out of this interval.

Similarly to what is done on the 1D poro-acoustic application, the larger 2D poro-acoustic application introduced in Section 4.5.2 is used to illustrate the convergence of the approximation around one central frequency. Following the study made in Section 4.5.2, the reduced set of equations for this 2D application is built including 355 porous modes in a non-optimized basis: precision rather than computational time is of interest in this section. The same procedure as for the 1D problem is applied, at a central frequency of 1000 Hz, L varying from 1 to 5. The results are presented in Fig. 5.4.

When compared to results obtained for the 1D problem, it is manifest that the increased complexity of the frequency response alters the interval of convergence of the approximation. Moreover, when considering the results obtained from the non-reduced problem (Fig. 5.4(a)-(e), left figures), it is confirmed that there is little significance in increasing the order of truncation above a certain limit to obtain substantial improvements in the convergence. For instance, the precision is not significantly improved between $(L = 3; M = 4)$ (Fig. 5.4(c)) and $(L = 4; M = 5)$ (Fig. 5.4(d)).

The observation of Fig. 5.4(c), for $(L = 3; M = 4)$, brings attention to some limitations inherent to an approximation in the form of a rational polynomial function. In fact, although there is a good agreement between the reconstructed and the reference responses between approximately 825 Hz and almost 1200 Hz, the reconstructed solution exhibits a peak at 950 Hz. This happens for the approximated solutions from both the non-reduced and reduced set of equations. Arguably, there is a local maximum at this point in the original solution, corresponding to a damped resonance of the cavity. However, without

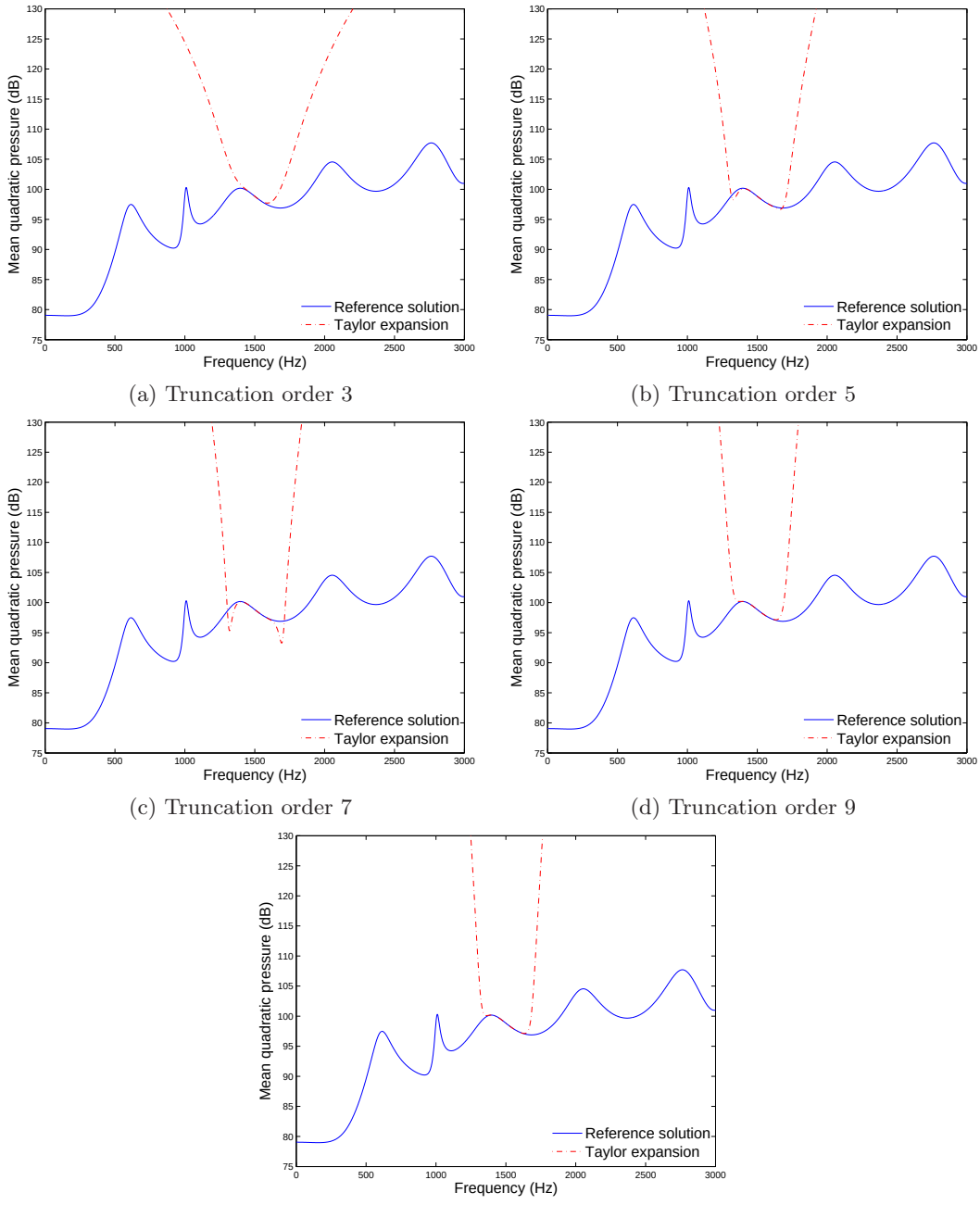

(a) Truncation order 3

(b) Truncation order 5

(c) Truncation order 7

(d) Truncation order 9

(e) Truncation order 11

Figure 5.3: Approximation using Taylor expansions - 1D poro-acoustic problem

error estimation or a posteriori control of the solution, such a reconstructed function could be physically misleading, not properly estimating the damping in the system. This is due to the possibility of encountering poles of the rational function within the interval of convergence. The reader is referred to the discussion found in [126] for further information

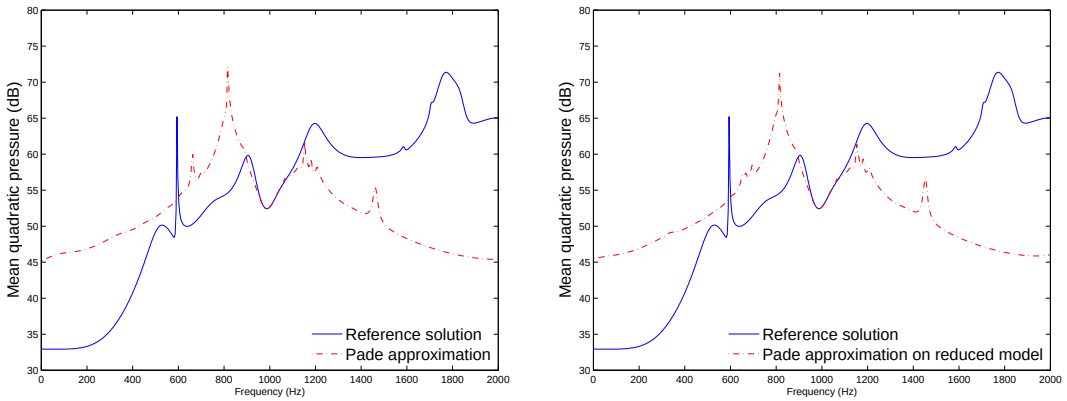

(a) $L = 1$; $M = 2$

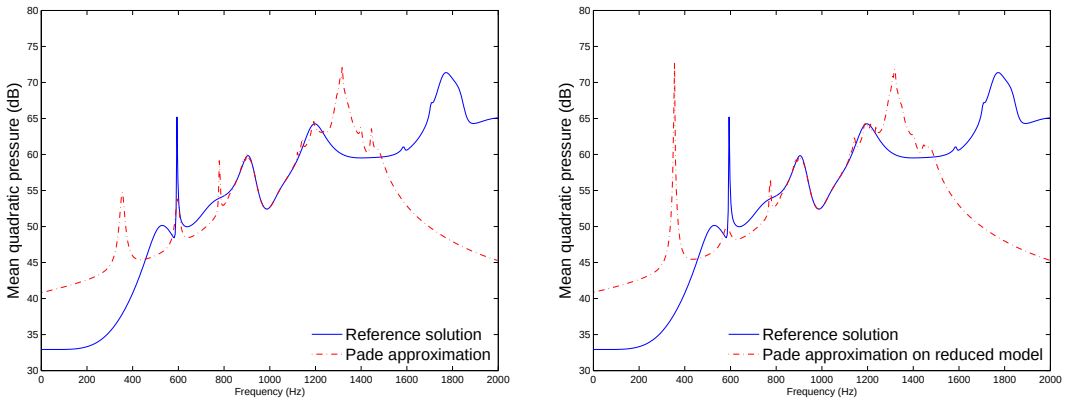

(b) $L = 2$; $M = 3$

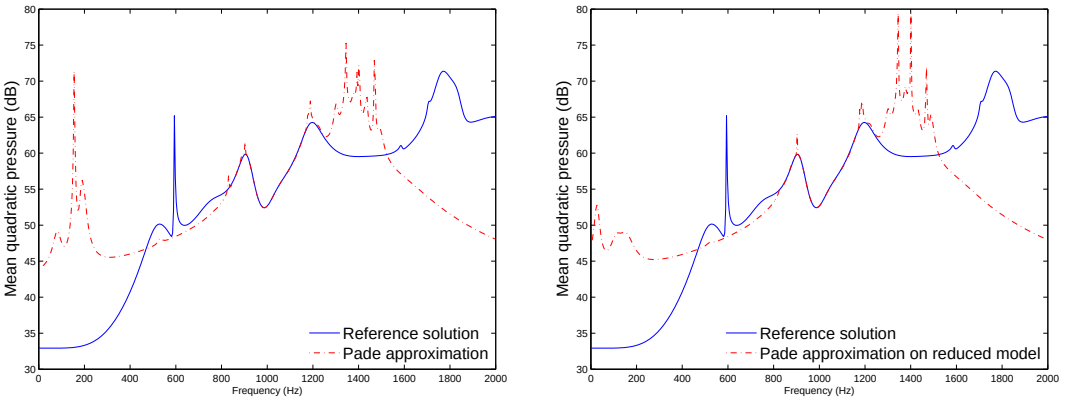

(c) $L = 3$; $M = 4$

Figure 5.4: Impact of increasing truncation order for power series - 2D poro-acoustic problem. Left: Padé on complete problem; Right: Padé on reduced problem.

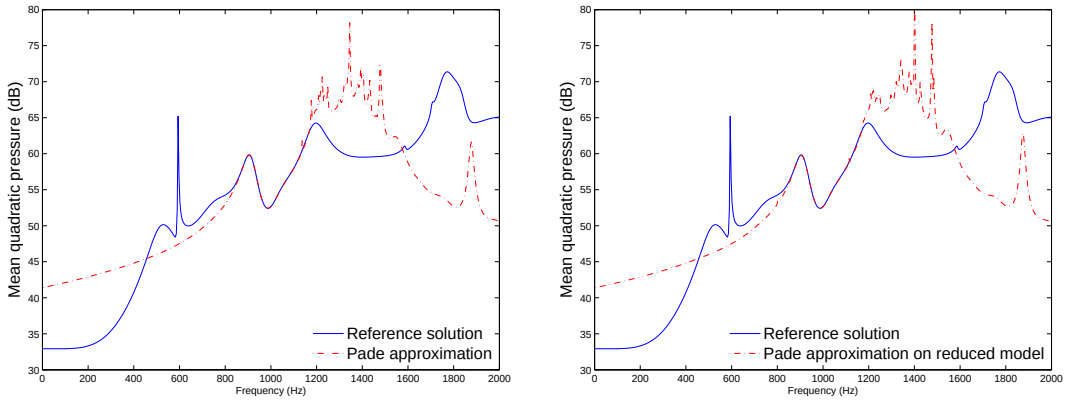

(d) $L = 4$; $M = 5$

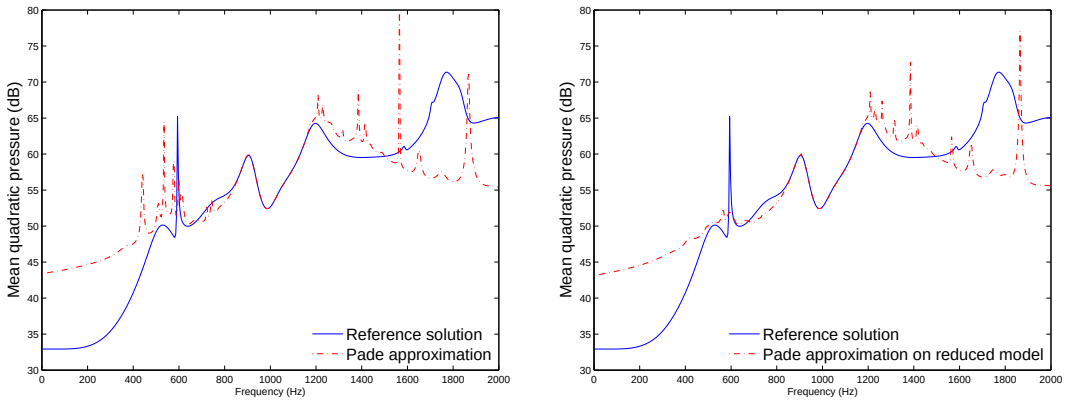

(e) $L = 5$; $M = 6$

Figure 5.4: Impact of increasing truncation order for power series - 2D poro-acoustic problem. Left: Padé on complete problem; Right: Padé on reduced problem.

and potential solutions to this issue. However, in the context of this work, this problem is supposedly avoided considering the highly damped nature of the tested applications, together with the fact that an error estimation is used in the automatic procedure proposed.

Finally, in agreement with the observations made for the 1D application, using the reduced set of equations for applying the reconstructing procedure does not hinder the approximated solution. The slight improvement suggested on the 1D problem is however not significant on this more complex application.

5.5.2 Adaptive Padé approximation on the 2D poro-acoustic application

The adaptive procedure presented in Fig. 5.1, to automatically define the central frequencies and the associated interval bounds, is applied to the same 2D poro-acoustic problem as in the previous section. The initial central frequency is chosen at 1900 Hz, and the maximum error estimation due to the reconstruction procedure is set to 0.1, as

done in Chapter 4. Following the observations made in the previous section, the order of truncation is fixed to $(L = 3; M = 4)$. The results, featuring the reference solution, the reconstructed solution, the successive intervals represented by their central frequency and their upper and lower bounds, are presented in Figs. 5.5. The solution at the central frequencies, on which is based the reconstruction procedure, is either the one from the complete set of equations (Fig. 5.5a), or from the reduced and optimized set of equations (Fig. 5.5b, see Section 4.5.2), established using 88 porous modes in the basis. The reference solution plotted is, in both cases, the one obtained using the complete set of equations. Figures 5.6 present the same mean quadratic pressure frequency responses, for which the reconstruction intervals have been removed for the sake of clarity. The reconstruction

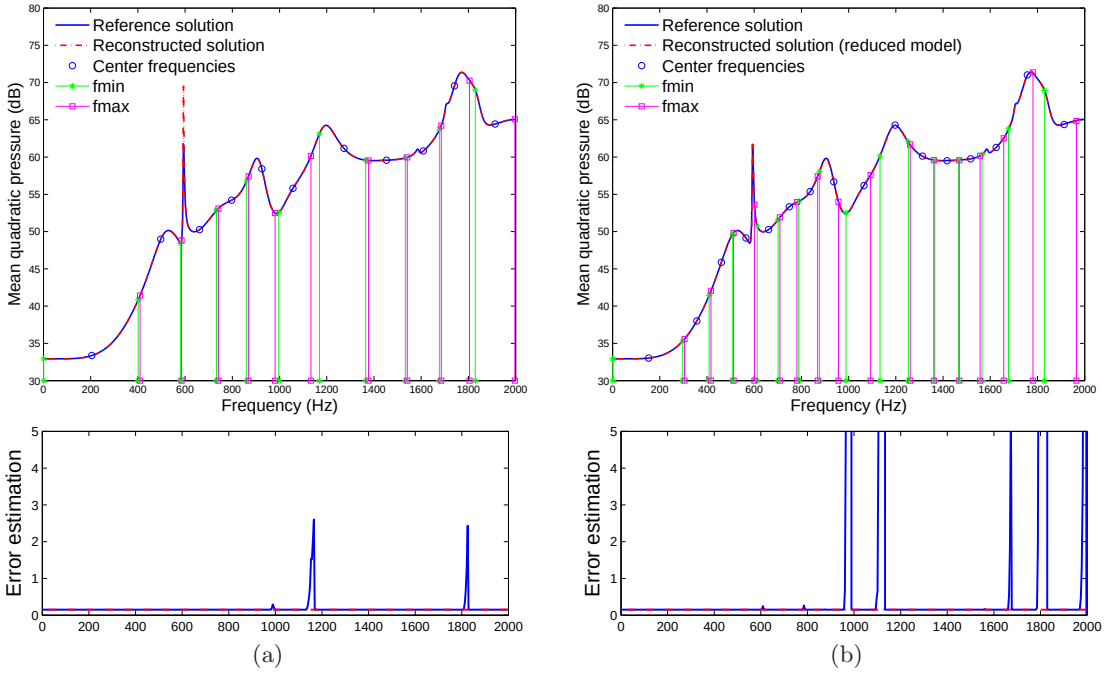

(a) (b)

Figure 5.5: Adaptive reconstruction procedure applied to 2D problem: (a) from non-reduced problem; (b) from optimized reduced problem.

based on the non-reduced reference solution is achieved over 11 frequency intervals. Even though the approximated solution exhibits perfect match with the reference frequency response, except for a non-relevant level mismatch at the peak of resonance around 600 Hz, the error estimation underlines three gaps between contiguous intervals. The first one, around 1000 Hz, is hardly noticeable on the error estimation plot itself, while the other two, around 1150 Hz and 1800 Hz are sufficiently small gaps in smooth ranges of the response to be unnoticeable on the reconstructed solution. Applying the Padé-based approximation to the reduced set of poro-acoustic equations (Fig. 5.5b) however amplifies those errors. This is rendered by the error estimation plot, where the 3 previous gaps

are found with higher estimated error levels, and 4 additional gaps are detected. Among the new gaps, two can be neglected (around 600 Hz and 800 Hz), one is of little width in a smooth area of the response (around 1700 Hz), and the last one corresponds to the upper range of the frequency range of interest not matching the upper bound of the initial interval. However, these gaps give rise to very little mismatch between the reference solution and the reconstructed one, barely amplifying the error committed by modal reduction (e.g. see around 1800 Hz). Consequently to the increase in error estimation, the adaptive decomposition into frequency intervals exhibits smaller intervals of convergence, thus increasing their number from 11 to 16. It is further mentioned at this point, that the results corresponding to a reduced set of equations without further downsize of the modal basis, as introduced in Chapter 4, are not presented for the sake of conciseness. They however give the same results as for the reduced and optimized basis. Thus, the interest of combining the Padé-based reconstruction to a reduced model stands only if the reduced number of times the Padé coefficients system (5.12) has to be solved compensates for the extra operations implied by the increased number of intervals and the construction of the reduced model itself.

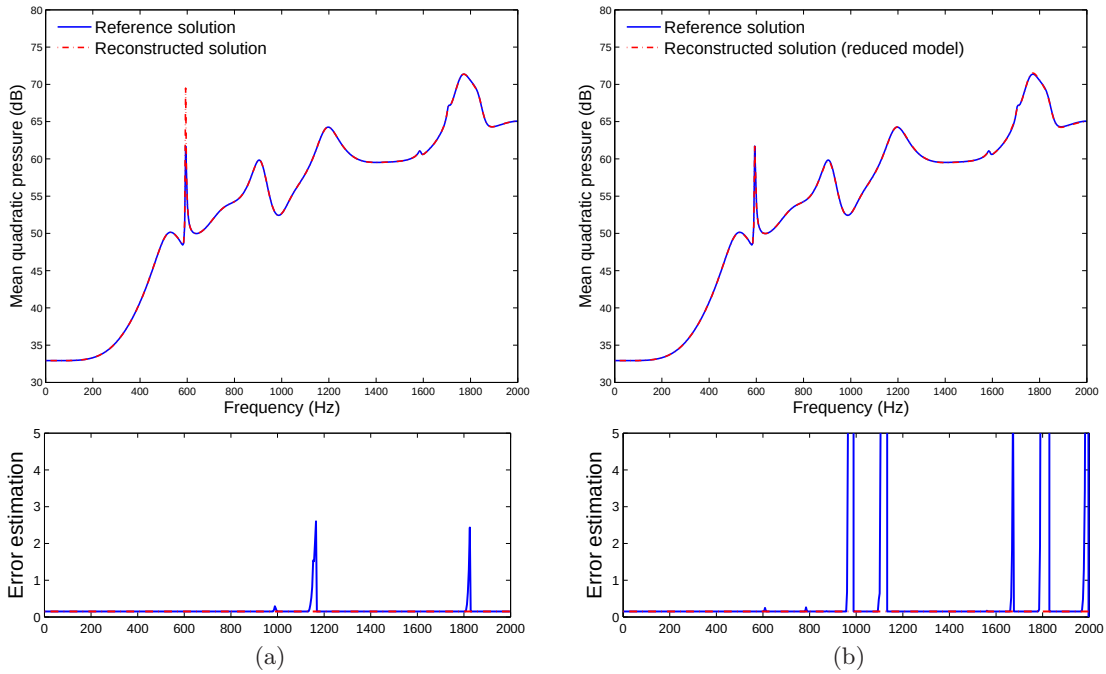

Figure 5.6: Adaptive reconstructed solution for 2D problem: (a) from non-reduced problem; (b) from optimized reduced problem.

A comparison of the CPU times needed for the computation of the direct reference solution, with the Padé-reconstructed solution based on (i) the complete set of equations, (ii)

the reduced set of equations, and (iii) the optimized-reduced set of equations, is presented in Fig. 5.7. Its interpretation gives a manifest contribution to answer the computational

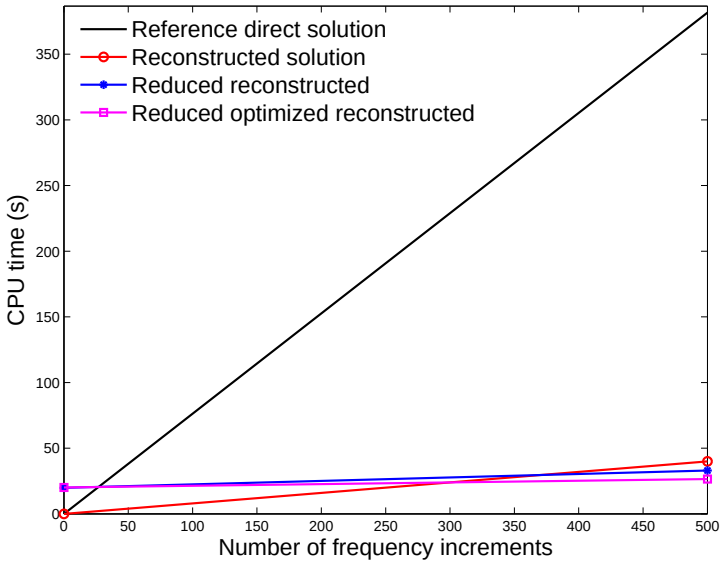

Figure 5.7: CPU time comparison for reconstructed solution from non-reduced, reduced, and optimzed reduced 2D problems, $(L = 3; M = 4)$

efficiency issue just raised. First, for a frequency-sweep with increments of 4 Hz, corresponding to 500 points of computation, the Padé-reconstructed solution based on the complete set of equations is more than 9.5 times as fast as the direct solution, thus confirming the potential of this approach. Of course, such an efficiency estimation is dependent, among other things, on the level of refinement for the frequency sweep, which is costless to increase in the case of the reconstructed solution. Then, for the considered application, applying the procedure to the problem with modal-based reduction (optimized or not) of the poroelastic domain is so computationally efficient that it compensates both for the cost of establishing the reduced model, and for the extra intervals needed to accurately rebuild the whole solution. Thus, not only does combining the Padé-based reconstruction with the modal reduction enable to save memory resources, but it also has the potential to improve the computational efficiency, while keeping a satisfactory level of precision.

5.5.3 Adaptive Padé approximation on the 3D poro-acoustic application

The proposed approach is further tested on the 3D poro-acoustic application introduced for modal-based reduction in Section 3.4.2, and further considered for enhanced modal reduction purposes in Section 4.5.3. Unlike for the 2D case, the results are however presented for two different truncations of the series expansion: $(L = 3; M = 4)$

and $(L = 5; M = 6)$. In both cases, the initial central frequency is chosen at 1975 Hz, while the error estimation limit is kept at 0.1. The results, featuring the reference solution together with the reconstructed solution and its associated intervals, are presented in Fig. 5.8 for the $(L = 3; M = 4)$ truncation, and in Fig. 5.9 for the $(L = 5; M = 6)$ truncation. Similarly to the 2D application, the Padé-based reconstruction is combined with the non-reduced, reduced, and enhanced-reduced sets of equations. For the sake of conciseness, only the former and latter need to be presented. The reference solution

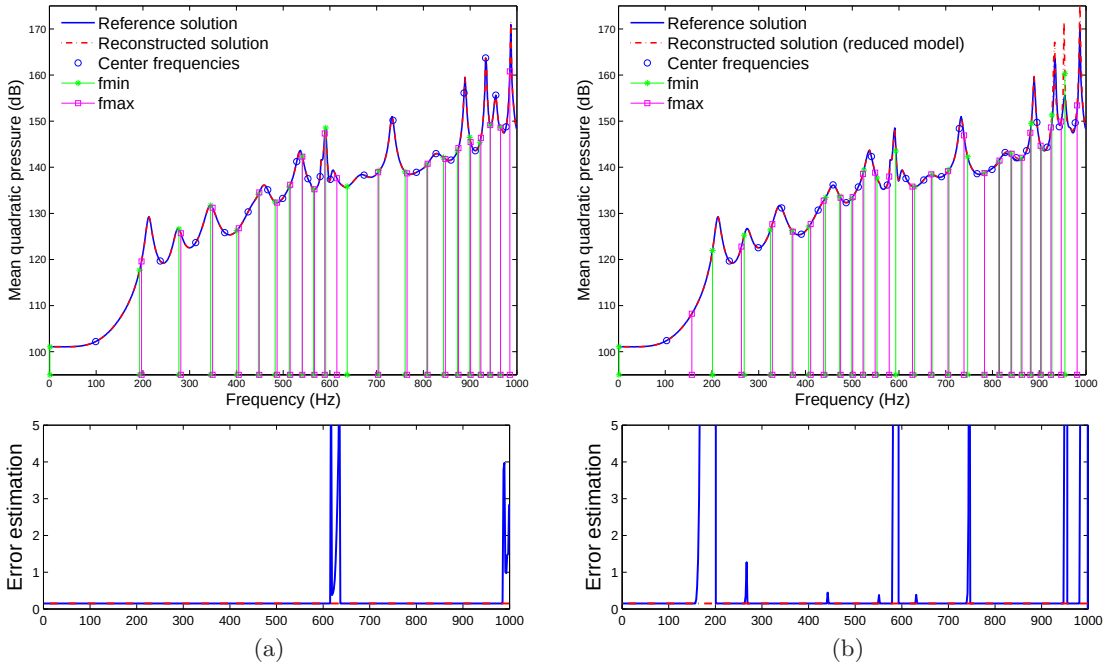

(a) (b)

Figure 5.8: Adaptive reconstruction procedure applied to 3D problem with $L = 3$, $M = 4$: (a) from non-reduced problem; (b) from optimized reduced problem.

corresponds to the solution without reduction of the poroelastic domain. The version of the results without plotting the reconstruction intervals is given in Fig. 5.10, for the Padé-based reconstruction combined with the enhanced-reduced set of equations, as being potentially the least accurate of the three results. The Padé reconstruction applied to the non-reduced set of equations is achieved over 21 frequency intervals for the $(L = 3; M = 4)$ truncation (Fig. 5.8a). It exhibits one gap between approximatively 615 Hz and 640 Hz, and a solution not converged in the very upper frequency range of interest due to the choice of initial central frequency. However, for the same reasons as for the 2D case (choice of limit for error estimation, smooth divergence of the method out of its convergence interval), the reconstructed solution accurately matches the reference solution. Again, use of the enhanced-reduced set of equations for the solution at central frequencies leads to a loss in precision (Fig. 5.8b). Follows an increase in the error estimation, thus achieving a

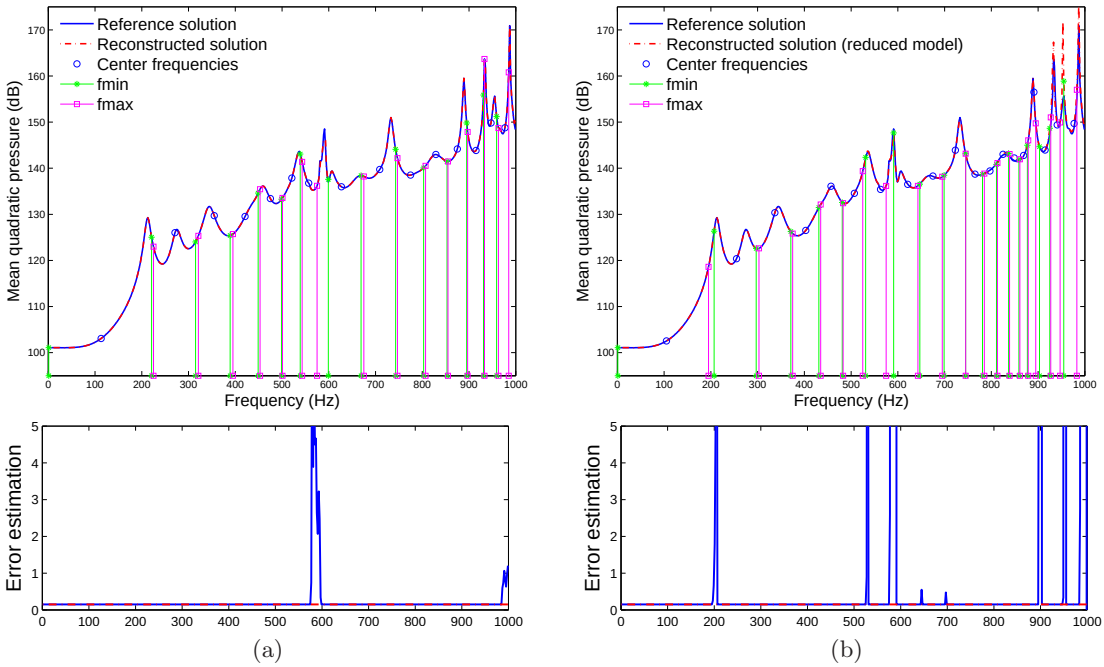

(a) (b)

Figure 5.9: Adaptive reconstruction procedure applied to 3D problem with $L = 5$, $M = 6$: (a) from non-reduced problem; (b) from optimized reduced problem.

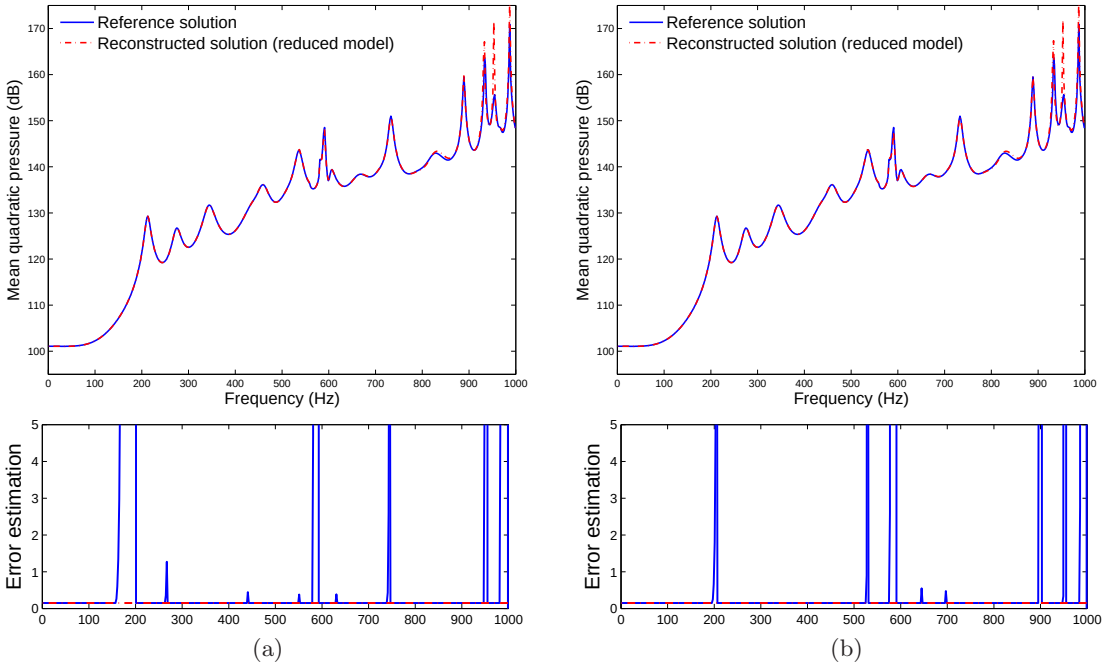

(a) (b)

Figure 5.10: Adaptive reconstructed solution for 3D problem from optimized reduced problem: (a) $L = 3$, $M = 4$; (b) $L = 5$, $M = 6$.

solution reconstructed over 24 intervals to be compared with the 21 intervals previously needed. In addition to the upper bound, 8 gaps have appeared, of which 4 can be neglected. Among the 4 remaining gaps, the one just below 600 Hz is of concern, considering its location around a resonance frequency, which could justify adding an interval to bridge the gap. However, its width is of approximately 10 Hz, it renders a peak in the frequency response, and its upper bound matches the lower bound of the contiguous interval. These, as confirmed by the comparison with the reference solution, very likely indicate a good approximation of the response. Finally, the gap between 160 Hz and 200 Hz is due to the special treatment applied to the lowest-frequency interval, not addressed in the presentation of the procedure, and not further detailed in this work. Again, the matching solution between the upper bound of the gap and the lower bound of the contiguous interval indicates a good approximation.

A similar analysis can be conducted when analyzing the results for the procedure with a truncation order of $(L = 5; M = 6)$ for the series expansions (Fig. 5.9). Increasing the order of truncation leads to reconstructed solutions over 15 and 18 intervals for the Padé-based procedure, when applied to the non-reduced and optimized-reduced sets of equations respectively. This is consistent with the larger interval of convergence observed in Section 5.5.1 when increasing the order of truncation. Again, a very good agreement can be observed between the reference solution and the reconstructed solutions. The only mismatch observed, similarly to what can be observed for the lower truncation order (Fig. 5.8b, 5.9b and 5.10), is the level of the 3 peaks of resonance above 900 Hz. Regarding those, it can be argued that they do not have prime physical significance considering how little damped these resonances are, and thus how frequency-shift-dependent their level determination is.

The impact of increasing the order of truncation is further estimated by comparing the CPU computational times. They are presented in Fig. 5.11, both for a truncation order of $(L = 3; M = 4)$ (Fig. 5.11a), and for a truncation order of $(L = 5; M = 6)$ (Fig. 5.11b). The computational efficiency observed for the 2D case is confirmed. Using a Padé-based reconstruction approach leads to a frequency sweep almost 9 times as fast as for a direct approach, considering frequency increments of 2 Hz for this 3D application. Combining it to a modal-based reduced set of equations does not substantially improve the overall computational time, if accounting for the time allocated to establish the reduced problem. However, the averaged time per frequency increment is greatly improved, so that it even compensates for the cost of building the reduced model if the optimized modal basis is used. Regarding the impact of increasing the order of truncation, it appears, when comparing Fig. 5.11a and Fig. 5.11b, that there is a trade-off to be found. In fact, as presented in Section 5.5.1, there is a limit above which, increasing the order of truncation does not

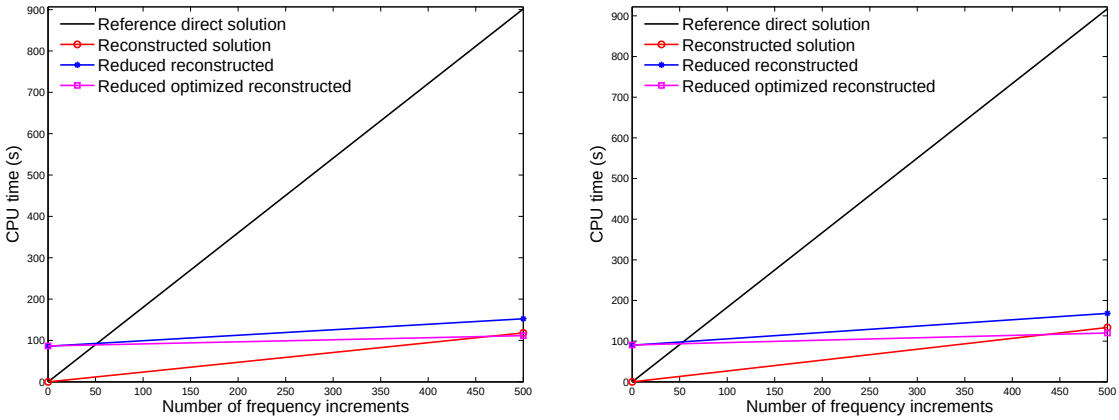

Figure 5.11: CPU time comparison for reconstructed solution from non-reduced, reduced, and optimzed reduced 3D problems: (a) $L = 3$, $M = 4$; (b) $L = 5$, $M = 6$.

substantially increase the intervals width of convergence, implying little reduction in the number of central frequencies at which the complete solution has to be calculated, thus not compensating for the increased size of the Padé coefficient system to solve (Eq. (5.12)) for each dof. For the applications considered in the scope of this work, the order of truncation ($L = 3; M = 4$), has proved a good compromise for computational efficiency, while ensuring a well-conditioned Padé coefficient system matrix.

5.6 Conclusion

In this chapter, the one-point Padé-based reconstruction method for efficient frequency sweep analysis was presented. It involves the approximation of frequency-dependent solutions by a rational function of power series expansions. It was restricted, in this work, to the general form of problems exhibiting frequency-independent global assembled matrices multiplied by frequency-dependent scalar functions. The finite element formulations established in the previous chapters, either in their non-reduced or modal-reduced form, satisfy this property. Therefore, this proved-efficient reconstruction scheme was applied to acoustic applications including 3D modelling of sound absorbing porous materials.

Beside tests made to choose an appropriate truncation order for the power series, an adaptive approach was proposed in order to automatically determine the main frequencies at which the complete direct solutions have to be computed, and around which the solution is approximated. This involves using an error estimation associated with the solution around each main frequency, thus establishing frequency intervals of converged solution. Such converged intervals are used to estimate a priori the frequency interval of conver-

gence for the neighbor main frequency before some a posteriori adjustments. This simple approach proved to produce accurate frequency responses in a very computationally efficient way for the configurations tested. Thus, the proposed method avoids an a priori knowledge of the dynamic behaviour of the problem for the choice of main frequencies. Furthermore, it reduces the risk of setting a too coarse or too fine a priori discretization in frequency intervals, that would respectively hamper the solution accuracy or efficiency.

Additionally, the Padé-based reconstruction method was tested in combination with modal-based reduced problems, as introduced in Chapters 4 and 5 for the poroelastic domain. Such a combined approach takes advantage of the complementary properties of these methods. First, using a modal-based reduced problem saves memory resources. The reconstruction approach then enhances dramatically the solution time for the frequency response over the range of interest. While very dependent on the application, and shown particularly efficient for very large applications, improvements by an order of magnitude were observed on the tested applications. Furthermore, the loss in precision due to the reduction implies the need for a finer decomposition into frequency intervals for the reconstruction scheme. However, this increase in the number of main frequencies is shown to be more than compensated by the improved efficiency of the reconstruction due to the reduced number of dofs. For the considered examples, the computational efficiency improvements due to this reduced set of dofs even compensates for the initial computational cost allocated to establish the reduced model.

Chapter 6

Applications, perspectives and conclusive remarks

Abstract: *In this chapter, the methods proposed in Chapters 2-6 are tested on an application larger than those used for validation purposes. It involves structural, acoustic and porous domains, thus allowing for an estimation and comparison of the potential of each of the approaches tested in the thesis. Conclusions are drawn in terms of performance, limitations and further research to be conducted following this work.*

Contents

6.1 Introduction

The aim of this last chapter is to test the methods proposed in the thesis on a more complex application than those tested for validation purposes in Chapters 2-6. The meaning of complexity in a dynamic problem may refer to several characteristics, e.g. its dimensions (size, multiscale), its frequency content and range, its phenomenology (multiphysics), its geometrical complexity. The application chosen here involves structural, acoustic and porous domains. It is close to the *concrete car* problem used in Chapter 2, thus presenting an increased complexity in terms of dimensions, frequency content, and phenomenology. This complexity is however limited both by regular geometries and the use of porous materials in simple configurations (single layer, backed with a rigid wall). It nevertheless enables to estimate the potential performance of the proposed methods (previously measured using indicators such as the sparsity, bandwidth and size enhancements of the problems to solve). The conclusions drawn also provide indications on further research and tests to be conducted in order to bring the necessary enhancements leading to a final methodology.

The chapter is organized around 3 sections. First, the poro-elasto-acoustic application is presented. Then, the modal-based methods presented in Chapters 2-4 are tested for their performance. The last part presents the results obtained applying a Padé-based reconstruction strategy, both for the complete model as well as in combination with a modal approach.

6.2 Presentation of the application

6.2.1 Validation case proposed by the Mid-Frequency project

6.2.1.1 Presentation of the problem

The validation case proposed by the "Mid-frequency" EU project [127] consists of a rigid acoustic cavity with one flexible wall (2 mm-thick steel plate), the rigid floor being covered with a 50 mm-thick melamine foam. The geometry and the FE model are presented in Fig. 6.1. The mesh includes:

- 12453 linear tetrahedron acoustic elements (mean size 0.09 m), i.e. approximately 8 elements per wavelength at 500 Hz, corresponding to 22983 nodes (and acoustic dofs),
- 16×34 linear quad shell elements (mean size 0.05 m), i.e. approximately 1 element per quarter structural bending wavelength at 500 Hz.

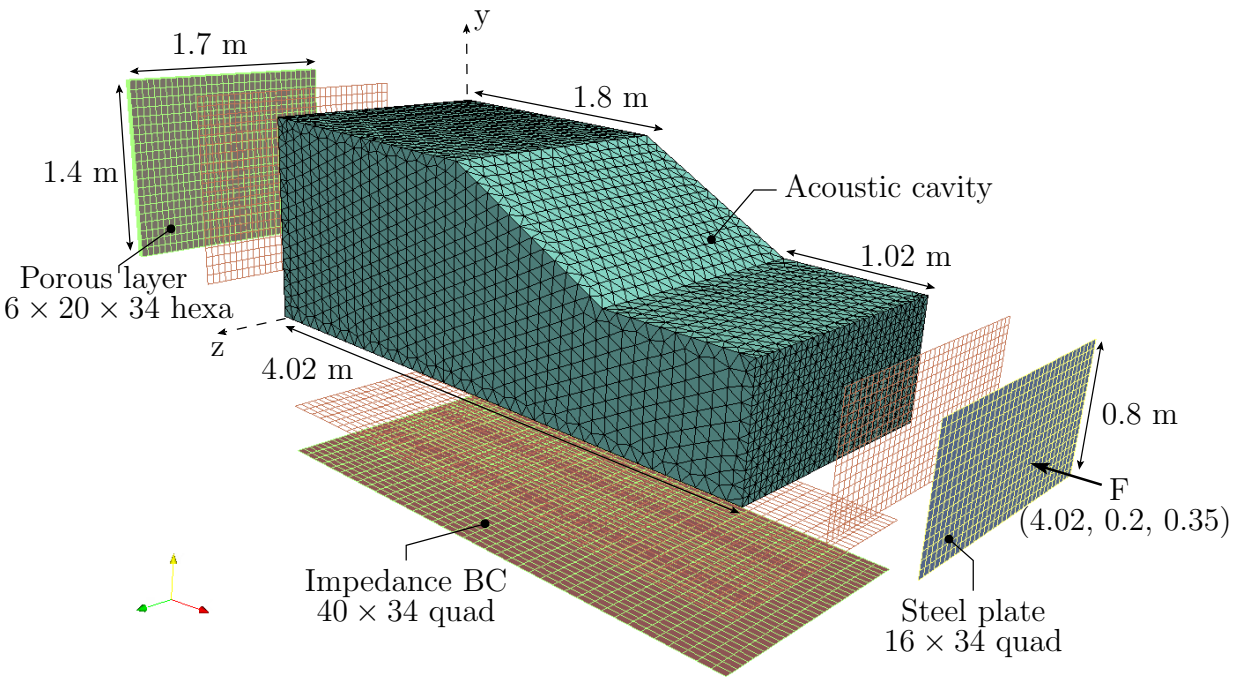

Figure 6.1: Geometry and mesh of the finite element model.

The plate is considered clamped along its edges, and is excited by a shaker at the position ($x = 4.02$ m, $y = 0.2$ m, $z = 0.35$ m). The melamine foam is modelled in the original problem by a normal acoustic impedance boundary condition, tabulated and provided in 1 Hz increments after measurements with a Kundt's tube (see Fig. 6.2).

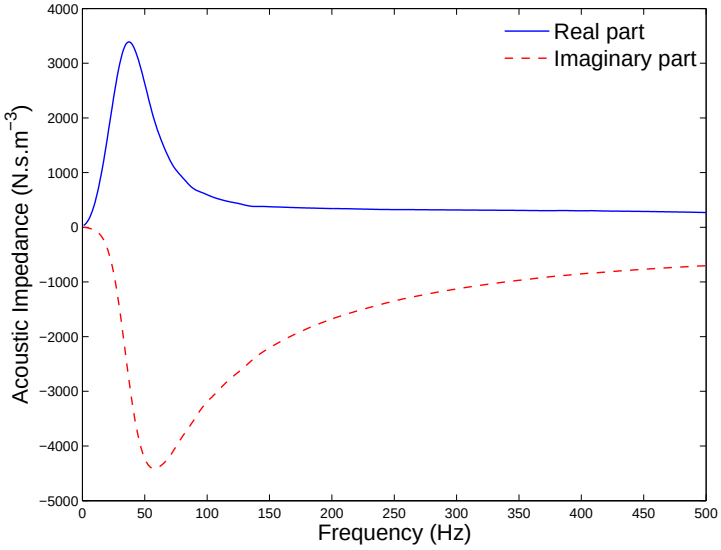

Figure 6.2: Normal acoustic impedance boundary condition.

In order to test the modal-based approach proposed in the thesis for poroelastic materials, a 5 cm-thick layer is optionally added on one wall of the acoustic cavity. It is modelled with a 3D mesh using the displacement formulation of the Biot-Allard theory. Similarly to the *concrete car* model in Chapter 2, the layer is attached to the back wall, while sliding boundary conditions are set on the side faces. The mesh, consisting of $6 \times 20 \times 34$ linear brick elements, involves 25116 poroelastic dofs. The case with 3D modelling of the porous layer is presented in Section 6.2.2 for the reference solution, and is further tested in Section 6.3 for the validation of the proposed modal-based reduction of the porous domain.

The reference response, without the 3D porous layer, is given at an output point in the acoustic cavity around position ($x = 0.51$ m, $y = 0.425$ m, $z = 0.5$ m), as suggested in the original model. Thus, Fig. 6.3 presents a reference solution for the sound pressure level at position ($x = 0.534$ m, $y = 0.403$ m, $z = 0.495$ m), for the model without addition of the 3D porous layer. Both the responses with and without the impedance boundary conditions are given for comparison. The non-damped solution illustrates the evolution

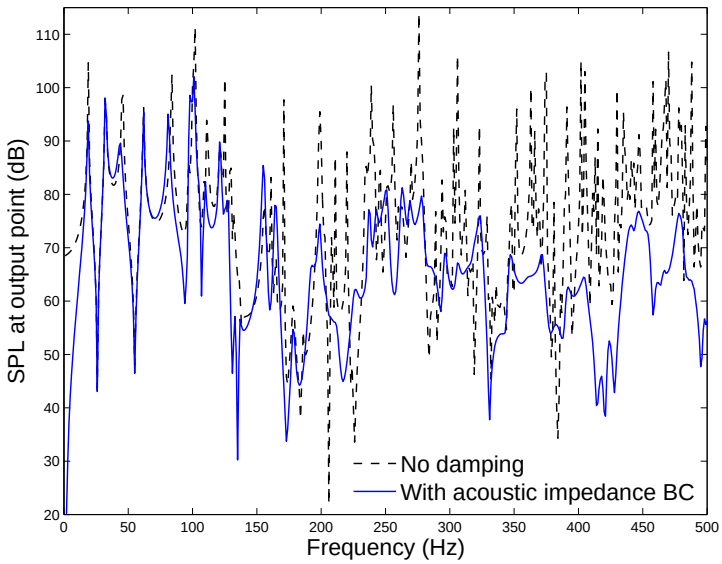

Figure 6.3: Reference sound pressure level response at output point, without 3D porous layer.

of the modal density along the frequency range of interest, which becomes challenging for a modal approach in its higher end. The response of the impedance-damped problem is not to be considered below ca. 20 Hz, considering the impedance measurement provided is irrelevant in this frequency range.

The use of a single point as an output is however not completely relevant for an analysis beyond the very low frequency region. As illustrated in Fig. 6.4, the response becomes very sensitive to small variations of the parameters with increasing frequencies (here illustrated

with small variations of the measurement position). A deterministic evaluation approach is

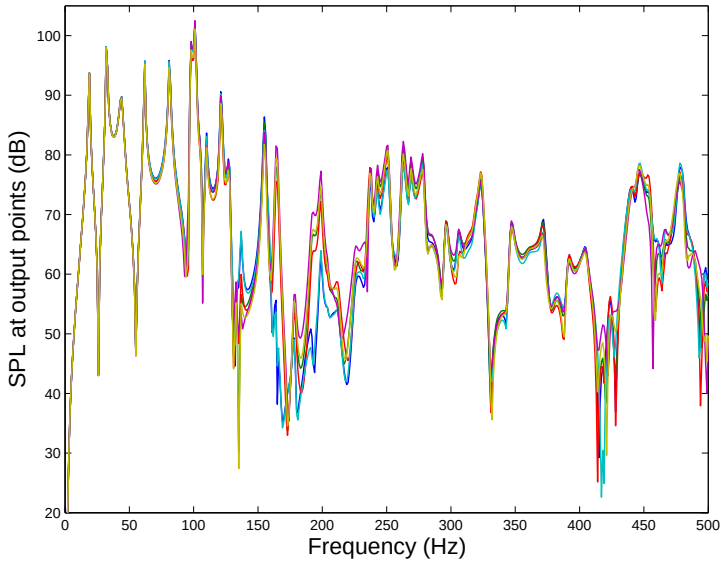

Figure 6.4: Spatial sensitivity of the response, 6 points in a cubic zone of $10 \times 10 \times 10$ cm^3.

thus not entirely relevant, and an averaged response over a significant volume could be more appropriate. However, for the sake of testing the modal reduction approaches proposed, the response at a single output point is a relevant reference to match. Nevertheless, for this reason, the comparisons between solutions of the non-reduced and reduced problems are sometimes completed by comparisons on the mean quadratic pressure in the acoustic cavity.

6.2.1.2 Modal reduction of the acoustic domain

First, on the model without the 3D porous layer, a restrained-interface modal reduction of the acoustic component is applied, according to the method discussed in Chapter 2. The acoustic "interface" (or master) dofs include those at the interface between the acoustic and structural domains, those at the applied impedance boundary, and the output dof. This represents 1931 acoustic master dofs. The responses for a modal basis truncated at 1060 Hz (ca. twice the highest frequency of interest) and 1250 Hz (2.5 times the highest frequency of interest) are presented in Figs. 6.5. The solution with an acoustic modal basis truncated at 1060 Hz already produces a good approximation of the solution, hardly noticeably improved, at the plotted scale, with a truncation at 1250 Hz. In both cases, the problem is dynamically condensed, from an initial problem of 25953 dofs to a reduced-problem of 4901 dofs. An estimate of the computational time is presented in Fig. 6.6, comparing the direct solution of the complete problem with its acoustic-reduced versions. Table 6.1 further details the CPU time allocated to each step of the reduction

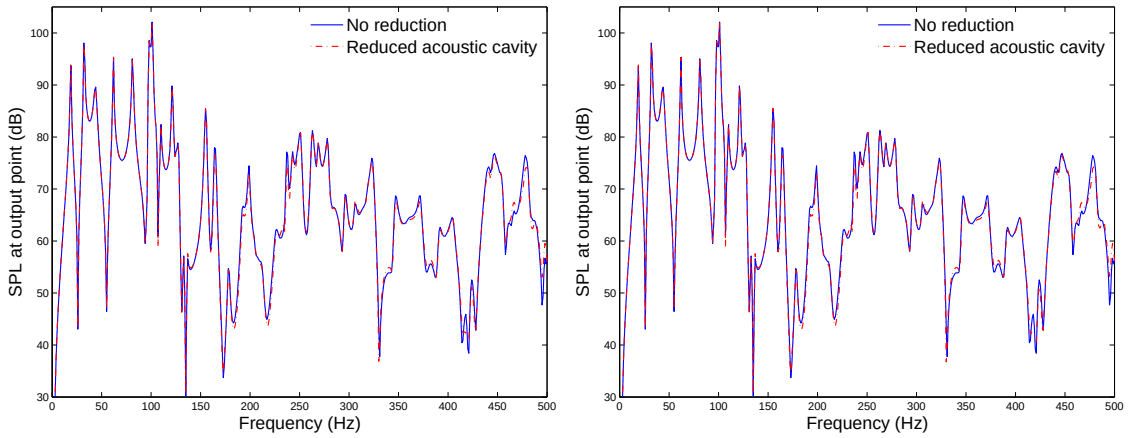

Figure 6.5: Sound pressure level at output point: dynamic condensation of acoustic domain, (a) modal truncation at 1060 Hz; (b) modal truncation at 1250 Hz.

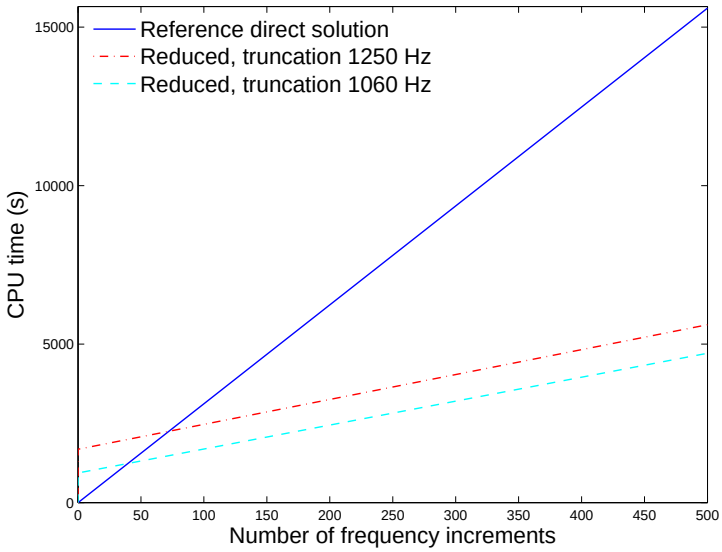

Figure 6.6: Computational time comparison, reference problem without 3D porous layer and dynamic condensation of acoustic domain.

process. These problems were run on a single processor, Intel T9500 at 2.6 GHz, with 3 GB of memory, in a Linux environment under Matlab 2006b. The dynamic condensation of the acoustic domain enables, for this problem, a solution of the frequency response approximatively 3 times as fast as for the initial problem. The speed-up is of a factor 4 if the initial step for the reduced model is not accounted for. Furthermore, in agreement with the observations made in Chapter 2, the computational time for the solution step is hardly affected by the increase in the number of modal coordinates, as they are dynamically

	Truncation 1060 Hz	*Truncation 1250 Hz*
No reduction [N dofs]	15600 s [25953]	15600 s [25953]
Eigenvalue problem [N modes]	714 s [840]	1460 s [1253]
Attachment functions [N vectors]	222 s [1931]	221 s [1931]
FRF reduced problem [N dofs]	3775 s [4901]	3931 s [4901]
Overall CPU, reduced problem	4711 s	5612 s

Table 6.1: Details for computational time comparison, reference problem without 3D porous layer and dynamic condensation of acoustic domain.

condensed at each frequency step.

6.2.2 Extension with addition of a porous layer

The version with addition of the porous layer modelled with 3D elements is run on a single processor, Intel W5590 at 3.33 GHz, with 48 GB of memory, in a Linux environment under Matlab 2010a. The 3D modelling of the porous layer using the ($\mathbf{u}_s$,$\mathbf{u}_f$) formulation involves 25116 poroelastic dofs. The same porous material as the one in Chapters 3-5 is used (see material parameters in Table 3.1). However, in this chapter, the structural damping in the frame, $\eta_s = 0.1$, is taken into account following the description made in Eqs. (3.10). Fig. 6.7 presents the reference solution, comparing the sound pressure level at the output point, for the problems with and without the porous layer in the range [0-400] Hz. Among the effects on the frequency response, a slight frequency shift towards

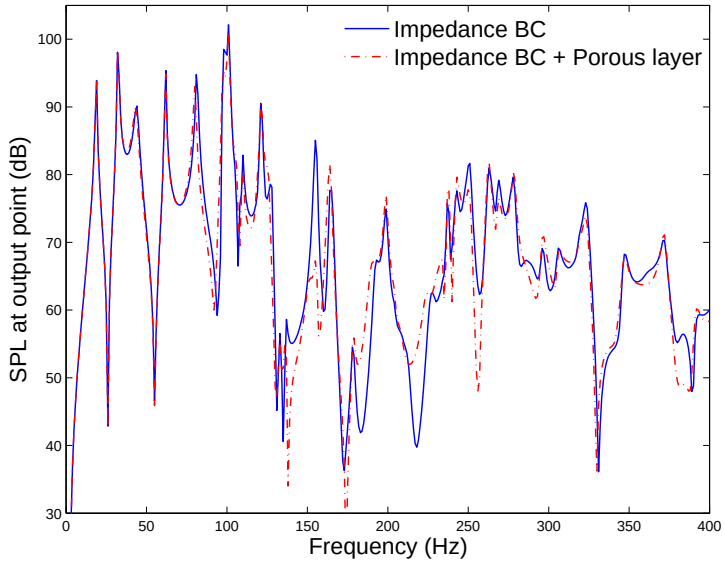

Figure 6.7: Reference sound pressure level response at output point, with 3D porous layer.

lower frequencies can be observed. The response remains close, in its dynamic content, to the case with only the impedance boundary conditions, with some level differences at resonances (e.g. at 150 Hz) or anti-resonances (e.g. at 175 Hz, 220 Hz, 255 Hz). The modal-based reductions of both the acoustic and porous domains are successively tested in the following section.

6.3 Modal approach for the acoustic and porous domains

In this section, after checking the dynamic condensation of the acoustic domain, the proposed methodology applied to the porous domain is tested. First, the modal-based reduction using a rule of thumb truncation criterion (twice the highest frequency of interest) is presented, followed by further reductions of the porous modal basis, before concluding with the combination of both the acoustic and porous domains reduced. However, further condensation of the coordinates corresponding to orthogonal porous modes (as presented in Section 3.3.3) is not discussed here, even though it is expected to bring substantial efficiency improvements considering the size of the modal bases involved. Finally, the computational times presented are only given for qualitative estimations. Quantitative estimations would require more attention given to the implementation, which is beyond the scope of the present work. The objective is primarily to validate the potential of the proposed approach on a larger scale problem.

6.3.1 Modal reduction of the acoustic domain

The dynamic condensation of the acoustic domain to its interfaces with (i) the structural domain, (ii) the impedance boundary conditions, and (iii) the porous layer is first tested alone. Thus, the complete problem is downsized from 51069 to 30717 dofs (2631 interface, 2970 structural and 25116 poroelastic dofs). The truncation of the modal basis is chosen at 1250 Hz as previously shown converged for the case without the porous layer. It then corresponds to a truncation at more than 3 times the highest frequency of interest, which is considered to be a safe truncation. This is confirmed in Fig. 6.8, presenting a superposition of the response at the output acoustic point for the complete and acoustic-reduced problems. An excellent match is observed in the low frequency range, up to 200 Hz, while presenting a few level errors above, around some anti-resonances (e.g. 220 Hz, 385 Hz). However, these small, localized convergence errors can be put into perspective with the spatial sensitivity plot in Fig. 6.4, and may be of very little significance on a spatially averaged output.

The computational time improvement is presented in the synthesis Table 6.3.

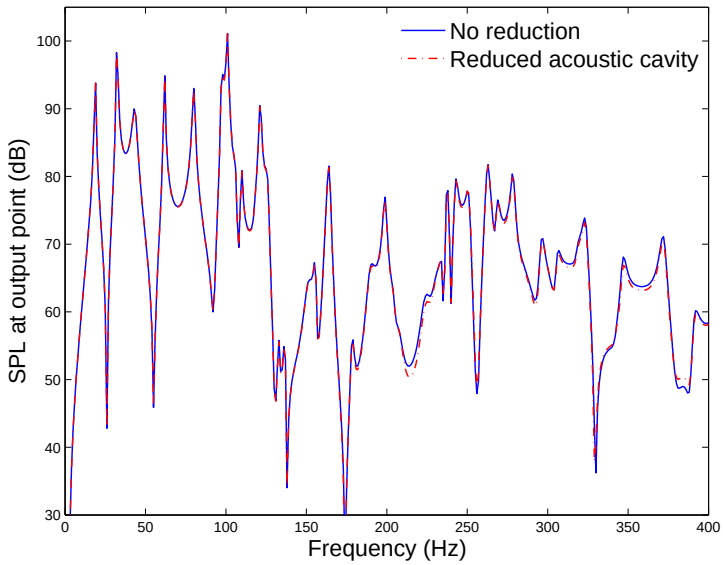

Figure 6.8: Sound pressure level at output point: dynamic condensation of acoustic domain, modal truncation at 1250 Hz.

6.3.2 Modal reduction of the porous domain

The modal-based reduction proposed in Chapter 3 is here applied to the porous layer. First, the truncation of the porous modal basis is set to twice the highest frequency of interest, 800 Hz. This leads to a large modal basis to be computed, including 4775 porous coupled modes. The corresponding SPL frequency response at the output point is given in

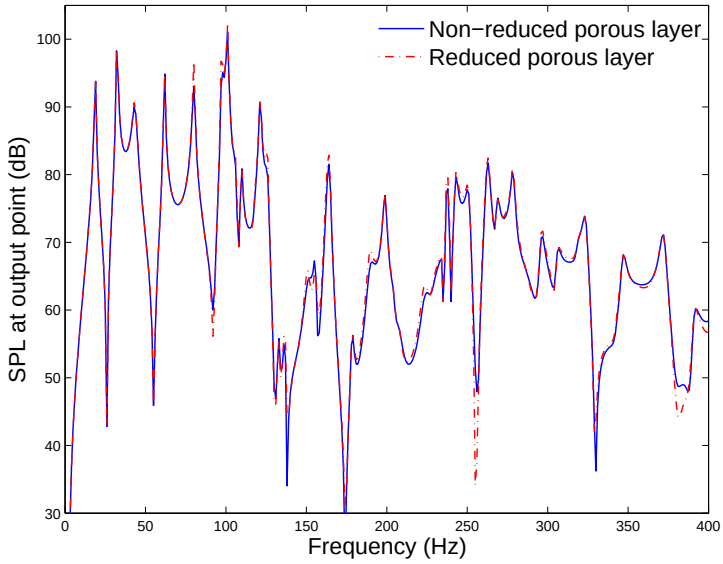

Figure 6.9: Modal reduction of porous domain, modal truncation at 800 Hz.

Fig. 6.9, together with the reference solution. It results in a fairly good approximation of the solution on the entire frequency range, with a few localized level errors. For instance, slight frequency shifts towards low frequencies can be observed in the ranges [175-230] Hz or [330-340] Hz. Thus, being very sensitive to slight frequency shifts, peaks of resonance or anti-resonance such as ca. 80 Hz, 95 Hz, 140 Hz, 255 Hz or 330 Hz are misevaluated. Overall, the dynamic response of the system as measured at the output point is globally well represented, and is expected to match even better for a local spatial average evaluation of the response. Furthermore, the slight frequency shift observed indicates the possibility of using a correction vector in the basis, which is one previously mentioned development to enhance the present work.

Before testing the mode selection procedure proposed in Chapter 4, a more severe truncation of the modal basis is attempted, with modes up to 400 Hz. This involves 3000 modes included in the basis. The corresponding SPL frequency response at the output point is presented in Fig. 6.10. For this specific problem, further truncation leads to minor

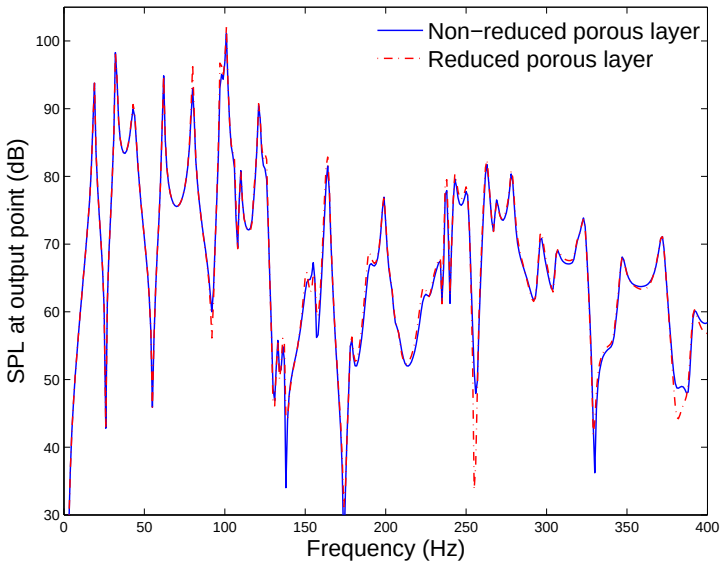

Figure 6.10: Sound pressure level at output point: modal reduction of porous domain, truncation at 400 Hz.

changes in the approximation made, mostly in the higher end of the frequency range. However, a wider range of tests on different types of applications would be required in order to modify the a priori truncation rule of thumb for poroelastic materials. This is considered a perspective to the present work. However, an a priori overestimation of the truncation is partly compensated by the further mode selection procedure applied in the following section.

In order to better illustrate the satisfactory level of precision achieved by the modal re-

duction, the mean quadratic pressure frequency response in the cavity is shown in Fig. 6.11, both for the reference and the reduced solutions (truncation at 400 Hz). A very good agree-

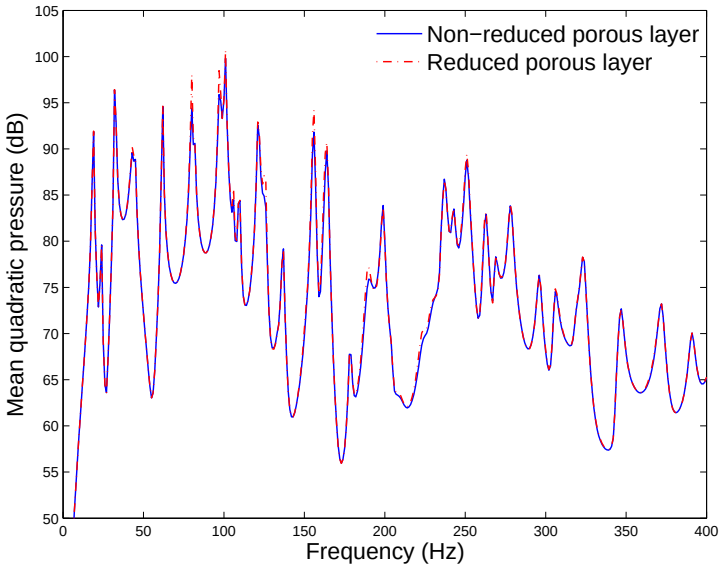

Figure 6.11: Mean quadratic pressure in cavity: reference solution and modal reduction of porous domain, truncation at 400 Hz.

ment between the two solutions can be observed on the response in terms of this volume averaged quantity, however still noticing a few localized minor discrepancies around some resonances (e.g. 125 Hz, 190 Hz, 225 Hz).

6.3.3 Enhanced modal reduction of the porous domain

Assuming that a classical truncation estimation is applied, in order to select the porous modes up to an eigenfrequency of 800 Hz (4775 modes), the mode sorting and further truncation procedure presented in Chapter 4 is tested. Considering the much more complex frequency content as compared to the applications previously tested, 10 residual responses are used for the procedure described in Algorithm 1. These are calculated for a problem where only the porous domain is reduced, including the first 15 porous modes in the modal basis. The number of modes for these poor approximate solutions is arbitrarily set to 15, thus at least capturing the very low frequency behaviour of the poroelastic domain. The 10 residual vectors are calculated at evenly distributed frequencies between 100 Hz and 370 Hz with increments of 30 Hz.

Fig. 6.12 illustrates the participation of each of the 4775 modes (sorted accordingly) to the real part of the residual response at 100 Hz. The same trend is observed for the participations to all other residual vectors, and it is to be compared with the mode

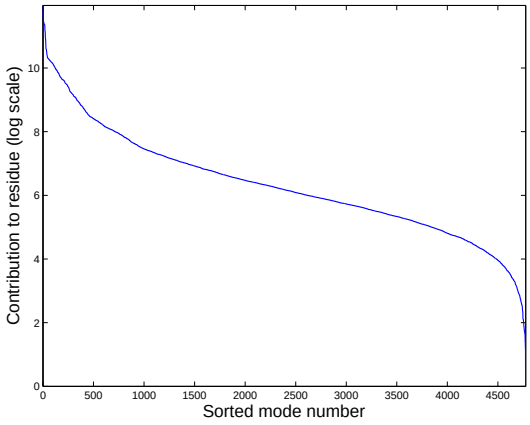

Figure 6.12: Normalized mode participations to the real part of the first residual response (100 Hz), logarithmic scale.

contributions estimated for the simple corner-excited cavity treated in Chapter 4, Fig. 4.6b. In the present application, the modes participation is more evenly spread, and it therefore indicates that a greater proportion of porous modes are excited (more complex source and acoustic field). Consequently, further truncation of the basis cannot be as beneficial as in the case of Chapter 4 (basis downsized to almost 10% of its original size, with a truncation limit of $\chi_{\max} = 0.27$).

The truncation limit, following the definition proposed in Eq. A.18, is set to $\chi_{\max} = 0.45$. The corresponding comparison of the response, with and without further reduction of the modal basis is presented in Fig. 6.13. The modal basis is thus downsized from 4775 to 2688 modes. A very good agreement between the two responses can be observed, except for mainly 3 peaks: the resonance around 150 Hz, which was already misevaluated, the anti-resonance around 255 Hz, which seems better evaluated with the further reduced basis, and the response around 380 Hz which is not well captured by either of the two bases. These results obtained for a more complex problem confirm the potential of the sorting and truncation procedure proposed in Chapter 4. It has its greatest potential when such large bases are generated, suitable for a wide range of solicitations, and need to be refined to perform best for a specific excitation. As previously mentioned, a natural improvement of this combination (costly generation of a large basis and problem-dependent downsize in a second step) is to attempt the generation of a load-dependent Ritz basis.

6.3.4 Modal reduction of the porous and acoustic domains

In this section, both the reduction of the porous domain and the dynamic condensation of the acoustic domain are combined. The truncations of the bases are chosen from the reduction experiences presented in the previous section: the acoustic basis is composed of

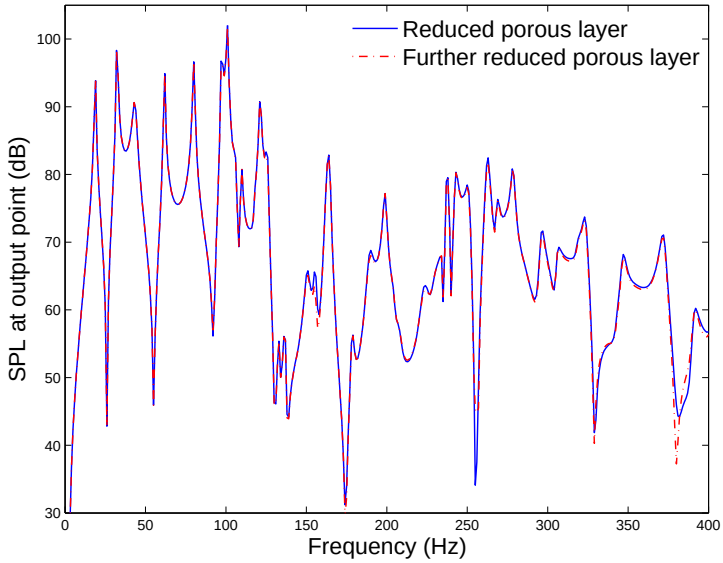

Figure 6.13: Sound pressure level at output point: response with modal truncation at 800 HZ, and further reduction with $\chi_{\max} = 0.45$.

modes whose eigenfrequencies are lower than 1250 Hz, and for the porous basis, modes whose eigenfrequencies are lower than 400 Hz are retained. This implies a reduction from 51069 to 8601 dofs in the problem considered. The sound pressure level frequency response at the output point is plotted in Fig. 6.14, and compared to the reference solution. The pollution of approximations due to the reduction of both domains remains limited,

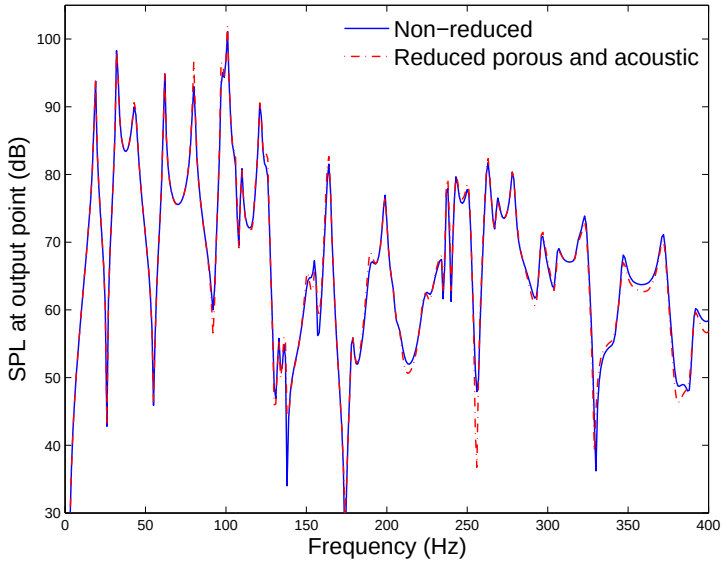

Figure 6.14: Sound pressure level at output point: modal reduction of acoustic (truncation 1250 Hz) and porous (truncation 400 Hz) domains.

thus offering a very good estimate of the frequency response. This is further emphasized when plotting the mean quadratic pressure frequency response in the acoustic cavity, as presented in Fig. 6.15. The dynamic content is very well represented, particularly in the

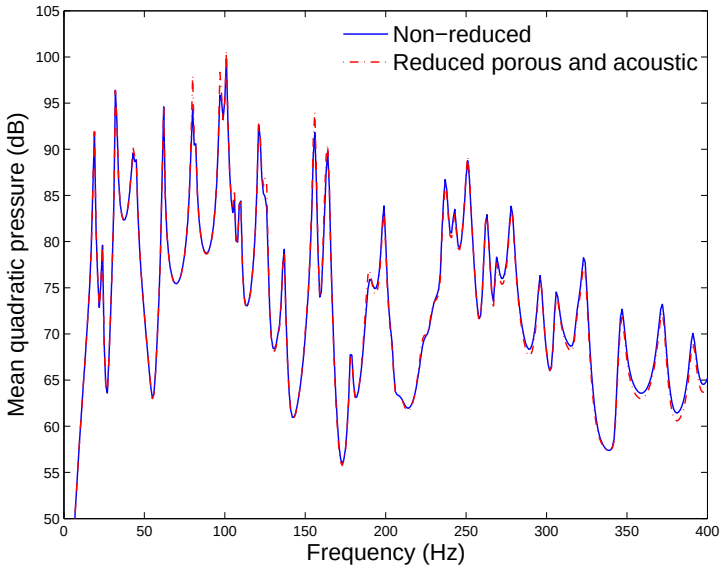

Figure 6.15: Mean quadratic pressure in cavity: modal reduction of acoustic (truncation 1250 Hz) and porous (truncation 400 Hz) domains.

low frequency range, while the response becomes slightly underestimated in the higher end of the frequency range.

After estimating the accuracy achieved for different combinations of modal-based reduced domains, the following section focuses on efficiency comparisons between these solutions.

6.3.5 Computational time estimates and comparisons

It is recalled that the computational time estimates provided in this section aim primarily at bringing qualitative conclusions for the different solution schemes tested. Accurate quantitative estimates would require more attention given to the implementation for the different methods.

Figs. 6.16 present an estimation of the computational times for the solutions made in the previous sections: the reference direct solution, the solutions with the acoustic dynamic condensation (truncation at 1250 Hz), with the modal-based reduction of the porous domain (800 Hz truncation, its further reduced version, and 400 Hz truncation), and with both the acoustic and porous domains reduced (truncation at 1250 Hz and 400 Hz respectively). For the sake of clarity, a detailed comparison between the reduced models is

plotted in Fig. 6.16b without the reference solution. Overall computational time enhance-

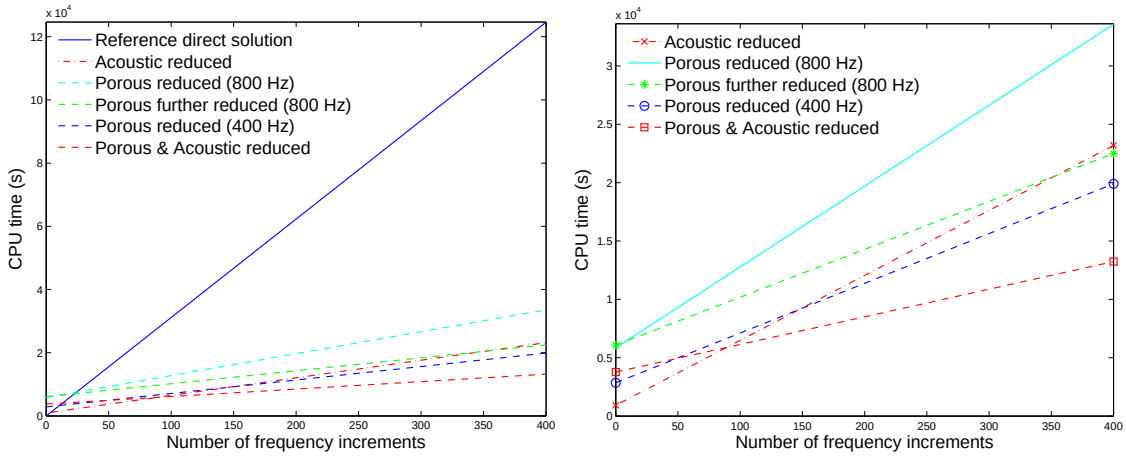

Figure 6.16: Computational time comparison: (a) comparison with reference solution, (b) detailed comparison for acoustic and/or porous reduced domains.

ments range from almost a factor 4 (porous reduction alone with truncation at 800 Hz) to almost a factor 10 (acoustic dynamic condensation, truncation at 1250 Hz together with porous modal reduction, truncation at 400 Hz) for this specific application. The heavy cost allocated to the computation of the porous modal basis (e.g. 800 Hz truncation, 4775 modes), is rapidly compensated due to the efficiency improvements. Use of further reduction procedures, as described in Chapter 4, enables to improve the frequency sweep in case of over estimation of the a priori truncation of the porous basis. Thus, the cost of the initial step is at worse compensated after 20 increments of the reference solution in the present case.

Tables 6.2 and 6.3 quantify the computational time allocated to the main steps of each calculation, illustrated in the detailed plot in Fig. 6.16b. A few conclusion can be drawn out of these estimates.

First, if only the porous reduction is considered, the solution effort greatly benefits from the downsize in the number of modal coordinates. This can be partly explained by the higher density of the porous reduced submatrices when compared, for instance, with acoustic matrices, and mostly by the cost induced by the attachment functions, fully coupling the interface dofs to the modal coordinates. The need for further work in order to establish sensible truncation estimates is thus highlighted. It also underlines the interest for the mode selection procedure proposed, in order to keep the size of the basis as small as possible and suitable for the considered analysis. In addition, although not tested on these examples, the identification of the modal coordinates corresponding to

	Porous (800 Hz)	***Porous (400 Hz)***
No reduction [N dofs]	124600 s [51069]	124600 s [51069]
Eigenvalue problem [N modes]	5740 s [4775]	2745 s [3000]
Attachment functions [N vectors]	105 s [735]	105 s [735]
FRF reduced problem [N dofs]	27720 s [30728]	17050 s [28953]
Overall CPU, reduced problem	33565 s	19900 s
Further reduction procedure	236 s	–
[N residual, $\chi_{\max}$, N modes]	[10, 0.45, 2688]	–
Further reduced problem [N dofs]	16410 s [28641]	–
Overall CPU, further reduced	22491 s	–

Table 6.2: Details for computational time comparison, modal-based reduction of porous layer.

	Acoustic (1250 Hz)	***Acoustic* & *Porous* (1250 Hz, 400 Hz)**
No reduction [N dofs]	124600 s [51069]	124600 s [51069]
Eigenvalue problem [N modes]	550 s [1253]	550 + 2745 s [1253, 3000]
Attachment functions [N vectors]	370 s [2631]	370 + 105 s [2631, 735]
FRF reduced problem [N dofs]	22270 s [30717]	9470 s [8601]
Overall CPU, reduced problem	23190 s	13240 s

Table 6.3: Details for computational time comparison, modal-based reduction of acoustic domain and porous layer.

linearly independent porous eigenvectors would enable their dynamic condensation, thus potentially greatly improving the efficiency (as shown in Chapter 3).

Furthermore, it appears that the modal reduction of the porous layer is advantageous in the present application due to the high inner-to-interface ratio of porous dofs. This raises another important well-known issue to further assess as an extension to this work: in more realistic setups where multilayer sound packages would be involved, the efficiency of a modal approach is then very dependent on the choice of the interface modelling. Considering the potentially large sizes of the bases, direct modal coupling from one layer to the other may then not offer the best answer. Use of generalized interface coordinates or Lagrange multipliers could be suitable solutions for this purpose, and remain as extensions to the present work.

Finally, downsizing the acoustic domain, as presented in Chapter 2, offers the same order of reduction as for the porous domain in this example. Due to a better preserved bandwidth (fully populated interface-sized submatrix only, as the attachment coupling submatrices are dynamically condensed), the corresponding CPU time is slightly enhanced at equal size of problem. Combining both the reduction of the acoustic and the porous

domains leads to a much further improved efficiency. Thus, such a reduced model is processed almost an order of magnitude as fast as the reference solution, even though 30% of the computational cost is associated with the initial reduction step. Put into perspective with the highly acceptable accuracy achieved (Section 6.3.4), such a combination thus offers an excellent cost versus accuracy tradeoff for the considered type of application. It is therefore retained for further tests in the following section, comparing the effects of using the Padé approximation on the complete model or its reduced version.

6.4 Padé reconstruction

In this section, the one-point Padé reconstruction procedure is applied to the reference solution of the elasto-poro-acoustic problem (Section 6.2.2), as well as to its porous- and acoustic-reduced version (Section 6.3.4). The adaptive decomposition into frequency intervals is not tested in this chapter. Rather, fixed frequency intervals are set a priori in order to estimate the potential of combining a modal-based reduction with the Padé reconstruction. In the next two sections, the performances are estimated for the reconstruction of the entire acoustic field only, checking the accuracy obtained on the sound pressure level frequency response at the output point.

6.4.1 Padé reconstruction of the reference solution

First, the one-point Padé reconstruction is applied to the full FE problem including the 3D modelling of the porous layer. After preliminary tests, frequency intervals of 10 Hz are found to be well suited for the entire frequency range, with a truncation order of $(L = 5; M = 6)$. Thus, 39 central frequencies, evenly distributed from 10 Hz to 390 Hz, are defined to estimate the solution in 1 Hz increments. The entire acoustic field solution is reconstructed (22983 dofs), while the accuracy is estimated at the output point only. For this purpose, the sound pressure level frequency response at the output point is plotted in Fig. 6.17. The excellent match with the reference solution, over the entire frequency range, confirms the accuracy of the Padé approximation. It is worth mentioning that in this case, 10 Hz intervals proved to be close to the actual average interval of convergence of the reconstruction around each central frequency. Thus, use of the adaptive decomposition in frequency intervals introduced in Chapter 5 would not bring substantial improvements to the procedure. The computational time estimates and comparisons are provided in Section 6.4.3.

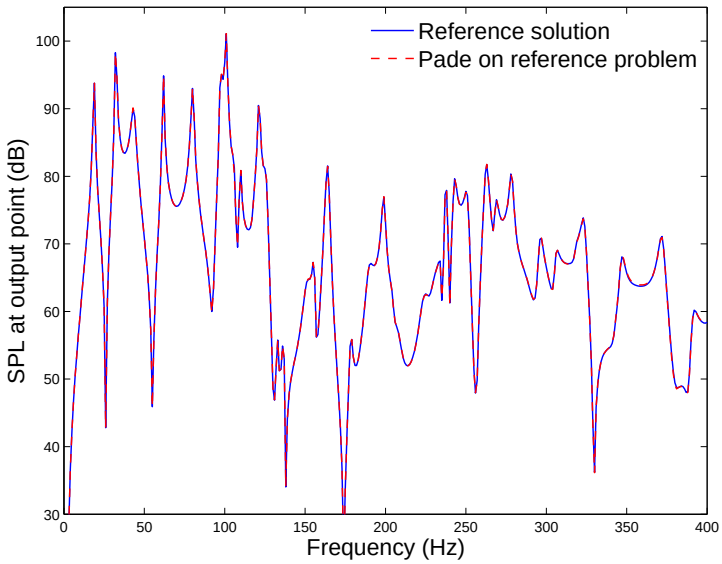

Figure 6.17: Sound pressure level at output point: Padé reconstruction on reference solution.

6.4.2 Padé reconstruction of the porous- and acoustic-reduced solution

To further estimate the potential of the Padé reconstruction applied to an approximate, reduced version of the problem, it is tested on the porous- and acoustic-reduced model. This problem, being the most reduced of all the tested ones in this chapter, has the potential for substantial computational time enhancements. However, it is also the one involving the highest level of approximations, which makes it a very good candidate to estimate the loss of accuracy when combining the two approximations. In fact, due to this loss in accuracy, preliminary tests suggest that frequency intervals downsized to 5 Hz are needed to properly render the solution over the entire frequency range (truncation order of $(L = 5; M = 6)$). Thus, 79 central frequencies, evenly distributed from 5 Hz to 395 Hz, are defined for the Padé procedure. The entire acoustic field solution is reconstructed (2631 acoustic interface dofs, followed by post-processing to reconstruct the acoustic field). The sound pressure level frequency response at the output point is plotted in Fig. 6.18 in order to estimate the achieved accuracy. It is compared to the porous- and acoustic-reduced solution, and the reference solution is also included as a dotted line. While very satisfying on average, the match between the porous- and acoustic-reduced solution and its Padé reconstructed version is not as good as the agreement observed in the previous section. Mismatches can be observed at specific frequencies such as around 95 Hz, 150 Hz, 190 Hz, 215 Hz, 255 Hz, 385 Hz. In fact, unlike for the reference solution, the interval of convergence for the reconstruction is very dependent on the given main frequency in this

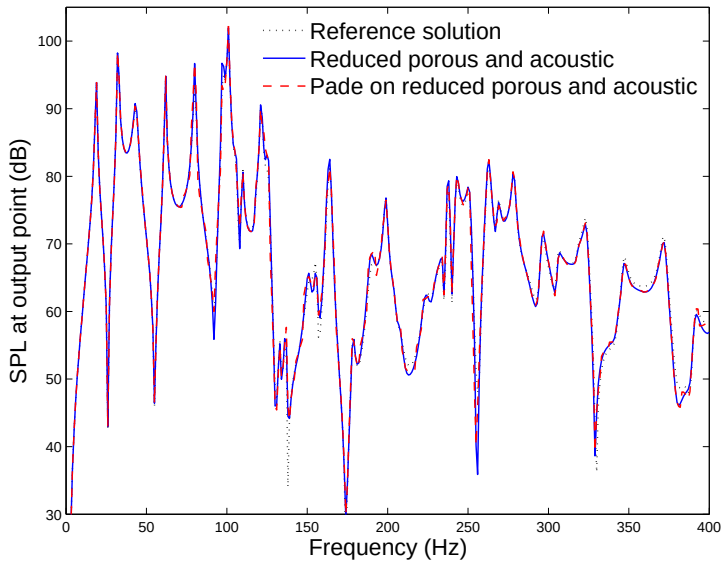

Figure 6.18: Sound pressure level at output point: Padé reconstruction on modal reduction of acoustic (truncation 1250 Hz) and porous (truncation 400 Hz) domains.

case. Thus, it can vary from as small as 2-3 Hz to more than 10 Hz around the central frequency. In this case, the adaptive procedure proposed in Chapter 5 may offer some improvements for both the accuracy and the efficiency of the reconstruction.

The next section discusses an estimated comparison of the computational efficiency with and without use of the Padé reconstruction.

6.4.3 Computational time estimates and comparisons

Figs. 6.19 presents a computational time comparison between the reference frequency sweep, the Padé reconstruction procedure (fixed frequency intervals) on the complete problem, the acoustic- and porous-reduced frequency response and its Padé reconstruction. A detailed plot excluding the complete frequency sweep is provided in Fig. 6.19b. The computational efficiency of a Padé reconstruction approach is once more demonstrated, being in this example almost as efficient as the solution with both the acoustic and porous domains reduced. Put into perspective with its achieved accuracy, its possible enhancements (e.g. a multi-point Padé approach), its ease of implementation with the constant-matrix arrangement proposed in Chapter 3 for the porous domain, it thus appears to be a very attractive method for the fast computation of frequency responses.

Furthermore, despite the cost of the initial reduction step for the modal approach, the combination of both methods proves to be very efficient in the present situation. Table 6.4 gives further insights into the time allocated to different steps of the procedure.

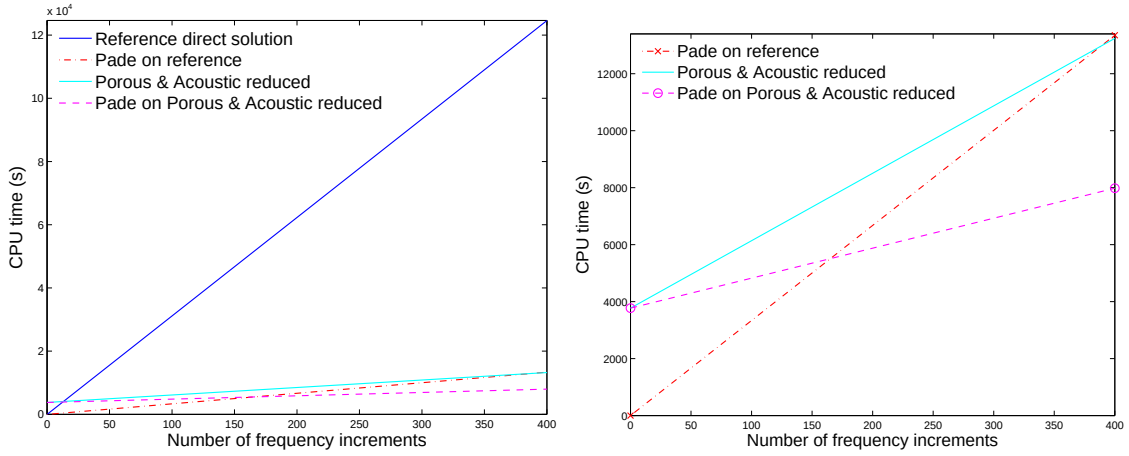

(a) (b)

Figure 6.19: Computational time comparison with Padé reconstruction: (a) comparison with reference solution, (b) detailed comparison for acoustic and porous reduced domains.

Thus, the reduced size of the problem to be solved at each main frequency (49 for the

	No reduction	***Acoustic* & *Porous* (1250 Hz, 400 Hz)**
Overall CPU, without Padé [N dofs]	124600 s [51069]	13240 s [8601]
Initial reduction step	–	3770 s
FRF with Padé [N intervals]	13350 s [49]	4210 s [79]
of which [Derivatives/Coefficients]	[12770 s/1080 s]	[4185 s/25 s]
Overall CPU with Padé	13350 s	7980 s

Table 6.4: Details for computational time comparison using a Padé reconstruction on the reference problem, and the acoustic- and porous-reduced problem.

reconstruction of the non-reduced problem, and 79 for the reconstruction of the reduced problem) greatly enhances the computation of the solution vector together with its $L+M+1 = 12$ derivatives. For the present application, this corresponds to a factor 3 reduction from CPU times of 12770 s for 49 frequencies of the complete problem, to 4185 s for 79 frequencies of the reduced model.

Another advantage of using a modal-reduced problem can be extracted from the detailed computational times. Being interested in the reconstruction of the acoustic field only, Padé coefficients corresponding to 22983 dofs are involved for the complete problem, while only the solution at interface dofs (2631 dofs) is sufficient for the modal-reduced problem. The complete solution in the acoustic domain is rebuilt from the interface solution in a post-processing step. Consequently, the time allocated to the determination of the Padé coefficients and the estimation of the solution is reduced from 1080 s to 25 s in

the considered example.

In conclusion, despite the fact that the loss of accuracy required a finer frequency discretization for the reconstruction, it is in this case more than compensated by the Padé procedure greatly benefiting from a substantial reduction of the model to be solved. Thus, for the present problem, combining a modal reduction of the acoustic and porous domains with a Padé reconstruction strategy over 400 Hz leads to a solution more than 15 times as efficient as the estimated solution with the complete FE model.

6.5 Conclusion

In this chapter, both the modal-based reduction approach and the one-point Padé reconstruction procedure were tested on a larger elasto-poro-acoustic application as compared to the validation cases used in the previous chapters. The following conclusions can be drawn out of the results obtained in terms of accuracy and computational time estimations:

- The dynamic condensation of the acoustic domain to its interface confirmed to be satisfactory in terms of accuracy and computational time enhancements. In the considered example, it is worth noticing that even though a direct modal approach could have been more appropriate considering the dimension of acoustic interfaces, the component approach remained computationally efficient. The a priori truncation of the acoustic modal basis at 2.5 times the highest frequency of interest proved satisfactory. Considering the small added cost, a truncation at 3 times the highest frequency of interest was mostly used in order to ensure accuracy of the acoustic response.

- The modal-based reduction of the porous media proposed in Chapter 3 proved to be efficient and satisfyingly accurate for the reduction of a single layer backed with a rigid wall. As expected, large porous modal bases are involved, which implies a costly initial step in the solution procedure (both in terms of computational time and memory management). The initial step is however shown to be well-compensated by the computational enhancements of the frequency sweep. An a priori truncation criterion of twice the highest frequency of interest was used. However, a truncation at one time the highest frequency of interest proved to be well suited, which raises the question of an appropriate a priori truncation estimate. Furthermore, while the sparsity of the reduced problem confirmed its consequences in terms of computational time enhancements, further condensation of the modal coordinates corresponding to the linearly independent modes was not tested. It is however expected to bring sub-

stantial efficiency improvements, considering the impact of a well preserved matrix bandwidth at larger model sizes.

- In case of an overestimated truncation, the mode selection and truncation procedure proposed in Chapter 4 was found to be appropriate for the task. In the considered application, it enabled the downsizing of the basis truncated at twice the highest frequency of interest to a smaller size than the one truncated at the highest frequency of interest, without a significant loss of accuracy. This is particularly encouraging when put into perspective with the much more evenly spread participation of the porous modes to the response. In this context, the question of the truncation is once more raised, and needs to be further evaluated on a wider range of applications.
- Finally, the Padé reconstruction strategy confirmed its high level of computational performances, achieving excellent accuracy under computational time improvements of almost an order of magnitude. The adaptive central frequency procedure proposed in Chapter 5 was not tested, and fixed frequency intervals were set instead. It may however prove to be most interesting when used in combination with a modal-based reduced model together with a Padé reconstruction approach. In fact, in such a solution scheme, the convergence of the Padé method was shown to be dependent on the choice of the main frequencies. However, even without the use of adaptive frequency intervals, such a combination of a reduced model (porous and acoustic domains in this case) with a Padé reconstruction offered benefits in the tradeoff between representation of the dynamic behavior and computational efficiency.

Following the analysis made of the results obtained, the following non-exhaustive list of suggestions for further works can be established:

- Considering the expensive generation of the porous modal bases, a more case-related way of generating the reduction basis, such as the generation of load-dependent Ritz vectors, may prove more efficient;
- In order to include the proposed reduction of porous materials in more complex configurations, the handling of interface functions has to be addressed, and the efficiency of a modal approach in such problems remains to be proven;
- The use of proper a priori truncation estimates for the porous modes needs to be further investigated in order to improve the initial reduction step of the modal approach;
- Proper, efficient error estimators are important tools to combine with reduced models. Therefore, refined estimators providing reliable levels are of utmost importance in order to provide guidance in the selection of the most efficient reduced models;

- Although not required for the levels of precision aimed for, the use of enrichment functions (e.g. orthogonalized pseudo-static responses or residual vectors) to enhance the achieved accuracy is a natural extension to this work.

Conclusion

The objective of the present work was to propose solution strategies for interior structural-acoustic applications including 3D modelling of homogeneous and isotropic poroelastic materials. Solutions were sought in the frequency domain, in response to time-harmonic excitations, and in the low frequency range. First, focus was given to the acoustic domain, implementing and testing a dynamic condensation method in an existing FE code (Fortran implementation). Some conclusions drawn from this preliminary study raised some questions, which oriented the choices made for the second part of the thesis, focusing on the porous domain. A porous modal approach, together with a solution reconstruction strategy using rational function expansions was thus proposed, and validated on simple poro-acoustic applications. The final part presented a synthesis of the tested methods, applied to a medium-sized academic application, comparing and demonstrating the potential of the contributions made.

Summary of the main contributions. In ***Chapter 2***, a CMS approach applied to the acoustic domain of a coupled elasto-poro-acoustic problem was tested. While very popular in structural dynamics, the investigation proposed for a medium-sized acoustic application allowed to emphasize both the performances and limitations of such an approach in vibroacoustics. It was implemented in a Fortran FE code (FEAP), in the aim to provide consistent results in terms of computational efficiency. Essentially, the conclusions drawn were (i) the computational interest of the approach for high volume-to-interface dofs ratios, (ii) the well-known need to propose a reduced set of attachment functions in order to maintain the computational efficiency of the method for large interfaces, and (iii) the potential need to enrich the reduction basis for accuracy purposes in frequency regions of strong interactions between coupled subdomains. This latter point was particularly taken into account for the choices made to propose a similar modal approach for porous materials. The results were presented in international conferences (ECCM 2010, WCCM 2010), partly published in a national conference [128], and fully published in an international peer-reviewed journal [114].

In ***Chapter 3***, an original way of solving the poroelastic equations was presented, using a rearrangement of the porous constitutive equation for the ($\mathbf{u}_s$,$\mathbf{u}_f$) formulation. Following the corresponding variational formulation, a modal approach was proposed for porous subdomains. It was validated on small 1D and 3D poro-acoustic applications for both its accuracy and computational efficiency. In addition, the potential of the method for larger scaled applications was estimated in terms of preserved system matrix sparsity and bandwidth. The original findings were partly published in an international conference [129], and are under revision for a contribution into an international peer-reviewed journal.

Chapter 4 was dedicated to some enhancements of the modal approach proposed for the porous materials. Due to the large modal bases involved in 3D applications, an original refinement procedure was proposed, including a sorting step followed by a further truncation of the basis. It was tested on 1D to 3D poro-acoustic validation cases, and showed to partly compensate for the unanswered question of an optimal a priori truncation criterion for the modal basis. The results were presented in a porous material dedicated international symposium (SAPEM 2011), partly published in an international peer-reviewed conference [130], and will be fully published in an article in preparation, to be submitted to an international peer-reviewed journal.

In ***Chapter 5***, the original rewriting of the porous equations in Chapter 3 was put to advantage in order to propose the combination of a modal-reduced model, together with a Padé-based reconstruction strategy. In addition, an adaptive decomposition in frequency intervals was proposed for the reconstruction approach. It enables to benefit from an enhanced tradeoff between computational efficiency and accuracy. The validation on 2D and 3D poro-acoustic test cases proved very promising for extension to larger and more complex applications. The results will be partly published in an international conference [131], and will be fully published in an article in preparation, to be submitted to an international peer-reviewed journal.

Chapter 6 presented a synthesis of most of the methods used in the previous chapters, both for the acoustic and porous domains. A benchmark of the different approaches was made on an academic validation case proposed within Marie-Curie European project "Mid-Frequency". Although entirely implemented in Matlab, this comparison offered very encouraging results in terms of accuracy and computational efficiency. Furthermore, it provided further insights into the most relevant perspectives to give to the present contributions.

Perspectives. Among the perspectives that have been mentioned along this work, the following points are particularly worth mentioning:

- In situations where better accuracy is sought than in the examples presented, use of improved attachment functions and other enrichments of the reduction basis (e.g. orthogonalized pseudo-static responses or residual vectors) could be considered, provided they can be integrated in a computationally efficient way;

- The modal approach for porous materials, proposed in this work, needs to be further tested in more complex situations: (i) in configurations where the solid frame of the porous materials would be more directly excited (e.g. in contact with a flexible structure, or with an impervious membrane), (ii) in sandwich configurations where

the question of well-chosen interface modelling for multilayer assemblies will become essential for the efficiency of the approach;

- Furthermore, such extensive testing could enable a refinement of the a priori truncation estimate for the porous modal bases;
- The reduced models have been compared to an efficient implementation of the $(\mathbf{u}_s, \mathbf{u}_f)$ porous formulation, and comparisons with the more efficient $(\mathbf{u}_s, p)$ porous formulation will be proposed in publications of the content of this work in international peer-reviewed journals.
- An approach based on the generation of a load-dependent Ritz basis could offer the possibility to partly overcome the high computational cost of the initial reduction step for the porous modal method;
- The close-to-diagonal (and diagonal-dominant) form of the modal-reduced porous system could benefit from an iterative solution scheme, where the modal coupling terms are handled as iterative corrections on the right-hand side vector,

Appendix A

Résumé étendu des travaux de thèse

A.1 Introduction

Dans le contexte de lutte contre les nuisances sonores, cette thèse porte sur le développement de méthodes de résolution efficaces par éléments finis, pour des problèmes de vibroacoustique interne avec interfaces dissipatives, dans le domaine des basses fréquences. L'étude se limite à l'utilisation de solutions passives telles que l'intégration de matériaux poreux homogènes et isotropes, modélisés par une approche fondée sur la théorie de Biot-Allard. Ces modèles étant coûteux en terme de résolution, un des objectifs de cette thèse est de proposer une approche modale pour la réduction du problème poroélastique, bien que l'adéquation d'une telle approche avec le comportement dynamique des matériaux poreux soit à démontrer.

Dans un premier temps, la résolution de problèmes couplés elasto-poro-acoustiques par sous-structuration dynamique des domaines acoustiques et poreux est établie. L'approche modale originale ensuite proposée pour les milieux poroélastiques, ainsi qu'une procédure de sélection des modes significatifs, sont validées sur des exemples 1D à 3D.

Une deuxième partie présente une méthode combinant l'utilisation des modèles réduits précédemment établis avec une procédure d'approximation de solution par approximants de Padé. Il est montré qu'une telle combinaison offre la possibilité d'accroître les performances de la résolution (allocation mémoire et ressources en temps de calcul).

Un chapitre dédié aux applications permet d'évaluer et comparer les approches sur un problème académique 3D, mettant en valeur leurs performances prometteuses. Afin d'améliorer les méthodes établies dans cette thèse, des perspectives à ces travaux de recherche sont apportées en conclusion.

Ce travail a été réalisé dans le cadre d'une cotutelle de thèse entre le Conservatoire National des Arts et Métiers (Cnam) à Paris, et le Royal Institute of Technology (KTH) à Stockholm, co-encadré par Pr. Jean-François Deü et Pr. Peter Göransson.

A.2 Chapitre 1: Introduction à la modélisation de matériaux poreux pour la réduction de bruit en vibro-acoustique interne

Dans ce chapitre, les principales hypothèses délimitant la portée du travail effectué sont énoncées, situant le contenu de la thèse dans son contexte scientifique. Les principales contributions menant à la théorie de Biot-Allard sur la propagation d'ondes acoustiques en milieux poroélastiques sont placées dans leur contexte historique. Un examen des récentes méthodes (analytiques, semi-analytiques, numériques) développées pour la modélisation de problèmes de vibroacoustique et de matériaux absorbants, permet de dégager les orientations de recherche dans lesquelles s'inscrit la présente thèse: la nécessité d'utiliser des modèles multiphysiques raffinés tout en offrant une efficacité de résolution industriellement compatible.

L'intérêt de modèles physiques raffinés, telle que la théorie de Biot-Allard pour les matériaux poreux, est illustré par une comparaison avec une modélisation par impédance localisée. Dans une configuration très favorable à cette dernière approche, une cavité rigide dont une face est recouverte d'un matériau poreux (Fig. A.1), est modélisée suivant ces deux hypothèses. La cavité est excitée en un coin opposé à la surface absorbante, alors que la pression acoustique moyenne dans la cavité est calculée comme grandeur d'intérêt.

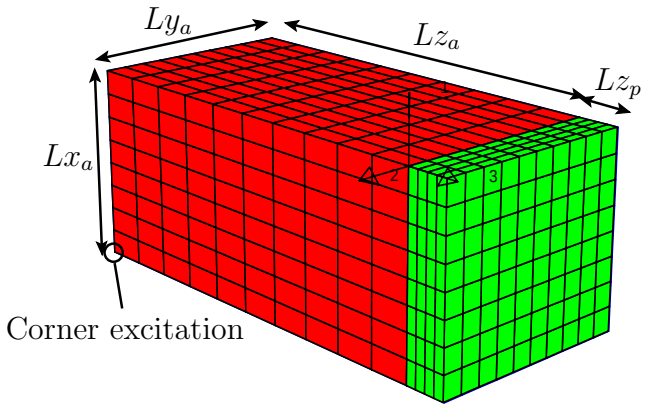

Figure A.1: Géométrie utilisée pour la comparaison entre modélisation 3D ou par impédance localisée pour un matériau poreux.

La comparaison des résultats est donnée Fig. A.2, pour deux cavités de dimensions proches. Bien que l'approche par impédance localisée soit très attractive, compte tenu

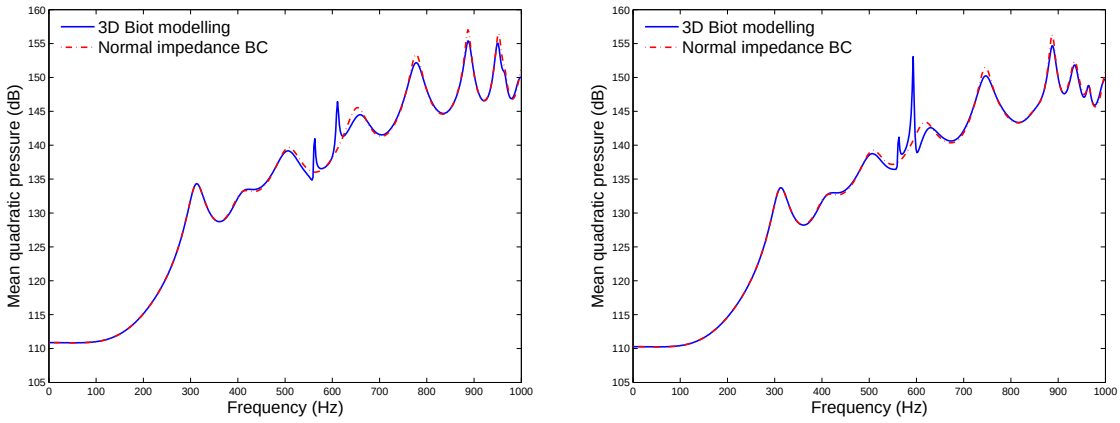

(a) (b)

Figure A.2: Pression quadratique moyenne dans la cavité, modèle de Biot 3D ou par impédance localisée, $Lz_p = 0.05$ m: (a) $(Lx_a, Ly_a, Lz_a) = (0.28, 0.4, 0.5)$ m; (b) $(Lx_a, Ly_a, Lz_a) = (0.3, 0.4, 0.5)$ m.

de sa simplicité et de son efficacité, elle ne permet pas, dans cette configuration pourtant favorable, de capturer les résonances du système couplé dans la bande [500 - 600] Hz. Cette discordance est accentuée par la représentation du champ de pression dans la cavité (Fig.A.3), à 593 Hz, pour la configuration présentée en Fig. A.2b

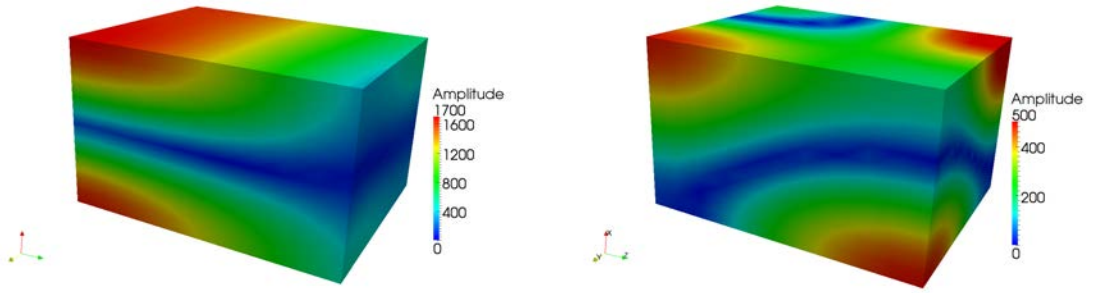

(a) (b)

Figure A.3: Amplitude du champ de pression acoustique, $(Lx_a, Ly_a, Lz_a) = (0.3, 0.4, 0.5)$ m, $Lz_p = 0.05$ m, à 593 Hz: (a) Modèle de Biot 3D pour le matériau poreux; (b) Condition limite d'impédance localisée.

Les principales équations dérivées dans la théorie de Biot-Allard sont ensuite présentées pour référence dans les chapitre ultérieures. Le chapitre conclut sur une discussion synthétique de la modélisation numérique de systèmes amortis par modèles réduits, aboutissant sur les choix de formulation effectués pour la thèse: une formulation ($\mathbf{u}_S$-p) pour le problème de vi-

broacoustique interne, ainsi que la formulation en déplacement ($\mathbf{u}_\mathrm{s}$,$\mathbf{u}_\mathrm{f}$) pour la modélisation de matériaux poreux. Une des raisons justifiant le choix d'une formulation en déplacement pour le matériau poreux, par rapport à une formulation mixte [51] plus efficace, est son potentiel à générer des modes fluides-structures couplés, pour la construction de modèles réduits.

A.3 Chapitre 2: Décomposition par sous-structuration pour problèmes de vibroacoustique amortis

Dans ce chapitre, une approche modale pour la partie fluide d'un problème de vibroacoustique interne est testée. Elle est intégrée dans un schéma de résolution par décomposition en sous-domaines acoustiques, analogue à la méthode classique de sous-structuration dynamique à interface fixe proposée par Craig et Bampton [85]. Une telle décomposition intègre directement la base tronquée de modes acoustiques (à pression acoustique nulle aux interfaces), ainsi qu'une correction des effets de troncature inclus dans les fonctions d'attache. Ces fonctions d'attache sont solutions de l'équation de Laplace, en réponse à une fluctuation de pression acoustique unitaire imposée successivement à chaque degré de liberté d'interface, les autres restant restreints. Il est établi qu'une telle transformation permet de limiter la résolution à celle d'un problème de la dimension des interfaces (pour les sous domaines condensés).

Ainsi, la forme générale suivante d'un problème éléments finis élasto-poro-acoustique est considérée,

$$\begin{bmatrix} \mathbf{K}_\mathrm{S}-\omega^2\mathbf{M}_\mathrm{S} & -\mathbf{C}_\mathrm{IS}^T & \mathbf{0} & \mathbf{0} & \mathbf{0} \\ -\omega^2\mathbf{C}_\mathrm{IS} & \mathbf{K}_{II}-\omega^2\mathbf{M}_{II} & \mathbf{K}_{I\bar{I}}-\omega^2\mathbf{M}_{I\bar{I}} & -\omega^2(1-\phi)\mathbf{C}_\mathrm{Is} & -\omega^2\phi\mathbf{C}_\mathrm{If} \\ \mathbf{0} & \mathbf{K}_{\bar{I}I}-\omega^2\mathbf{M}_{\bar{I}I} & \mathbf{K}_{\bar{I}\bar{I}}-\omega^2\mathbf{M}_{\bar{I}\bar{I}} & \mathbf{0} & \mathbf{0} \\ \mathbf{0} & -(1-\phi)\mathbf{C}_\mathrm{Is}^T & \mathbf{0} & \widetilde{\mathbf{K}}_\mathrm{ss}-\omega^2\widetilde{\mathbf{M}}_\mathrm{ss} & \widetilde{\mathbf{K}}_\mathrm{sf}-\omega^2\widetilde{\mathbf{M}}_\mathrm{sf} \\ \mathbf{0} & -\phi\mathbf{C}_\mathrm{If}^T & \mathbf{0} & \widetilde{\mathbf{K}}_\mathrm{fs}-\omega^2\widetilde{\mathbf{M}}_\mathrm{fs} & \widetilde{\mathbf{K}}_\mathrm{ff}-\omega^2\widetilde{\mathbf{M}}_\mathrm{ff} \end{bmatrix} \times \begin{bmatrix} \mathbf{U}_\mathrm{S} \\ \mathbf{P}_I \\ \mathbf{P}_{\bar{I}} \\ \mathbf{U}_\mathrm{s} \\ \mathbf{U}_\mathrm{f} \end{bmatrix} = \begin{bmatrix} \mathbf{F}_\mathrm{Sb} \\ \omega^2\mathbf{U}_\mathrm{Ib} \\ \mathbf{0} \\ \mathbf{0} \\ \mathbf{0} \end{bmatrix}, \tag{A.1}$$

où le vecteur des inconnues nodales est constitué de $\mathbf{U}_\mathrm{S}$, inconnues du champ de déplacement de la structure, $\mathbf{P}_I$, inconnues du champ de pression acoustique situées aux interfaces, $\mathbf{P}_{\bar{I}}$, inconnues du champ de pression acoustique interne, $\mathbf{U}_\mathrm{s}$ et $\mathbf{U}_\mathrm{f}$, inconnues des champs de déplacement des phases solide et fluide respectivement, du matériau poreux. Après changement de base et condensation des inconnues modales aux interfaces, il est établi que le

problème A.1 se résume à la résolution du problème réduit suivant,

$$\begin{bmatrix} \mathbf{K}_{\mathrm{S}} - \omega^2 \mathbf{M}_{\mathrm{S}} & -\mathbf{C}_{\mathrm{IS}}^T & \mathbf{0} & \mathbf{0} \\ -\omega^2 \mathbf{C}_{\mathrm{IS}} & \mathbf{K}_{II}^\star - \omega^2 \mathbf{M}_{II}^\star - \omega^4 \mathbf{M}_{II}^\circ(\omega) & -\omega^2(1-\phi)\mathbf{C}_{\mathrm{Is}} & -\omega^2 \phi \mathbf{C}_{\mathrm{If}} \\ \mathbf{0} & -(1-\phi)\mathbf{C}_{\mathrm{Is}}^T & \widetilde{\mathbf{K}}_{\mathrm{ss}} - \omega^2 \widetilde{\mathbf{M}}_{\mathrm{ss}} & \widetilde{\mathbf{K}}_{\mathrm{sf}} - \omega^2 \widetilde{\mathbf{M}}_{\mathrm{sf}} \\ \mathbf{0} & -\phi \mathbf{C}_{\mathrm{If}}^T & \widetilde{\mathbf{K}}_{\mathrm{fs}} - \omega^2 \widetilde{\mathbf{M}}_{\mathrm{fs}} & \widetilde{\mathbf{K}}_{\mathrm{ff}} - \omega^2 \widetilde{\mathbf{M}}_{\mathrm{ff}} \end{bmatrix} \times \begin{bmatrix} \widehat{\mathbf{U}}_{\mathrm{S}} \\ \widehat{\mathbf{P}}_I \\ \widehat{\mathbf{U}}_{\mathrm{s}} \\ \widehat{\mathbf{U}}_{\mathrm{f}} \end{bmatrix} = \begin{bmatrix} \mathbf{F}_{\mathrm{Sb}} \\ \omega^2 \mathbf{U}_{\mathrm{Ib}} \\ \mathbf{0} \\ \mathbf{0} \end{bmatrix}, \tag{A.2}$$

où $\mathbf{P}_{\bar{I}}$, le vecteur des inconnues du champ de pression acoustique interne ne figure plus explicitement, et avec $\mathbf{K}_{II}^\star$, $\mathbf{M}_{II}^\star$ et $\mathbf{M}_{II}^\circ(\omega)$ obtenus par procédure d'assemblage sur les n sous-domaines acoustiques,

$$\mathbf{K}_{II}^\star = \sum_{j=1}^{n} {\boldsymbol{\beta}_{JI}^{(j)}}^T \hat{\mathbf{K}}_{JJ} \boldsymbol{\beta}_{JI}^{(j)}, \tag{A.3a}$$

$$\mathbf{M}_{II}^\star = \sum_{j=1}^{n} {\boldsymbol{\beta}_{JI}^{(j)}}^T \left[\hat{\mathbf{M}}_{JJ} + {\boldsymbol{\Psi}_{\bar{J}J}}^T \hat{\mathbf{M}}_{\bar{J}J} \right] \boldsymbol{\beta}_{JI}^{(j)}, \tag{A.3b}$$

$$\mathbf{M}_{II}^\circ(\omega) = \sum_{j=1}^{n} {\boldsymbol{\beta}_{JI}^{(j)}}^T \left[\left[\boldsymbol{\Phi}_{\bar{J}m}^T \hat{\mathbf{M}}_{\bar{J}J} \right]^T \left(\boldsymbol{\Omega}_m - \omega^2 \, \mathbf{1}_m \right)^{-1} \left[\boldsymbol{\Phi}_{\bar{J}m}^T \hat{\mathbf{M}}_{\bar{J}J} \right] \right] \boldsymbol{\beta}_{JI}^{(j)}. \tag{A.3c}$$

Plusieurs configurations sont ensuite testées afin d'identifier les performances et limites de l'approche modale par décomposition en sous-domaines acoustiques. Les conclusions ont pour intérêt de donner des orientations pour étendre l'approche à la réduction de milieux dissipatifs tels que les matériaux poreux. Une des applications de référence utilisée dans ce chapitre est issue d'une collaboration au sein du projet européen Marie-Curie "Smart Structures", donnant lieu au modèle numérique *concrete car*. Il s'agit, à l'origine, d'un dispositif expérimental composé de deux cavités rigides (murs en béton), reliées par l'intermédiaire d'un évidemment sur une des faces, pouvant être obstrué par une plaque. Le modèle numérique associé est présenté sur la figure A.4, les grandeurs d'intérêt étant la pression quadratique moyenne dans chacune des deux cavités: la cavité moteur, et la cavité passager. Afin d'estimer l'impact de l'ajout d'une couche de revêtement poreux sur une des faces de la cavité passager, deux modèles numériques sont établis, avec et sans matériau poreux. La fonction de réponse en fréquence de référence est présentée sur la figure A.5 pour les deux configurations, illustrant l'effet d'absorption acoustique dans la cavité passager.

La réponse avec matériau absorbant est utilisée comme référence pour comparaison avec des solutions calculées avec modèles réduits (Eq. A.2), pour différentes troncatures

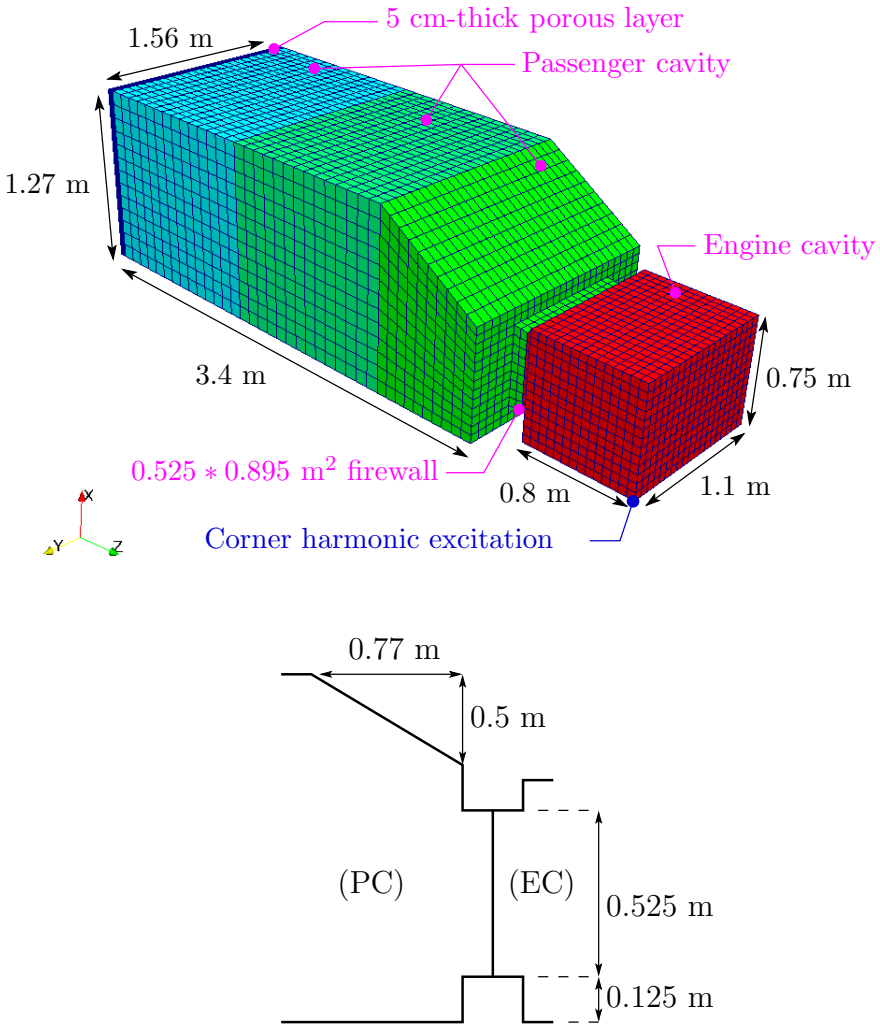

Figure A.4: Modèle EF *Concrete car* et dimensions extérieures.

de la base modale. Les figures A.6 présentent une comparaison des fonctions de réponse en fréquence, de référence ou avec troncature à 1980 Hz (supérieure à trois fois la fréquence maximale d'intérêt), ainsi qu'une illustration de la convergence en fonction de la fréquence propre de troncature. La représentation choisie de l'erreur commise est une représentation interpolée par courbes de Bézier, de la différence point par point, entre les réponses. Bien que discutable à plusieurs niveaux (e.g. l'erreur non significative au niveau des pics de résonances implique une sur-évaluation de l'erreur commise), elle permet une bonne illustration de la convergence de la réduction. Ces résultats mettent en évidence une excellente approximation de la réponse dans la cavité moteur, tandis que l'erreur commise dans la cavité passager est plus importante. Un ensemble de cas tests permet par la suite

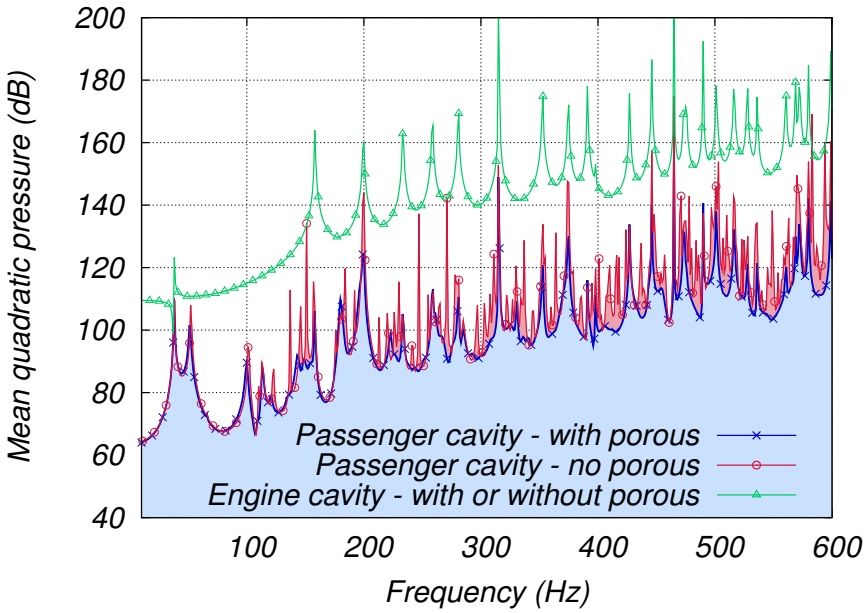

Figure A.5: FRF de référence avec et sans traitement poreux.

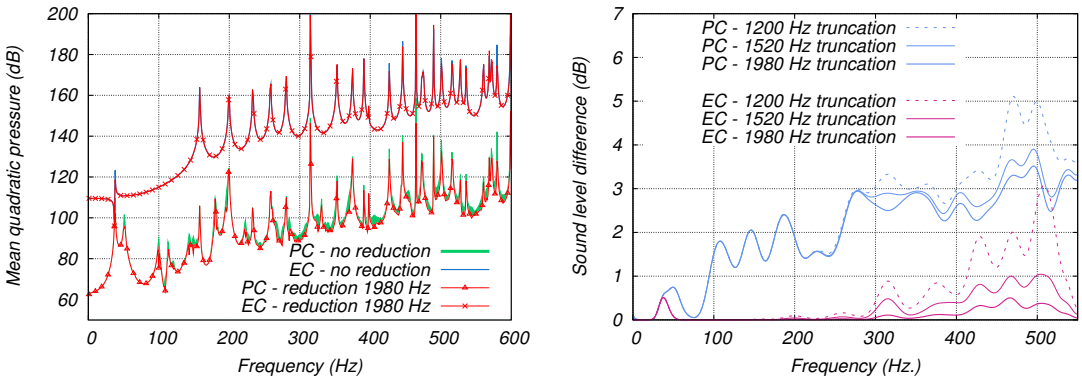

(a) (b)

Figure A.6: Résultats avec troncature jusqu'à 1980 Hz: (a) FRF, pression quadratique moyenne; (b) différence (dB) à la solution du problème non réduit.

d'identifier les sources d'erreur, ainsi que d'envisager des solutions permettant d'améliorer la précision de la réponse approximée. Il est ainsi mis en évidence que les bandes de fréquences où la réponse est dominée par des modes de résonance de plaque présentaient des difficultés de convergence. Il en est de même pour les domaines fréquentiels où les conditions absorbantes ont un impact important sur la réponse du système. L'utilisation de modes d'attache raffinés (e.g. pseudo-statiques), ou d'enrichissements de la base modale par des vecteurs de réponses ou de résidus orthogonalisés sont des extensions envisagées, ex-

istantes dans la littérature, permettant potentiellement de répondre à cette problématique.

D'un point de vue performance en termes de temps de calcul, l'approche modale, introduite dans le cadre d'une décomposition en sous-domaines acoustiques, est présentée sur la figure A.7. Au-delà de la réduction en temps de calcul, le coût de l'étape initiale

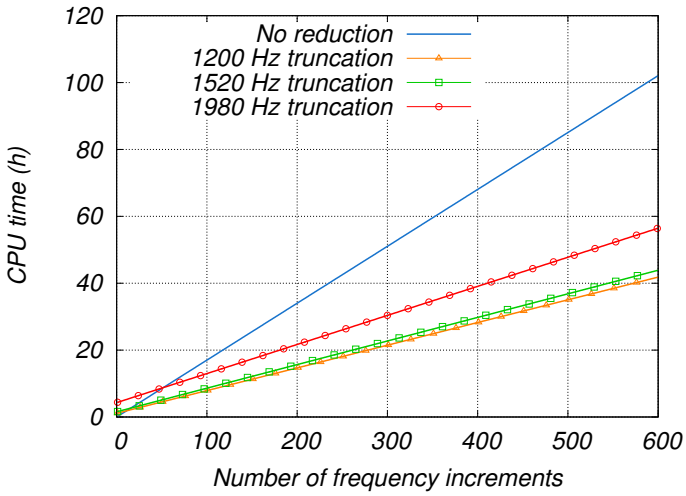

Figure A.7: Comparaison du temps de calcul, CPU.

de calcul des modes et de projection du problème est mise en évidence. De plus, la condensation dynamique des inconnues modales permet d'observer un faible impact de l'augmentation de la taille la base modale sur le temps de calcul par incrément de fréquence.

En termes d'orientation au regard des objectifs de la thèse (e.g. approche modale pour les matériaux poreux), les difficultés de convergence observées, pour la réduction modale des sous-domaines acoustiques du problème de vibroacoustique lors d'interactions fortes entre sous-domaines, permettent d'apporter d'autres indications quant aux choix effectués. Ainsi, pour les matériaux poreux, caractérisés par un couplage fort, volumique (en opposition à un couplage surfacique dans le cas de la sous-structuration) entre la phase fluide et la phase solide, il apparaît qu'une approche fondée sur des modes couplés intégrant le couplage des phases solide et fluide permettra une meilleure prise en compte du comportement multiphysique des milieux poreux. En conséquence, l'extension de l'approche modale à la réduction des milieux poroélastiques est menée en ce sens dans les chapitres suivants, impliquant une reconsidération des équations de la formulation ($\mathbf{u}_s$,$\mathbf{u}_f$) pour la modélisation de matériaux poreux.

A.4 Chapitre 3: Approche modale pour les matériaux poreux

Dans ce chapitre, les équations de la formulation ($\mathbf{u}_\mathrm{s}$,$\mathbf{u}_\mathrm{f}$) sont réarrangées afin d'être exploitables pour une approche par synthèse modale. Ainsi, les effets visqueux et inertiels, traditionnellement intégrés dans l'expression d'une masse volumique équivalente, sont considérés séparément. Par ailleurs, la loi de comportement est séparée en une composante basse fréquence et plus haute fréquence. Ce dernier point est établi sous l'hypothèse d'un module de compression du matériau de la matrice très supérieur aux modules de compression de la matrice ou du fluide saturant le matériau (typiquement le cas pour les matériaux poreux à application acoustique). Dès lors, les lois de comportement peuvent être réécrites en fonction du module de compression équivalent de la phase fluide, $\widetilde{K}_\mathrm{f}(\omega)$, complexe et dépendant de la fréquence, pouvant s'écrire sous la forme

$$\widetilde{K}_\mathrm{f} = \frac{\gamma P_0}{\gamma - (\gamma-1)\left[1 + \frac{8\eta}{i\omega Pr\Lambda'^2\rho_\mathrm{f}}\left(1 + \frac{i\omega Pr\Lambda'^2\rho_\mathrm{f}}{16\eta}\right)^{\frac{1}{2}}\right]^{-1}} = P_0 + \left(\widetilde{K}_\mathrm{f} - P_0\right), \tag{A.4}$$

séparant la limite à fréquence nulle, de la dépendance en fréquence (qui est à valeurs complexes). Par conséquence, la loi de comportement, prenant en compte la séparation précédente, peut s'écrire sous la forme

$$\boldsymbol{\sigma}_\mathrm{s} = \mathbf{D}_\mathrm{s}^{(1)}\,\boldsymbol{\varepsilon}(\mathbf{u}_\mathrm{s}) + \mathbf{D}_\mathrm{sf}^{(1)}\,\boldsymbol{\varepsilon}(\mathbf{u}_\mathrm{f}) + \left(\widetilde{K}_\mathrm{f} - P_0\right)\left(\mathbf{D}_\mathrm{s}^{(2)}\,\boldsymbol{\varepsilon}(\mathbf{u}_\mathrm{s}) + \mathbf{D}_\mathrm{sf}^{(2)}\,\boldsymbol{\varepsilon}(\mathbf{u}_\mathrm{f})\right), \tag{A.5a}$$

$$\boldsymbol{\sigma}_\mathrm{f} = \mathbf{D}_\mathrm{sf}^{(1)}\,\boldsymbol{\varepsilon}(\mathbf{u}_\mathrm{s}) + \mathbf{D}_\mathrm{f}^{(1)}\,\boldsymbol{\varepsilon}(\mathbf{u}_\mathrm{f}) + \left(\widetilde{K}_\mathrm{f} - P_0\right)\left(\mathbf{D}_\mathrm{sf}^{(2)}\,\boldsymbol{\varepsilon}(\mathbf{u}_\mathrm{s}) + \mathbf{D}_\mathrm{f}^{(2)}\,\boldsymbol{\varepsilon}(\mathbf{u}_\mathrm{f})\right), \tag{A.5b}$$

avec

$$\begin{aligned}
\mathbf{D}_\mathrm{s}^{(1)} &= 2\widetilde{\mu}\,\mathbf{D}' + \left(\widetilde{\lambda} + \frac{(1-\phi)^2}{\phi}P_0\right)\mathbf{D},\\
\mathbf{D}_\mathrm{sf}^{(1)} &= (1-\phi)\,P_0\,\mathbf{D},\\
\mathbf{D}_\mathrm{f}^{(1)} &= \phi\,P_0\,\mathbf{D},\\
\mathbf{D}_\mathrm{s}^{(2)} &= \frac{(1-\phi)^2}{\phi}\mathbf{D},\\
\mathbf{D}_\mathrm{sf}^{(2)} &= (1-\phi)\,\mathbf{D},\\
\mathbf{D}_\mathrm{f}^{(2)} &= \phi\,\mathbf{D},
\end{aligned}$$

où

$$\mathbf{D}' = \begin{bmatrix} 1 & 0 & 0 & 0 & 0 & 0 \\ 0 & 1 & 0 & 0 & 0 & 0 \\ 0 & 0 & 1 & 0 & 0 & 0 \\ 0 & 0 & 0 & \frac{1}{2} & 0 & 0 \\ 0 & 0 & 0 & 0 & \frac{1}{2} & 0 \\ 0 & 0 & 0 & 0 & 0 & \frac{1}{2} \end{bmatrix} \quad \text{et} \quad \mathbf{D} = \begin{bmatrix} 1 & 1 & 1 & 0 & 0 & 0 \\ 1 & 1 & 1 & 0 & 0 & 0 \\ 1 & 1 & 1 & 0 & 0 & 0 \\ 0 & 0 & 0 & 0 & 0 & 0 \\ 0 & 0 & 0 & 0 & 0 & 0 \\ 0 & 0 & 0 & 0 & 0 & 0 \end{bmatrix}.$$

Cette décomposition permet ainsi, après formulation variationnelle, d'écrire le problème éléments finis poroélastique sous la forme de quatre matrices globales, réelles et constantes, la dépendance en fréquence étant portée par des fonctions scalaires en facteur: deux parties pour la matrice de rigidité, une matrice pour les effets visqueux, puis une matrice pour les effets inertiels. Suivant les notations présentées sur la figure A.8, séparant les degrés de liberté acoustiques d'interface et internes, le problème poro-acoustique d'intérêt pour

Figure A.8: Description du problème pour la réduction du domaine poreux.

l'approche modale s'écrit sous la forme

$$\left[\begin{array}{c|c|c} \mathbf{K}_{\bar{I}\bar{I}} - \omega^2 \mathbf{M}_{\bar{I}\bar{I}} & \mathbf{K}_{\bar{I}I} - \omega^2 \mathbf{M}_{\bar{I}I} & \mathbf{0} \\ \hline \mathbf{K}_{I\bar{I}} - \omega^2 \mathbf{M}_{I\bar{I}} & \mathbf{K}_{II} - \omega^2 \mathbf{M}_{II} & -\omega^2 \mathbf{A}_{I\mathrm{P}} \\ \hline \mathbf{0} & -\mathbf{A}_{I\mathrm{P}}^T & \begin{array}{c} \mathbf{K}_{\mathrm{P}}^{(1)} + \left(\widetilde{K}_{\mathrm{f}} - P_0\right) \mathbf{K}_{\mathrm{P}}^{(2)} + \\ \mathrm{i}\,\omega\,\widetilde{b}\,\mathbf{C}_{\mathrm{P}} - \omega^2 \mathbf{M}_{\mathrm{P}} \end{array} \end{array}\right] \begin{bmatrix} \mathbf{P}_{\bar{I}} \\ \mathbf{P}_I \\ \mathbf{U}_{\mathrm{P}} \end{bmatrix} = \begin{bmatrix} \omega^2 \mathbf{U}_{\bar{I}\mathrm{b}} \\ \mathbf{0} \\ \mathbf{0} \end{bmatrix}. \quad \text{(A.7)}$$

Le problème peut être symétrisé en divisant les équations acoustiques (lignes 1 et 2) par ω^2 ($\omega \neq 0$).

Une approche modale basse fréquence peut ensuite être définie à partir du problème aux valeurs propres

$$\left(\mathbf{K}_{\mathrm{P}}^{(1)} - \omega^2 \mathbf{M}_{\mathrm{P}}\right) \boldsymbol{\phi} = \mathbf{0}, \quad \text{(A.8)}$$

sélectionnant les modes classés par fréquence propre ascendante, après normalisation par rapport à la matrice de masse $\mathbf{M}_{\mathrm{P}}$. Ces modes s'avèrent être séparables entre ceux qui présentent la caractéristique d'être orthogonaux (o modes "orthogonaux") au problème poroélastique de départ, et ceux qui présentent un faible couplage constitutif ou visqueux (n modes "non-orthogonaux"). La base modale tronquée est complétée par des modes d'attache, définis comme la réponse du domaine poroélastique à une pression unitaire

successivement imposée à chaque degré de liberté acoustique d'interface, les autres étant restreints,

$$\begin{bmatrix} -\mathbf{A}_{I\mathrm{P}}^T & \mathbf{K}_{\mathrm{P}}^{(1)} \end{bmatrix} \begin{bmatrix} \mathbf{1}_I \\ \mathbf{\Psi}_{\mathrm{P}I} \end{bmatrix} = \begin{bmatrix} \mathbf{0} \end{bmatrix} \Rightarrow \mathbf{\Psi}_{\mathrm{P}I} = \mathbf{K}_{\mathrm{P}}^{(1)^{-1}} \mathbf{A}_{I\mathrm{P}}^T. \tag{A.9}$$

Ainsi, la transformation appliquée au problème (A.7) s'écrit

$$\begin{bmatrix} \widehat{\mathbf{P}}_{\bar{I}} \\ \widehat{\mathbf{P}}_I \\ \widehat{\mathbf{U}}_{\mathrm{P}} \end{bmatrix} = \begin{bmatrix} \mathbf{1}_{\bar{I}} & \mathbf{0} & \mathbf{0} & \mathbf{0} \\ \mathbf{0} & \mathbf{1}_I & \mathbf{0} & \mathbf{0} \\ \mathbf{0} & \mathbf{\Psi}_{\mathrm{P}I} & \mathbf{\Phi}_{\mathrm{P}n} & \mathbf{\Phi}_{\mathrm{P}o} \end{bmatrix} \begin{bmatrix} \widehat{\mathbf{P}}_{\bar{I}} \\ \widehat{\mathbf{P}}_I \\ \widehat{\boldsymbol{\alpha}}_n \\ \widehat{\boldsymbol{\alpha}}_o \end{bmatrix}, \tag{A.10}$$

avec $\widehat{\boldsymbol{\alpha}}_n$ et $\widehat{\boldsymbol{\alpha}}_o$ les coordonnées modales associées aux modes "non-orthogonaux" et "orthogonaux" respectivement. Le symbole $\widehat{\ }$ fait référence à une approximation du vecteur solution.

L'application de la transformation (A.10) au système (A.7) symétrisé donne

$$\left(\left[\begin{array}{c|c|c|c} \frac{1}{\omega^2}\mathbf{K}_{\bar{I}\bar{I}} - \mathbf{M}_{\bar{I}\bar{I}} & \frac{1}{\omega^2}\mathbf{K}_{\bar{I}I} - \mathbf{M}_{\bar{I}I} & \mathbf{0} & \mathbf{0} \\ \hline \frac{1}{\omega^2}\mathbf{K}_{I\bar{I}} - \mathbf{M}_{I\bar{I}} & \frac{1}{\omega^2}\mathbf{K}_{II} - \mathbf{M}_{II} - \mathbf{K}_{\mathrm{P}_{II}}^{(1)} & \mathbf{0} & \mathbf{0} \\ \hline \mathbf{0} & \mathbf{0} & \mathbf{\Omega}_n & \mathbf{0} \\ \hline \mathbf{0} & \mathbf{0} & \mathbf{0} & \mathbf{\Omega}_o \end{array}\right] + \left(\widetilde{K}_{\mathrm{f}} - P_0\right) \begin{bmatrix} \mathbf{0} & \mathbf{0} & \mathbf{0} & \mathbf{0} \\ \mathbf{0} & \mathbf{K}_{\mathrm{P}_{II}}^{(2)} & \mathbf{K}_{\mathrm{P}_{In}}^{(2)} & \mathbf{K}_{\mathrm{P}_{Io}}^{(2)} \\ \mathbf{0} & \mathbf{K}_{\mathrm{P}_{nI}}^{(2)} & \boldsymbol{\kappa}_n & \mathbf{0} \\ \mathbf{0} & \mathbf{K}_{\mathrm{P}_{oI}}^{(2)} & \mathbf{0} & \boldsymbol{\kappa}_o \end{bmatrix} \right.$$
$$\left. + \mathrm{i}\,\omega\,\widetilde{b} \begin{bmatrix} \mathbf{0} & \mathbf{0} & \mathbf{0} & \mathbf{0} \\ \mathbf{0} & \mathbf{C}_{\mathrm{P}_{II}} & \mathbf{C}_{\mathrm{P}_{In}} & \mathbf{C}_{\mathrm{P}_{Io}} \\ \mathbf{0} & \mathbf{C}_{\mathrm{P}_{nI}} & \boldsymbol{\zeta}_n & \mathbf{0} \\ \mathbf{0} & \mathbf{C}_{\mathrm{P}_{oI}} & \mathbf{0} & \boldsymbol{\zeta}_o \end{bmatrix} - \omega^2 \begin{bmatrix} \mathbf{0} & \mathbf{0} & \mathbf{0} & \mathbf{0} \\ \mathbf{0} & \mathbf{M}_{\mathrm{P}_{II}} & \mathbf{M}_{\mathrm{P}_{In}} & \mathbf{M}_{\mathrm{P}_{Io}} \\ \mathbf{0} & \mathbf{M}_{\mathrm{P}_{nI}} & \mathbf{1}_n & \mathbf{0} \\ \mathbf{0} & \mathbf{M}_{\mathrm{P}_{oI}} & \mathbf{0} & \mathbf{1}_o \end{bmatrix} \right) \begin{bmatrix} \widehat{\mathbf{P}}_{\bar{I}} \\ \widehat{\mathbf{P}}_I \\ \widehat{\boldsymbol{\alpha}}_n \\ \widehat{\boldsymbol{\alpha}}_o \end{bmatrix} = \begin{bmatrix} \mathbf{U}_{\mathrm{Fb}} \\ \mathbf{0} \\ \mathbf{0} \\ \mathbf{0} \end{bmatrix}, \tag{A.11}$$

avec pour $\mathbf{B}_{\mathrm{P}} \in \{\mathbf{K}_{\mathrm{P}}^{(1)}, \mathbf{K}_{\mathrm{P}}^{(2)}, \mathbf{C}_{\mathrm{P}}, \mathbf{M}_{\mathrm{P}}\}$,

$$\begin{aligned} \mathbf{B}_{\mathrm{P}_{II}} &= \mathbf{\Psi}_{\mathrm{P}I}^T \mathbf{B}_{\mathrm{P}} \mathbf{\Psi}_{\mathrm{P}I}, \\ \mathbf{B}_{\mathrm{P}_{In}} &= \mathbf{\Psi}_{\mathrm{P}I}^T \mathbf{B}_{\mathrm{P}} \mathbf{\Phi}_{\mathrm{P}n} = \mathbf{B}_{\mathrm{P}_{nI}}^T, \\ \mathbf{B}_{\mathrm{P}_{Io}} &= \mathbf{\Psi}_{\mathrm{P}I}^T \mathbf{B}_{\mathrm{P}} \mathbf{\Phi}_{\mathrm{P}o} = \mathbf{B}_{\mathrm{P}_{oI}}^T. \end{aligned}$$

La transformation est appliquée lors d'une étape initiale, permettant ensuite une résolution par balayage en fréquence sur un problème réduit. Une condensation dynamique des coordonnées modales associées aux modes orthogonaux est également présentée, permettant d'améliorer d'avantage l'efficacité de résolution.

Une étude de convergence est ensuite menée sur une application unidimensionnelle, présentée sur la figure A.9, dont les paramètres matériaux sont donnés dans le tableau A.1. Pour cette exemple, il est montré qu'une convergence satisfaisante est obtenue en incluant les 4 à 6 premiers modes dans la base modale (correspondant ainsi à une troncature à

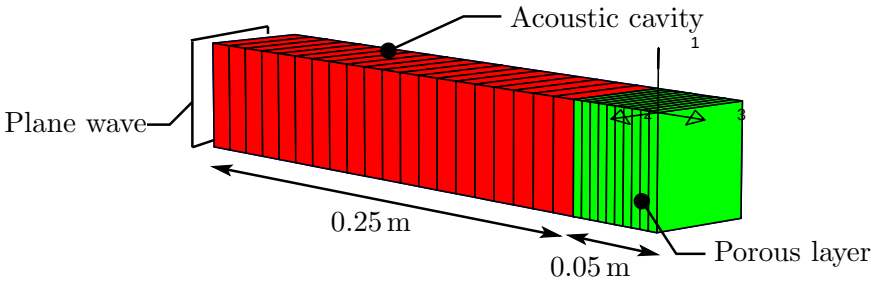

Figure A.9: Maillage et dimensions pour le problème 1D.

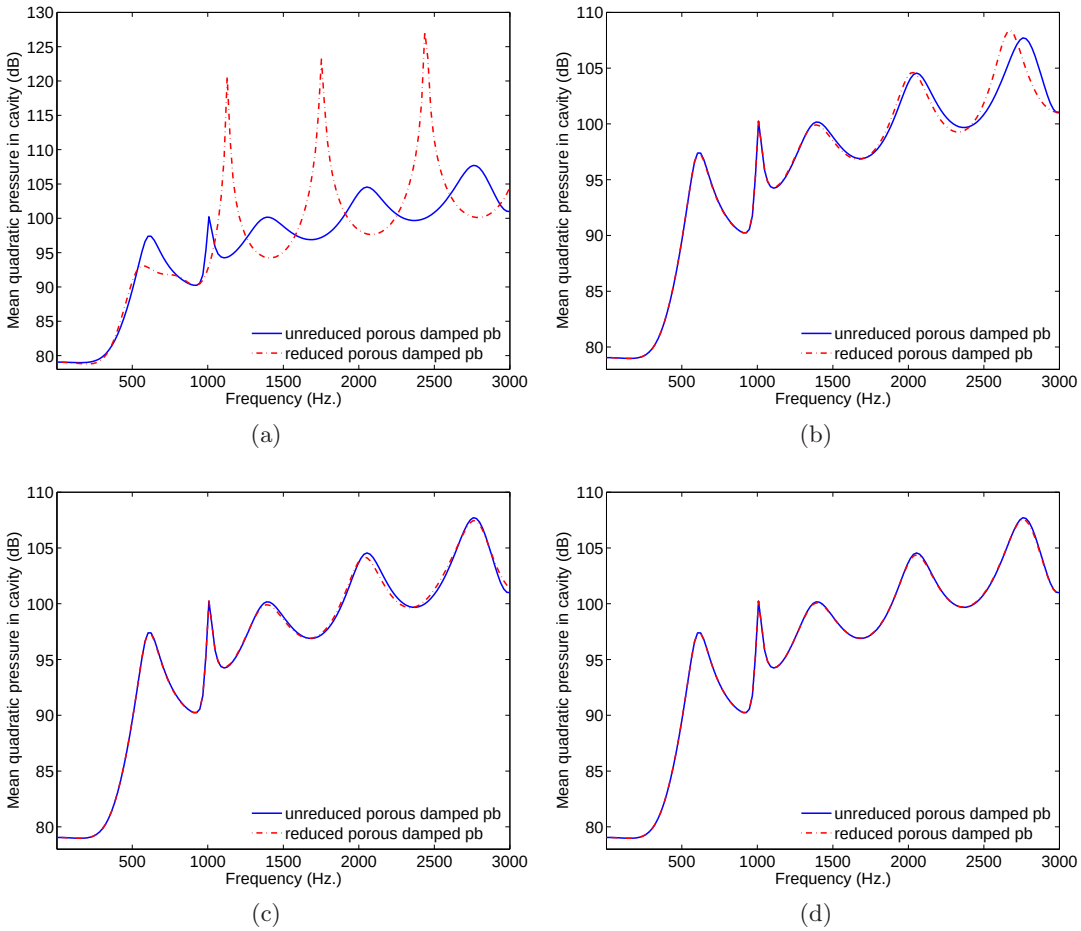

Figure A.10: FRF, pression quadratique moyenne: Convergence du modèle réduit vers la solution de référence: (a) 1 mode, (b) 2 modes, (c) 3 modes, (d) 4 modes.

deux fois la fréquence maximale d'intérêt). La convergence est présentée sur la figure A.10 pour les 4 premiers modes. Un enrichissement de la base modale par une réponse basse fréquence du système est également proposée afin d'accélérer la convergence. Les déformées

Frame	***Fluid***	***Porous***
	$c_0 = 343$ m/s	$\phi = 0.96$
$\lambda = 905357$ Pa	$\gamma = 1.4$	$\sigma = 32$ kNs/m^4
$\mu = 264062$ Pa	$Pr = 0.71$	$\alpha_\infty = 1.7$
$(1-\phi)\rho_\mathrm{s} = 30$ kg/m^3	$\rho_\mathrm{f} = 1.21$ kg/m^3	$\Lambda = 90\ \mu$m
	$\eta = 1.84 \cdot 10^{-5}$ Ns/m^2	$\Lambda' = 165\ \mu$m

Table A.1: Paramètres matériaux pour l'air et le matériau poreux.

modales des 6 premiers modes sont présentées sur la figure A.11. Il apparaît manifeste,

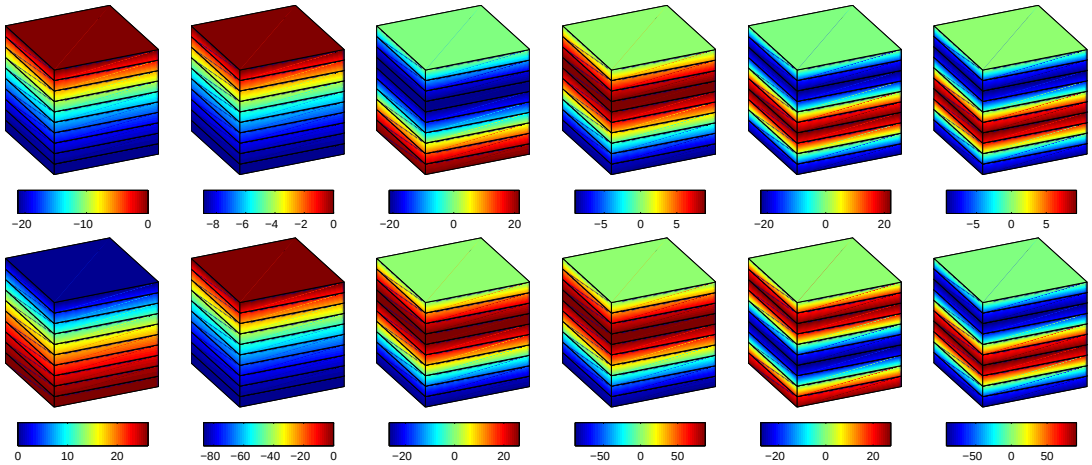

(a) 944 Hz (b) 1136 Hz (c) 2856 Hz (d) 3435 Hz (e) 4839 Hz (f) 5819 Hz

Figure A.11: Six premiers modes de la couche poreuse 1D: (a) – (f), phases solide (haut) et fluide (bas). Maillage et champ de déplacement.

tant par la convergence de la réponse que par l'observation des déformées, que les modes fonctionnent par paires, au sein desquelles le déplacement des phases solides et fluides sont soit en phase, soit en opposition de phase.

Une estimation du potentiel de l'approche modale en termes de performance est réalisée sur un cas test poro-acoustique 3D, présenté sur la figure A.12. Afin d'estimer la performance de la réduction, sont quantifiés la convergence du problème réduit, le remplissage des matrices pour le problème réduit, ainsi qu'une estimation du temps de calcul. Tout d'abord, une convergence satisfaisante est atteinte dans la bande de fréquence $[1-1000]$ Hz pour 800 modes retenus dans la base, comme illustré par la convergence sur la figure A.13. Il apparaît cependant que la convergence n'est pas progressive en bande de fréquence avec l'ajout de modes dans la base. Ainsi, avec 500 modes, la convergence n'est pas satisfaisante au delà de 200 Hz. Cette limite de l'approche est partiellement abordée dans le chapitre

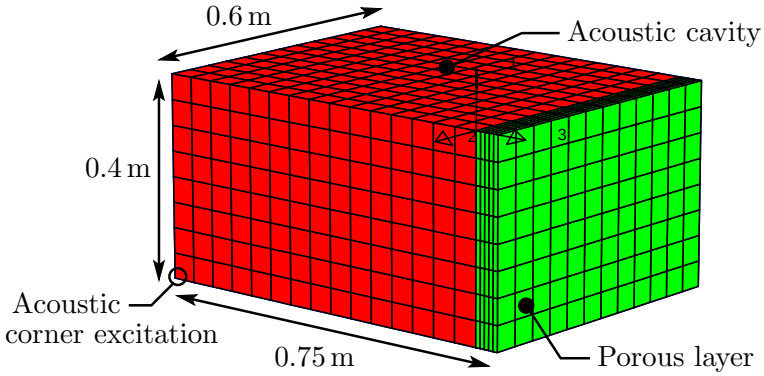

Figure A.12: Maillage et dimensions de la cavité 3D.

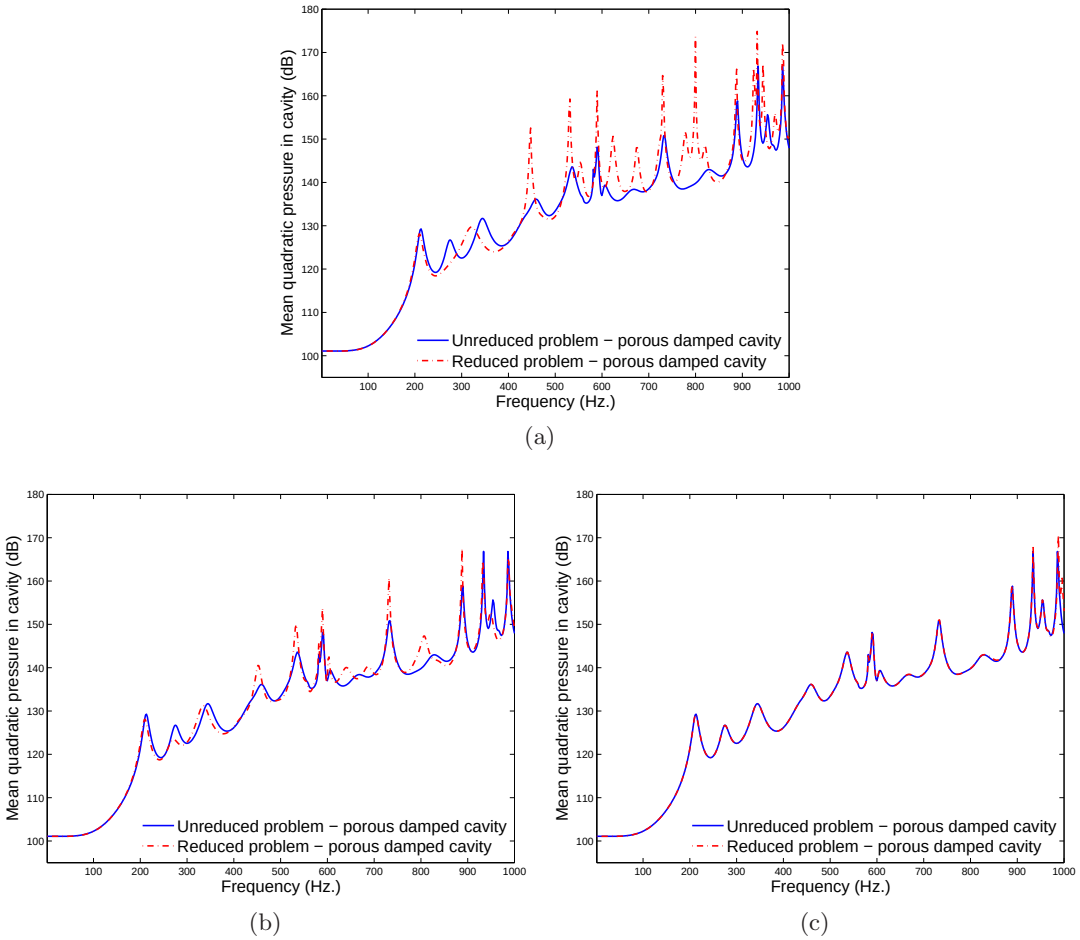

Figure A.13: FRF, pression quadratique moyenne. Convergence du modèle réduit vers la solution de référence: (a) 100 modes, (b) 500 modes, (c) 800 modes.

suivant. Admettant une convergence satisfaisante dans la bande de fréquence d'intérêt, pour 800 modes inclus dans la base modale, la transformation ainsi effectuée permet de

réduire la partie poroélastique du problème de 3070 à 800 degrés de liberté. Le remplissage des matrices éléments finis correspondantes est présenté sur la figure A.14. Ainsi,

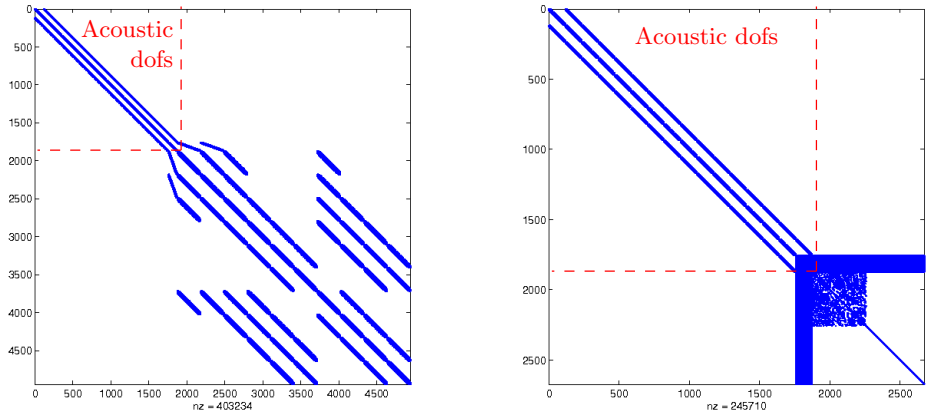

(a) (b)

Figure A.14: Remplissage du système matriciel (a) non-réduit, (b) avec domaine poroélastique réduit.

l'approche modale permet non seulement de réduire le nombre d'inconnues, mais également de conserver le remplissage creux des matrices globales, élément clé de l'efficacité des solveurs utilisés pour la méthode des éléments finis. La combinaison de ces deux critères permet d'anticiper le potentiel d'une telle approche dans son extension à plus grande échelle. La figure A.15 illustre la combinaison d'une réduction du nombre d'inconnues et du remplissage creux des matrices préservé, qui se traduit naturellement par une amélioration du temps de résolution de la réponse. Pour le problème considéré, la résolution par une approche modale s'avère ainsi 2.6 à 3.5 fois plus rapide que la solution de référence, suivant que l'étape initiale soit prise en compte ou non. Dans le cas ou les inconnues associées aux modes orthogonaux sont dynamiquement condensées, le facteur d'accélération de la résolution atteint 3.1 à 4.4 suivant que l'étape initiale soit prise en compte ou non. Ces performances sont améliorées dans le chapitre suivant où un filtrage du contenu de la base modale est proposé.

A.5 Chapitre 4: Classification et sélection des modes poreux significatifs

Dans ce chapitre, la question du contenu de la base modale tronquée, générée par la résolution du problème aux valeurs propres (A.8), est détaillée. En s'appuyant sur des applications poro-acoustiques de moindre complexité (problèmes 2D), une approche est proposée afin d'ordonner les modes de la base en fonction de leur influence dans la

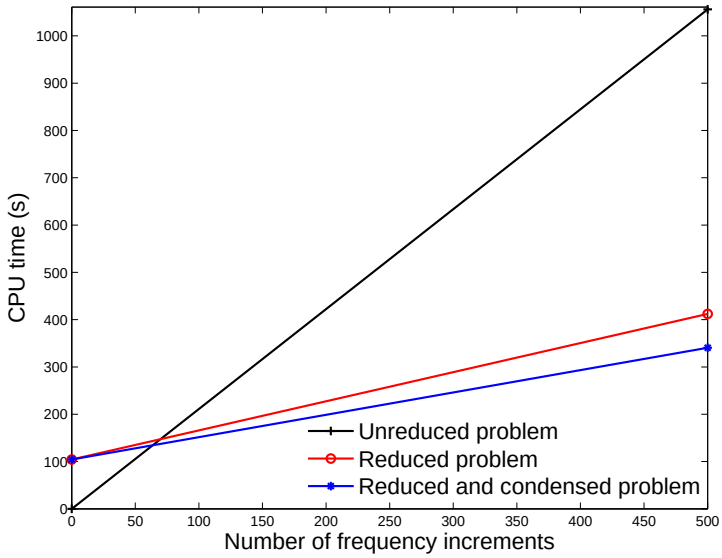

Figure A.15: Comparaison du temps de calcul, CPU, de fonctions de réponse en fréquence.

bande de fréquence d'intérêt, par fréquence croissante. Dans un deuxième temps, après arrangement des modes dans la base, une seconde troncature est proposée afin de ne conserver que les modes ayant une contribution significative pour le problème d'intérêt.

Le principe de sélection des composantes modales significatives est fondé sur leur comparaison avec un résidu en force, calculé à une ou plusieurs fréquences prédéterminées du domaine d'intérêt en fonction de la complexité de la réponse. Ainsi, étant donné une pulsation ω_0, une grossière estimation de la réponse est donnée par la solution du problème projeté sur une base n'incluant que les quelques premiers modes de la base (base modale basse fréquence $\mathbf{\Phi}_{\mathrm{P_{LF}}}$, comprenant par exemple un seul mode). La solution correspondante est donnée par la transformation

$$\begin{bmatrix} \widehat{\mathbf{P}}_{\bar{I}} \\ \widehat{\mathbf{P}}_{I} \\ \widehat{\mathbf{U}}_{\mathrm{P}} \end{bmatrix}_{\omega_0} = \begin{bmatrix} \mathbf{I}_{\bar{I}} & \mathbf{0} & \mathbf{0} \\ \mathbf{0} & \mathbf{I}_{I} & \mathbf{0} \\ \mathbf{0} & \mathbf{\Psi}_{\mathrm{P}I} & \mathbf{\Phi}_{\mathrm{P_{LF}}} \end{bmatrix} \begin{bmatrix} \widehat{\mathbf{P}}_{\bar{I}} \\ \widehat{\mathbf{P}}_{I} \\ \widehat{\boldsymbol{\alpha}}_{\mathrm{LF}} \end{bmatrix}_{\omega_0}, \tag{A.12}$$

où $\widehat{\boldsymbol{\alpha}}_{\mathrm{LF}}$ correspond au vecteur des inconnues modales, de très petite dimension. Cette réponse grossière est donc très efficace à calculer. Si elle ne permet pas une bonne approximation de la réponse, le calcul du résidu associé fournit une excellente source d'information sur les composantes manquantes dans la base modale. Le résidu en force correspondant, suivant le problème (A.7), s'écrit

$$\mathbf{R}_{\mathrm{F_P}}(\omega_0) = \mathbf{A}_{I\mathrm{P}}^{T}\widehat{\mathbf{P}}_{I_{\omega_0}} - \left(\mathbf{K}_{\mathrm{P}}^{(1)} + \left(\widetilde{K}_{\mathrm{f}}(\omega_0) - P_0\right)\mathbf{K}_{\mathrm{P}}^{(2)} + \mathrm{i}\,\omega_0\,\widetilde{b}(\omega_0)\,\mathbf{C}_{\mathrm{P}} - \omega_0^2\mathbf{M}_{\mathrm{P}}\right)\widehat{\mathbf{U}}_{\mathrm{P}_{\omega_0}} \tag{A.13}$$

Le résidu en déplacement associé, fondé sur la limite à fréquence nulle de la matrice de rigidité, $\mathbf{K}_{\mathrm{P}}^{(1)}$, s'écrit

$$\mathbf{R}_{\mathrm{U_P}}(\omega_0) = \mathbf{K}_{\mathrm{P}}^{(1)^{-1}} \mathbf{R}_{\mathrm{F_P}}(\omega_0) \tag{A.14}$$

Ce résidu en déplacement est utilisé pour comparaison aux modes, calculant ainsi la participation modale de chacun par rapport à la partie réelle du résidu en déplacement. Ce calcul peut être complété par une comparaison à la partie imaginaire du résidu, mais n'a pas apporté d'information complémentaire pour les tests effectués. Ainsi, après quelques étapes de calcul, la participation modale de chaque mode i au vecteur résiduel j est donnée par

$$\mu_{ij} = \frac{|\mathbf{\Phi}_{\mathrm{P}i} \cdot \Re(\mathbf{R}_{\mathrm{F}_j})|}{{\omega_i}^2 \|\Re(\mathbf{R}_{\mathrm{F}_j})\|}. \tag{A.15}$$

Écrit ainsi, le calcul des facteurs de participation n'exige que des opération très simples, et ces facteurs ne sont donc pas coûteux à établir. Un ensemble de N modes d'une base donnée est ensuite ordonné par contribution décroissante,

$$\mu_{1j} > \cdots > \mu_{ij} > \cdots > \mu_{\mathrm{N}j}. \tag{A.16}$$

Chaque mode est affecté d'une participation modale normalisée sur la plus petite contribution,

$$\forall\, i \in [1..\mathrm{N}] \;\; \bar{\mu}_{ij} = \frac{\mu_{ij}}{\mu_{\mathrm{N}j}} \geqslant 1. \tag{A.17}$$

Les figures A.16 illustrent la différence de contribution des modes sur le problème 3D considéré dans le chapitre précédent. Il apparaît manifeste, compte tenu des différences

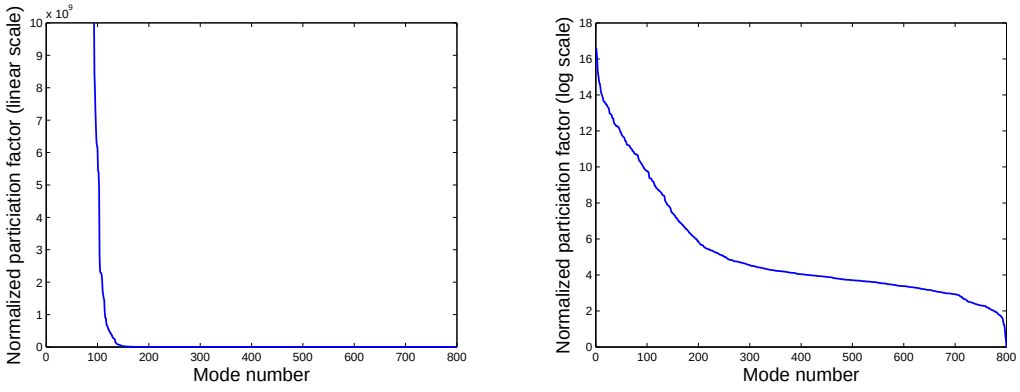

(a) (b)

Figure A.16: Exemple de facteurs de participation modale normalisés: (a) échelle linéaire (b) échelle logarithmique.

observées, que les modes de faible contribution (au delà des 200 premiers modes) peuvent être retirés de la base sans détériorer significativement la précision de la réponse.

Plusieurs approchent ont été testées afin de proposer un critère de troncature de la base ainsi réordonnée, et la solution retenue consiste à établir un rapport de contributions logarithmiques cumulées,

$$\chi_{\mathrm{n}j} = \frac{\sum_{i=1}^{\mathrm{n}} \log(\bar{\mu}_{ij})}{\sum_{i=1}^{\mathrm{N}} \log(\bar{\mu}_{ij})} \leqslant \chi_{\max}, \tag{A.18}$$

avec $\chi_{\max}$ une limite empirique, dans l'intervalle $]0, 1]$. Pour les applications considérées, une limite fixée à 0.4 s'est avérée satisfaisante.

À titre d'illustration, la procédure proposée est présentée sur un exemple poro-acoustique 2D (figure A.17), dont les 26 premières déformées modales sont présentées sur la figure 4.4.

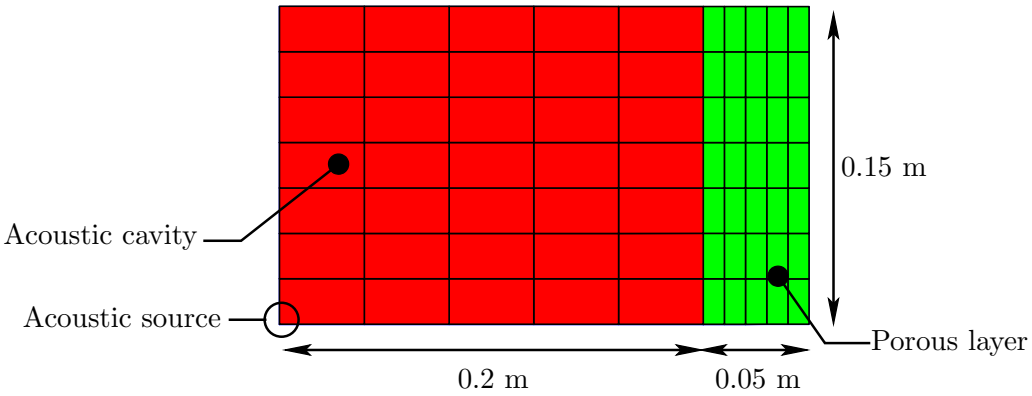

Figure A.17: Maillage et dimensions - problème 2D.

La convergence de l'approche modale telle que présentée dans le chapitre précédent est illustrée sur la figure A.18. En accord avec les observations du chapitre 3, la convergence en ajoutant des modes dans la base ne suit pas strictement la logique d'une fréquence limite de convergence croissante, comme habituellement constaté pour la synthèse modale. Ainsi, 26 modes sont nécessaires pour obtenir une convergence satisfaisante dans le domaine de fréquence [1-1500] Hz.

L'application de la procédure de sélection des contributions modales significatives permet d'extraire les modes présentés dans le tableau A.2, et la figure A.19. Elle est appliquée en calculant un résidu associé à une base modale ne comportant que le premier mode, pour une réponse à la fréquence de 375 Hz, arbitrairement choisie. $\chi_{\max}$ est fixé à 0.4.

La convergence de la solution du problème réduit, utilisant la base modale réordonnée avec la procédure proposée, est présentée figure A.20. Ainsi, l'approche établie a permis d'extraire les composantes modales significatives, qui se trouvent classées suivant leur contribution dans le domaine fréquentiel considéré. Cette procédure a ainsi permis de

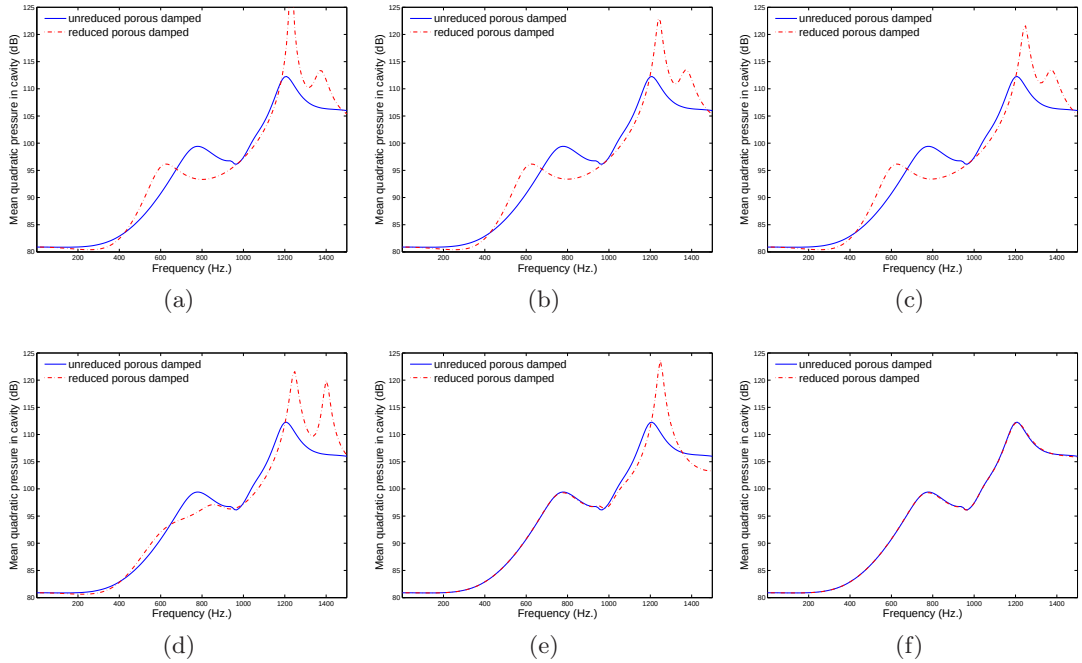

Figure A.18: Convergence - superposition des modes manuellement sélectionnés: (a) Mode 1, (b) Modes $1, 2$; (c) Modes $1, 2, 4, 12$; (d) Modes $1, 2, 4, 12, 15$; (e) Modes 1, 2, 4, 12, 15, 16, 21; (f) Modes $1, 2, 4, 12, 15, 16, 21, 26$

Mode	Fréquence propre (Hz)	μ_{ij}	$\chi_{\mathrm{n}j}$
1	83	(0)	(1)
2	161	12.9	0.06
21	1139	12.0	0.12
15	947	11.9	0.17
4	299	11.1	0.23
12	787	10.4	0.28
26	1343	10.3	0.32
16	951	9.8	0.37
7	468	9.2	0.4

Table A.2: Sélection des contributions modales significatives.

réduire la taille de la base modale de 26 modes à 8 modes.

L'application de cette méthode au problème 3D considéré dans le chapitre 3 permet de réduire la taille de la base modale de 800 à 83 composantes, améliorant ainsi le temps de calcul associé à la réponse du problème réduit.

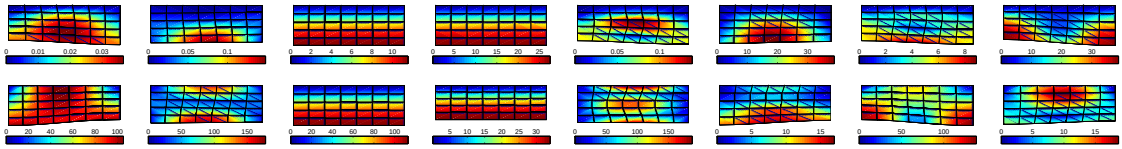

(a) 83 Hz (b) 161 Hz (c) 1139 Hz (d) 947 Hz (e) 299 Hz (f) 787 Hz (g) 1343 Hz (h) 951 Hz

Figure A.19: Déformée des modes poreux 2D sélectionnés 1, 2, 21, 15, 4, 12, 26, 16: phases solide (haut) et fluide (bas). Maillage en configuration déformée et champ de déplacement.

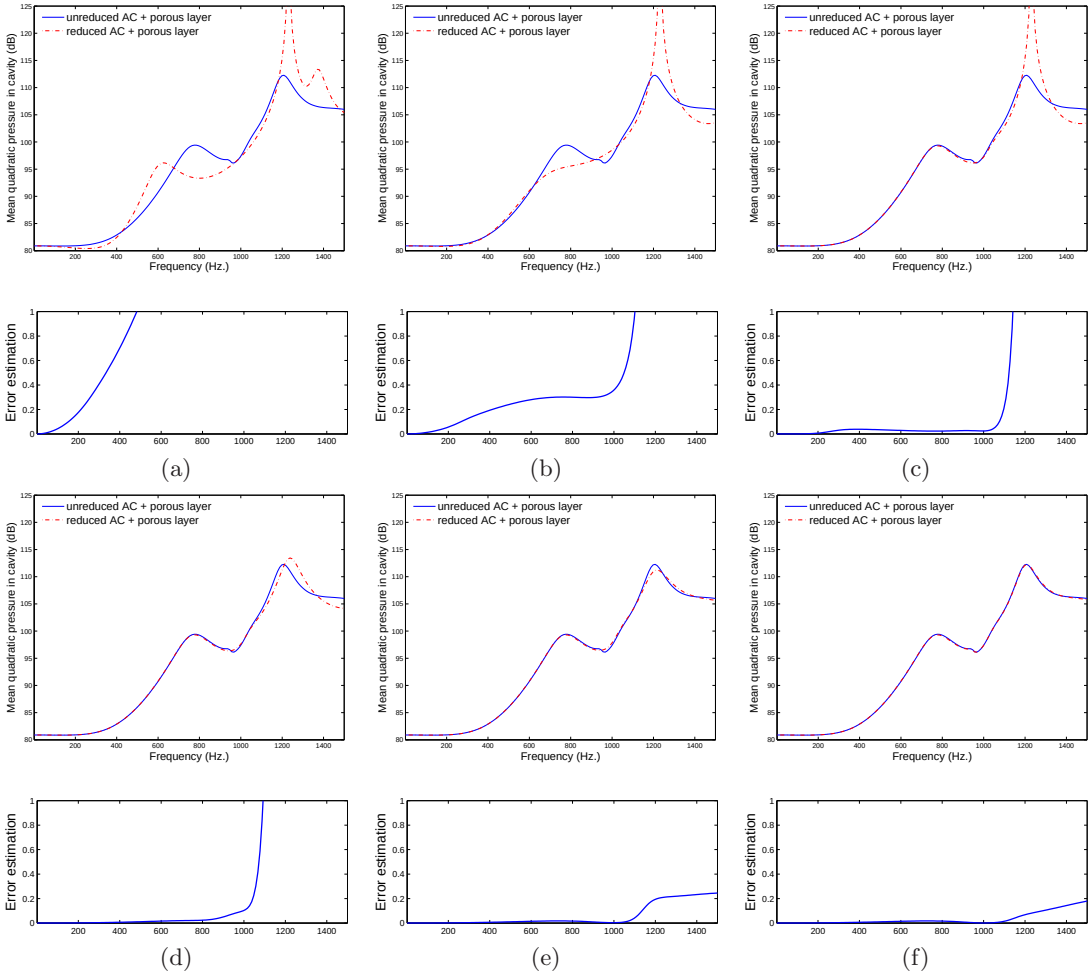

Figure A.20: Convergence - superposition des modes sélectionnés, $\chi_{\max} = 0.4$: (a) Mode 1, (b) Modes 1, 2, 21; (c) Modes 1, 2, 21, 15; (d) Modes $1, 2, 21, 15, 4$; (e) Modes 1, 2, 21, 15, 4, 12, 26; (f) Modes 1, 2, 21, 15, 4, 12, 26, 16

A.6 Chapitre 5: Reconstruction de fonctions de réponse en fréquences par approximants de Padé

Le chapitre 5 est consacré à une approche complémentaire de la synthèse modale, pour la reconstruction rapide de fonctions de réponse en fréquence. La réduction précédemment établie permet de réduire le nombre d'équations à résoudre à chaque incrément de fréquence. Avec l'utilisation d'approximants de Padé pour la reconstruction de la solution, l'objectif est de réduire le nombre de fréquences auxquelles la solution complète doit être calculée, et d'interpoler la solution entre ces fréquences. Cette approche est facilitée par l'expression de la dépendance en fréquence sous la forme de fonctions scalaires en facteur des matrices globales, comme proposé dans cette thèse. Le problème d'intérêt est donc de la forme

$$\mathbf{Z}(\omega)\mathbf{u}(\omega) = \mathbf{F}(\omega), \tag{A.19}$$

avec pour $\omega \neq 0$,

$$\mathbf{Z}(\omega) = \frac{1}{\omega^2}\mathbf{K}_{\mathrm{F}} + \mathbf{A} + \left(\widetilde{K}_{\mathrm{f}}(\omega) - P_0\right)\mathbf{K}_{\mathrm{P}}^{(2)} + \mathrm{i}\,\omega\,\widetilde{b}(\omega)\,\mathbf{C}_{\mathrm{P}} - \omega^2\mathbf{M}_{\mathrm{P}}, \tag{A.20}$$

où $\mathbf{K}_{\mathrm{F}}$, $\mathbf{A}$, $\mathbf{K}_{\mathrm{P}}^{(2)}$, $\mathbf{C}_{\mathrm{P}}$ et $\mathbf{M}_{\mathrm{P}}$ sont des matrices symétriques, constantes, réelles, pour le problème couplé poro-acoustique. Sous cette forme, $\mathbf{A}$ comprend la matrice de "masse" du problème acoustique, les termes de couplage poro-acoustique, ainsi que la matrice de rigidité $\mathbf{K}_{\mathrm{P}}^{(1)}$ du problème poroélastique. À partir d'une solution à ω_0, $\mathbf{U}(\omega_0)$, la solution aux alentours est cherchée sous la forme d'une fraction de développements en séries de Taylor, pour chaque composante u_j du vecteur solution,

$$u(\omega_0 + \Delta\omega) \approx \frac{P_L(\Delta\omega)}{Q_M(\Delta\omega)}. \tag{A.21}$$

$P_L(\Delta\omega)$ et $Q_M(\Delta\omega)$ sont deux séries de Taylor, tronquées à l'ordre L et M respectivement,

$$P_L(\Delta\omega) = \sum_{k=0}^{L} p_k(\Delta\omega)^k, \text{ et } Q_M(\Delta\omega) = \sum_{k=0}^{M} q_k(\Delta\omega)^k. \tag{A.22}$$

L'approximation de $u(\omega_0 + \Delta\omega)$ est donnée par la détermination unique des coefficients p_k et q_k. Une approche efficace afin de déterminer ces coefficients est de les identifier aux coeffcients d'un développement en série de Taylor $A_{L+M}(\Delta\omega)$ à l'ordre $L+M$, autorisant des pôles pour la fonction rationnelle ($Q_M(\Delta\omega) = 0$), soit le système d'équations linéaires suivant à résoudre,

$$P_L(\Delta\omega) - A_{L+M}(\Delta\omega)Q_M(\Delta\omega) = 0, \tag{A.23}$$

Ce système peut se résoudre efficacement sous forme matricielle, impliquant les dérivées jusqu'à l'ordre $L+M$ du vecteur solution,

$$[\mathbf{A}]^{(j)} \begin{bmatrix} p_0 \\ \vdots \\ p_L \\ q_1 \\ \vdots \\ q_M \end{bmatrix}^{(j)} = \begin{bmatrix} u(\omega_0) \\ \vdots \\ u^{(L)}(\omega_0) \\ u^{(L+1)}(\omega_0) \\ \vdots \\ u^{(L+M)}(\omega_0) \end{bmatrix}^{(j)} , \text{ for } j = 1, \ldots, N. \tag{A.24}$$

Ces dérivées successives peuvent être calculées par une formule de récurrence, entraînant la résolution d'un système linéaire à plusieurs second membres, ce qui est d'un point de vue numérique très efficace (une seule décomposition de la matrice de coefficients à effectuer),

$$\mathbf{Z}(\omega_0)\,\mathbf{u}^{(k)}(\omega_0) = \mathbf{f}^{(k)}(\omega_0) - \sum_{j=0}^{(k-1)} \binom{k}{j} \mathbf{Z}^{(k-j)}(\omega_0)\,\mathbf{u}^{(j)}(\omega_0), \text{ for } k = 1, \ldots, (L+M). \tag{A.25}$$

Les détails théoriques et pratiques d'implémentation sont donnés dans la thèse, incluant notamment une approche permettant la reconstruction de la réponse sur un intervalle de fréquence d'intérêt par la reconstruction sur plusieurs intervalles contigus. Ainsi, le problème poro-acoustique 3D considéré dans les chapitres précédents, dans sa version complète ou modale, est résolu par une telle approche, comme illustré sur la figure A.21. Comme illustré sur la figure A.22, la combinaison des deux approches, modèle réduit et interpolation de la réponse par approximants de Padé, permet d'obtenir une estimation de la réponse extrêmement efficace, tout en conservant un excellent degré de précision. L'approche modale devient particulièrement intéressante dans le cas de système à plusieurs cas de charge. Dès lors, l'étape initiale ne doit être effectuée que pour la première résolution, et seule la sélection des modes significatifs, étape peu coûteuse, est mise à jour pour les calculs suivants.

A.7 Chapitre 6: Validations, perspectives et remarques conclusives

Le chapitre 6 est un chapitre de validation, consacré à la mise en oeuvre des méthodes développées dans les chapitre précédents sur une application plus complexe, en termes de géométrie et de comportement dynamique. L'application considérée, présentée sur la figure A.23, est issue des cas tests de validation pour le projet européen Marie-Curie Mid-Frequency. Le détail des calculs ainsi que leur analyse sont détaillés dans la thèse.

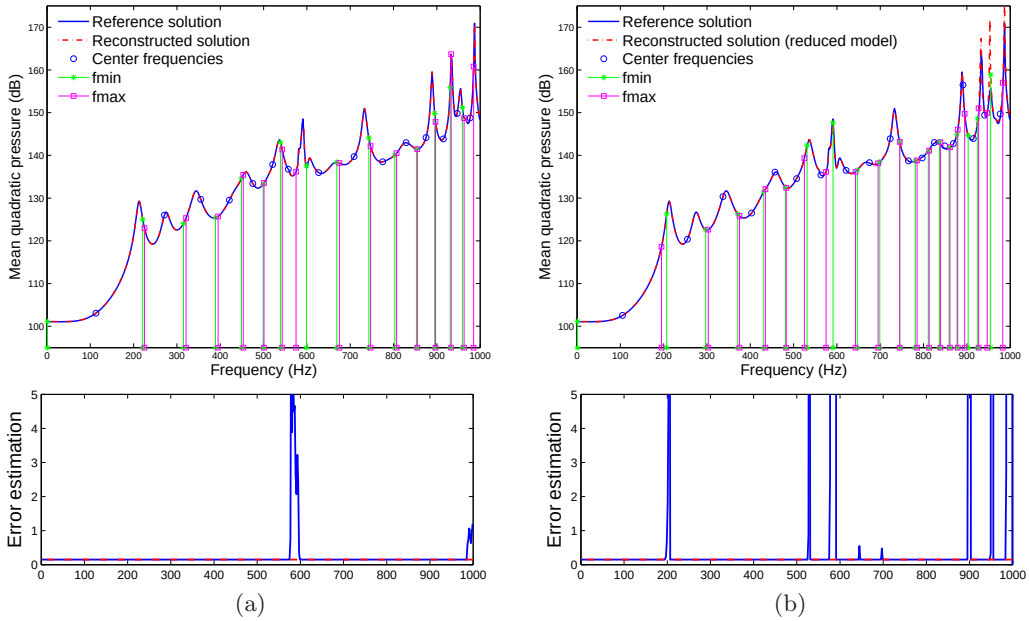

(a) (b)

Figure A.21: Procédure de reconstruction adaptative de la réponse du problème 3D, avec $L = 5$, $M = 6$: (a) problème non réduit; (b) problème réduit.

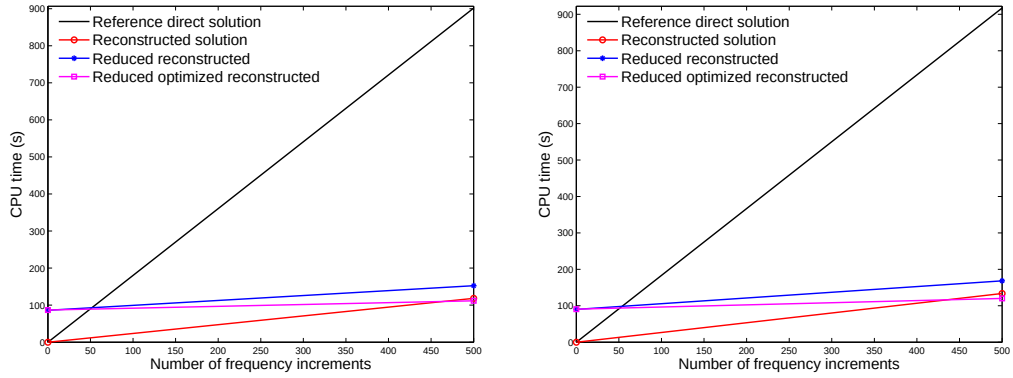

(a) (b)

Figure A.22: Comparaison des temps de calcul avec reconstruction par approximants de Padé, problèmes non réduit, réduit, et réduit optimisé: (a) $L = 3$, $M = 4$; (b) $L = 5$, $M = 6$.

A.8 Conclusion

La présente thèse a permis de mettre en oeuvre deux approches complémentaires pour le traitement efficace de matériaux poreux, décrits par un modèle de Biot, dans le cadre d'applications en vibroacoustique interne. Dans un premier temps, une approche modale originale est proposée, reposant sur des modes couplés réels poreux. Une méthode per-

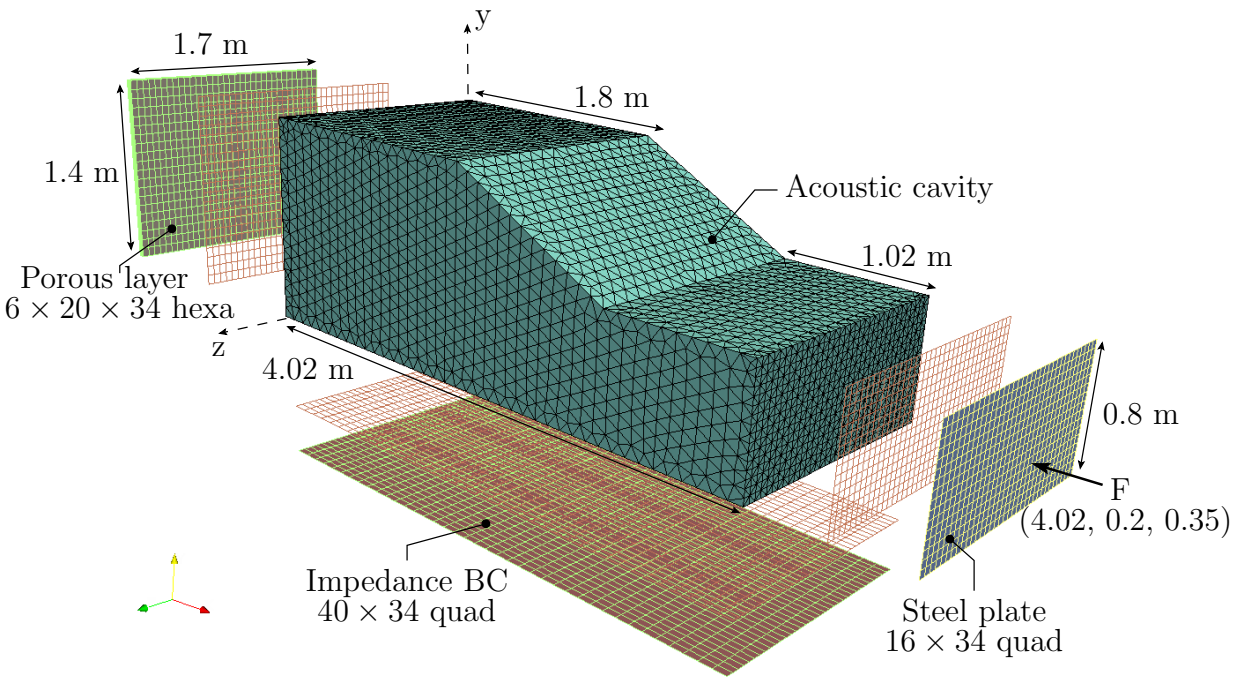

Figure A.23: Géométrie et maillage du modèle éléments finis.

mettant d'extraire les modes significatifs est détaillée afin d'améliorer les performances de la réduction. Dans un second temps, une approche complémentaire est envisagée, dont l'objectif est d'interpoler la solution en fréquence, afin de limiter le calcul de la solution complète à un nombre restreint de fréquences de la bande d'intérêt. Pour cela, une interpolation de la fonction de réponse en fréquence par approximants de Padé est proposée. Les méthodes et leur combinaison sont validées sur des applications simples 1D à 3D, puis étendues à un problème académique plus complexe dans le dernier chapitre.

Parmis les perspectives de travail mentionnées dans la thèse, les suivantes peuvent être soulignées:

- Dans une configuration où la précision de la solution approximée est essentielle, l'utilisation de fonctions d'attache améliorées, ainsi que l'enrichissement de la base de réduction sont des solutions envisageables, proposées dans la littérature en dynamique des structures. L'enjeu est d'établir un compromis entre la précision recherchée, et le coût additionnel engendré par une approche enrichie.

- L'approche modale pour matériaux poreux proposée dans ce travail de thèse doit être étendue et validée dans un cadre plus complexe: (i) dans un configuration où la matrice solide du matériau poreux serait excitée plus directement (e.g. en contact avec une structure flexible, une membrane imperméable), (ii) dans un assemblage

sandwich, où la question du choix du couplage entre couches devient un facteur essentiel de l'efficacité de la méthode modale.

- Une comparaison de l'efficacité des approches proposées à une implémentation de la formulation $(\mathbf{u}_s, p)$ serait également un complément intéressant, et sera inclue lors de la publication de ces travaux dans des revues internationales.

- La génération d'un problème réduit spécifique à chaque bande de fréquence, en combinaison à la reconstruction par approximants de Padé est également une perspective en cours d'étude.

Bibliography

[1] P. Leroy, N. Atalla, A. Berry, and P. Herzog. Three dimensional finite element modeling of smart foam. *The Journal of the Acoustical Society of America*, 126(6):2873–2885, 2009. 1

[2] M. A. Biot. Theory of propagation of elastic waves in a fluid-saturated porous solid. I. Low-frequency range. *The Journal of the Acoustical Society of America*, 28:168–178, 1956. 8, 10, 34, 36

[3] C. Zwikker and C.W. Kosten. *Sound absorbing materials*. Elsevier, 1949. 9

[4] K. Attenborough. Acoustical characteristics of rigid fibrous absorbents and granular materials. *The Journal of the Acoustical Society of America*, 73(3):785–799, 1983. 10

[5] M.E. Delany and E.N. Bazley. Acoustical properties of fibrous absorbent materials. *Applied Acoustics*, 3(2):105–116, 1970. 10

[6] M. A. Biot. Theory of propagation of elastic waves in a fluid-saturated porous solid. II. Higher frequency range. *The Journal of the Acoustical Society of America*, 28(2):179–191, 1956. 10, 34, 36

[7] M. A. Biot. Generalized theory of acoustic propagation in porous dissipative media. *The Journal of the Acoustical Society of America*, 34(9):1254–1264, 1962. 10, 11, 34

[8] D. L. Johnson, J. Koplik, and R. Dashen. Theory of dynamic permeability and tortuosity in Fluid-Saturated porous media. *Journal of Fluid Mechanics*, 176:379–402, 1987. 10, 20, 21

[9] Y. Champoux and J.-F. Allard. Dynamic tortuosity and bulk modulus in air-saturated porous media. *Journal of Applied Physics*, 70(4):1975–1979, 1991. 10, 20, 21

[10] J.-F. Allard. *Sound propagation in porous media: modelling sound absorbing materials*. Elsevier, London, 1993. 10, 11, 13, 22, 24, 34, 36, 69, 70

[11] J.-F. Allard and N. Atalla. *Propagation of sound in porous media: modelling sound absorbing materials*. Wiley, 2009. 11, 12, 20, 21, 22

[12] D. Lafarge, P. Lemarinier, J.-F. Allard, and V. Tarnow. Dynamic compressibility of air in porous structures at audible frequencies. *The Journal of the Acoustical Society of America*, 102(4):1995–2006, 1997. 11, 20, 21

[13] H.J. Rice and P. Göransson. A dynamical model of light fibrous materials. *International journal of mechanical sciences*, 41(4-5):561–579, 1999. 11

[14] P. Khurana, L. Boeckx, W. Lauriks, P. Leclaire, O. Dazel, and J.-F. Allard. A description of transversely isotropic sound absorbing porous materials by transfer matrices. *The Journal of the Acoustical Society of America*, 125(2):915–921, 2009.

[15] P. Göransson, R. Guastavino, and N.-E. Hörlin. Measurement and inverse estimation of 3D anisotropic flow resistivity for porous materials. *Journal of Sound and Vibration*, 327(3-5):354–367, 2009.

[16] N.-E. Hörlin and P. Göransson. Weak, anisotropic symmetric formulations of biot's equations for vibro-acoustic modelling of porous elastic materials. *International Journal for Numerical Methods in Engineering*, 84(12):1519–1540, 2010.

[17] P. Göransson and N.-E. Hörlin. Vibro-acoustic modelling of anisotropic porous elastic materials: a preliminary study of the influence of anisotropy on the predicted performance in a multi-layer arrangement. *Acta Acustica united with Acustica*, 96(2):258–265, 2010. 11

[18] W. Larbi, J. F Deü, and R. Ohayon. A new finite element formulation for internal acoustic problems with dissipative walls. *International Journal for Numerical Methods in Engineering*, 68(3):381–399, 2006. 11

[19] J. F Deü, W. Larbi, and R. Ohayon. Dissipative interface modeling for vibroacoustic Problems-A new symmetric formulation. In *III European Conference on Computational Mechanics*, pages 27–27, 2006.

[20] J.-F Deü, W. Larbi, and R. Ohayon. Vibration and transient response of structural-acoustic interior coupled systems with dissipative interface. *Computer Methods in Applied Mechanics and Engineering*, 197(51-52):4894–4905, 2008. 16

[21] A. Bermúdez and R. Rodríguez. Modelling and numerical solution of elastoacoustic vibrations with interface damping. *International Journal for Numerical Methods in Engineering*, 46(10):1763–1779, December 1999.

[22] A. Bermúdez, L. Hervella-Nieto, and R. Rodríguez. Finite element computation of the vibrations of a plate-fluid system with interface damping. *Computer Methods in Applied Mechanics and Engineering*, 190(24-25):3021–3038, 2001.

[23] B. Faverjon and C. Soize. Equivalent acoustic impedance model. part 1: experiments and semi-physical model. *Journal of Sound and Vibration*, 276(3-5):571–592, 2004.

[24] B. Faverjon and C. Soize. Equivalent acoustic impedance model. part 2: analytical approximation. *Journal of Sound and Vibration*, 276(3-5):593–613, 2004. 11

[25] J.F. Allard, Y. Champoux, and C. Depollier. Modelization of layered sound absorbing materials with transfer matrices. *The Journal of the Acoustical Society of America*, 82:1792–1796, 1987. 11

[26] M. Villot, C. Guigou, and L. Gagliardini. Predicting the acoustical radiation of finite size multi-layered structures by applying spatial windowing on infinite structures. *Journal of sound and vibration*, 245(3):433–455, 2001. 12

[27] S. Ghinet and N. Atalla. Vibro-acoustic behaviour of multi-layer orthotropic panels. *Canadian Acoustics*, 30(3):72–73, 2002. 12

[28] W. Desmet. *A wave based prediction technique for coupled vibro-acoustic analysis*. PhD thesis, K.U.Leuven, division PMA, Leuven, 1998. 12

[29] W. Desmet. Mid-frequency vibro-acoustic modelling: challenges and potential solutions. *Proceedings of ISMA 2002*, 2, 2002. 12

[30] W. Desmet, B. Van Hal, P. Sas, and D. Vandepitte. A computationally efficient prediction technique for the steady-state dynamic analysis of coupled vibro-acoustic systems. *Advances in Engineering Software*, 33(7-10):527–540, 2002.

[31] B. Pluymers, W. Desmet, D. Vandepitte, and P. Sas. Application of an efficient wave-based prediction technique for the analysis of vibro-acoustic radiation problems. *Journal of computational and applied mathematics*, 168(1):353–364, 2004.

[32] B. van Hal, W. Desmet, and D. Vandepitte. Hybrid finite element–wave-based method for steady-state interior structural-acoustic problems. *Computers & Structures*, 83(2-3):167–180, 2005.

[33] B. Pluymers, W. Desmet, D. Vandepitte, and P. Sas. On the use of a wave based prediction technique for steady-state structural-acoustic radiation analysis. *Journal of Computer Modeling in Engineering & Sciences (CMES)*, 7(2):173–184, 2005. 12

[34] E. Deckers, N.-E. Hörlin, D. Vandepitte, and W. Desmet. A novel wave based prediction technique for the efficient dynamic modelling of poro-elastic materials. In *Proceedings of Euronoise*, Edinburgh, Scotland, 2009. 12

[35] E. Deckers, B. Van Genechten, D. Vandepitte, and W. Desmet. Efficient treatment of stress singularities in poroelastic wave based models using special purpose enrichment functions. *Computers & Structures*, 89(11-12):1117–1130, 2011. 12

[36] I. Harari and T. J.R. Hughes. A cost comparison of boundary element and finite element methods for problems of time-harmonic acoustics. *Computer Methods in Applied Mechanics and Engineering*, 97(1):77–102, 1992. 12

[37] J. P. Coyette. The use of finite-element and boundary-element models for predicting the vibro-acoustic behaviour of layered structures. *Advances in Engineering Software*, 30(2):133–139, 1999. 12

[38] A. Craggs. A finite element model for rigid porous absorbing materials. *Journal of Sound and Vibration*, 61(1):101–111, 1978. 13

[39] L. Beranek and L. Ver. *Noise and vibration control engineering: principles and applications*. Wiley. New York, 1992. 13

[40] R. Panneton. *Modélisation numérique tridimensionnelle par éléments finis des milieux poroélastiques*. PhD thesis, University of Sherbrooke, Canada, 1996. 13

[41] M.J. Brennan and W.M. To. Acoustic properties of rigid-frame porous materials – an engineering perspective. *Applied Acoustics*, 62(7):793–811, July 2001. 13

[42] P. Göransson. Acoustic finite element formulation of a flexible porous material-a correction for inertial effects. *Journal of Sound and Vibration*, 185(4):559–580, 1995. 13

[43] Y. J Kang and J. S Bolton. Finite element modeling of isotropic elastic porous materials coupled with acoustical finite elements. *The Journal of the Acoustical Society of America*, 98:635, 1995. 13, 49

[44] R. Panneton and N. Atalla. An efficient finite element scheme for solving the three-dimensional poroelasticity problem in acoustics. *The Journal of the Acoustical Society of America*, 101(6):3287–3298, 1997. 13, 74

[45] N. Dauchez, S. Sahraoui, and N. Atalla. Convergence of poroelastic finite elements based on Biot displacement formulation. *The Journal of the Acoustical Society of America*, 109:33–40, 2001. 13

[46] J.-P. Coyette and H. Wynendaele. A finite element model for predicting the acoustic transmission characteristics of layered structures. In *Proceedings of Inter-noise*, volume 95, pages 1279–1282, 1995. 13

[47] T.F. Johansen, J.-F. Allard, and B. Brouard. Finite element method for predicting the acoustical properties of porous samples. *Acta Acustica*, 3(5):487–491, 1995. 13

[48] P. Göransson. A 3-D, symmetric, finite element formulation of the biot equations with application to acoustic wave propagation through an elastic porous medium. *International Journal for Numerical Methods in Engineering*, 41(1):167–192, 1998. 13

[49] P. Göransson. A weighted residual formulation of the acoustic wave propagation through a flexible porous material and a comparison with a limp material model. *Journal of Sound and Vibration*, 182(3):479–494, 1995. 14

[50] N. Atalla, R. Panneton, and P. Debergue. A mixed displacement-pressure formulation for poroelastic materials. *The Journal of the Acoustical Society of America*, 104:1444–1452, 1998. 14

[51] N. Atalla, M. A. Hamdi, and R. Panneton. Enhanced weak integral formulation for the mixed (u,p) poroelastic equations. *The Journal of the Acoustical Society of America*, 109(6):3065–3068, 2001. 14, 28, 180

[52] N. E Hörlin, M. Nordström, and P. Göransson. A 3-D hierarchical FE formulation of Biot's equations for elasto-acoustic modelling of porous media. *Journal of Sound and Vibration*, 245(4):633–652, 2001. 14

[53] S. Rigobert, N. Atalla, and F. C. Sgard. Investigation of the convergence of the mixed displacement-pressure formulation for three-dimensional poroelastic materials using hierarchical elements. *The Journal of the Acoustical Society of America*, 114:2607–2617, 2003.

[54] S. Rigobert, F. C. Sgard, and N. Atalla. A two-field hybrid formulation for multilayers involving poroelastic, acoustic, and elastic materials. *The Journal of the Acoustical Society of America*, 115(6):2786–2797, 2004.

[55] N. E Hörlin. 3D hierarchical hp-FEM applied to elasto-acoustic modelling of layered porous media. *Journal of Sound and Vibration*, 285(1-2):341–363, 2005. 14

[56] H. J.-P. Morand and R. Ohayon. *Fluid Structure Interaction*. Wiley (Chichester and New York and Paris), 1995. 14, 15, 16, 30, 36, 69

[57] O. Dazel, F. Sgard, C. H Lamarque, and N. Atalla. An extension of complex modes for the resolution of finite-element poroelastic problems. *Journal of Sound and Vibration*, 253(2):421–445, 2002. 15, 31

[58] O. Dazel, F. Sgard, and C. -H. Lamarque. Application of generalized complex modes to the calculation of the forced response of three-dimensional poroelastic materials. *Journal of Sound and Vibration*, 268(3):555–580, 2003. 31

[59] O. Dazel, B. Brouard, N. Dauchez, and A. Geslain. Enhanced Biot's finite element displacement formulation for porous materials and original resolution methods based on normal modes. *Acta Acustica united with Acustica*, 95(3):527–538, 2009. 29, 32, 87

[60] O. Dazel, B. Brouard, N. Dauchez, A. Geslain, and C. H Lamarque. A free interface CMS technique to the resolution of coupled problem involving porous materials, application to a monodimensional problem. *Acta Acustica united with Acustica*, 96(2):247–257, 2010. 15, 32, 87

[61] G. E. Sandberg, P.-A. Hansson, and M. Gustavsson. Domain decomposition in acoustic and structure-acoustic analysis. *Computer Methods in Applied Mechanics and Engineering*, 190(24-25):2979–2988, 2001. 15

[62] W. Larbi. *Modélisation d'interfaces dissipatives intelligentes en interaction fluide-structure: Application aux structures composites de révolution avec fluide interne.* PhD thesis, Conservatoire National des Arts et Métiers, France, 2006. 16

[63] Q.H. Tran. *Analyse robuste et optimisation de problèmes vibroacoustiques avec interfaces absorbantes.* PhD thesis, Université de Franche-Comté, France, 2009. 30, 31, 101

[64] M. Ouisse and E. Sadoulet-Reboul. Efficiency comparison of CMS vibroacoustic formulations for uncertain damped problems. In *Proceedings of the 29th IMAC*, volume 9, pages 161–175, 2011. 15

[65] O.C. Zienkiewicz and R.E. Newton. Coupled vibrations of a structure submerged in a compressible fluid. In *Proccedins of the Symposium on the FEM Technique*, 1969. 15

[66] A. Craggs. The transient response of a coupled plate-acoustic system using plate and acoustic finite elements. *Journal of Sound and Vibration*, 15(4):509–528, 1971.

[67] A. Craggs. The use of simple three-dimensional acoustic finite elements for determining the natural modes and frequencies of complex shaped enclosures. *Journal of Sound and Vibration*, 23(3):331–339, 1972. 15

[68] V. Kehr-Candille and R. Ohayon. Elasto-acoustic damped vibrations-Finite element and modal reduction methods. In *(DGLR and AIAA, Aeroacoustics Conference, 14th, Aachen, Federal Republic of Germany, May 11-14, 1992) ONERA, TP no. 1992-52, 1992, 8 p. Research sponsored by Aerospatiale.*, volume 1, 1992. 15, 16

[69] R. Ohayon. Reduced models for fluid-structure interaction problems. *International Journal for Numerical Methods in Engineering*, 60(1):139–152, 2004. 16, 69

[70] Q. H Tran, M. Ouisse, and N. Bouhaddi. A robust component mode synthesis method for stochastic damped vibroacoustics. *Mechanical Systems and Signal Processing*, 24(1):164–181, 2010. 16, 30, 31, 65, 83, 93, 101

[71] R. Ohayon. Linear vibrations of structures coupled with an internal fluid. *Eccomas School*, 3(7), 2006. 16, 30

[72] G.C. Everstine. A symmetric potential formulation for fluid-structure interaction. *Journal of Sound Vibration*, 79:157–160, 1981. 16

[73] L.G. Olson and K.J. Bathe. Analysis of fluid-structure interactions. a direct symmetric coupled formulation based on the fluid velocity potential. *Computers & Structures*, 21(1-2):21–32, 1985. 16

[74] L. Kiefling and G.C. Feng. Fluid-structure finite element vibrational analysis. *AIAA Journal*, 14:199–203, 1976. 16

[75] A. Bermúdez and R. Rodriguez. Finite element computation of the vibration modes of a fluid-solid system. *Computer Methods in Applied Mechanics and Engineering*, 119(3-4):355–370, 1994. 16

[76] KU Ingard. Locally and nonlocally reacting flexible porous layers - a comparison of acoustical properties. *ASME Journal of Engineering for Industry*, 103:302–313, 1981. 17

[77] N. Atalla and R. Panneton. The effects of multilayer sound-absorbing treatments on the noise field inside a plate backed cavity. *Noise Control Engineering Journal*, 44(5):235–244, 1996. 17

[78] F.X. Bécot and F. Sgard. On the use of poroelastic materials for the control of the sound radiated by a cavity backed plate. *The Journal of the Acoustical Society of America*, 120:2055–2066, 2006. 17

[79] K. Dovstam. Augmented hooke's law in frequency domain. a three dimensional, material damping formulation. *International Journal of Solids and Structures*, 32(19):2835–2852, 1995. 24

[80] P. Göransson. Tailored acoustic and vibrational damping in porous solids-Engineering performance in aerospace applications. *Aerospace Science and Technology*, 12(1):26–41, 2008. 24, 58

[81] O. Dazel, F. Sgard, F. X Becot, and N. Atalla. Expressions of dissipated powers and stored energies in poroelastic media modeled by {u, U} and {u, P} formulations. *The Journal of the Acoustical Society of America*, 123:2054–2063, 2008. 29

[82] O. Dazel, B. Brouard, C. Depollier, and S. Griffiths. An alternative Biot's displacement formulation for porous materials. *The Journal of the Acoustical Society of America*, 121(6):3509–3516, 2007. 29

[83] S. Boily and F. Charron. The vibroacoustic response of a cylindrical shell structure with viscoelastic and poroelastic materials. *Applied Acoustics*, 58(2):131–152, 1999. 30

[84] M. Tournour and N. Atalla. Pseudostatic corrections for the forced vibroacoustic response of a structure-cavity system. *The Journal of the Acoustical Society of America*, 107:2379, 2000. 30, 65

[85] R. R Craig and M. C.C Bampton. Coupling of substructures for dynamic analysis. *AIAA journal*, 6(7):1313–1319, 1968. 30, 43, 180

[86] R. R. Craig and C.-J. Chang. A review of substructure coupling methods for dynamic analysis. *Advances in Engineering Science NASA*, 2:393–408, 1976. 31, 68

[87] R. R. Craig Jr. Substructure methods in vibration. *Journal of Vibration and Acoustics*, 117:207, 1995.

[88] D. Rixen, C. Farhat, and M. Géradin. A two-step, two-field hybrid method for the static and dynamic analysis of substructure problems with conforming and non-conforming interfaces. *Computer methods in applied mechanics and engineering*, 154(3-4):229–264, 1998. 93

[89] D. M. Tran. Component mode synthesis methods using interface modes. application to structures with cyclic symmetry. *Computers & Structures*, 79(2):209–222, 2001.

[90] M. A Tournour, N. Atalla, O. Chiello, and F. Sgard. Validation, performance, convergence and application of free interface component mode synthesis. *Computers & Structures*, 79(20-21):1861–1876, 2001. 54, 93

[91] C. Soize and S. Mziou. Dynamic substructuring in the medium-frequency range. *AIAA journal*, 41(6):1113–1118, 2003.

[92] O. Chiello, F. C. Sgard, and N. Atalla. On the use of a component mode synthesis technique to investigate the effects of elastic boundary conditions on the transmission loss of baffled plates. *Computers & Structures*, 81(28-29):2645–2658, 2003. 54

[93] D.J. Rixen. A dual Craig-Bampton method for dynamic substructuring. *Journal of Computational and applied mathematics*, 168(1):383–391, 2004. 93

[94] K. C. Park and Y. H Park. Partitioned component mode synthesis via a flexibility approach. *AIAA journal*, 42(6), 2004.

[95] D. Markovic, K. C. Park, and A. Ibrahimbegovic. Reduction of substructural interface degrees of freedom in flexibility-based component mode synthesis. *International journal for numerical methods in engineering*, 70(2):163–180, 2007.

[96] D. M Tran. Component mode synthesis methods using partial interface modes: Application to tuned and mistuned structures with cyclic symmetry. *Computers & Structures*, 87(17-18):1141–1153, 2009. 52, 89

[97] R.J. Guyan. Reduction of stiffness and mass matrices. *AIAA journal*, 3(2):380, 1965.

[98] W.C. Hurty. Vibrations of structural systems by component mode synthesis. *Journal of the Engineering Mechanics Division*, 86(4):51–70, 1960.

[99] R.H. MacNeal. A hybrid method of component mode synthesis. *Computers & Structures*, 1(4):581–601, 1971.

[100] S. Rubin. Improved component-mode representation for structural dynamic analysis. *AiAA Journal*, 13:995–1006, 1975. 30

[101] M. Maess and L. Gaul. Substructuring and model reduction of pipe components interacting with acoustic fluids. *Mechanical Systems and Signal Processing*, 20(1):45–64, 2006. 30

[102] E. Balmès. Use of generalized interface degrees of freedom in component mode synthesis. In *Proceedings of IMAC*, pages 204–210, 1996. 31, 93, 114

[103] G. Kergourlay, E. Balmès, and D. Clouteau. Model reduction for efficient FEM/BEM coupling. In *Proceedings of the International Seminar on Modal Analysis*, volume 3, pages 1167–1174, 2001. 97, 101

[104] J. Herrmann, M. Maess, and L. Gaul. Substructuring including interface reduction for the efficient vibro-acoustic simulation of fluid-filled piping systems. *Mechanical Systems and Signal Processing*, 24(1):153–163, 2010. 31, 93, 114

[105] E. Balmès. Optimal ritz vectors for component mode synthesis using the singular value decomposition. *AIAA journal*, 34(6):1256–1260, 1996. 31, 93

[106] E. Balmès. Model reduction for systems with frequency dependent damping properties. *Proceedings of International Modal Analysis Conference*, pages 223–229, 1997.

[107] E. Balmès, M. Corus, and S. Germès. Model validation for heavily damped structures. application to a windshield joint. In *Proceedings of ISMA 2006*, 2006. 101

[108] O. Sauvage, E. Balmès, J. M Lagache, and F. Quique. Simulation des vibrations d'organes moteur complexesa amortissement non-standard par méthodes modales étendues. 2009. 31

[109] P. Davidsson and G. Sandberg. A reduction method for structure-acoustic and poroelastic-acoustic problems using interface-dependent lanczos vectors. *Computer Methods in Applied Mechanics and Engineering*, 195(17-18):1933–1945, 2006. 31, 48, 88

[110] R. L Taylor. FEAP - a finite element analysis program - version 8.2 user manual. 2008. 34

[111] J. L Batoz and M. B Tahar. Evaluation of a new quadrilateral thin plate bending element. *International Journal for Numerical Methods in Engineering*, 18(11):1655–1677, 1982. 46

[112] A. Ibrahimbegovic, R. L Taylor, and E. L Wilson. A robust quadrilateral membrane finite element with drilling degrees of freedom. *International Journal for Numerical Methods in Engineering*, 30(3):445–457, 1990. 46

[113] P. Davidsson. *Structure-acoustic analysis; finite element modelling and reduction methods*. PhD thesis, Lund University, Sweden, 2004. 49

[114] R. Rumpler, A. Legay, and J.-F Deü. Performance of a restrained-interface substructuring FE model for reduction of structural-acoustic problems with poroelastic damping. *Computers & Structures*, 89(23-24):2233–2248, 2011. 74, 92, 93, 173

[115] M. Junge, D. Brunner, J. Becker, and L. Gaul. Interface-reduction for the Craig-Bampton and Rubin method applied to FE-BE coupling with a large fluid-structure interface. *International Journal for Numerical Methods in Engineering*, 77(12):1731–1752, 2009. 89

[116] E. Balmès. Modes and regular shapes. how to extend component mode synthesis theory. *Proceedings of the XI DINAME-Ouro Preto-MG-Brazil*, 2005. 101

[117] G. Masson, B. Ait Brik, S. Cogan, and N. Bouhaddi. Component mode synthesis (CMS) based on an enriched ritz approach for efficient structural optimization. *Journal of Sound and Vibration*, 296(4-5):845–860, 2006. 101

[118] A. Bouazzouni, G. Lallement, and S. Cogan. Selecting a ritz basis for the reanalysis of the frequency response functions of modified structures. *Journal of Sound and Vibration*, 199(2):309–322, 1997. 101

[119] J.K. Bennighof and R.B. Lehoucq. An automated multilevel substructuring method for eigenspace computation in linear elastodynamics. *SIAM Journal on Scientific Computing*, 25(6):2084–2106, 2004. 116

[120] E.L. Wilson, M.-W. Yuan, and J.M. Dickens. Dynamic analysis by direct superposition of Ritz vectors. *Earthquake Engineering & Structural Dynamics*, 10(6):813–821, 1982. 116

[121] R. Djellouli, C. Farhat, and R. Tezaur. A fast method for solving acoustic scattering problems in frequency bands. *Journal of Computational Physics*, 168(2):412–432, 2001. 120, 125

[122] P. Avery, C. Farhat, and G. Reese. Fast frequency sweep computations using a multi-point padé-based reconstruction method and an efficient iterative solver. *International Journal for Numerical Methods in Engineering*, 69(13):2848–2875, 2007. 121, 123, 125, 133

[123] J.D. Chazot, B. Nennig, and A. Chettah. Harmonic response computation of viscoelastic multilayered structures using a ZPST shell element. *Computers & Structures*, 89(23-24):2522–2530, 2011. 120

[124] C.M. Bender and S.A. Orszag. *Advanced mathematical methods for scientists and engineers: Asymptotic methods and perturbation theory*, volume 1. Springer Verlag, 1978. 121

[125] G.A. Baker and P.R. Graves-Morris. *Padé approximants*, volume 59. Cambridge University Press, 1996. 122

[126] B. Cochelin, N. Damil, and M. Potier-Ferry. *Méthode Asymptotique Numérique, une technique de résolution des équations non linéaires*. 2007. 121, 135

[127] D8 - definition of academic validation cases. Technical report, MID-FREQUENCY - CAE Methodologies for Mid-Frequency Analysis in Vibration and Acoustics, www.midfrequency.org, 2011. 148

[128] R. Rumpler, A. Legay, and J.-F Deü. Réduction de problèmes vibro-acoustique avec interfaces dissipatives par décomposition de domaines. In *10e Colloque National en Calcul des Structures*, Giens, France, 2011. 173

[129] R. Rumpler, J.-F. Deü, and P. Göransson. A substructuring FE model for structural-acoustic problems with modal-based reduction of poroelastic interface. In *International Conference on Computational Methods for Coupled Problems in Science and Engineering*, Kos, Greece, 2011. 173

[130] R. Rumpler, J.-F. Deü, and P. Göransson. An enhanced Modal-Based reduction of 3D porous materials modelling for efficient computation of Structural-Acoustic finite element applications. In *International Symposium on the Computational Modelling and Analysis of Vehicle Body Noise and Vibration*, Brighton, England, 2012. 174

[131] R. Rumpler, J.-F. Deü, and P. Göransson. A padé approximant reconstruction scheme for fast resolution of Structural-Acoustic finite element models including porous materials. In *International Conference on Noise and Vibration: Emerging Methods*, Sorrento, Italy, 2012. 174

le cnam

Romain RUMPLER

Efficient Finite Element Approach for Structural-Acoustic Applications including 3D Modelling of Sound Absorbing Porous Materials

KTH VETENSKAP OCH KONST
ROYAL INSTITUTE OF TECHNOLOGY

Résumé :
Dans le contexte de lutte contre les nuisances sonores, cette thèse porte sur le développement de méthodes de résolution efficaces par éléments finis, pour des problèmes de vibroacoustique interne avec interfaces dissipatives, dans le domaine des basses fréquences. L'étude se limite à l'utilisation de solutions passives telles que l'intégration de matériaux poreux homogènes et isotropes, modélisés par une approche fondée sur la théorie de Biot-Allard. Ces modèles étant coûteux en terme de résolution, un des objectifs de cette thèse est de proposer une approche modale pour la réduction du problème poroélastique, bien que l'adéquation d'une telle approche avec le comportement dynamique des matériaux poreux soit à démontrer.
Dans un premier temps, la résolution de problèmes couplés elasto-poro-acoustiques par sous-structuration dynamique des domaines acoustiques et poreux est établie. L'approche modale originale proposée pour les milieux poroélastiques, ainsi qu'une procédure de sélection des modes significatifs, sont validées sur des exemples 1D à 3D.
Une deuxième partie présente une méthode combinant l'utilisation des modèles réduits précédemment établis avec une procédure d'approximation de solution par approximants de Padé. Il est montré qu'une telle combinaison offre la possibilité d'accroître les performances de la résolution (allocation mémoire et ressources en temps de calcul).
Un chapitre dédié aux applications permet d'évaluer et comparer les approches sur un problème académique 3D, mettant en valeur leurs performances encourageantes. Afin d'améliorer les méthodes établies dans cette thèse, des perspectives à ces travaux de recherche sont apportées en conclusion.

Mots clés :
Matériaux poroélastiques, Modèles réduits, Sous-structuration dynamique, Approximants de Padé, Vibroacoustique interne, Éléments finis, Interaction fluid-structure.

Abstract :
In the context of interior noise reduction, the present work aims at proposing Finite Element (FE) solution strategies for interior structural-acoustic applications including 3D modelling of homogeneous and isotropic poroelastic materials, under time-harmonic excitations, and in the low frequency range. A model based on the Biot-Allard theory is used for the poroelastic materials, which is known to be very costly in terms of computational resources. Reduced models offer the possibility to enhance the resolution of such complex problems. However, their applicability to porous materials remained to be demonstrated.
First, this thesis presents FE resolutions of poro-elasto-acoustic coupled problems using modal-based approaches both for the acoustic and porous domains. The original modal approach proposed for porous media, together with a dedicated mode selection and truncation procedure, are validated on 1D to 3D applications.
In a second part, modal-reduced models are combined with a Padé approximants reconstruction scheme in order to further improve the efficiency.
A concluding chapter presents a comparison and a combination of the proposed methods on a 3D academic application, showing promising performances. Conclusions are then drawn to provide indications for future research and tests to be conducted in order to further enhance the methodologies proposed in this thesis.

Keywords :
Noise reduction, Poroelastic materials, Reduced model, Component mode synthesis, Padé approximants, Structural-acoustics, Finite element method, Fluid-structure interaction.